BEILSTEIN JOURNAL OF NANOTECHNOLOGY

# Nanostructures for sensors, electronics, energy and environment III

Edited by Nunzio Motta

# Imprint

Beilstein Journal of Nanotechnology
www.bjnano.org
ISSN 2190-4286
Email: journals-support@beilstein-institut.de

The *Beilstein Journal of Nanotechnology* is published by the Beilstein-Institut zur Förderung der Chemischen Wissenschaften.

Beilstein-Institut zur Förderung der Chemischen Wissenschaften
Trakehner Straße 7–9
60487 Frankfurt am Main
Germany
www.beilstein-institut.de

BEILSTEIN JOURNAL OF NANOTECHNOLOGY

# Nanostructures for sensors, electronics, energy and environment III

Nunzio Motta

Editorial

Open Access

Address:
School of Chemistry, Physics and Mechanical Engineering and Institute for Future Environments, Queensland University of Technology, 2 George St., Brisbane 4001, Australia

Email:
Nunzio Motta - n.motta@qut.edu.au

Keywords:
biosensors; electronics; energy; environment; gas sensors; solar cells

*Beilstein J. Nanotechnol.* **2017,** *8,* 1530–1531.
doi:10.3762/bjnano.8.154

Received: 09 June 2017
Accepted: 28 June 2017
Published: 27 July 2017

This article is part of the Thematic Series "Nanostructures for sensors, electronics, energy and environment III".

Editor-in-Chief: T. Schimmel



This Thematic Series on nanostructures for sensors, electronics, energy and environment is the third edition of the successful series born from the NanoS-E3 conference. The areas of nanoscale science and technology are continually evolving, leading to new approaches for the creation and characterization of nanoscale components.

Nanotechnology spans from the foundation of atomic-scale devices, such as those developed for quantum computing, where single atoms are placed at desired locations (as suggested by Feynman in his famous speech at the American Physical Society meeting in 1959 [1]), to the realm of medicine and pharmacology, where nanoparticles are the carriers of drugs targeted on the disease (i.e., only the sick cells). In the middle there is a plethora of different materials and approaches, including nanotubes and two-dimensional materials such as graphene, and graphene-like materials (e.g., silicene, phosphorene, transition metal dichalcogenides, MXenes), which now number more than 6,000.

The topic of nanoparticles is the focus of this Thematic Series, the use of which spans from biosensing to gas detection and from removing pollutants from water to new generations of solar cells.

The interaction between light and plasma electrons generated by gold nanoparticles is critical for the development of biosensing platforms [2] and for sensors based on surface enhanced Raman scattering [3]. New methods for creating thin films are expected to provide enhanced efficiency in solar cells [4] at a fraction of the cost. This is a growing research field which is very promising to help solve the increasing demand for clean energy in the modern world.

These applications are changing our world, little by little, allowing for example for smaller, less expensive and lighter sensing devices. These, together with more powerful batteries and supercapacitors connected in a smart way to the network, will be part of the “internet of things”, allowing ubiquitous

environmental and health monitoring with immediate access to this critical information from anywhere in the world.

Nanotechnology is bringing forth a technological revolution, which has parallel only in the discovery of thermal engines and in the advent of electronics. The number of applications resulting from this revolution was not imaginable even ten years ago, and this Thematic Series is a small contribution to this goal.

Nuzio Motta

Brisbane, June 2017

## References

1. Feynman, R. *Eng. Sci.* **1960,** *23,* 22–36.
2. Barroso, M. F.; Luna, M. A.; Tabares, J. S. F.; Delerue-Matos, C.; Correa, N. M.; Moyano, F.; Molina, P. G. *Beilstein J. Nanotechnol.* **2016,** *7,* 655–663. doi:10.3762/bjnano.7.58
3. Liu, Z.; Bai, L.; Zhao, G.; Liu, Y. *Beilstein J. Nanotechnol.* **2016,** *7,* 1028–1032. doi:10.3762/bjnano.7.95
4. Kärber, E.; Katerski, A.; Acik, I. O.; Mere, A.; Mikli, V.; Krunks, M. *Beilstein J. Nanotechnol.* **2016,** *7,* 1662–1673. doi:10.3762/bjnano.7.158

## License and Terms

BEILSTEIN JOURNAL OF NANOTECHNOLOGY

# Gold nanoparticles covalently assembled onto vesicle structures as possible biosensing platform

M. Fátima Barroso[1,2], M. Alejandra Luna[1], Juan S. Flores Tabares[1], Cristina Delerue-Matos[2], N. Mariano Correa[1], Fernando Moyano[*1] and Patricia G. Molina[*1]

Full Research Paper

Open Access

Address:
[1]Departamento de Química. Facultad de Ciencias Exactas, Físico-Químicas y Naturales. Universidad Nacional de Río Cuarto. Agencia Postal Nº 3 - (5800) Río Cuarto, Argentina and [2]REQUIMTE/LAQV, Instituto Superior de Engenharia do Porto, Instituto Politécnico do Porto, Rua Dr. António Bernardino de Almeida 431, 4200-072 Porto, Portugal

Email:
Fernando Moyano[*] - fmoyano@exa.unrc.edu.ar; Patricia G. Molina[*] - pmolina@exa.unrc.edu.ar

* Corresponding author

Keywords:
covalently decorated vesicles; gold nanoparticles; immunosensors design; synthesis

*Beilstein J. Nanotechnol.* **2016,** *7,* 655–663.
doi:10.3762/bjnano.7.58

Received: 09 December 2015
Accepted: 15 April 2016
Published: 02 May 2016

This article is part of the Thematic Series "Nanostructures for sensors, electronics, energy and environment III".

Guest Editor: N. Motta



## Abstract

In this contribution a strategy is shown to covalently immobilize gold nanoparticles (AuNPs) onto vesicle bilayers with the aim of using this nanomaterial as platform for the future design of immunosensors. A novel methodology for the self-assembly of AuNPs onto large unilamellar vesicle structures is described. The vesicles were formed with 1,2-dioleoyl-*sn*-glycero-3-phosphocholine (DOPC) and 1-undecanethiol (SH). After, the AuNPs photochemically synthesized in pure glycerol were mixed and anchored onto SH–DOPC vesicles. The data provided by voltammetry, spectrometry and microscopy techniques indicated that the AuNPs were successfully covalently anchored onto the vesicle bilayer and decorated vesicles exhibit a spherical shape with a size of 190 ± 10 nm. The developed procedure is easy, rapid and reproducible to start designing a possible immunosensor by using environmentally friendly procedures.

## Introduction

Vesicles are spherical structures composed primarily of phospholipids and these are organized in bilayers. These vesicles contain an internal aqueous phase and are suspended in an external aqueous phase. Therefore, the vesicles may contain lipophilic substances, which are located in the hydrophobic bilayer as well as water-soluble substances. These structures are the best mimetic agents of biological membranes and represent the environment in which many proteins and enzymes show activity [1,2]. The advantages that the vesicles have over synthetic materials are: lack of toxicity, biodegradability and biocom-

patibility, so that they are utilized as versatile carriers in the fields of medical and analytical applications [1-4]. Several strategies employing vesicles in analytical fields have been reported, namely their use as signal amplifiers in the development of biosensors [3,5] to fulfil performance criteria such as high sensitivity and low limit of detection. In this context, vesicles can be used in the construction of biosensors as supporting film to coat Au or Ag electrodes [3]. Self-assembly of nanoparticles onto organised systems combines the advantages of nanomaterials – very small size, high loading of signal tags, high surface area and dynamic character for signal amplification [6].

Some types of nanomaterials have been self-assembled into vesicle structures for different purposes. Béalle et al. [7] describe the use of super-paramagnetic iron oxide nanoparticles to decorate vesicles that could be used as a model system to illustrate controlled delivery of molecules under mild hyperthermia. These systems were prepared by using cetyltrimethylammonium chloride and myristic acid, and the nanomaterial was synthetized in aqueous alkaline solution by a co-precipitation process of $FeCl_2$ and $FeCl_3$. Using an adsorptive process the vesicles structure was incorporated with super-paramagnetic iron oxide nanoparticles [7]. Additionally, the molecular deposition of silica from water was carried out [8]. Silica-coated unilamellar surfactant vesicles were prepared by hydrolysis and condensation of silicon alkoxides into organized inorganic materials (dioctadecyldimethylammonium bromide and didodecyldimethylammonium bromide).

Thus, gold nanoparticles (AuNPs) form stable complexes with hydrophobic drugs and dyes. These drugs and dyes are successfully released into cells [9]. The AuNPs were prepared in aqueous media, with a diameter of 2.5 nm, and were used to decorate amphiphilic monolayers composed by a hydrophobic alkanethiol and hydrophilic tetraethylene glycol. Furthermore, it was reported the usage of AuNPs of 27 nm of diameter to decorate small receptors composed by per-6-thio-β-cyclodextrin accomplished via covalent gold–thiol bonds [10]. These AuNPs provide an excellent platform for drug delivery due to the functional versatility of their monolayers. The vesicles with AuNPs are suitable for applications such as transport inside cells [11], photodynamic inactivation and also in biosensors [12].

There are many properties that depend on the shape of the nanostructures. In this regard, there have been many studies with different ways to synthesize them [13-17]. For example, tips and edges located in the nanoparticles have regions of high electric fields, which improve the optical effects [16]. Also, nanoparticles with different faces having different densities of adsorption sites and may exhibit different catalytic properties [18].

Some reports [19,20] have demonstrated that metallic nanoparticles (gold and silver) can slowly precipitate in vesicle systems and, in doing so, lose the specific qualities of nanoparticles [21]. Moreover, the conventional synthesis of AuNPs is carried out in water and uses chemicals such as $NaBH_4$, which is toxic and can damage functional groups. In addition, some nanomaterial syntheses need involve high temperatures, which destroy or modify these systems [11].

In this contribution a strategy is shown to covalently immobilize AuNPs onto vesicle bilayers with the aim of using this nanomaterial as a platform for the future design of immunosensors (Figure 1), which can be used to detect different analytes by electrochemical impedance spectroscopy or square wave voltammetry [22,23]. It is known that antibodies can be immobilized onto AuNPs without losing their biological properties [24,25]. Thus, the covalent immobilization of vesicles decorated with AuNPs on a gold surface could increase the amount of immobilized antibodies, which would result in an increase in sensitivity. Moreover, since the conjugate antigen–antibody is broken with changes of the values of pH or ionic strength [25], is very important that the AuNPs are covalently attached to the vesicles. Otherwise, if the binding is electrostatic, the AuNPs will be lost. In this way only the antigen–antibody complex would be broken and the sensor will be reusable.

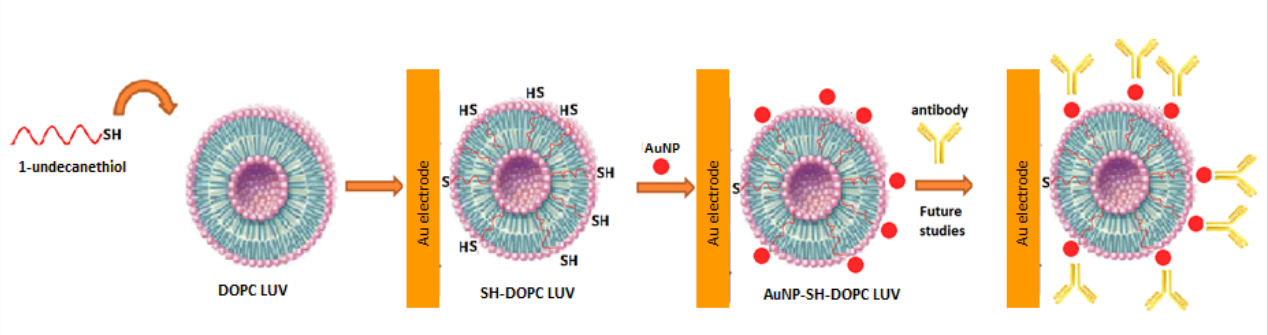


**Figure 1:** Platform to design a possible immunosensor.

Although, the preparation of nanomaterials in aqueous and organic media has been extensively studied, to our knowledge, there are no studies concerning the surface decoration of vesicles by using AuNPs photochemically synthetized in glycerol and using a covalent bond between the nanoparticle and the surface. Recently, we have reported [26] the synthesis of AuNPs in pure glycerol without additional stabilizers and using ultraviolet irradiation for a few minutes. In this synthesis, the glycerol acts as the solvent for the synthesis reaction as well as the reducing agent.

Therefore, this work describes the self-assembly of AuNPs photochemically synthesized with two different irradiation times (8 and 13 min) in glycerol onto vesicle structures. After the optimization of some analytical features of the AuNPs synthesis (irradiation time, $HAuCl_4$ concentration), these AuNPs were covalently immobilized onto large unilamellar vesicles (LUVs) composed by the phospholipid DOPC (1,2-dioleoyl-*sn*-glycero-3-phosphocholine). For this purpose 1-undecanethiol (SH) was incorporated into the bilayer in order to covalently bind the AuNPs to the bilayer and to immobilize the vesicle on the Au electrode. This nanosystem was characterized by using UV–vis spectroscopy, transmission electron microscopy (TEM), dynamic light scattering (DLS) and cyclic voltammetry (CV). The results show that the vesicles were decorated with AuNPs with the advantage that the method is fast, non-polluting and reliable since no nanoparticles extraction is needed. This study offers a basic understanding of a new nanomaterial and its characteristics can help future applications.

## Results and Discussion

This work reports different studies performed on the surface decoration of vesicle structures with AuNPs formed in pure glycerol by using a photochemical process with two irradiation times (8 and 13 min). For that, firstly the AuNP synthesis and the vesicles preparation were carried out. After that the self-assembly of the AuNPs onto modified vesicle structures (SH–DOPC LUVs) was promoted (see Figure 1). Several techniques were used to characterize this new system, which is described below.

### Characterization of AuNPs

Usually, the synthesis of AuNPs is performed in aqueous media by promoting a chemical reaction between a gold precursor and a reducing agent [27,28]. After this chemical process, it is necessary to extract the AuNPs from the reaction media in order to use them in the desired scientific field. Recently, we reported [26] an alternative and simple approach to synthesize AuNPs in an organic medium, namely glycerol, by using a photochemical process instead of a chemical process. Under our experimental conditions, we observed that 8 min is enough to convert $Au^{3+}$ ions in $Au^0$ nanoparticles in glycerol (the typical change of colour from yellow to pink appears). We have seen as a novelty that the nanoparticles are very sensible to the conditions under which they are formed. As the irradiation time modifies the nanoparticle morphology we decided to irradiate for longer time, in this case, 13 min. Some techniques, such as UV–vis spectroscopy and TEM were used to perform the morphological characterization of the AuNPs.

Figure 2 shows the absorption spectra of the glycerol solutions of the metallic precursor and the AuNPs synthesized with different times of irradiation ($\lambda_{irridiation}$ = 300 nm). Glycerol acts as solvent and as the reducing agent and the glycerol oxidation products are able to stabilize the AuNPs [26]. Note, that when the AuNPs are formed after 8 and 13 min of UV irradiation, bands corresponding to the surface plasmon resonance (SPR) around 520 or 550 nm appeared. This maximum wavelength ($\lambda_{max}$) is in accordance with other reported studies [26,29,30], and the small differences founded in the $\lambda_{max}$ may indicate different sizes of the obtained nanoparticles. Besides, the UV–vis spectra exhibit a band half-width of around 50 nm suggesting a narrow size of distribution of AuNPs. We highlight that the AuNPs solutions were prepared without any additional stabilizer and that they remain stable for two months. After this period, $\lambda_{max}$ shifts to the blue (hypsochromic shift) and the solutions turn blue, indicating that the AuNPs are aggregated.

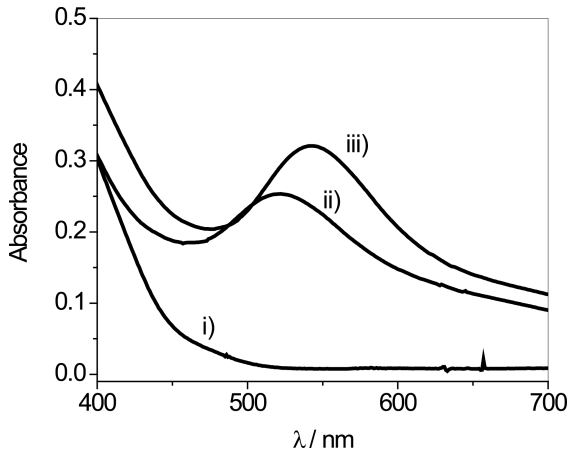


**Figure 2:** UV–vis spectra in glycerol: i) the $HClAu_4$ precursor; ii) the AuNPs synthesized with 8 min of irradiation time; iii) the AuNPs synthesized with 13 min of irradiation time ($\lambda_{irradiation}$ = 300 nm).

In order to show the morphology of the AuNPs, TEM images of different nanoparticles are shown in Figure 3. As it can be observed, the AuNPs formed after 8 min of UV radiation are shape with a size of 10 ± 2 nm (Figure 3i), while the AuNPs formed after 13 min exhibit a hollow spherical shape with a size

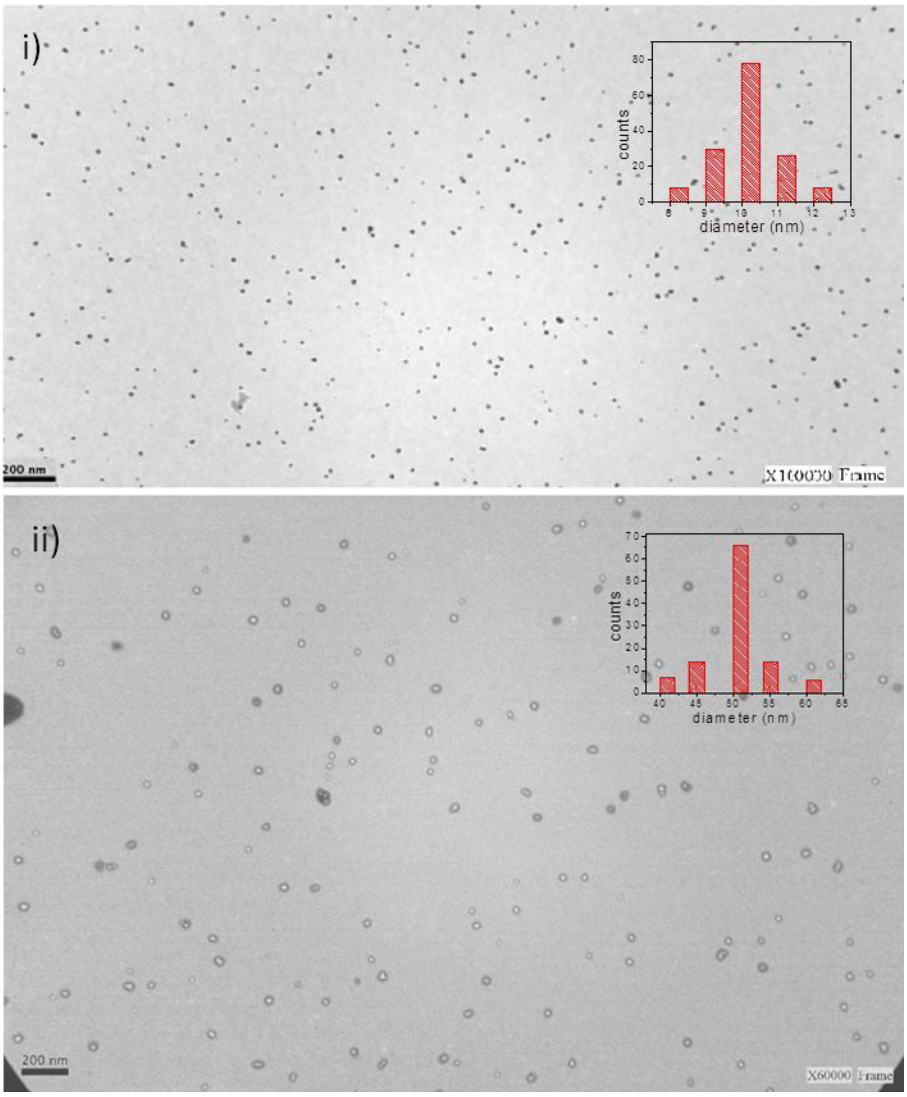


**Figure 3:** TEM images of AuNPs synthesized in glycerol by using ultraviolet irradiation for i) 8 min and ii) 13 min. The inset gives the histograms of diameters of the AuNPs based on the inspection of i) 150 particles and ii) 110 particles.

of 50 ± 10 nm (Figure 3ii). Recently, the hollow nanoparticles have been used in the construction of biosensors because they can accelerate the transfer of electrons due to their excellent electrocatalytic activity [17]. For this reason, studies were conducted to immobilize both types of nanoparticles on the vesicles as will be shown below.

## Characterization of vesicles

### Effect of glycerol on the stability of the vesicles

Considering that the nanoparticles synthesized in glycerol are not extracted from the reaction medium and will be subsequently immobilized on SH–DOPC LUVs, these LUVs were prepared with different percentage of glycerol in order to verify if this organic solvent has some effect on their size measured by DLS.

Figure 4 shows the effect that glycerol content, ranging from 0 to 50% (v/v), has on the diameter and on the polydispersity index of the SH–DOPC LUVs. The sizes of the SH–DOPC LUVs mixed with glycerol were between 145 and 175 nm and the polydispersity index was between 0.20 and 0.25. Therefore, the glycerol has no influence on the size and the polydispersity index of the SH–DOPC LUVs since these values are within the experimental error.

### Optimization of the SH/DOPC ratio for electrochemical measurements

Different SH/DOPC ratios in the formation of vesicles were explored in order to find the optimal conditions for anchoring the AuNPs on the vesicles. The LUV solutions were prepared in the same phosphate buffer solution, which is used for electro-

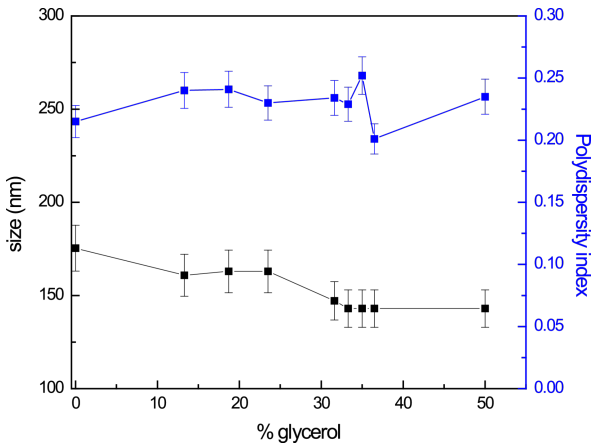


**Figure 4:** Variation of diameter and polydispersity index of SH–DOPC LUVs with glycerol content.

chemical measurements, employing different molar ratios of SH and DOPC as it is described in subsection "Vesicles preparation" of the Experimental section. All diameters of these organized systems were around 175 nm with a polidispersity of 0.2 determined by DLS indicating that the size of the LUVs does not change significantly by the incorporation of SH to the bilayer.

A question may arise here about the orientation of the thiol molecules in the bilayer. That is, whether there are thiol molecules anchored in the bilayer oriented to the outer water phase. CV was used in order to determine the incorporation and orientation of SH in the bilayer of DOPC LUVs since, the SH molecules have the function of immobilizing the AuNPs onto the bilayer and to anchor the decorated vesicles on the Au electrode (AuE). For that, a simple and well-defined redox system was used consisting of $K_4[Fe(CN)_6]$ [26], which first was employed to characterize the surface properties of the AuE modified with the SH–DOPC LUVs without AuNPs.

To perform this electrochemical characterization, firstly a clean AuE surface was exposed and immersed in the SH–DOPC LUV solution for 30 min, enough time to form bonds between AuE and SH/DOPC [25]. This procedure was carried out in order to covalently bond the vesicles on the AuE through the thiol incorporated in the bilayer. Then, the AuE modified with SH–DOPC LUVs was immersed in an aqueous solution of $1.0 \times 10^{-3}$ M $[Fe(CN)_6]^{4-}$ in phosphate buffer solution (pH 7.0) and CV was carried out in the potential range of 0.0–0.4 V vs AgCl/Ag. Figure 5 shows the cyclic voltammograms obtained in these experiments. In Figure 5a a reversible redox peak of $[Fe(CN)_6]^{4-}$ at +0.277 V (anodic potential peak) and +0.210 V (cathodic potential peak) vs AgCl/Ag was observed when a bare AuE or a AuE previously immersed for 30 min in a solution with DOPC LUVs (without the thiol incorporation) was used. This indicates that DOPC LUVs are not adsorbed on the AuE surface. However, when the AuE surface was modified with LUVs formed at different SH/DOPC ratios, a decrease of the peak intensity of $[Fe(CN)_6]^{4-}$ and a displacement of the peak potentials (oxidation and reduction) was observed (Figure 5b). This behaviour can be explained by invoking the resistance to the electron transport generated by the SH–DOPC LUVs covalently bonded to the AuE surface (Figure 1).

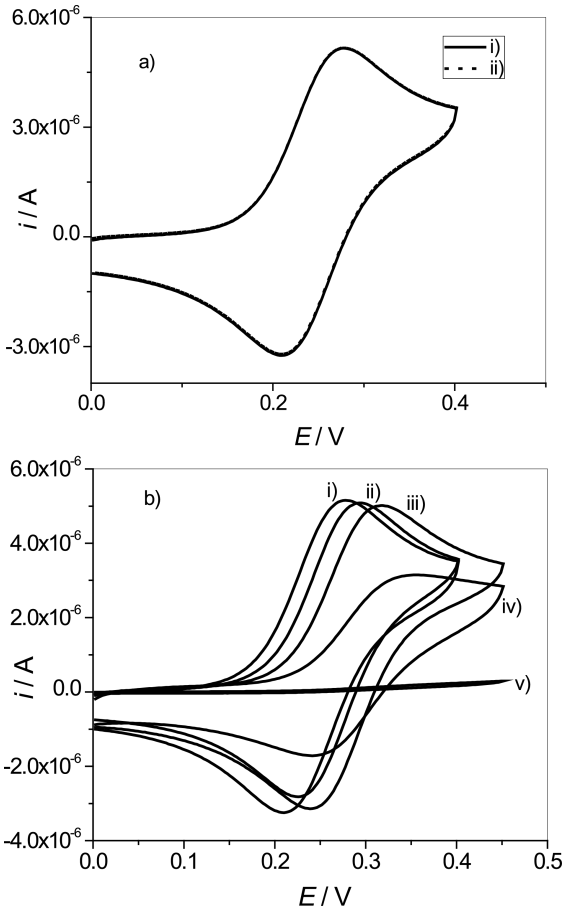


**Figure 5:** Cyclic voltammograms of $K_4[Fe(CN)_6]$ in phosphate buffer solution (pH 7.0) using a) (i) bare AuE , (ii) AuE previously immersed in a solution of DOPC LUVs for 30 min, washed and taken to the electrochemical cell. b) Cyclic voltammograms of $K_4Fe(CN)_6$ in phosphate buffer solution (pH 7.0) by using AuE previously immersed in different SH–DOPC LUV solutions for 30 min, washed and taken to the electrochemical cell. The following SH/DOPC molar ratios were used: i) bare AuE ii) 0.003:1; iii) 0.033:1; iv) 0.33:1 and v) 0.66:1 ($c^*_{K_4[Fe(CN)_6]} = 1 \times 10^{-3}$ M; $v = 100$ mV·s$^{-1}$).

As the SH/DOPC ratio was increased, a decrease of the $[Fe(CN)_6]^{4-}$ peak intensity of the current (oxidation and reduction) was observed. Moreover, at a ratio of SH/DOPC = 0.66:1, the $[Fe(CN)_6]^{4-}$ couple redox peak intensity of the current decreases drastically indicating that the AuE surface was

blocked and the electron transfer between the modified electrode surface and the $[Fe(CN)_6]^{4-}$ is hindered.

The next step was to verify the electrochemical behaviour with regard to $[Fe(CN)_6]^{4-}$ of the decorated vesicles (AuNPs–SH–DOPC LUVs) with AuNPs formed after 8 min anchored on AuE, by using SH/DOPC ratios of 0.33:1 and 0.66:1. Figure 6 shows the electrochemical studies of an electrode modified with AuNPs–SH–DOPC LUVs for both ratios of SH/DOPC. At an SH/DOPC ratio of 0.33:1 a good and reproducible electrochemical signal was obtained (Figure 6i), whereas for the ratio of 0.66:1 the current falls dramatically (Figure 6ii). This means that the 0.66:1 SH:DOPC ratio has limitations considering the use as a platform for an electrochemical immunosensor, since in its development it is required to obtain an electrochemical response that scales with the antigen concentration.

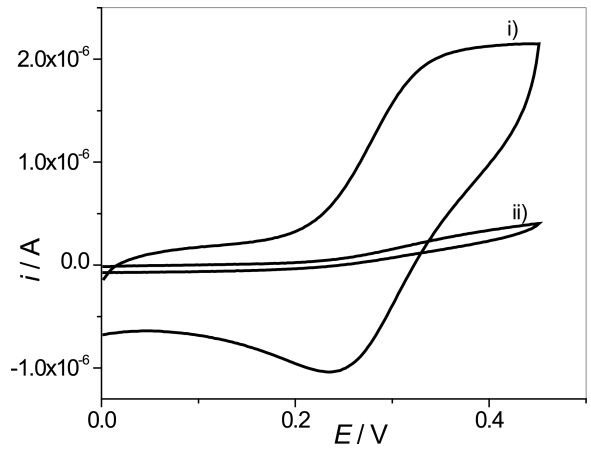


**Figure 6:** Cyclic voltammograms of $K_4[Fe(CN)_6]$ generated in phosphate buffer solution (pH 7.0) by using AuE previously modified with AuNPs–SH–DOPC LUVs using SH/DOPC molar ratios of i) 0.33:1 and ii) 0.66:1 ($c^*_{K_4[Fe(CN)_6]}$ = 1 × $10^{-3}$ M, $v$ = 100 mV·$s^{-1}$).

It should be noted that, the same procedure was performed using modified electrodes with decorated vesicles with AuNPs formed after 13 min but no reproducible voltammograms were obtained (data not shown).

### TEM measurements of AuNPs–SH–DOPC LUVs

In order to obtain the size and the morphology of the AuNPs–SH–DOPC LUV systems, TEM images were recorded. Figure 7a,b shows the TEM images of the AuNPs–SH–DOPC LUVs by using AuNPs formed after 8 min for SH/DOPC ratios of 0.33:1 and 0.66:1, respectively. As can be seen, the AuNPs were successfully anchored on the vesicle structures. Furthermore, the AuNPs anchored on the SH–DOPC LUVs with a molar ratio of 0.33:1 (Figure 7a) present a well-defined morphology with spherical shape and a size of 190 ± 10 nm. Figure 7b shows that surface of the vesicles becomes saturated with AuNPs when a 0.66:1 SH/DOPC ratio is used. This could affect the anchoring of the antibodies in futures studies because a certain spacing of the AuNPs is required for its proper orientation [25]. Figure 7c shows a TEM image of the LUVs decorated with AuNPs formed after 13 min of irradiation. The morphology of the AuNPs anchored on the vesicles shows hollow, nearly spherical structures as it was shown in Figure 3ii but aggregations without defined structures are observed. Hence, the major part of the hollow AuNPs assembles in a non-uniform manner on the vesicles, and the reproducibility of the sensor would be affected.

Based on these results, using AuNPs formed after 8 min of irradiation and a molar SH/DOPC ratio of 0.33:1 yields the following advantages: a) decorated vesicles of regular size are formed, which would favour the reproducibility of the sensor b) AuNPs are conveniently spaced to anchor the antibody correctly and c) – as discussed previously in subsection "Optimization of the SH/DOPC ratio for electrochemical measurements" – the electrochemical signal on the electrode opens the possibility for a future design of an immunosensor.

## Conclusion

In the present work, the covalent self-assembly of AuNPs on vesicles with thiol incorporated in the bilayer was achieved. The developed procedure consisted of mixing AuNPs photochemically synthesized in glycerol media in vesicle structures composed by DOPC and 1-undecanethiol with the different molar ratios. The developed methodology is rapid and easy to perform and provides a non-polluting and sustainable methodology. This nanomaterial offers interesting possibilities and future applications such as its use in the design of immunosensors. Moreover, the developed methodology can be a promising candidate for other applications as optical addressable delivery system and affinity columns.

## Experimental

### Synthesis of gold nanoparticles

AuNPs were synthesized by using a solution of 1.15 × $10^{-3}$ M $HAuCl_4$ (SIGMA, USA) in glycerol (Sintorgan, HPLC grade). Briefly, the solution of $HAuCl_4$ in glycerol was placed in a 2 mL quartz cuvette and exposed to ultraviolet irradiation (300 nm) for 8 or 13 min. The Rayo Net chamber lamps (Model RPR-100) yield 32 W and controlled by dual switches located on the front panel. The dimensions of the reactor chamber were 16 inch depth and 10 inch diameter, with 2/8 inch openings at the top [26]. The AuNPs solutions were of pink color and were stored in a dark glass bottle at 6 °C for further use.

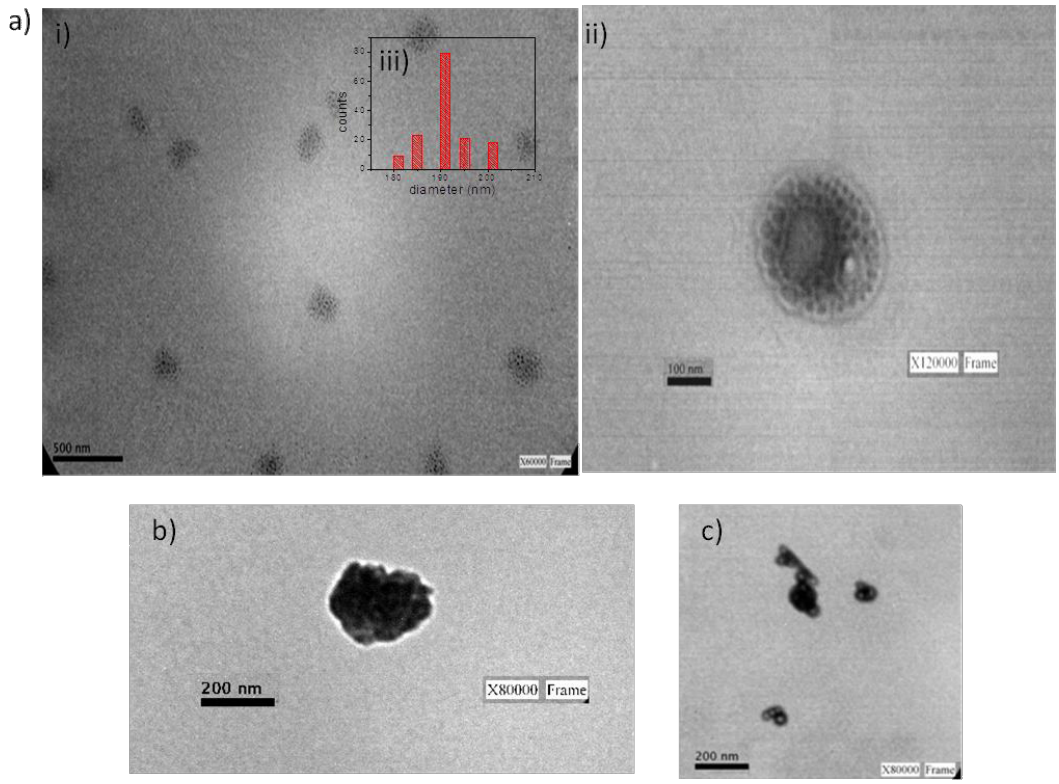


**Figure 7:** TEM images of AuNPs–SH–DOPC LUVs. a) i) and ii) TEM images of AuNPs–SH–DOPC LUVs using AuNPs synthesized in glycerol with 8 min of irradiation time and LUVs prepared with a SH/DOPC molar ratio of 0.33:1. iii) Diameter histograms of the AuNPs–SH–DOPC LUVs based on the inspection of 150 LUVs. b) AuNPs–SH–DOPC LUVs using AuNPs synthesized in glycerol with 8 min of irradiation time and LUVs prepared with a SH/DOPC molar ratio of 0.66:1. c) AuNPs–SH–DOPC LUVs by using AuNPs synthesized in glycerol with 13 min of irradiation time and LUVs prepared with a SH/DOPC molar ratio of 0.33:1.

## Vesicles preparation

The large unilamellar vesicles (LUVs) were formed, at 20.0 ± 0.1 °C, by using the phospholipid 1,2-di-oleoyl-*sn*-glycero-3-phosphatidylcholine (DOPC) which has a phase transition temperature of −17.3 °C [31]. The DOPC solution in chloroform was obtained from Avanti Polar Lipids, Inc., USA. The LUVs of DOPC loaded with 1-undecanethiol (SH) were prepared by the extrusion method [32]. The typical procedure was: a) An appropriate amount of DOPC was transferred into a volumetric flask by using a calibrated microsyringe and then SH solution in chloroform is added to reach the desired concentration (Sigma, USA). Always, the final concentration of DOPC was $1.27 \times 10^{-3}$ M and the SH/DOPC ratios prepared were 0.0033:1; 0.033:1; 0.33:1 and 0.66:1. b) The chloroform was evaporated and the film was dried under reduced pressure. c) Large multilamellar vesicles (LMVs) of SH–DOPC were obtained by hydrating the dry lipid film through mixing (vortex-2-Genie) for about 5 min at room temperature with using ultrapure water (Labconco equipment model 90901-01) or phosphate buffer solution (pH 7.0, Merck) to carry out the morphologic/topographic or the electrochemical studies, respectively.

During the preparation of LUVs the following procedure was followed [1]: The LMV suspension was extruded ten times (Extruder, Lipex biomembranes) through two stacked polycarbonate filters of pore size 200 nm under nitrogen pressure up to 3.4 atm. In order to obtain the decorated vesicles (AuNPs–SH–DOPC LUVs) 5 mL of a solution of SH–DOPC LUVs and 1 mL of different AuNPs glycerol solutions (irradiation times of 8 and 13 min) are mixed and they are allowed to react for 30 min. All samples were used immediately after preparation and the presence of decorated AuNPs–SH–DOPC LUV was verified by different techniques discussed below.

## Nanomaterial characterization

### Dynamic light scattering (DLS)

The diameters of the LUVs were determined by DLS (Malvern 4700 with goniometer and 7132 correlator) with an argon ion laser operating at 488 nm. All the measurements were performed by using a scattering angle of 90° at a temperature of 20.0 ± 0.1 °C. The measurements were made by diluting the samples in a cuvette with distilled water. The water was filtered three times by using an Acrodisc with 0.45 µm Nylon membrane (Agilen) to remove dust or particles. To obtain valid

results from DLS measurements, the knowledge of the refractive index and the viscosity of the system is required in addition to well-defined conditions [33]. Since we worked with diluted solutions, the refractive indices and viscosities for the vesicle solutions were assumed to be the same as those of the external solvent [34]. Multiple samples for each size were made, and thirty independent size measurements were made for each individual sample at the scattering angle of 90°. The instrument was calibrated before and during the course of experiments by using several different size standards. Thus, we are confident that the magnitudes obtained by DLS measurements can be statistically significant for all the systems investigated. The algorithm used was CONTIN and the DLS experiments shown that the polydispersities of the LUVs were less than 5%.

### UV–vis spectroscopy

In order to study the formation of AuNPs, UV–vis studies were performed by using Shimadzu 2401 equipment. The path length used in the absorption measurement was 1 cm.

### Transmission electron microscopy (TEM)

The observation of the TEM micrographs was performed by using a Philips CM-12 microscope at 20–120 kV with a Megaview-II Docu camera and SIS NT Docu software. To carry out the experiment a drop of AuNPs or AuNPs–SH–DOPC LUV was suspended onto a copper coated grid and dried in a desiccator.

### Cyclic voltammetry (CV)

CV was performed with an Autolab PGSTAT 10 potentiostat controlled by GPES software (EcoChemie, Netherlands). A conventional three-electrode cell was used, which included a Au electrode (0.07 $cm^2$) as the working electrode, a Pt counter electrode and a $Ag|AgCl|KCl_{sat}$ reference electrode. Before used, the Au electrode was polished, sonicated and rinsed with ultrapure water. CV measurements were carried out in aqueous media by using as molecular probe $K_4[Fe(CN)_6]$ ($1 \times 10^{-3}$ M) in phosphate buffer solution (pH 7.0) at a scan rate of 100 $mV \cdot s^{-1}$ and using a potential scan between +0.0 and +0.4 V vs AgCl/Ag. For the electrochemical studies, the Au electrode was placed in different DOPC LUV and SH–DOPC LUV solutions for 30 min. Then the Au electrode was rinsed and placed into the cell containing $K_4[Fe(CN)_6]$ ($1 \times 10^{-3}$ M) in a phosphate buffer solution (pH 7.0) to record the voltammograms. For the electrochemical experiments with the decorated vesicles first SH–DOPC LUV were immobilized on the Au electrode as described above, then the modified Au electrode was immersed in the glycerol solution containing the AuNPs for 30 min. The modified Au electrode was subsequently rinsed and taken to the electrochemical cell.

## Acknowledgements

This work was financially supported by Consejo Nacional de Investigaciones Científicas y Técnicas (CONICET), Universidad Nacional de Río Cuarto, and Agencia Nacional de Promoción Científica y Técnica, Marie Curie Actions, International Research Staff Exchange Scheme FP7-PEOPLE-2013-IRSES (612545), and by the European Union (FEDER funds through COMPETE) and National Funds (FCT-Fundação para a Ciência e a Tecnologia) through UID/QUI/50006/2013 and through grants no. PEst-C/EQB/LA0006/2013 and FCOMP-01-0124-FEDER-037285. Fátima Barroso is grateful to FCT by the grant SFRH/BPD/78845/2011, respectively financed by POPH–QREN–Tipologia 4.1–Formação Avançada, subsidized by Fundo Social Europeu and Ministério da Ciência, Tecnologia e Ensino Superior is gratefully acknowledged.

## References

1. Tabares, J. S. F.; Blas, M. L.; Sereno, L. E.; Silber, J. J.; Correa, N. M.; Molina, P. G. *Electrochim. Acta* **2011,** *56,* 10231–10237. doi:10.1016/j.electacta.2011.09.021
2. Patil, Y. P.; Jadhav, S. *Chem. Phys. Lipids* **2014,** *177,* 8–18. doi:10.1016/j.chemphyslip.2013.10.011
3. Liua, Q.; Boyd, B. J. *Analyst* **2013,** *138,* 391–409. doi:10.1039/C2AN36140J
4. Moyano, F.; Biasutti, M. A.; Silber, J. J.; Correa, N. M. *J. Phys. Chem. B* **2006,** *110,* 11838–11846. doi:10.1021/jp057208x
5. Bilek, G.; Kremser, L.; Wruss, J.; Blaas, D.; Kenndler, E. *Anal. Chem.* **2007,** *79,* 1620–1625. doi:10.1021/ac061728m
6. Busseron, E.; Ruff, Y.; Moulin, E.; Giuseppone, N. *Nanoscale* **2013,** *5,* 7098–7140. doi:10.1039/c3nr02176a
7. Béalle, G.; Lartigue, L.; Wilhelm, C.; Ravaux, J.; Gazeau, F.; Podor, R.; Carrière, D.; Ménager, C. *Phys. Chem. Chem. Phys.* **2014,** *16,* 4077–4081. doi:10.1039/c3cp54484b
8. Hubert, D. H. W.; Jung, M.; Frederik, P. M.; Bomans, P. H. H.; Meuldijk, J.; German, A. L. *Adv. Mater.* **2000,** *12,* 1286–1290. doi:10.1002/1521-4095(200009)12:17<1286::AID-ADMA1286>3.0.CO;2-7
9. Kim, C. K.; Ghosh, P.; Pagliuca, C.; Zhu, Z.-J.; Menichetti, S.; Rotello, V. M. *J. Am. Chem. Soc.* **2009,** *131,* 1360–1361. doi:10.1021/ja808137c
10. Park, C.; Youn, H.; Kim, H.; Noh, T.; Kook, Y. H.; Oh, E. T.; Park, H. J.; Kim, C. *J. Mater. Chem.* **2009,** *19,* 2310–2315. doi:10.1039/b816209c
11. Sau, T. K.; Urbana, A. S.; Dondapati, S. K.; Fedoruk, M.; Horton, M. R.; Rogach, A. L.; Stefani, F. D.; Rädler, J. O.; Feldmann, J. *Colloids Surf., A* **2009,** *342,* 92–96. doi:10.1016/j.colsurfa.2009.04.014
12. Viswanathan, S.; Rani, C.; Delerue-Matos, C. *Anal. Chim. Acta* **2012,** *726,* 79–84. doi:10.1016/j.aca.2012.03.025
13. Murphy, C. J.; Sau, T. K.; Gole, A. M.; Orendorff, C. J.; Gao, J.; Gou, L.; Hunyadi, S. E.; Li, T. *J. Phys. Chem. B* **2005,** *109,* 13857–13870. doi:10.1021/jp0516846
14. Burda, C.; Chen, X.; Narayanan, R.; El-Sayed, M. A. *Chem. Rev.* **2005,** *105,* 1025–1102. doi:10.1021/cr030063a
15. Viswanath, B.; Kundu, P.; Halder, A.; Ravishankar, N. *J. Phys. Chem. C* **2009,** *113,* 16866–16883. doi:10.1021/jp903370f
16. Huang, X. H.; Neretina, S.; El-Sayed, M. A. *Adv. Mater.* **2009,** *21,* 4880–4910. doi:10.1002/adma.200802789

17. Zhang, J.; Chen, S.; Ruo, Y.; Zhong, X.; Wu, X. *Anal. Bioanal. Chem.* **2015,** *407,* 447–453. doi:10.1007/s00216-014-8290-x
18. Cuenya, B. R. *Thin Solid Films* **2010,** *518,* 3127–3150. doi:10.1016/j.tsf.2010.01.018
19. Faure, C.; Derreĭ, A.; Neri, W. *J. Phys. Chem. B* **2003,** *107,* 4738–4746. doi:10.1021/jp027449u
20. He, P.; Urban, M. W. *Biomacromolecules* **2005,** *6,* 1224–1225. doi:10.1021/bm0501961
21. Robertson, D.; Tiersch, B.; Kosmella, S.; Koetz, J. *J. Colloid Interface Sci.* **2007,** *305,* 345–351. doi:10.1016/j.jcis.2006.09.079
22. Prodromidis, M. I. *Electrochim. Acta* **2010,** *55,* 4227–4233. doi:10.1016/j.electacta.2009.01.081
23. Liu, X.; Duckworth, P. A.; Wong, D. K. Y. *Biosens. Bioelectron.* **2010,** *25,* 1467–1473. doi:10.1016/j.bios.2009.10.047
24. Liu, S.; Leech, D.; Ju, H. *Anal. Lett.* **2003,** *36,* 1–19. doi:10.1081/AL-120017740
25. Monerris, M. J.; Arévalo, F. J.; Fernández, H.; Zón, M. A.; Molina, P. G. *Sens. Actuators, B* **2015,** *208,* 525–531. doi:10.1016/j.snb.2014.11.048
26. Gobelli, D.; Correa, N. M.; Barroso, M. F.; Moyano, F.; Molina, P. G. *Electroanalysis* **2015,** *27,* 1883–1891. doi:10.1002/elan.201500022
27. Bethell, D.; Brust, M.; Schiffrin, D. J.; Kiely, C. *J. Electroanal. Chem.* **1996,** *409,* 137–143. doi:10.1016/0022-0728(96)04533-0
28. Eastoe, J.; Hollamby, M. J.; Hudson, L. *Adv. Colloid Interface Sci.* **2006,** *128–130,* 5–15. doi:10.1016/j.cis.2006.11.009
29. Chen, H.; Kou, X.; Yang, Z.; Ni, W.; Wang, J. *Langmuir* **2008,** *24,* 5233–5237. doi:10.1021/la800305j
30. Doak, J.; Gupta, R. K.; Manivannan, K.; Ghosh, K.; Kahol, P. K. *Physica E* **2010,** *42,* 1605–1609. doi:10.1016/j.physe.2010.01.004
31. Correa, N. M.; Schelly, Z. A. *Langmuir* **1998,** *14,* 5802–5805. doi:10.1021/la980662q
32. Mayer, L. D.; Hope, M. J.; Cullis, P. R. *Biochim. Biophys. Acta* **1986,** *858,* 161–168. doi:10.1016/0005-2736(86)90302-0
33. Girardi, V. R.; Silber, J. J.; Correa, N. M.; Falcone, R. D. *Colloids Surf., A* **2014,** *457,* 354–362. doi:10.1016/j.colsurfa.2014.05.077
34. Bohidar, H. B.; Behboudina, M. *Colloids Surf., A* **2001,** *178,* 313–323. doi:10.1016/S0927-7757(00)00736-6

## License and Terms

BEILSTEIN JOURNAL OF NANOTECHNOLOGY

# Sandwich-like layer-by-layer assembly of gold nanoparticles with tunable SERS properties

Zhicheng Liu*[1], Lu Bai[2], Guizhe Zhao[1] and Yaqing Liu*[1]

Letter

Open Access

Address:
[1]Shanxi Province Key Laboratory of Functional Nanocomposites, School of Materials Science and Engineering, North University of China, Taiyuan 030051, China and [2]School of Chemical and Environmental Engineering, North University of China, Taiyuan 030051, China

Email:
Zhicheng Liu* - zcliu11@gmail.com; Yaqing Liu* - zfflyq98@163.com

* Corresponding author

Keywords:
assembly; layer-by-layer; multilayer thin film; nanoparticle; polyelectrolyte

*Beilstein J. Nanotechnol.* **2016,** *7,* 1028–1032.
doi:10.3762/bjnano.7.95

Received: 11 March 2016
Accepted: 26 June 2016
Published: 15 July 2016

This article is part of the Thematic Series "Nanostructures for sensors, electronics, energy and environment III".

Guest Editor: N. Motta



## Abstract

Sandwich-like layer-by-layer thin films consisting of polyelectrolytes and gold nanoparticles were utilized to construct surface-enhanced Raman scattering (SERS) substrates with tunable SERS properties. It is found that both the size of the nanoparticles in the layers and the interlayer distance significantly influence the SERS performance of the multilayered thin film. These simple, low-cost, easily processable and controllable SERS substrates have a promising future in the field of molecular sensing.

## Introduction

Surface-enhanced Raman scattering (SERS) spectroscopy, which relies on metal nanostructures made of noble metals (Au, Ag and Cu) that sustain localized surface plasmon resonance (LSPR), is applied as a promising analytical tool for detecting and identifying trace amounts of molecular species [1-3]. The fabrication of excellent SERS substrates using simple and low-cost methods is currently an attractive topic in this field [4]. Engineering metal nanoparticle assemblies with tunable plasmonic coupling properties shows high potential for that purpose [5].

Among various top-down and bottom-up techniques, layer-by-layer (LbL) assembly is a facile and cost-efficient way for the controllable deposition of numerous components [6-8]. Multilayer nanostructures with complex morphologies and functions could be prepared conveniently through the LbL assembly process, which is mainly driven by electrostatic interaction. Especially, multilayer thin films consisting of polymers and metal nanoparticles (NPs) have been extensively explored, and show interesting optical and SERS properties [9-14]. Wang and Dong et al. reported that polyelectrolyte–gold nanorod multilayer thin films could be obtained using LbL assembly techniques via electrostatic interactions [15]. By controlling the number of deposition layers, the plasmonic properties as well as the SERS properties could be tuned easily. Moreover, Kim and co-workers showed that gold nanoparticles (Au NPs) could be

assembled onto polyelectrolyte multilayer films and act as seeds for the following NP growth [16]. The grown NP films were demonstrated to be stable and reproducible SERS substrates. In addition to assembling only one type of NPs, Zhang et al. fabricated bimetallic gold–silver multilayer films by alternating the adsorption of polyethyleneimine–silver ions and Au NPs onto substrates and the subsequent in situ reduction of the silver ions [17]. Compared with the parallel samples, the bimetallic LbL film showed improved SERS properties. Although a few examples of SERS substrates based on LbL strategy have been given, the design and engineering of such SERS substrates is still challenging, and the probing of the structure-dependent SERS performance remains a considerable issue.

Recently, we have shown that highly reproducible and stable SERS substrates could be obtained via LbL assembly of polyelectrolyte and Au NPs [18]. The tuning of SERS intensities was realized by varying the number of deposited Au NP layer. Here, we present that SERS properties of LbL thin film could be controlled by assembling Au NPs of different sizes or changing the interlayer distance between Au NP layers. Sandwich-like LbL thin films with three bilayers, which were fabricated by alternating deposition of polyelectrolytes and Au NPs, are designed to explore the relationship between multilayer nanostructures and SERS performance.

## Experimental

All chemicals such as poly(diallyldimethylammonium chloride) (PDDA, $M_w$ = 200,000–350,000), poly(sodium 4-styrenesulfonate) (PSS, $M_w$ = 70000), and 4-aminothiophenol (4-ATP) were obtained from Sigma-Aldrich and used without further treatment. Negatively charged citrate-stabilized Au NPs were prepared using the classic Turkevich method [19-21]. Briefly, a 50 mL aqueous solution that contained 0.5 mL 1 wt % aqueous $HAuCl_4$ solution was heated to boil under gentle stirring. Then, a certain amount of 1 wt % sodium citrate solution was added quickly. The obtained red-wine colored NP solution was stored at 4 °C and used for the LbL assembly. Hydrophilic quartz slides were used to deposit the first PDDA layer. Sandwich-like LbL thin films were obtained by alternative immersion of PDDA (1 mg/mL, with 1.5 M NaCl, 30 min) and Au NP solution (12 h). After each immersion step, the thin film was rinsed with water and dried under $N_2$. Since only two different sizes of Au NPs were utilized, four kinds of sandwich-like LbL thin films consisting of NP layers of different NP sizes were achieved. The LbL thin film with three layers of small Au NPs is marked as SSS, while the one with three layers of big Au NPs is marked as BBB. Similarly, two other kinds of thin films, namely SBS and BSB, were also obtained. In order to control the interlayer distance between the Au NP layers, different numbers of PDDA/PSS bilayers were inserted into the sandwich-like nanostructure to separate the NP layers. Before SERS measurements, 50 μL of 0.1 mM 4-ATP ethanol solution was dropped on the as-prepared substrate and left to dry in the air.

The as-synthesized Au NP solution was characterized by UV–visible (UV–vis) spectroscopy (Cary 5000). Field emission scanning electron microscopy (FE-SEM, Hitachi S-4800) and transmission electron microscopy (TEM, JEOL JEM 1011) were used to image the LbL thin films and the NPs, respectively. SERS spectra excited at 1064 nm were recorded with a Thermo Nicolet FT-Raman 960 spectrometer at a power of 200 mW. All the spectra were collected by averaging 1024 scans.

## Results and Discussion

Au NPs are regarded as certified and promising nanoscale building blocks for both LbL assembly and SERS substrates. Two different sizes of Au NPs were synthesized by simple control of the added volume of sodium citrate solution. Small Au NPs (17.0 ± 1.2 nm) were obtained when 2 mL sodium citrate solution was injected, while big Au NPs (42.9 ± 5.4 nm) were obtained when 0.65 mL sodium citrate solution was injected, as shown in Figure 1. The optical absorption peaks located at 520 and 532 nm indicate the strong surface plasmon resonance of the NPs. These uniform negatively charged citrate-protected Au NPs could be readily used in electrostatic LbL assembly.

Typical sandwich-like multilayer thin films were prepared by sequential deposition of polyelectrolytes and Au NPs. For example, the BSB thin film formed after the substrate was alternately dipped into PDDA/big Au NP/PDDA/small Au NP/PDDA/big Au NP solutions. From the point of view of Au NPs, these sandwich-like nanostructures are ideal for the evaluation of NP size effects on the SERS performance of NP assemblies. Figure 2 presents the SEM images of the SSS, SBS, BSB and BBB multilayer thin films. Undoubtedly, both small and big Au NPs were assembled into the thin films, and the NP size did not change during the assembly process. It is clear that the sandwich-like LbL assembly of Au NPs occurs via lateral expansion mode, which is consistent with previous results [18,22,23]. Interestingly, compared with the BSB thin film, there were more small Au NPs in the SBS thin film, though the number of big Au NPs was about the same. This phenomenon may result from the steric hindrance of the pre-assembled big Au NPs. In other words, the first big NP layer in the BSB thin film is more unfavorable for the following deposition of small NPs, resulting in less small NPs in the non-stratified thin film. What is more, these LbL thin films are relatively uniform (Figure S1, Supporting Information File 1), which is important for reproducible SERS performance [18].

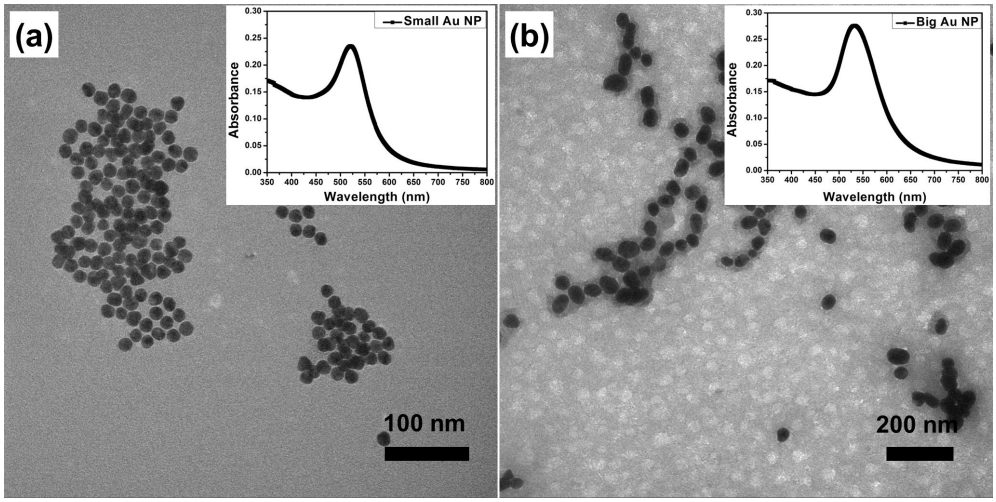


**Figure 1:** TEM images of the obtained Au NPs: (a) small Au NP, (b) big Au NP. The insets show the UV–vis spectra of the corresponding Au NP solutions.

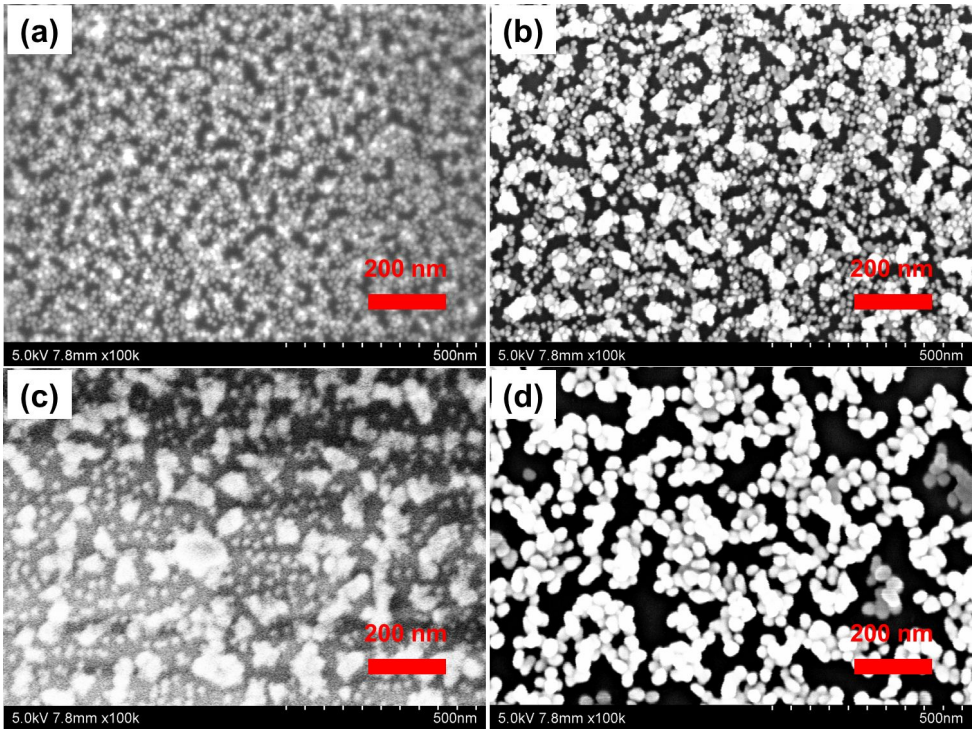


**Figure 2:** SEM images of multilayer thin films consisted of PDDA and Au NPs of different sizes: (a) SSS, (b) SBS, (c) BSB, (d) BBB.

In order to evaluate the SERS performance of the sandwich-like nanostructures, 4-ATP was chosen as SERS probing molecule because of its well-defined Raman vibrational signatures [24]. Figure 3a shows the SERS spectra of the corresponding multilayer thin films. It is noted that the spectra are dominated by the $a_1$ vibration modes, which show distinct peaks at 1587 $cm^{-1}$ ($\nu_{C-C}$) and 1078 $c^{-1}$ ($\nu_{C-S}$). It suggests that the electromagnetic field enhancement dominates the SERS performance [15]. The relative SERS intensities of the films follow the order: BBB > SBS > BSB > SSS. Moreover, the actual SERS performance, which is described by the enhancement factors (EF) of these multilayer thin films, was calculated using the equation $EF = (I_{SERS}/N_{ads})/(I_{bulk}/N_{bulk})$, where $I_{SERS}$ and $I_{bulk}$ are the intensity of a vibrational mode in the SERS spectrum and bulk

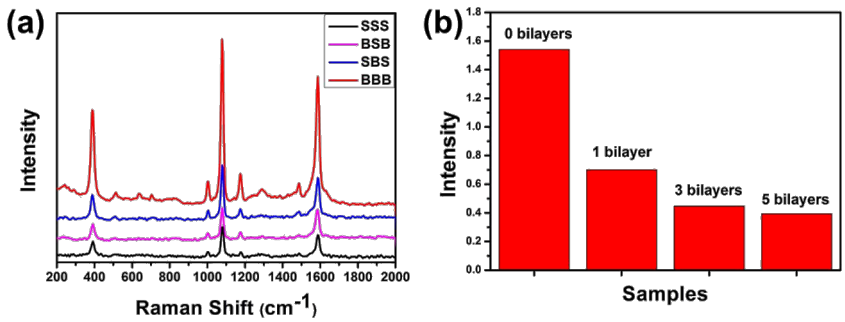


**Figure 3:** (a) SERS spectra of the sandwich-like multilayer thin films; (b) SERS intensity variations at 1078 $cm^{-1}$ for LbL thin films inserted with different numbers of PDDA/PSS bilayers.

sample, and $N_{ads}$ and $N_{bulk}$ are the number of molecules adsorbed on the SERS substrate and bulk molecules excited by the laser, respectively. Using the 1587 $cm^{-1}$ band, the EF values for the SSS, SBS, BSB and BBB thin films are calculated to be about $5.9 \times 10^4$, $5.4 \times 10^4$, $5.0 \times 10^4$ and $3.6 \times 10^4$, respectively (see Supporting Information File 1 for the detailed calculation). It is known that SERS activity is impacted by multiple factors such as size, shape and interparticle coupling of NPs. Compared with the BBB thin film, the increase of the enhancement factor of the SSS thin film could be primarily ascribed to electromagnetic enhancement of increased NP numbers, since there might be more hot-spots in the SSS thin film [25,26]. As shown in Figure 2b and Figure 2c, more hot-spots would also be generated for the SBS thin film, resulting in a better SERS performance than the BSB thin film. Though NP size was demonstrated to greatly impact the SERS performance, it is difficult to obtain dense large NPs layer using the LbL assembly, which is critical for the improved electromagnetic enhancement.

It has been shown that the distance between adjacent NP layers has notable effects on the optical, magnetic and electrochemical properties of LbL NP thin films [27-33]. However, this interesting effect on SERS properties is almost unexplored [34]. Since the interparticle distance may strongly influence the SERS performance, PDDA/PSS bilayers were introduced to separate the neighboring NP layers. Figure 3b displays the SERS intensities at 1078 $cm^{-1}$ for sandwich-like thin films inserted with different numbers of PDDA/PSS bilayers. Obviously, the SERS intensity decreased significantly with increasing number of separating PDDA/PSS bilayers. This is possibly because localized surface plasmon from Au NPs of neighboring layer was not coupled intensively, after the interlayer gap was broadened by inserting bilayers [35]. It is noteworthy that NP layers separated by three polyelectrolyte monolayer provided the strongest SERS signals, as recently presented by Carsten Rockstuhl and co-workers [34]. Nevertheless, the fact that the multilayer NP thin film without separating layers possesses the strongest SERS performance is reasonable, because the thickness of one polyelectrolyte monolayer assembled at high salt concentration (1.5 M NaCl, this work) may be similar to that of three polyelectrolyte monolayers assembled at low salt concentration (0.1 M NaCl, work of Rockstuhl et al.) [36]. Overall, controlling the interlayer distance of the NP layers is another efficient way to tune the SERS properties of multilayer thin films.

## Conclusion

Sandwich-like LbL assemblies of Au NPs were designed as model SERS substrate. The SERS performance could be readily tuned by using Au NPs of different sizes or introducing insert layers with controllable thickness. The methods and strategies involved in this work are rather simple. The fabricated SERS substrates may pave the way for highly efficient and sensitive sensing of small molecules.

## Supporting Information

### Supporting Information File 1

Additional experimental data.
[http://www.beilstein-journals.org/bjnano/content/supplementary/2190-4286-7-95-S1.pdf]

## Acknowledgements

This work was supported by National Natural Science Foundation of China (Grant 21444005, 21504083 and 21505123) and Scientific and Technological Innovation Programs of Higher Education Institutions in Shanxi.

## References

1. Schlücker, S. *Angew. Chem., Int. Ed.* **2014,** *53,* 4756–4795. doi:10.1002/anie.201205748
2. Moskovits, M. *Phys. Chem. Chem. Phys.* **2013,** *15,* 5301–5311. doi:10.1039/c2cp44030j

3. Pieczonka, N. P. W.; Aroca, R. F. *Chem. Soc. Rev.* **2008,** *37,* 946–954. doi:10.1039/b709739p
4. Ko, H.; Singamaneni, S.; Tsukruk, V. V. *Small* **2008,** *4,* 1576–1599. doi:10.1002/smll.200800337
5. Tong, L.; Zhu, T.; Liu, Z. *Chem. Soc. Rev.* **2011,** *40,* 1296–1304. doi:10.1039/C001054P
6. Jiang, C.; Tsukruk, V. V. *Adv. Mater.* **2006,** *18,* 829–840. doi:10.1002/adma.200502444
7. Borges, J.; Mano, J. F. *Chem. Rev.* **2014,** *114,* 8883–8942. doi:10.1021/cr400531v
8. Richardson, J. J.; Björnmalm, M.; Caruso, F. *Science* **2015,** *348,* 411. doi:10.1126/science.aaa2491
9. Abalde-Cela, S.; Ho, S.; Rodríguez-González, B.; Correa-Duarte, M. A.; Álvarez-Puebla, R. A.; Liz-Marzán, L. M.; Kotov, N. A. *Angew. Chem., Int. Ed.* **2009,** *48,* 5326–5329. doi:10.1002/anie.200901807
10. Bao, Y.; Vigderman, L.; Zubarev, E. R.; Jiang, C. *Langmuir* **2012,** *28,* 923–930. doi:10.1021/la203993m
11. Tian, R.; Li, M.; Teng, H.; Luo, H.; Yan, D.; Wei, M. *J. Mater. Chem. C* **2015,** *3,* 5167–5174. doi:10.1039/C4TC02714K
12. Aoki, P. H. B.; Alessio, P.; De Saja, J. A.; Constantino, C. J. L. *J. Raman Spectrosc.* **2010,** *41,* 40–48. doi:10.1002/jrs.2415
13. dos Santos, D. S.; Goulet, P. J. G.; Pieczonka, N. P. W.; Oliveira, O. N.; Aroca, R. F. *Langmuir* **2004,** *20,* 10273–10277. doi:10.1021/la048328j
14. Zhang, F.; Srinivasan, M. P. *J. Colloid Interface Sci.* **2008,** *319,* 450–456. doi:10.1016/j.jcis.2007.12.008
15. Hu, X.; Cheng, W.; Wang, T.; Wang, Y.; Wang, E.; Dong, S. *J. Phys. Chem. B* **2005,** *109,* 19385–19389. doi:10.1021/jp052706r
16. Koo, H. Y.; Choi, W. S.; Park, J.-H.; Kim, D.-Y. *Macromol. Rapid Commun.* **2008,** *29,* 520–524. doi:10.1002/marc.200700683
17. Zhang, L.; Wang, C.; Zhang, Y. *Appl. Surf. Sci.* **2012,** *258,* 5312–5318. doi:10.1016/j.apsusc.2012.01.101
18. Liu, Z.; Yan, Z.; Bai, L. *Appl. Surf. Sci.* **2016,** *360,* 437–441. doi:10.1016/j.apsusc.2015.09.151
19. Enustun, B. V.; Turkevich, J. *J. Am. Chem. Soc.* **1963,** *85,* 3317–3328. doi:10.1021/ja00904a001
20. Liu, Z.; Chang, T.; Huang, H.; He, T. *RSC Adv.* **2013,** *3,* 20464–20470. doi:10.1039/c3ra43394c
21. Liu, Z.; Chang, T.; Huang, H.; He, T. *ACS Appl. Mater. Interfaces* **2015,** *7,* 25938–25945. doi:10.1021/acsami.5b08751
22. Ostrander, J. W.; Mamedov, A. A.; Kotov, N. A. *J. Am. Chem. Soc.* **2001,** *123,* 1101–1110. doi:10.1021/ja0029578
23. Yuan, W.; Li, C. M. *Langmuir* **2009,** *25,* 7578–7585. doi:10.1021/la901443x
24. Huang, Y.-F.; Wu, D.-Y.; Zhu, H.-P.; Zhao, L.-B.; Liu, G.-K.; Ren, B.; Tian, Z.-Q. *Phys. Chem. Chem. Phys.* **2012,** *14,* 8485–8497. doi:10.1039/c2cp40558j
25. Fang, P.-P.; Li, J.-F.; Yang, Z.-L.; Li, L.-M.; Ren, B.; Tian, Z.-Q. *J. Raman Spectrosc.* **2008,** *39,* 1679–1687. doi:10.1002/jrs.2066
26. Joseph, V.; Matschulat, A.; Polte, J.; Rolf, S.; Emmerling, F.; Kneipp, J. *J. Raman Spectrosc.* **2011,** *42,* 1736–1742. doi:10.1002/jrs.2939
27. Schmitt, J.; Decher, G.; Dressick, W. J.; Brandow, S. L.; Geer, R. E.; Shashidhar, R.; Calvert, J. M. *Adv. Mater.* **1997,** *9,* 61–65. doi:10.1002/adma.19970090114
28. Jiang, G.; Baba, A.; Ikarashi, H.; Xu, R.; Locklin, J.; Kashif, K. R.; Shinbo, K.; Kato, K.; Kaneko, F.; Advincula, R. *J. Phys. Chem. C* **2007,** *111,* 18687–18694. doi:10.1021/jp075986e
29. Vial, S.; Pastoriza-Santos, I.; Pérez-Juste, J.; Liz-Marzán, L. M. *Langmuir* **2007,** *23,* 4606–4611. doi:10.1021/la063753t
30. Kiel, M.; Mitzscherling, S.; Leitenberger, W.; Santer, S.; Tiersch, B.; Sievers, T. K.; Möhwald, H.; Bargheer, M. *Langmuir* **2010,** *26,* 18499–18502. doi:10.1021/la103609f
31. Chaikin, Y.; Leader, H.; Popovitz-Biro, R.; Vaskevich, A.; Rubinstein, I. *Langmuir* **2011,** *27,* 1298–1307. doi:10.1021/la103913u
32. Pichon, B. P.; Louet, P.; Felix, O.; Drillon, M.; Begin-Colin, S.; Decher, G. *Chem. Mater.* **2011,** *23,* 3668–3675. doi:10.1021/cm201139s
33. Schmidt, A. R.; Nguyen, N. D. T.; Leopold, M. C. *Langmuir* **2013,** *29,* 4574–4583. doi:10.1021/la400359x
34. Mühlig, S.; Cialla, D.; Cunningham, A.; März, A.; Weber, K.; Bürgi, T.; Lederer, F.; Rockstuhl, C. *J. Phys. Chem. C* **2014,** *118,* 10230–10237. doi:10.1021/jp409688p
35. Yi, Z.; Yi, Y.; Luo, J.; Ye, X.; Wu, P.; Ji, X.; Jiang, X.; Yi, Y.; Tang, Y. *RSC Adv.* **2015,** *5,* 1718–1729. doi:10.1039/C4RA06141A
36. McAloney, R. A.; Sinyor, M.; Dudnik, V.; Goh, M. C. *Langmuir* **2001,** *17,* 6655–6663. doi:10.1021/la010136q


## License and Terms

BEILSTEIN JOURNAL OF NANOTECHNOLOGY

# NO gas sensing at room temperature using single titanium oxide nanodot sensors created by atomic force microscopy nanolithography

Li-Yang Hong and Heh-Nan Lin*

Full Research Paper

Open Access

Address:
Department of Materials Science and Engineering, National Tsing Hua University, Hsinchu 30013, Taiwan

Email:
Heh-Nan Lin* - hnlin@mx.nthu.edu.tw

* Corresponding author

Keywords:
atomic force microscopy nanolithography; photo-activation; photo-recovery; resistive NO gas sensor; titanium oxide nanodot sensor

*Beilstein J. Nanotechnol.* **2016,** *7,* 1044–1051.
doi:10.3762/bjnano.7.97

Received: 08 March 2016
Accepted: 05 July 2016
Published: 20 July 2016

This article is part of the Thematic Series "Nanostructures for sensors, electronics, energy and environment III".

Guest Editor: N. Motta



## Abstract

In this work, the fabrication of single titanium oxide nanodot (ND) resistive sensors for NO gas sensing at room temperature is reported. Two atomic force microscopy nanolithography methods, nanomachining and nano-oxidation, are employed. A single titanium nanowire (NW) is created first along with contact electrodes and a single titanium oxide ND is subsequently produced in the NW. Gas sensing is realized by the photo-activation and the photo-recovery approaches. It is found that a sensor with a smaller ND has better performance than a larger one. A response of 31%, a response time of 91 s, and a recovery time of 184 s have been achieved at a concentration of 10 ppm for a ND with a size of around 80 nm. The present work demonstrates the potential application of single metal oxide NDs for gas sensing with a performance that is comparable with that of metal oxide nanowire gas sensors.

## Introduction

In recent years, gas sensors have been widely used in a variety of fields, such as medical diagnosis [1,2], environmental monitoring [3] and combustion emission control [4]. Among all types of gas sensors, resistor-type gas sensors based on semiconducting metal oxide nanomaterials [5-8] are more attractive than conventional devices [9]. The advantages include high sensitivity, high stability, fast detection and recovery, low power consumption, relatively low cost, and small size [9,10]. These advantages enable semiconducting metal oxide sensors to be implemented on integrated circuits for portable applications [5,11].

Semiconducting metal oxide gas sensors generally need to work at high temperatures due to the high energy required for surface reactions [5,12,13]. However, a high operating temperature results in issues with durability and reliability of the device [5]. To overcome this drawback, light-assisted approaches including photo-activation [12-21] and photo-recovery [22,23] have

been shown effective to enable gas sensing at room temperature.

The sensing material in a semiconducting metal oxide sensor is commonly synthesized by a bottom-up approach, such as chemical vapour deposition [11,15,16,23], thermal deposition [12], solution growth [19], and electrospinning [24]. Alternatively, a lithographic approach is also suitable for producing the sensing metal oxide material. Previously, atomic force microscopy (AFM) nano-oxidation has been utilized for the fabrication of titanium oxide nanowire (NW) gas sensors [25,26].

NO gas sensing at low concentrations is beneficial for human health [1,2] and environmental monitoring [3]. Various types of metal oxide nanomaterials have been utilized for NO or $NO_2$ gas sensing, e.g., $SnO_2$ [12,15-17], ZnO [13,14,17-20,23], $In_2O_3$ [22], and $TiO_2$ [24,27-29]. AFM nanolithography is a valuable technique for the fabrication of nanostructures and sensors [30,31]. Recently, we have reported on the fabrication of single titanium oxide nanodot (ND) ultraviolet (UV) sensors by AFM nanomachining and nano-oxidation [32]. In the present work, the application of single titanium oxide ND sensors for NO gas sensing at room temperature is reported. The performance of the ND gas sensors compares reasonably with metal oxide NW gas sensors reported in the literature.

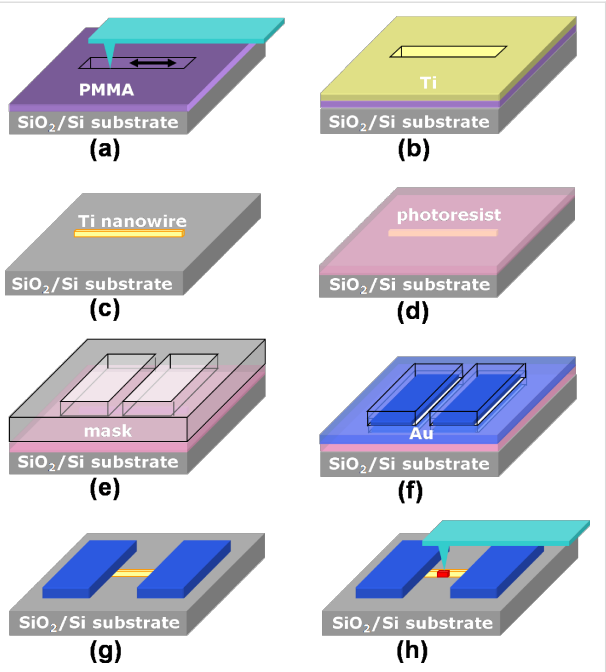


**Figure 1:** A schematic diagram showing the fabrication of a single titanium oxide ND gas sensor. (a) PMMA spin-coated and AFM nanomachining, (b) Ti deposition, (c) PMMA lift-off, (d) photoresist spin-coated, (e) exposure and development, (f) Au deposition, (g) photoresist lift-off, and (h) AFM nano-oxidation. (Adapted from [32]).

## Experimental

A schematic diagram of the AFM nanolithography [30,32] procedure is shown in Figure 1. A 40 nm thick poly(methylmethacrylate) (PMMA) film was spin-coated on a Si substrate that had a thick oxide layer. By using an AFM (Smena, NT-MDT, Russia), a straight nanogroove was generated in the PMMA film. A Ti film was deposited by electron-beam deposition and a single Ti NW was created after lift-off. Au contact electrodes were subsequently created on the sides of the NW by standard photolithography. The details can be found in our previous reports [33,34]. For nano-oxidation, the tip was moved to the middle of the NW and a voltage pulse (−10 V and 500 ms) was applied to the tip. A single titanium oxide ND sensor was thus obtained [32]. The morphologies of the NW and the ND were examined by another AFM (Dimension Icon, Bruker, U.S.A.).

The fabricated ND sensor was put in a vacuum chamber and connected to a Keithley 2400 source measure unit. Prior to a sensing cycle, the chamber was pumped to low vacuum (ca. $10^{-3}$ Torr) and the valve was closed. A mixture of NO (500 ppm) and $N_2$ gas was injected into the chamber and a sensing cycle was started. With a mass flow controller, a specific NO concentration was quickly established in the chamber for sensing. After a sufficient sensing time (which is shown in blue in the current-response figures), the chamber was evacuated again for NO desorption (which is shown in white in the current-response figures). After the pumping, the sensing cycle ended and the next cycle was started. The time-dependent current of the sensor at a bias voltage of 10 or 5 V was recorded. A UV light-emitting diode (310 nm at 0.3 $mW{\cdot}cm^{-2}$) was placed above the sensor for UV-assisted sensing. Two sensing modes were applied. For the first, called UV-activation mode, the sensor was under constant UV illumination through the whole measurement. For the second, called UV-recovery mode, the UV light was turned on after sensing for NO desorption. (Note that the chamber was under pumping.) The UV light was then turned off after a certain time. (Note that the chamber was still under pumping after the light was turned off.)

## Results and Discussion

Two ND gas sensors with different sizes have been fabricated. The smaller one will be called sensor A and the larger one sensor B. An AFM topographic image of sensor A is shown in Figure 2a and a cross-sectional plot is shown Figure 2c. The ND has a length, a width and a height of around 50, 80 and 26 nm, respectively. A topographic image of sensor B is shown in Figure 2b and a cross-sectional plot is shown in Figure 2d. The ND is larger with a length, a width and a height of around 134, 120 and 16 nm, respectively. The surface to volume ratio is an important factor for the sensing performance. Taking the NDs

as simple rectangular cuboids, the estimated volume and surface area (only five surfaces) for sensor A are around $104 \times 10^3$ nm$^3$ and $10.8 \times 10^3$ nm$^2$, respectively. The surface to volume ratio is roughly 0.103 nm$^{-1}$. The estimated volume and surface area for sensor B are around $257 \times 10^3$ nm$^3$ and $24.2 \times 10^3$ nm$^2$, respectively. The surface to volume ratio is roughly 0.094 nm$^{-1}$. Therefore, sensor A has a larger surface to volume ratio.

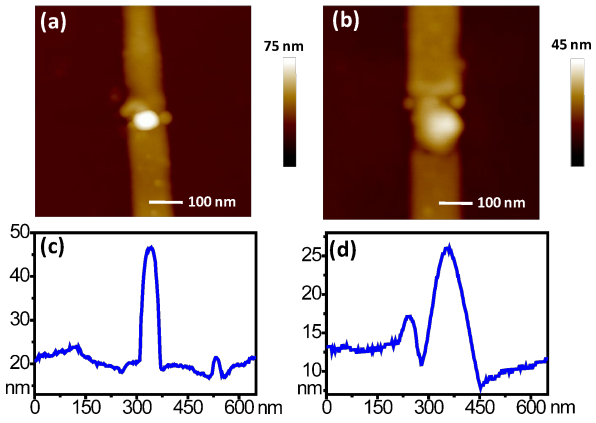


**Figure 2:** (a,b) AFM topographic images of the two NDs of sensors A and B, respectively. (c,d) Cross-sectional plots of the two NDs.

The generation of the NDs after nano-oxidation shown in Figure 2 is clear evidence of the formation of titanium oxide. Also, Auger electron spectroscopy analysis confirmed that the Ti was oxidized [32]. The compositions of the NDs, however, cannot be exactly determined and are simply $TiO_x$. Also, sensor A has a larger resistance due to the smaller ND size. (The current–voltage relationships of the two ND sensors before NO sensing are shown in Figure S1 in Supporting Information File 1.) We discussed the electrical properties of the sensors in our previous report [32]. A $TiO_x$ ND behaves like an n-type semiconductor due to oxygen vacancies. When NO molecules (or $O_2$ molecules under ambient environment) adsorb on the ND surface, they become negatively charged by catching electrons. The conductance of the ND with NO (or $O_2$) adsorption is thus smaller than that in the pristine state of the ND (i.e., without adsorbed molecules). Under UV illumination, the ND conductance becomes larger since the adsorbed NO (or $O_2$) molecules are neutralized by photo-generated holes and leave the ND surface [35]. Detailed mechanisms will be discussed later.

Figure 3a shows the current response of sensor A at 15 ppm NO and a bias of 10 V in the UV-activation mode. (Note that it was confirmed first that pure $N_2$ gas had no effect on the sensor current.) The starting current (ca. 0.9 µA) is larger than the current under ambient environment since the sensor is under UV irradiation. The current decreases after NO injection (blue region) and stabilizes after a certain time. (The NO exposure times in the blue regions in Figure 3a are around 215, 305 and 230 s, respectively.) It gradually increases when the NO gas is pumped out (white region). As can be seen, the current variations are consistent for the three cycles. Figure 3b shows the current response at 10, 15 and 20 ppm. (The exposure times in Figure 3b are 155, 230 and 315 s, respectively.) It is clear that the current decrease becomes larger as the concentration rises, because more molecules adsorb on the surface. Furthermore, it takes longer time for the current to return to its original value as the concentration gets higher. Figure 3c shows the current response at 10, 15, and 20 ppm NO and at 5 V. (The exposure times in Figure 3c are 170, 315, 230 and 370 s.) In comparison with Figure 3b, it takes longer time for the current to return to

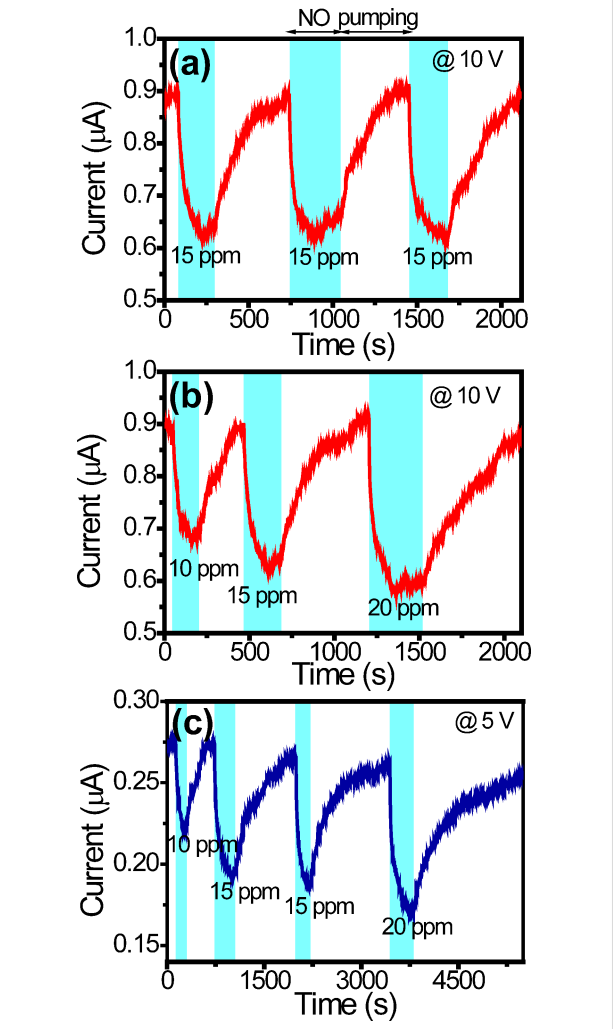


**Figure 3:** (a) The current response of sensor A at 10 V and 15 ppm NO, and (b,c) the current responses at 10 and 5 V, respectively, for various concentrations in the UV-activation mode. The blue regions indicate NO presence and the white regions indicate pumping.

its original value. The faster recovery (i.e., faster NO desorption) in Figure 3b is caused by the self-heating effect [36,37]. When operating at a larger bias, the sensor temperature is higher owing to more Joule heat. The rate of desorption increases accordingly. A larger operating voltage is thus beneficial for sensing, but at the cost of higher risk of breaking down.

Figure 4 shows the performance of sensor A at 10 V calculated from Figure 3b. The response $S$ is defined as $S = \Delta R/R_0$, where $\Delta R$ is the resistance increase after NO adsorption and $R_0$ the initial resistance in a blue region in Figure 3b. The responses are 31, 41, and 52% for 10, 15, and 20 ppm, respectively, and plotted in Figure 4a. (The resistances before and after NO adsorption are shown in Table S1 in Supporting Information File 1.) The response time $t_{res}$ is defined as the time required for the current to decrease to 10% of the initial current during NO exposure. The results are 91, 86, and 81 s for 10, 15, and 20 ppm, respectively, and plotted in Figure 4b. The recovery time $t_{rec}$ is defined as the time required for the current to increase to 90% of the original current when NO is being pumped out. The results are 184, 363, and 477 s for 10, 15, and 20 ppm, respectively, and also plotted in Figure 4b. Response and recovery time both increase as the concentration rises. Since there are more adsorbed molecules on the ND surface at a higher concentration, it is reasonable that the response becomes larger. Also, it takes a longer time for the molecules to leave the surface during recovery. On the other hand, the response time has an opposite trend. This can be attributed to faster molecular adsorption on the ND surface at a higher concentration.

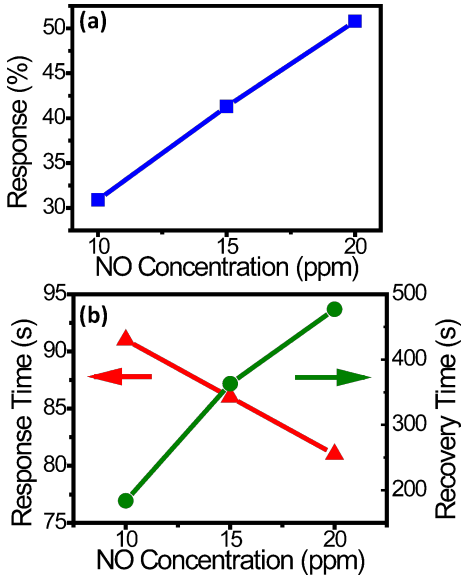


**Figure 4:** (a) Response and (b) response time and recovery time as a function of the concentration for sensor A at 10 V in the UV-activation mode calculated from Figure 3b.

Figure 5a shows the current response of sensor A at 10 V in the UV-recovery mode. At the beginning, the UV irradiation is turned on for $O_2$ desorption (the chamber is also under pumping) and the current rises immediately. When the current reaches a high value (roughly 1.1 µA in Figure 5a), the UV irradiation is then turned off. The current gradually decreases due to re-adsorption of $O_2$. (Note that re-adsorption occurs due to the low vacuum in spite that the chamber is still under pumping.) When it reaches an approximately steady value of 0.8 µA, NO is injected and the sensing starts. (A finer time scale current response is shown in Figure S2 in Supporting Information File 1 and it reveals the current is approximately steady at 0.8 µA.) After a sufficient sensing time, the UV irradiation is turned on (yellow region) for NO desorption and the process repeats. From the current response, the responses are

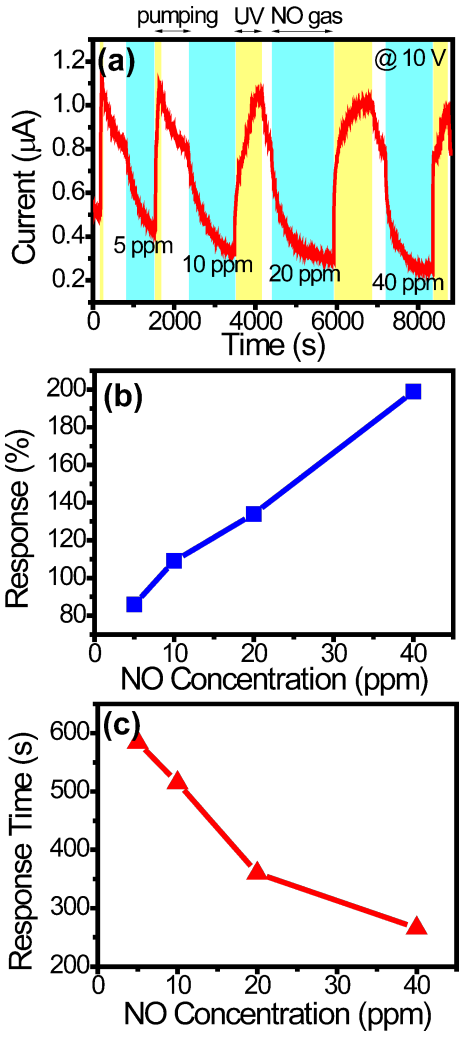


**Figure 5:** (a) The current response of sensor A at 10 V in the UV-recovery mode. (b) Response and (c) response time as a function of the concentration.

86, 108, 134, and 199% for 5, 10, 20, and 40 ppm, respectively, and plotted in Figure 5b. The response times are 584, 515, 360, and 266 s, respectively, and plotted in Figure 5c. It is difficult to determine the recovery times in the UV-recovery mode and, therefore, they are not shown.

The responses in Figure 5b are roughly three times as high as those in Figure 4a, suggesting that the UV-recovery mode is more sensitive. In the UV-activation mode, desorption occurs to some extent during NO exposure because of the UV irradiation. On the contrary, in the UV-recovery mode, there is no desorption during NO exposure. Consequently, there are more adsorbed molecules and the response is larger. The response times in Figure 5c are much longer than those in Figure 4b, suggesting that the UV-recovery mode has a slower response. This can be explained again by molecular adsorption and desorption. In the UV-activation mode, the adsorption and desorption of NO molecules rapidly reach a dynamic equilibrium under UV illumination during NO exposure. In the UV-recovery mode, it takes much longer time to reach full adsorption during NO exposure. Therefore, the response is much slower.

Figure 6a shows the current response of sensor B at 10 V between 50 and 500 ppm in the UV-activation mode. (The current response at 5 V in the UV-activation mode is shown in Figure S3 in Supporting Information File 1 for comparison.) The responses are 9, 16, 27, and 47% for 50, 100, 250, and 500 ppm, respectively, and plotted in Figure 6b. (The resistances before and after NO adsorption are also shown in Table S1 in Supporting Information File 1.) As expected, the response increases as the NO concentration rises. The response times are 138, 94, 40, and 16 s, and the recovery times are 100, 160, 180, and 210 s for the four concentrations, respectively. They are all plotted in Figure 6c. Similarly to the results in Figure 4, the response time decreases and the recovery time increases as the concentration rises.

A summary of the responses, the response times, and the recovery times of the two sensors obtained at 10 V in the UV-activation mode is shown in Table 1. As has been discussed previously, the response and the recovery time both increase as the concentration rises, whereas the response time has an opposite trend. Furthermore, sensor A has larger and faster response, but longer recovery than sensor B. The first two benefits can be explained by two factors. One is that the ND in sensor A has a larger surface to volume ratio. The other is due to the fact that the depletion layer thickness after adsorption is roughly equal to the Debye length [5,17,38]. Therefore, the conduction channel in the ND of sensor A after adsorption is narrower than that in sensor B. The combination of the two

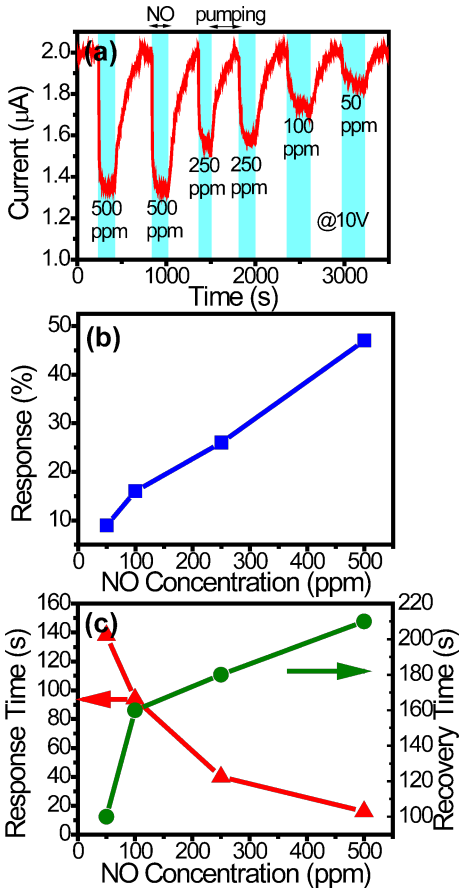


**Figure 6:** (a) The current responses of sensor B at 10 V in the UV-activation mode. (b) The response and (c) the response time and the recovery time versus the concentration.

factors makes the smaller sensor A more sensitive. The longer recovery of sensor A may be explained by the following argument: There are more photo-generated charge carriers in sensor B than in sensor A under UV illumination since sensor B is larger. The adsorbed NO molecules can thus be more efficiently neutralized and leave the ND surface. As a result, sensor B has shorter recovery.

Additionally, it is worth mentioning that the background $N_2$ pressure was 2000 times that of the NO pressure and roughly a few percents of one atmosphere in the above measurements. In order to verify if a higher $N_2$ pressure affected the sensing results, a measurement was conducted with the $N_2$ pressure raised to one atmosphere after NO sensing. It was found that there was no change in the current response. (The current response is shown in Figure S4 in Supporting Information File 1.) It is therefore reasonable to expect that the present sensing results will not change in a high-pressure $N_2$ environment.

**Table 1:** A summary of the responses, the response times, and the recovery times for the two sensors obtained at 10 V in the UV-activation mode. *C* is the NO concentration.

| sensor | *C* (ppm) | *S* (%) | $t_{res}$ (s) | $t_{rec}$ (s) |
|---|---|---|---|---|
| A | 10 | 31 | 91 | 184 |
| | 15 | 41 | 86 | 363 |
| | 20 | 52 | 81 | 477 |
| B | 50 | 9 | 138 | 100 |
| | 100 | 16 | 94 | 160 |
| | 250 | 27 | 40 | 180 |
| | 500 | 47 | 16 | 210 |

Possible mechanisms for NO or $NO_2$ sensing by using semiconducting metal oxide nanomaterials have been proposed and discussed in previous works [19,20,26,38]. Based on these works, Figure 7 shows the gas sensing mechanisms for the single titanium oxide ND sensor in the UV-recovery and the UV-activation modes. In the UV-recovery mode, $O_2$ and NO molecules react with electrons to form chemisorbed oxygen ions ($O_2^-{}_{(ads)}$) and nitric oxide ions ($NO^-_{(ads)}$) prior to UV irradiation, which are shown in Figure 7a and Figure 7b. The chemical reactions for NO are described by [20,38]:

$$NO_{(g)} + e^- \rightarrow NO^-_{(ads)}\,, \quad (1)$$

$$2NO_{(g)} + e^- \rightarrow N_{2(g)} + O^-_{2(ads)}\,. \quad (2)$$

Without UV illumination, the chemisorbed ions are too stable to be removed by pumping. Under UV illumination, the ions are first neutralized by photogenerated holes and then react again with photogenerated electrons [13], which is shown in Figure 7c. The chemical reactions for NO can be similarly described by:

$$NO_{(g)} + e^-_{(hv)} \rightarrow NO^-_{(hv)}\,, \quad (3)$$

$$2NO_{(g)} + e^-_{(hv)} \rightarrow N_{2(g)} + O^-_{2(hv)}\,. \quad (4)$$

Unlike the chemisorbed ions, the photoinduced ions ($O_2^-{}_{(hv)}$ and $NO^-_{(hv)}$) are only weakly bound to the ND surface. They can be easily removed by pumping as shown in Figure 7d. In the UV-activation mode, the ND is under continuous UV irradiation. There are no chemisorbed ions before NO sensing, which is shown in Figure 7e. Photoinduced ions are then created after NO injection as shown in Figure 7f. The photoinduced ions are finally removed by pumping as shown in Figure 7g.

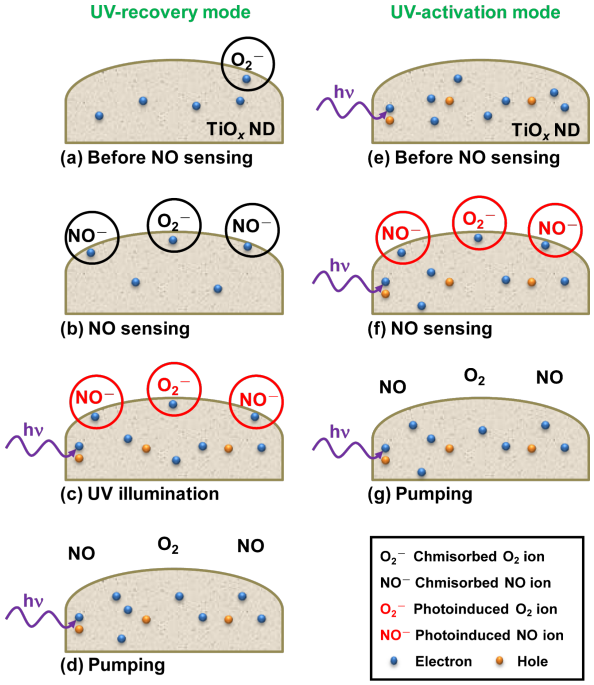


**Figure 7:** Diagram illustrating NO gas sensing mechanisms for the single titanium oxide ND sensor in the UV-recovery and the UV-activation modes.

Table 2 shows a comparison of sensing performances of NO or $NO_2$ metal oxide sensors operated in the photo-activation mode

**Table 2:** Comparison of performances of sensors operated in the photo-activation mode at room temperature reported in the literature. Note that the listed responses are based on our present definition $S = \Delta R/R_0$ and some are different from the original values in the references.

| material | gas | *C* (ppm) | *S* (%) | $t_{res}$ (s) | $t_{rec}$ (s) | light intensity (mW·cm$^{-2}$) | ref. |
|---|---|---|---|---|---|---|---|
| CdS/ZnO NWs | $NO_2$ | 1 | 337 | 40 | 230 | 0.68 (@ 468 nm) | [21] |
| Au-ZnO nanocomposites | NO | 2 | 388 | ca. 1000 | — | — (@ 550 nm) | [20] |
| ZnO NWs<br>SnO2 NWs<br>SnO2/ZnO NWs | $NO_2$ | 5 | 4<br>80<br>519 | 110<br>90<br>100 | 230<br>220<br>220 | 1.2 (@ 365 nm) | [17] |
| ZnO nanosheets<br>Au/ZnO nanosheets | $NO_2$ | 5 | 37<br>355 | 8<br>6 | 290<br>320 | 1.2 (@ 365 nm) | [18] |
| ZnO nanoline | $NO_2$ | 20 | 108 | ca. 600 | ca. 300 | 25 (@ 365 nm) | [14] |
| $TiO_x$ ND | NO | 10 | 31 | 91 | 184 | 0.3 (@ 310 nm) | this work |

at room temperature reported in the literature. Although not better, the performance of sensor A compares reasonably with these reported results. Furthermore, it can be seen that the performances of metal oxides with Au are much better those of pure metal oxides, which is due to the plasmonic effect [18,20]. It is expected that the present ND sensors can be improved in a similar fashion, e.g., by creating Au nanoparticles on the ND surface.

## Conclusion

In summary, single titanium oxide ND sensors are realized by AFM nanolithography and used for NO gas sensing. A Ti NW is generated first by AFM nanomachining and a titanium oxide ND is then produced in the NW by AFM nano-oxidation. With contact electrodes, a resistive ND gas sensor is created. For gas sensing at room temperature, light-assisted approaches, namely the UV-activation and the UV-recovery modes, are utilized. Two ND sensors have been fabricated. For the smaller sensor with a ND size of 80 nm, a response of 31%, a response time of 91 s, and a recovery time of 184 s have been achieved at 10 ppm NO in the UV-activation mode. For the larger sensor with a ND size of 120 nm, a response of 9%, a response time of 138 s, and a recovery time of 100 s have been achieved at 50 ppm NO in the UV-activation mode. The better performance of the smaller sensor can be attributed to the larger surface to volume ratio and smaller dimensions than the Debye length. The present work reveals the usefulness of single metal oxide NDs for gas sensing with reasonable performance that can be compared with metal oxide NW gas sensors.

## Supporting Information

Supporting Information features the current–voltage curves of sensors A and B before NO sensing, the resistances of sensors A and B before and after NO adsorption obtained from the current responses at a bias of 10 V as shown in the Figures, a finer time scale current response of sensor A at 10 V in the UV-recovery mode, the current response of sensor B at 5 V in the UV-activation mode, and the current response of sensor B at 10 V due to the injection of 500 ppm NO and subsequent high-pressure $N_2$.

### Supporting Information File 1

Additional experimental data.
[http://www.beilstein-journals.org/bjnano/content/supplementary/2190-4286-7-97-S1.pdf]

## Acknowledgements

This work was supported by the Ministry of Science and Technology, Taiwan, under Grant No. 104-2221-E-007-074.

## References

1. Righettoni, M.; Amann, A.; Pratsinis, S. E. *Mater. Today* **2015,** *18,* 163–171. doi:10.1016/j.mattod.2014.08.017
2. Di Natale, C.; Paolesse, R.; Martinelli, E.; Capuano, R. *Anal. Chim. Acta* **2014,** *824,* 1–17. doi:10.1016/j.aca.2014.03.014
3. Wetchakun, K.; Samerjai, T.; Tamaekong, N.; Liewhiran, C.; Siriwong, C.; Kruefu, V.; Wisitsoraat, A.; Tuantranont, A.; Phanichphant, S. *Sens. Actuators, B* **2011,** *160,* 580–591. doi:10.1016/j.snb.2011.08.032
4. Docquier, N.; Candel, S. *Prog. Energy Combust. Sci.* **2002,** *28,* 107–150. doi:10.1016/S0360-1285(01)00009-0
5. Comini, E.; Sberveglieri, G. *Mater. Today* **2010,** *13,* 36–44. doi:10.1016/S1369-7021(10)70126-7
6. Chen, X.; Wong, C. K. Y.; Yuan, C. A.; Zhang, G. *Sens. Actuators, B* **2013,** *177,* 178–195. doi:10.1016/j.snb.2012.10.134
7. Ramgir, N.; Datta, N.; Kaur, M.; Kailasaganapathi, S.; Debnath, A. K.; Aswal, D. K.; Gupta, S. K. *Colloids Surf., A* **2013,** *439,* 101–116. doi:10.1016/j.colsurfa.2013.02.029
8. Shen, G.; Chen, P.-C.; Ryu, K.; Zhou, C. *J. Mater. Chem.* **2009,** *19,* 828–839. doi:10.1039/B816543B
9. Liu, X.; Cheng, S.; Liu, H.; Hu, S.; Zhang, D.; Ning, H. *Sensors* **2012,** *12,* 9635–9665. doi:10.3390/s120709635
10. Franke, M. E.; Koplin, T. J.; Simon, U. *Small* **2006,** *2,* 36–50. doi:10.1002/smll.200500261
11. Hernandez-Ramirez, F.; Prades, J. D.; Tarancon, A.; Barth, S.; Casals, O.; Jiménez-Diaz, R.; Pellicer, E.; Rodriguez, J.; Juli, M. A.; Romano-Rodriguez, A.; Morante, J. R.; Mathur, S.; Helwig, A.; Spannhake, J.; Mueller, G. *Nanotechnology* **2007,** *18,* 495501. doi:10.1088/0957-4484/18/49/495501
12. Law, M.; Kind, H.; Messer, B.; Kim, F.; Yang, P. *Angew. Chem., Int. Ed.* **2002,** *41,* 2405–2408. doi:10.1002/1521-3773(20020703)41:13<2405::AID-ANIE2405>3.0.CO;2-3
13. Fan, S.-W.; Srivastava, A. K.; Dravid, V. P. *Appl. Phys. Lett.* **2009,** *95,* 142106. doi:10.1063/1.3243458
14. Fan, S.-W.; Srivastava, A. K.; Dravid, V. P. *Sens. Actuators, B* **2010,** *144,* 159–163. doi:10.1016/j.snb.2009.10.054
15. Prades, J. D.; Jimenez-Diaz, R.; Hernandez-Ramirez, F.; Barth, S.; Cirera, A.; Romano-Rodriguez, A.; Mathur, S.; Morante, J. R. *Sens. Actuators, B* **2009,** *140,* 337–341. doi:10.1016/j.snb.2009.04.070
16. Prades, J. D.; Jimenez-Diaz, R.; Manzanares, M.; Hernandez-Ramirez, F.; Cirera, A.; Romano-Rodriguez, A.; Mathur, S.; Morante, J. R. *Phys. Chem. Chem. Phys.* **2009,** *11,* 10881–10889. doi:10.1039/b915646a
17. Park, S.; An, S.; Mun, Y.; Lee, C. *ACS Appl. Mater. Interfaces* **2013,** *5,* 4285–4292. doi:10.1021/am400500a
18. Mun, Y.; Park, S.; An, S.; Lee, C.; Kim, H. W. *Ceram. Int.* **2013,** *39,* 8615–8622. doi:10.1016/j.ceramint.2013.04.035
19. Lu, G.; Xu, J.; Sun, J.; Yu, Y.; Zhang, Y.; Liu, F. *Sens. Actuators, B* **2012,** *162,* 82–88. doi:10.1016/j.snb.2011.12.039
20. Gogurla, N.; Sinha, A. K.; Santra, S.; Manna, S.; Ray, S. K. *Sci. Rep.* **2014,** *4,* 6483. doi:10.1038/srep06483
21. Yang, Z.; Guo, L. J.; Zu, B. Y.; Guo, Y. N.; Xu, T.; Dou, X. C. *Adv. Opt. Mater.* **2014,** *2,* 738–745. doi:10.1002/adom.201400086
22. Zhang, D.; Liu, Z.; Li, C.; Tang, T.; Liu, X.; Han, S.; Lei, B.; Zhou, C. *Nano Lett.* **2004,** *4,* 1919–1924. doi:10.1021/nl0489283
23. Verma, V. P.; Das, S.; Hwang, S.; Choi, H.; Jeon, M.; Choi, W. *Mater. Sci. Eng., B* **2010,** *171,* 45–49. doi:10.1016/j.mseb.2010.03.066
24. Kim, I.-D.; Rothschild, A.; Lee, B. H.; Kim, D. Y.; Jo, S. M.; Tuller, H. L. *Nano Lett.* **2006,** *6,* 2009–2013. doi:10.1021/nl061197h

25. Li, Z.; Wu, M.; Liu, T.; Wu, C.; Jiao, Z.; Zhao, B. *Ultramicroscopy* **2008,** *108,* 1334–1337. doi:10.1016/j.ultramic.2008.04.059
26. Archanjo, B. S.; Silveira, G. V.; Goncalves, A.-M. B.; Alves, D. C. B.; Ferlauto, A. S.; Lacerda, R. G.; Neves, B. R. A. *Langmuir* **2009,** *25,* 602–605. doi:10.1021/la803105f
27. Lin, C.-Y.; Chen, J.-G.; Feng, W.-Y.; Lin, C.-W.; Huang, J.-W.; Tunney, J. J.; Ho, K.-C. *Sens. Actuators, B* **2011,** *157,* 361–367. doi:10.1016/j.snb.2011.04.056
28. Ruiz, A. M.; Sakai, G.; Cornet, A.; Shimanoe, K.; Morante, J. R.; Yamazoe, N. *Sens. Actuators, B* **2003,** *93,* 509–518. doi:10.1016/S0925-4005(03)00183-7
29. Vyas, R.; Sharma, S.; Gupta, P.; Vijay, Y. K.; Prasad, A. K.; Tyagi, A. K.; Sachdev, K.; Sharma, S. K. *J. Alloys Compd.* **2013,** *554,* 59–63. doi:10.1016/j.jallcom.2012.11.059
30. Garcia, R.; Knoll, A. W.; Riedo, E. *Nat. Nanotechnol.* **2014,** *9,* 577–587. doi:10.1038/nnano.2014.157
31. Chiesa, M.; Cardenas, P. P.; Otón, F.; Martinez, J.; Mas-Torrent, M.; Garcia, F.; Alonso, J. C.; Rovira, C.; Garcia, R. *Nano Lett.* **2012,** *12,* 1275–1281. doi:10.1021/nl2037547
32. Hong, L.-Y.; Lin, H.-N. *Sens. Actuators, A* **2015,** *232,* 94–98. doi:10.1016/j.sna.2015.05.013
33. Chen, Y.-J.; Hsu, J.-H.; Lin, H.-N. *Nanotechnology* **2005,** *16,* 1112–1115. doi:10.1088/0957-4484/16/8/020
34. Lin, H.-Y.; Chen, H.-A.; Lin, H.-N. *Anal. Chem.* **2008,** *80,* 1937–1941. doi:10.1021/ac701911j
35. Soci, C.; Zhang, A.; Xiang, B.; Dayeh, S. A.; Aplin, D. P. R.; Park, J.; Bao, X. Y.; Lo, Y. H.; Wang, D. *Nano Lett.* **2007,** *7,* 1003–1009. doi:10.1021/nl070111x
36. Prades, J. D.; Jimenez-Diaz, R.; Hernandez-Ramirez, F.; Barth, S.; Cirera, A.; Romano-Rodriguez, A.; Mathur, S.; Morante, J. R. *Appl. Phys. Lett.* **2008,** *93,* 123110. doi:10.1063/1.2988265
37. Prades, J. D.; Jimenez-Diaz, R.; Hernandez-Ramirez, F.; Cirera, A.; Romano-Rodriguez, A.; Morante, J. R. *Sens. Actuators, B* **2010,** *144,* 1–5. doi:10.1016/j.snb.2009.09.040
38. Afzal, A.; Cioffi, N.; Sabbatini, L.; Torsi, L. *Sens. Actuators, B* **2012,** *171–172,* 25–42. doi:10.1016/j.snb.2012.05.026

## License and Terms

BEILSTEIN JOURNAL OF NANOTECHNOLOGY

# Photocurrent generation in carbon nanotube/cubic-phase $HfO_2$ nanoparticle hybrid nanocomposites

Protima Rauwel[*1,2], Augustinas Galeckas[2], Martin Salumaa[3], Frédérique Ducroquet[4] and Erwan Rauwel[3]

Full Research Paper

Open Access

Address:
[1]Institute of Physics, University of Tartu, Ravila 14c, 51014 Tartu, Estonia, [2]Department of Physics, University of Oslo. P.O. Box 1048 Blindern, 0316 Oslo, Norway, [3]Tartu College, Tallinn University of Technology, Puiestee 78, 51008 Tartu, Estonia, and [4]IMEP-LAHC, CNRS, Université de Grenoble-Alpes, Minatec campus, 38016 Grenoble, France

Email:
Protima Rauwel[*] - protima.rauwel@fys.uio.no

* Corresponding author

Keywords:
carbon nanotubes; $HfO_2$; nanoparticles; photocurrent

*Beilstein J. Nanotechnol.* **2016,** *7,* 1075–1085.
doi:10.3762/bjnano.7.101

Received: 12 April 2016
Accepted: 06 July 2016
Published: 26 July 2016

This article is part of the Thematic Series "Nanostructures for sensors, electronics, energy and environment III".

Guest Editor: N. Motta



## Abstract

A hybrid material consisting of nonfunctionalized multiwall carbon nanotubes (MWCNTs) and cubic-phase $HfO_2$ nanoparticles (NPs) with an average diameter of 2.6 nm has been synthesized. Free standing $HfO_2$ NPs present unusual optical properties and a strong photoluminescence emission in the visible region, originating from surface defects. Transmission electron microscopy studies show that these NPs decorate the MWCNTs on topological defect sites. The electronic structure of the C K-edge in the nanocomposites was probed by electron energy loss spectroscopy, highlighting the key role of the MWCNT growth defects in anchoring $HfO_2$ NPs. A combined optical emission and absorption spectroscopy approach illustrated that, in contrast to $HfO_2$ NPs, the metallic MWCNTs do not emit light but instead expose their discrete electronic structure in the absorption spectra. The hybrid material manifests characteristic absorption features with a gradual merger of the MWCNT π-plasmon resonance band with the intrinsic defect band and fundamental edge of $HfO_2$. The photoluminescence of the nanocomposites indicates features attributed to combined effects of charge desaturation of $HfO_2$ surface states and charge transfer to the MWCNTs with an overall reduction of radiative recombination. Finally, photocurrent generation under UV–vis illumination suggests that a $HfO_2$ NP/MWCNT hybrid system can be used as a flexible nanodevice for light harvesting applications.

## Introduction

Nanoparticles (NPs) have emerged as promising candidates for many applications due to their unique electronic, optical and magnetic properties compared to their bulk counterparts. During the last decade, composite materials have spurred large interest, and with the rise of nanotechnology, the development of new nanocomposite materials promoting new properties has taken a

step forward. These nanocomposite materials will be the key components for the development of new applications in the field of nanotechnology. It is well known that by combining different classes of materials, one can obtain nanocomposites exhibiting properties of the individual materials along with new characteristics as a result of hybridization. For instance, the combination of nanoparticles with carbon nanotubes (CNTs) has proven to greatly broaden the area of potential applications, such as gas sensors [1,2], solar cells [3,4], bioimaging [5] and IR detectors [6], most of which require efficient charge transfer from the nanoparticle to the CNT and charge conduction via the CNT. To date, numerous studies have been reported on the decoration of CNTs with metal oxides including $TiO_2$ [7,8] and ZnO [9] for solar cell applications and $SnO_2$ for gas sensors. Reports on the fabrication of an all carbon nanocomposite combining CNTs, graphene and carbon quantum dots (CQDs) are available [10]. Recently, Yu et. al studied the charge transfer mechanism in CQD–graphene composite and have emphasized its potential as a hot carrier, solar cell material [11]. However, CQDs still need further investigation as their optical properties tend to vary with the synthesis route, their size and the functional groups surrounding them [12].

$HfO_2$ compounds and their solid solutions have been recognized as important materials in the development of technology [13], and more particularly, in the field of transistor technology [14]. In fact, $HfO_2$ is a dielectric material with a band gap of 5.7 eV [14,15]. $HfO_2$ has already been integrated in numerous technologies and has been chosen for the replacement of Si-based gate oxides in advanced complementary metal-oxide semiconductors (CMOS) [16]. Many efforts have been made towards the stabilization of the cubic phase of $HfO_2$ due to its more interesting properties such as higher dielectric permittivity via doping [17] and substrate-induced strain. Many systems and processes were developed to reach this goal. One advantage of studying this material for other properties is that the microelectronic industry already produces and employs $HfO_2$-based devices and can therefore facilitate its integration into nanosystems. This further expedites the development and integration of new technologies based on $HfO_2$ owing to already existing technological platforms. Major efforts are being directed worldwide towards mastering the dimensionality of nanoparticles; among established methods ensuring control of both size and shape is the nonaqueous sol–gel route [18,19]. In our previous studies, a strong photoluminescence in the visible range was observed from $HfO_2$ nanoparticles under below-bandgap excitation [20,21] and attributed to surface-located intrinsic and extrinsic defects arising from $Hf^{3+}$ and $O^{2-}$ vacancies. The small diameter of the nanoparticles in the present study, 2.6 nm on average, implies a very high surface-to-volume ratio, and consequently, enhanced surface-defect-related luminescence. Furthermore, for the cubic-phase $HfO_2$ nanoparticles, oxygen vacancies acting as luminescence trap states are present in large amounts [22]. In the variety of different techniques used to decorate CNTs, the first step is usually the dispersion of the CNTs in a liquid solution as they exist in the form of bundled ropes [23]. Acid treatment of the CNTs is typically the preferred method offering a two-fold advantage; not only does it debundle the CNTs, but it also creates functionalized groups on the side walls which, in turn, prevent the CNTs from rebundling. In addition, these functional groups also act as anchor sites for nanoparticles in the process of CNT decoration. In fact, acid treatment creates defects (vacancies and holes in the side walls) on the CNT surfaces along with carboxyl groups in the case of carboxylic acid treatment [24]. The bond with these carboxyl groups is then created via hydroxyl groups present on the surface of the nanoparticles on forming esters [25]. Moreover, π–π stacking has also proven effective in attaching inorganic metal oxide nanoparticles to the surface of nonfunctionalized nanotubes. In this approach, the aromatic ring of the CNT is directly connected to the benzyl ring of the inorganic nanoparticles [26,27]. Birojou et al. have also observed that in the case of nonfunctionalized graphene decorated by gold nanoparticles via electrostatic interactions, the defect sites on the graphene are preferentially decorated by the Au nanoparticles with an increase in the $sp^2$ hybridization of graphene in these regions [28]. In another approach, chemical functionalization is usually combined with ultrasonication. In fact, the latter tends to create defects on the walls of the CNT along with C dangling bonds along with a change in the carbon hybridization from $sp^2$ to $sp^3$ [29]. Nevertheless, studies have been conducted where ultrasonication without functionalizing agents has been used for successfully debundling CNTs with minimal damage to the tube walls [23].

CNTs produced via CVD methods typically contain various imperfections, such as residual impurities of metal catalysts, graphene sheets, amorphous carbon and different defects [30,31], generally qualified as either topological or localized. The most common defects are comprised of edges and dangling bonds in addition to pentagonal and heptagonal defects, creating bends in the CNTs known to accommodate foreign atoms in the $sp^2$-hybridized carbon matrix [32,33]. Some defects, including five-membered rings responsible for closing the ends of nanotubes, are also present at bends, Y-junctions and kinks in nanotubes. In general, these defect sites are highly reactive and provide anchor sites to fix nanoparticles whose surfaces have organic moieties [34]. Furthermore, certain defects also produce nanotube curvature, which in turn creates π-orbital mismatch and consequently creates more active sites on the CNT. In any case, the presence of these defects is known to affect the band structure of the carbon nanotubes and thus can be

studied by means of optical absorption and photoluminescence spectroscopy [25].

We have already reported elsewhere that the free-standing cubic $HfO_2$ nanoparticles are luminescent on their own with characteristic emission in the blue-green region of the visible spectra. This may be attributed to surface defects including Hf and O vacancies [21]. The motivation of the present work is different from other well-studied luminescent nanocomposites containing $TiO_2$ and ZnO that are investigated around band gap excitation. Here, contrary to the previous two semiconductors, novel optical properties and photocurrent generation are expected from the hybrid material studied in under band gap excitation conditions. Nevertheless, one has to also consider that nanoparticles in contact with the CNT may undergo surface passivation along with corresponding changes in the electron trap states within the band gap [35]. Furthermore, since the CNTs are not functionalized in the present study, a direct insight into the role of intrinsic defects in the as-grown CNTs can be attained in the process of attaching nanoparticles to their surfaces. Similarly, the absence of functional groups on the CNT provides a direct electrical contact between the CNT and $HfO_2$ NP along with a better understanding of the individual contribution of CNTs to the photoluminescence properties and photocurrent generation in the hybrid material.

# Results and Discussion

## Structure and morphology

The overall morphology of the hybrid material was studied by TEM. The various HAADF-STEM images presented here give an overview of the morphology of the hybrid nanomaterial. Most of the $HfO_2$ nanoparticles are agglomerated and appear to be attached only in certain particular regions of the CNT. In our previous study we observed that cubic $HfO_2$ nanoparticles on their own show a tendency to agglomerate [20]. The MWCNTs used in this study exhibited kinks, coils and buckling.

In Figure 1a, an overview of the hybrid material shows successful attachment of the nanoparticles to the CNT. The cubic $HfO_2$ nanoparticles exhibit an average diameter of 2.6 nm [20]. In the overview of Figure 1a, the nanoparticles seem to decorate only specific sites either singularly or in agglomerates. A higher magnification HAADF-STEM image in Figure 1b further reinforces the selective decoration of the $HfO_2$ nanoparticles as several regions of the CNT are devoid of nanoparticles. An explanation to this selective anchoring is provided below and also in the EELS section. In Figure 1c, a HAADF-HRSTEM image exhibits small agglomerates of these nanoparticles on the MWCNT, where the diameter of the MWCNT has reduced due to buckling. The nanoparticles remain crystalline as displayed by the atomic column resolution, even after 2 h of sonication. In Figure 1e, a defective nanotube presenting successive kinks is shown with the $HfO_2$ nanoparticles preferentially attached around the kinked area. A HRSTEM image in one such buckled/kinked regions of the MWCNT is illustrated in Figure 1f, where the nanoparticles are attached to two different kinked areas. In effect, in the kinked region, there is a breakdown in the curvature and CNTs with individual walls exhibit different curvatures. Moreover, when the MWCNT is bent, the changes in the curvature induce a modified atomic arrangement and local break down of symmetry. This implies a local change of the electronic structure [36] along with an increase in π mismatch. This in turn accentuates the reactivity of these MWCNTs and converts these defects into receptors for functional groups on the surface of the nanoparticles. Buckling and kinking of the MWCNT arises due to rearrangement of C atoms around the curved area giving rise to vacancies and dangling bonds. These defective areas are well known for their high reactivity to foreign atoms [37].

In Figure 1d, nanoparticles are attached to the side walls of the MWCNT. It has to be emphasized here that according to literature reports, attachment of nanoparticles to the sidewalls of MWCNTs appears to be only possible via functionalization of the sidewalls. In our case, no functionalization has taken place, nor in the image do we observe the presence of curved regions or topological defects that facilitate the decoration of these nanoparticles to the MWCNT. This mechanism of anchoring to the sidewalls is further probed in the EELS section. On the other hand, the side walls of the MWCNT do not appear to be atomically flat, and the outermost walls are not distinct, indicating damage to the walls of the MWCNT which is a result of the sonication treatment and will be discussed in a forthcoming paper. This provokes a breakdown in the graphitic structure, which once again affects the electronic structure and increases the reactivity of the MWCNT to foreign atoms.

## Optical properties

The distinctive optical properties of CNTs derive from electronic transitions within the one-dimensional density of states (DOS), which is discontinuous in nature and exhibits sharp peaks called van Hove singularities (vHS) [38]. The energy separations between the vHS in the valence and conduction bands depend on the nanotube structure, thus optical absorption and emission spectroscopy allow identification of the CNT chirality and diameter as well as quality in terms of nontubular carbon content and structural defects. The characterization of multiwalled CNTs, however, is challenging because of the involvement of several shells with different structure and typically higher defect concentration compared to single-walled CNTs. The optical absorption properties of the hybrid MWCNT:$HfO_2$ nanocomposites deduced from the room temperature transmit-

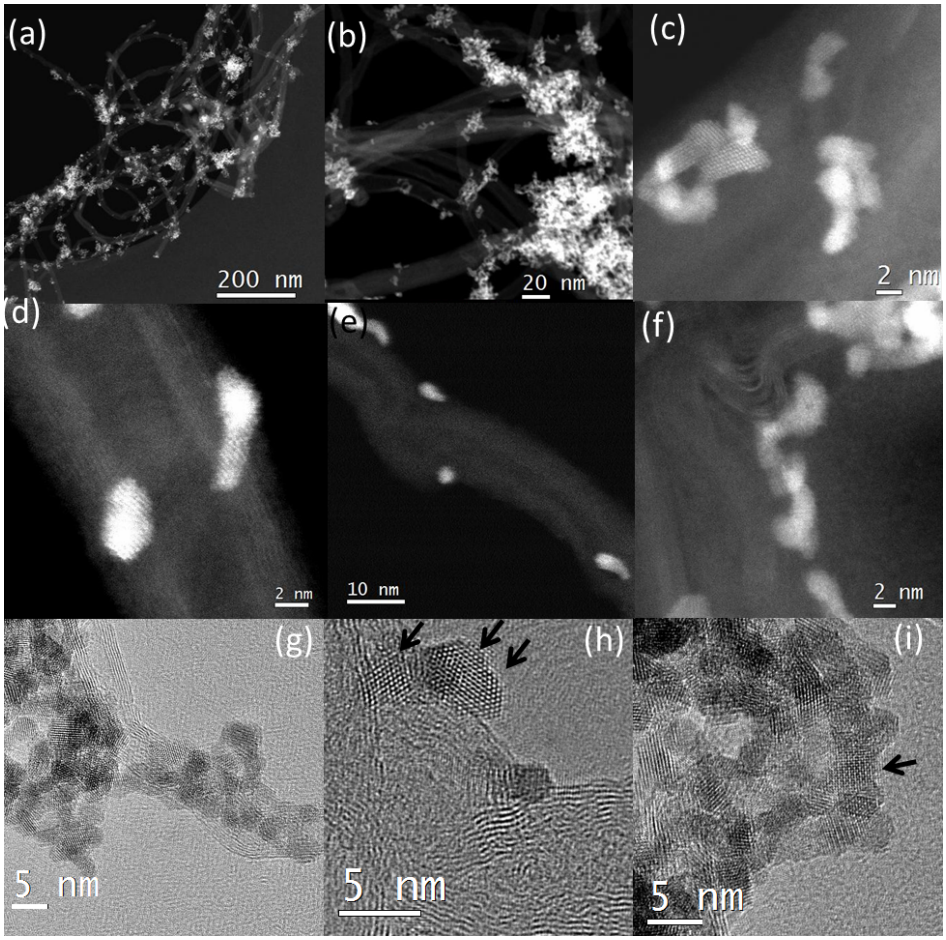


**Figure 1:** (a) HAADF-STEM image of the MWCNT:$HfO_2$, (b) higher magnification image of (a), (c) HAADF-HRSTEM images of the $HfO_2$ NPs on the MWCNTs, (d) NPs attached to the side walls of a MWCNT, (e) NPs attached at buckled edges of the MWCNT, (f) wall of the nanotube showing defects and irregularities to which nanoparticles are attached, (g) HRTEM images of randomly oriented agglomerates, (h) <110>-oriented, and (i) <001>-oriented nanoparticles indicated by arrows and all attached to curved regions of the CNT.

tance measurements of a colloidal suspension in ethanol are summarized in Figure 2.

The fine structure of the absorption spectrum in the UV–vis region revealed upon background subtraction and ×100-fold magnification is represented by the grey curve in Figure 2a. One can observe an apparent double feature in the absorption spectrum in the photon energy region 1.5–3.5 eV, where typically the vHS-related bandgap transitions are observed in CNTs, such as $E_{22}$ from the semiconducting SWCNT and $E_{11}$ from the metallic SWCNT [39]. At higher photon energies, a broad absorption band emerging at around 4.5 eV is likely due to the π-plasmon resonance [40,41]. This feature gradually merges with the fundamental absorption edge of $HfO_2$ building up at around 5.6 eV. These assertions are supported by the similarity of the absorption edge and absence of CNT-related features in the spectrum of free-standing cubic $HfO_2$ nanoparticles obtained earlier from the diffuse reflectance measurements [21] and put alongside for comparison in Figure 2. The absorption thresholds marked by the dashed lines in the Tauc plot in Figure 2b are consistent with the reported bandgap energies for hafnia (theoretical 4.9–5.7 eV and experimental 5–6 eV [14,42]) as well as with defect-related absorption showing up close to the fundamental edge and commonly associated with oxygen vacancies [43,44]. With regard to the latter, a noteworthy discrepancy (at ≈0.1 eV) of the absorption thresholds in the case of CNT-embedded and free-standing $HfO_2$ nanoparticles likely points towards different charge states of oxygen vacancies or differently coordinated vacancies in the same charge state. Both scenarios seem feasible bearing in mind that the comparison involves suspended colloidal versus free-standing particles and that the relevant defects are located predominantly near or on the surface. It is noteworthy in this respect that theoretical calculations of the electronic properties of oxygen vacancies in monoclinic $HfO_2$ [45] predict single- and double-ionized vacancy states at 4.7 eV and 4.9 eV above

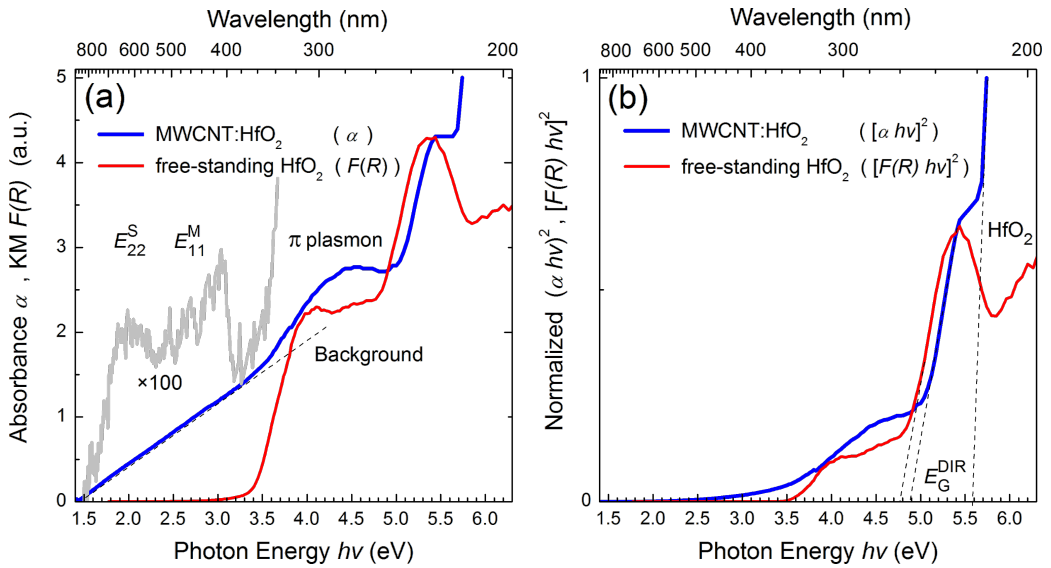


**Figure 2:** (a) Absorption spectrum of MWCNTs decorated with cubic $HfO_2$ nanoparticles obtained from the transmittance measurements of colloidal suspension in ethanol (blue curve) against that of free-standing $HfO_2$ nanoparticles from the diffuse reflectance measurements (red curve). (b) Tauc plots of the corresponding dependencies, absorbance (α) and Kubelka–Munk function (KM *F*(*R*)), representing the case of direct optical transitions.

the valence band, which appear very close to the experimentally observed absorption thresholds in Figure 2b.

The electronic properties of CNTs are known to vary depending upon the chirality (wrapping angle) and diameter of the graphene sheet, generally exhibiting either semiconducting, or metallic behavior [46-48], the latter being observed in part of single-walled and in all multiwalled CNTs. In metallic CNTs, the electrons can be optically excited via a series of valence-to-conduction band transitions, resulting in characteristic vHS peaks in absorption spectra. However, since holes are instantly filled with readily available electrons, no excitons are formed, and consequently, no photoluminescence (PL) occurs in MWCNTs. Hence, PL measurements of our hybrid nanocomposites rather address mutual interaction of the radiative centers on the surface of $HfO_2$ nanoparticles and metallic CNT framework, conceivably acting either as a surface-passivating agent or as an antenna enhancing light interaction with attached nanoparticles. Indeed, the nanotubes are known to induce optical quenching due to charge transfer from the nanoparticle to the CNT [49-51]. This charge transfer within conjugate species and CNTs usually occurs in the excited state [52]. In the reported case of CdSe/ZnS attached to CNTs, the optical quenching was attributed to a nonradiative energy transfer from the quantum dot to the SWCNT in the ground state [53].

In the present study, we observe an overall decrease in the PL intensity when the $HfO_2$ nanoparticles are attached to the CNT compared to the PL emission of the free-standing nanoparticles [21]. Figure 3 shows room temperature PL spectra of the hybrid nanocomposites dispersed in ethanol as a colloidal suspension and of the free-standing $HfO_2$ nanoparticles. As one can deduce from the PL intensity scales in Figure 3a,b, the total quantum yield in the case of nanocomposites is two orders of magnitude lower compared to free-standing nanoparticles. In a first approximation, this could be attributed to the different densities of the photo-excited nanoparticles in both instances and also to charge transfer effects in CNTs. To gain some insight into the matter, the spectral content of the PL emission from nanocomposites and free-standing $HfO_2$ nanoparticles was analyzed in more detail. As evident from Figure 3, the key constituents of the broad emission bands in both cases are represented by the same Gaussian deconvolution components centered at around 3.1, 2.8, 2.5 and 2.2 eV, albeit with a notable discrepancy in the relative strength of the 3.1 eV emission component. In the case of free-standing cubic $HfO_2$ nanoparticles, the nature of strong visible emission combines surface defects that act as charge trapping centers and oxygen vacancies due to the large presence of $Hf^{3+}$ in the structure. The photon energy range from 2 to 3 eV is identified in the literature as the typical response of the luminescent extrinsic centers associated with surface defects or impurities introduced during the synthesis of the nanoparticles. In particular, the characteristic green luminescence at around 2.5 eV is usually attributed to deep-level traps generated by oxygen vacancies, whereas the prominent emission component centered at 3.1 eV is related to $Hf^{3+}$ defects on the surface of the nanoparticles. The attachment of the nanoparticles to a CNT not only provides a conducting pathway

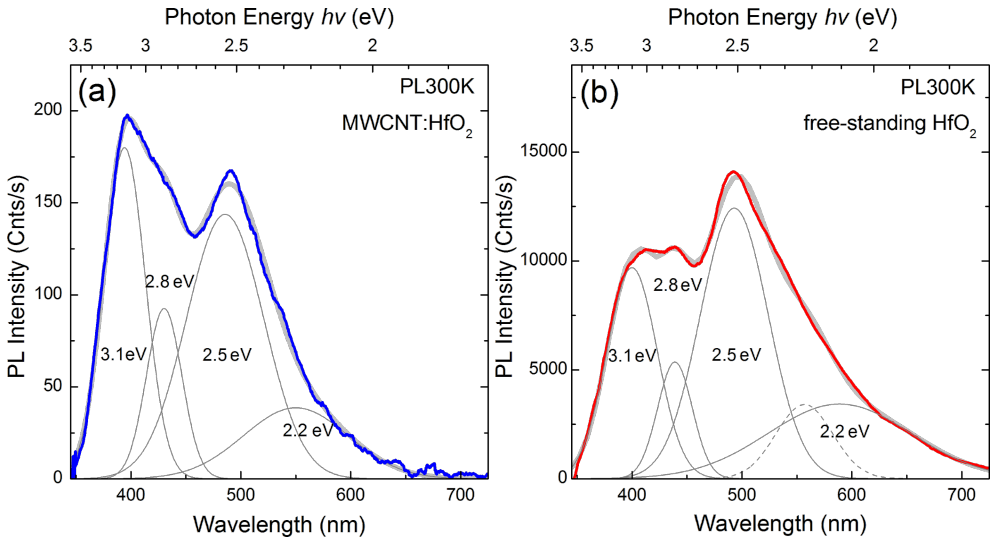


**Figure 3:** (a) Room temperature photoluminescence spectra of MWCNTs decorated with cubic $HfO_2$ nanoparticles (from a colloidal suspension in ethanol) compared to (b) free-standing $HfO_2$ nanoparticles. Grey curves represent the Gaussian deconvolution components. Note different the photoluminescence intensity scales in (a) and (b).

to evacuate the charges accumulated on the surface but also reduces the heating effects of the material due to nonradiative recombination.

## Core loss EELS C K-edge

Most nanoparticles are attached to sites with defects and changes in CNT curvature, creating π-orbital mismatches that increase the reactivity and allow nanoparticles with organic moieties to attach. However, there are regions on the CNT that have almost no curvature, as illustrated in Figure 1d. Since we have not functionalized the CNT, there are no functional groups created on the walls that facilitate NP anchorage. In such a case, it is relevant to gain insight into the nature of the graphitic layers in such areas of the CNT by probing their electronic structure with regards to sp hybridization. Energy loss near edge structure (ELNES) of the C K-edge was therefore used to probe the local electronic structure of the CNT at the nanoparticle interface in the noncurved regions of the CNT anchoring nanoparticles. In fact, several EELS spectra were taken from the hybrid nanocomposite at different places near the nanoparticles attached to the CNT. The EELS spectra were acquired from regions located far away from the carbon film of the TEM grid in order to exclude or minimize its influence on the C K-edge measurement. These areas of interest were at the holes of the holey carbon grid. Differences in the electronic structure along various points of the carbon nanotubes were probed in order to understand the affinity of these nanoparticles to only certain regions of the CNT. Accordingly, spectrum 1 in Figure 4b was

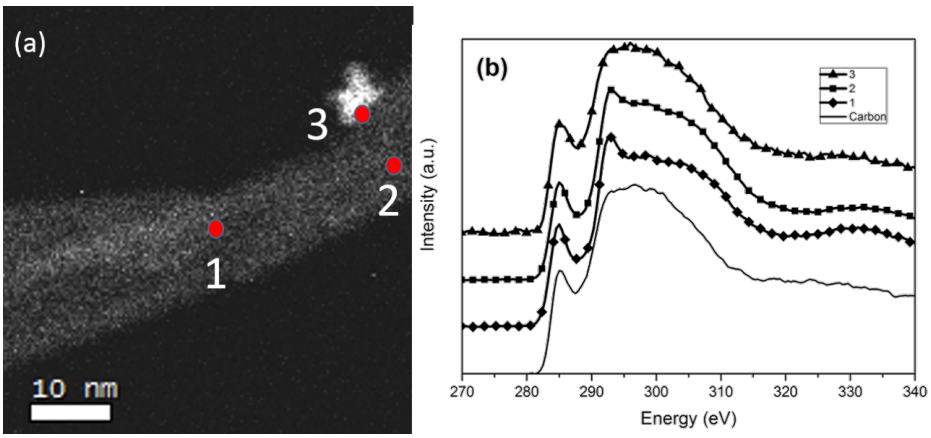


**Figure 4:** (a) HAADF-STEM image of the area of interest where EELS was performed, (b) C K-edge core loss EELS spectra on the area of interest indicated in Figure 2a.

acquired from point 1 in Figure 4a, which is devoid of nanoparticles, and indicates typical peaks for $sp^2/sp^3$ hybridization corresponding to multiwalled CNTs. The π* peak at 285 eV is related to the 1s to unoccupied antibonding π* transitions, and the exciton peak σ* at 292 eV arises due to transitions to the antibonding σ*. As we approach the region of the CNT decorated by nanoparticles (point 2, Figure 4a), we observe that the σ* peak in Figure 4b is smeared out along with a decrease in the intensity of the π* 285 eV edge. This smear is manifested as a broad hump starting above 288 eV and extending up to 305 eV, corresponding to the C 1s → σ* transition for disordered carbon–carbon bonds. On a similar note, other noticeable features are usually observed via X-ray absorption spectroscopy (XAS) in the region between π* and σ* transitions. These resonances are ascribed to the oxygen containing functional groups, i.e., a peak at 288.2 eV related to carbonyl (C=O) and another peak at 289.7 eV related to carboxylic (–COOH) [54]. In our case, we have not functionalized the nanotubes, therefore, the slight increase in the π*/σ* in ELNES C K-edge, arises due to the damage of the CNT walls [55], resulting in a loss of features in the σ* peak [54,56-58]. In the region of the CNT decorated by nanoparticles represented by point 3 in Figure 4a, we observe that the σ* peak in spectrum 3 of Figure 4b is even more smeared out with an increase in the intensity of the 285 eV edge and an even more featureless broad hump starting above 288 eV and extending up to 305 eV due to the C 1s → σ* transition, typical for extremely disordered carbon-carbon bonds. In fact, the smearing of this edge is characteristic of amorphous carbon, similar to the C-K edge of the amorphous carbon support of the TEM grid used as a reference, shown in Figure 4b.

Moreover, the apparent increase in the integrated area of the π* peak indicates an increase in the $sp^2$ bonding fraction compared to other regions of the CNT and could be attributed to pyrolytic carbon as a result of sonication. Since a CNT is a rolled up sheet of graphite, defects in graphene include $sp^2$ hybridized amorphous carbon harboring C–C defects with high reactivity, exploitable for the functionalization of graphene [59]. The breaking of the C–C bond is manifested as damage to the walls of the CNT and complete loss of medium to long range ordering [60]. This appears to be most conspicuous in places where the nanoparticles are attached to the CNT. Furthermore, amorphous carbon usually present in as-grown MWCNT contains a large number of dangling bonds [61] that also act as anchor sites via noncovalently bonded species. This further implies that C defects with dangling bonds act as anchor sites for nanoparticles whose surfaces are covered with functional groups, including amine groups. In our previous study, it was demonstrated that the $HfO_2$ nanoparticles have amine-type capping layers around them. Furthermore, nitrogen species were observed from the XPS survey spectra performed on these free-standing $HfO_2$ nanoparticles [20]. Thermo gravimetric analysis further confirmed that the surfaces of these nanoparticles are covered by organic species (14 wt %) that are mainly amine and reaction by-products typical of nonaqueous sol–gel routes using precursors that do not contain hydrate species. Here, the amine species capping acts not only as a surfactant but also as a shape and size controlling agent during growth of the NP. Since our MWCNTs were not acid treated, the particles are therefore not attached via a C–O–H bond. We can also exclude π–π interaction between the C ring of the CNT and the benzyl ring of probable benzylamine organic species on the surface of the nanoparticles. This implies that the most probable bonding mechanism is via a C dangling bond and N from the amine-type capping layer.

## Photocurrent response

For the electrical characterization, the nanocomposite is deposited on a glass slide and contacted using a micromanipulator manual probe station as shown in inset of Figure 5a. The dark current–voltage characteristic is mostly linear, as expected

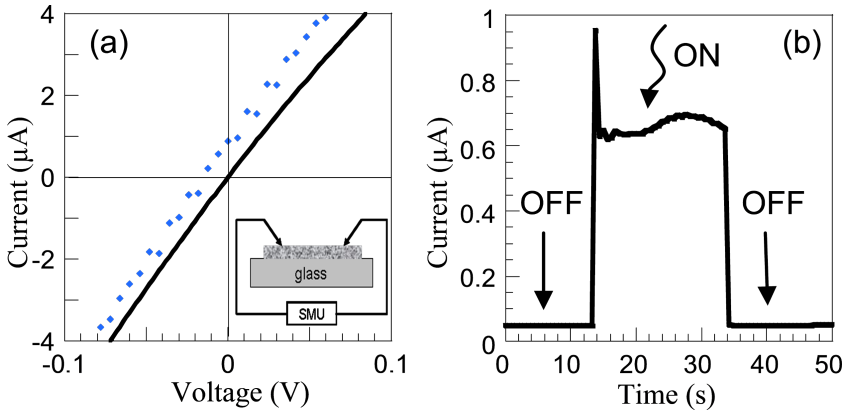


**Figure 5:** (a) *I–V* characteristic of a nanohybrid material in the dark (full line) and under illumination (dots) vs bias voltage. In the inset, a schematic illustration of the measurement set up is given. (b) On/off cycle photoresponse of MWCNT:$HfO_2$ excited with UV–vis light (at 10 mV).

for an ohmic conduction through metallic MWCNTs (Figure 5a). No influence of the concentration of $HfO_2$ NPs decorating the MWCNTs is noticed in the dark *I–V* curves. UV illumination (365 nm) also has no detectable effect on bare MWCNTs. Although it was reported that MWCNTs generate a photocurrent [62], this effect is generally weak with respect to the dark current in the absence of additional Schottky or p–n junction to enhance the photoresponse [63]. This agrees well with the PL measurements of the nanocomposites (see Figure 2) showing no additional spectral features apart from emission peaks associated with $Hf^{3+}$ and $O^{2-}$ states in $HfO_2$ and thus supporting the metallic nature of the MWCNTs. For the MWCNT:$HfO_2$ hybrid material, a clear shift of the *I–V* curve is observed in Figure 5a upon UV illumination. In the present experiment, the short-circuit current ($I_{SC}$) is 0.7 μA and the open-circuit voltage ($V_{oc}$) is −12 mV. The photoresponse under UV excitation is sizeable with a higher quantity of the agglomerated $HfO_2$:CNT density. The *I–V* characteristic is still mainly linear, with a relatively weak decrease of the resistivity, which is consistent with the fact that the electrical transport is dominated by the conduction through the metallic MWCNTs [64]. Under zero bias a photocurrent is generated, indicating that the MWCNT:$HfO_2$ nanocomposite acts as a photovoltaic cell. The on/off cycle measurements show a square and well-defined photoresponse after turn-on and turn-off illumination (Figure 5b).

After turn-on illumination, the photocurrent first presents a rapid response time defined by an initial spiking of the photocurrent, indicating a rapid filling and discharging of the defects states. This is followed by a rather stable and reproducible photoresponse, suggesting that the photogenerated electrons are effectively transferred from the NP towards the CNT. Correspondingly, when the light is turned off, the photogenerated charges are rapidly dissipated. Similar to MWCNT:ZnO [64,65], the rapid response of the photocurrent could be related to the intimate contact between the $HfO_2$ NP and the MWCNT further enhanced by the absence of functional groups on the surface of the CNT.

In our previous work, we reported on the time evolution of the PL response from the $HfO_2$ nanoparticles [21]. At this point, it is worth noting that the time evolution of the luminescence from the cubic $HfO_2$ nanoparticles under constant UV exposure (325 nm) shows a steady decline during the first 60 s and the most prominent decrease occurs for emission at 3.1 eV, which is related to $Hf^{3+}$ defects via oxygen vacancies [19]. These defects are located mainly close to the surface and thus dominate the PL due to the large surface-to-volume ratio of the nanoparticles. This also suggests that particular band bending and charge state conditions at the surface define the radiative or nonradiative behavior of the defect center and in turn determine both the spectral features and photoresponse of the hybrid material. Apparently, these surface defects act as radiative centers upon contacting $HfO_2$ NPs with CNTs (Figure 3a) and also produce a continuous, quantifiable photocurrent during the on cycle. The abrupt decrease to zero photocurrent during light-off conditions confirms that the remaining trapping centers and nonradiative recombination sites are rapidly dissipated.

These preliminary results demonstrate the potential of the $HfO_2$ NP/MWCNT nanocomposite for functional interactions in energy harvesting applications. Quantum efficiency measurements are under investigation in order to precisely evaluate the origin of the photocurrent. Moreover, in order to optimize the structure, it would be necessary to further understand the role of surface defects, notably $Hf^{3+}$ and oxygen vacancies during the photoemission process. In particular, the role of the defects should be evaluated because charge accumulation within them during illumination may induce band bending in the electronic structure, amenable to photocurrent generation.

## Conclusion

We have successfully synthesized a hybrid material composed of nonfunctionalized CNTs and $HfO_2$ nanoparticles capable of generating a photocurrent under UV excitation. STEM studies have shown us that the $HfO_2$ nanoparticles remain undamaged upon sonication and are preferentially attached to defects in the CNT, such as bends, kinks and buckles. Furthermore, the nanoparticles also tend to anchor on side walls of the CNTs, where amorphous carbon or wall damage is present. Defect sites and amorphous carbon contain a large number of C dangling bonds that act as anchoring sites. The origin of this amorphous carbon is certainly the result of wall damage or C–C bond breaking due to the sonication treatment. Optical measurements have revealed unique features of the hybrid material. In fact, the π-plasmon peak of the CNT gradually overlaps with the band gap absorption edge of the $HfO_2$ nanoparticles. This implies that a possible antenna effect of the CNTs on $HfO_2$ is likely if the material is excited in the deep UV region. The photocurrent measurements further indicate that evacuation of charges from the surface states of $HfO_2$ nanoparticles via direct contact with MWCNTs turns them from radiative to nonradiative recombination centers and contributes to photocurrent generation in the material. Such a material therefore finds interest for applications in photovoltaics owing to an increase in its spectral range along with the plasmonic effect of the CNTs, which also serves to conduct charges from the surface states of the nanoparticles to an external load. To put the present work into perspective, we note that fabrication of all-carbon nanocomposites by replacing $HfO_2$ by carbon quantum dots (CQDs) might appear as an appealing continuation of this study considering the very attrac-

tive properties of CQDs (e.g., stability, high conductivity, strong and tunable photoluminescence emission throughout the visible spectrum) [66]. However, recent reports show that the quenching in such a system is static and no electron transfer is available for the generation of a photocurrent [11].

## Experimental

Synthesis: The procedure for synthesizing cubic $HfO_2$ NPs was carried out in a glove box ($O_2$ and $H_2O$, <1 ppm). In a typical synthesis, hafnium *tert*-butoxide ($(Hf(O\textit{t}\text{-}Bu)_4$) precursor (STREM 99.9%) (0.87 mmol) was added to 20 mL (183 mmol) of benzylamine (purified by redistillation (99.5%), Aldrich). The reaction mixture was transferred into a stainless steel autoclave and carefully sealed. Thereafter, the autoclave was taken out of the glove box and heated in a furnace at 300 °C for 2 days. The resulting milky suspensions were centrifuged; the precipitates were thoroughly washed with ethanol and dichloromethane and subsequently dried in air at 60 °C [21]. NANOCYL NC7000 MWCNTs with an average diameter and length of 10 nm and 1.5 μm, respectively, were used in the synthesis. The nanoparticles were then dispersed in pure ethanol along with the MWCNTs and sonicated for a total of 2 h [67].

Characterization: High angle annular dark field scanning transmission electron microscopy (HAADF-STEM) was carried out on a probe-corrected Titan G2 80–200 kV operating at 80 kV to reduce beam damage. The probe size and therefore the point-to-point resolution was ≈1 Å in STEM mode. High resolution transmission electron microscopy (HRTEM) carried out on the same microscope at 200 kV provided a point-to-point resolution of 2.4 Å. Electron energy loss spectroscopy (EELS) was acquired in STEM mode with an Enfinium spectrometer at 80 kV. For the EELS data acquisition, the convergence and collection angles were set to 14.6 mrad and 24 mrad, respectively, for a camera length of 4 cm, a condenser aperture of 50 μm and a spectrometer slit of 3 mm. For these values, the energy resolution measured as the full width at half maximum of the zero-loss peak is 0.9 eV and the dispersion was set to 0.4 eV/channel.

The absorption properties were derived from the transmittance measurements performed at room temperature using a UV–vis spectrophotometer (Thermo Scientific, EVO-600). PL was investigated at a room temperature by employing a 325 nm wavelength CW He–Cd laser with an output power of 6 mW as an excitation source. The emission was collected by a microscope and directed to a fiber optic spectrometer (Ocean Optics, USB4000) with a spectral resolution of 2 nm. The electrical measurements were carried out using a source measure unit (Agilent 4156). The sample was illuminated by a 125 W Hg lamp emanating a wavelength of 365 nm.

## Acknowledgements

The authors wish to acknowledge the Estonian Research Council (grant PUT431), the European Regional Development Fund project TK134 (TAR16019) and MENESR and MAEDI French ministries (Parrot program n°33787YJ), the Norwegian Research Council, and the Estonian Road Map infrastructure NAMUR project for financial support to this work.

## References

1. Yujin, C.; Chunling, Z.; Taihong, W. *Nanotechnology* **2006,** *17,* 3012. doi:10.1088/0957-4484/17/12/033
2. Willinger, M.-G.; Neri, G.; Rauwel, E.; Bonavita, A.; Micali, G.; Pinna, N. *Nano Lett.* **2008,** *8,* 4201–4204. doi:10.1021/nl801785b
3. Kamat, P. V. *J. Phys. Chem. C* **2008,** *112,* 18737–18753. doi:10.1021/jp806791s
4. Jeong, S. Y.; Lim, S. C.; Bae, D. J.; Lee, Y. H.; Shin, H. J.; Yoon, S.-M.; Choi, J. Y.; Cha, O. H.; Jeong, M. S.; Perello, D.; Yun, M. *Appl. Phys. Lett.* **2008,** *92,* 243103. doi:10.1063/1.2944813
5. Huang, H.-C.; Barua, S.; Sharma, G.; Dey, S. K.; Rege, K. *J. Controlled Release* **2011,** *155,* 344–357. doi:10.1016/j.jconrel.2011.06.004
6. Fernandes, G. E.; Liu, Z.; Kim, J. H.; Hsu, C.-H.; Tzolov, M. B.; Xu, J. *Nanotechnology* **2010,** *21,* 465204. doi:10.1088/0957-4484/21/46/465204
7. Kongkanand, A.; Kamat, P. V. *ACS Nano* **2007,** *1,* 13–21. doi:10.1021/nn700036f
8. Jang, S.-R.; Vittal, R.; Kim, K.-J. *Langmuir* **2004,** *20,* 9807–9810. doi:10.1021/la049022f
9. Khanderi, J.; Hoffmann, R. C.; Gurlo, A.; Schneider, J. J. *J. Mater. Chem.* **2009,** *19,* 5039–5046. doi:10.1039/B904822G
10. Ramuz, M. P.; Vosgueritchian, M.; Wei, P.; Wang, C.; Gao, Y.; Wu, Y.; Chen, Y.; Bao, Z. *ACS Nano* **2012,** *6,* 10384–10395. doi:10.1021/nn304410w
11. Yu, P.; Wen, X.; Toh, Y.-R.; Lee, Y.-C.; Huang, K.-Y.; Huang, S.; Shrestha, S.; Conibeer, G.; Tang, J. *J. Mater. Chem. C* **2014,** *2,* 2894–2901. doi:10.1039/C3TC32395A
12. Roy, P.; Chen, P.-C.; Periasamy, A. P.; Chen, Y.-N.; Chang, H.-T. *Mater. Today* **2015,** *18,* 447–458. doi:10.1016/j.mattod.2015.04.005
13. Wang, J.; Li, H. P.; Stevens, R. *J. Mater. Sci.* **1992,** *27,* 5397–5430. doi:10.1007/BF00541601
14. Robertson, J. *Rep. Prog. Phys.* **2006,** *69,* 327–396. doi:10.1088/0034-4885/69/2/R02
15. Dubourdieu, C.; Rauwel, E.; Millon, C.; Chaudouët, P.; Ducroquet, F.; Rochat, N.; Rushworth, S.; Cosnier, V. *Chem. Vap. Deposition* **2006,** *12,* 187–192. doi:10.1002/cvde.200506397
16. Choi, J. H.; Mao, Y.; Chang, J. P. *Mater. Sci. Eng., R* **2011,** *72,* 97–136. doi:10.1016/j.mser.2010.12.001
17. Dubourdieu, C.; Rauwel, E.; Roussel, H.; Ducroquet, F.; Holländer, B.; Rossell, M.; Van Tendeloo, G.; Lhostis, S.; Rushworth, S. *J. Vac. Sci. Technol., A* **2009,** *27,* 503. doi:10.1116/1.3106627
18. Rauwel, E.; Galeckas, A.; Rauwel, P.; Sunding, M. F.; Fjellvåg, H. *J. Phys. Chem. C* **2011,** *115,* 25227–25233. doi:10.1021/jp208487v
19. Rauwel, E.; Galeckas, A.; Rauwel, P.; Fjellvåg, H. *Adv. Funct. Mater.* **2012,** *22,* 1174–1179. doi:10.1002/adfm.201101013
20. Rauwel, P.; Rauwel, E.; Persson, C.; Sunding, M. F.; Galeckas, A. *J. Appl. Phys.* **2012,** *112,* 104107. doi:10.1063/1.4766272
21. Rauwel, E.; Galeckas, A.; Rauwel, P. *Mater. Res. Express* **2014,** *1,* 015035. doi:10.1088/2053-1591/1/1/015035

22. Li, Y.; Tang, J.; He, L.; Liu, Y.; Liu, Y.; Chen, C.; Tang, Z. *Adv. Mater.* **2015,** *27,* 4075–4080. doi:10.1002/adma.201501779
23. Dumée, L.; Sears, K.; Schütz, J.; Finn, N.; Duke, M.; Gray, S. *Nanomaterials* **2013,** *3,* 70–85. doi:10.3390/nano3010070
24. Navarro de Miranda, A.; Pardini, L. C.; Moreira dos Santos, C. A.; Vieira, R. *Mater. Res. (Sao Carlos, Braz.)* **2011,** *14,* 560–563. doi:10.1590/S1516-14392011005000083
25. Zhang, W.-D.; Xu, B.; Jiang, L.-C. *J. Mater. Chem.* **2010,** *20,* 6383–6391. doi:10.1039/B926341A
26. Tasis, D.; Tagmatarchis, N.; Georgakilas, V.; Prato, M. *Chem. – Eur. J.* **2003,** *9,* 4000–4008. doi:10.1002/chem.200304800
27. Eder, D.; Windle, A. H. *Adv. Mater.* **2008,** *20,* 1787–1793. doi:10.1002/adma.200702835
28. Biroju, R. K.; Giri, P. K. *J. Phys. Chem. C* **2014,** *118,* 13833–13843. doi:10.1021/jp500501e
29. Rossell, M. D.; Kuebel, C.; Ilari, G.; Rechberger, F.; Heiligtag, F. J.; Niederberger, M.; Koziej, D.; Erni, R. *Carbon* **2013,** *61,* 404–411. doi:10.1016/j.carbon.2013.05.024
30. Li, H.; Zhao, N.; He, C.; Shi, C.; Du, X.; Li, J. *Mater. Sci. Eng., A* **2008,** *473,* 355–359. doi:10.1016/j.msea.2007.04.003
31. Salzmann, C. G.; Llewellyn, S. A.; Tobias, G.; Ward, M. A. H.; Huh, Y.; Green, M. L. H. *Adv. Mater.* **2007,** *19,* 883–887. doi:10.1002/adma.200601310
32. Sumpter, B. G.; Huang, J.; Meunier, V.; Romo-Herrera, J. M.; Cruz-Silva, E.; Terrones, H.; Terrones, M. *Int. J. Quantum Chem.* **2009,** *109,* 97–118. doi:10.1002/qua.21893
33. Hashim, D. P.; Narayanan, N. T.; Romo-Herrera, J. M.; Cullen, D. A.; Hahm, M. G.; Lezzi, P.; Suttle, J. R.; Kelkhoff, D.; Muñoz-Sandoval, E.; Ganguli, S.; Roy, A. K.; Smith, D. J.; Vajtai, R.; Sumpter, B. G.; Meunier, V.; Terrones, H.; Terrones, M.; Ajayan, P. M. *Sci. Rep.* **2012,** No. 363. doi:10.1038/srep00363
34. Hirsch, A. *Angew. Chem., Int. Ed.* **2002,** *41,* 1853–1859. doi:10.1002/1521-3773(20020603)41:11<1853::AID-ANIE1853>3.0.CO;2-N
35. Azimi, H.; Kuhri, S.; Osvet, A.; Matt, G.; Khanzada, L. S.; Lemmer, M.; Luechinger, N. A.; Larsson, M. I.; Zeira, E.; Guldi, D. M.; Brabec, C. J. *J. Am. Chem. Soc.* **2014,** *136,* 7233–7236. doi:10.1021/ja502221r
36. Yano, T.-a.; Ichimura, T.; Kuwahara, S.; H'Dhili, F.; Uetsuki, K.; Okuno, Y.; Verma, P.; Kawata, S. *Nat. Commun.* **2013,** No. 2592. doi:10.1038/ncomms3592
37. Zhang, Y. Y.; Xiang, Y.; Wang, C. M. *J. Appl. Phys.* **2009,** *106,* 113503. doi:10.1063/1.3261760
38. Van Hove, L. *Phys. Rev.* **1953,** *89,* 1189–1193. doi:10.1103/PhysRev.89.1189
39. An, K. H.; Lee, Y. H. *NANO* **2006,** *01,* 115–138. doi:10.1142/S1793292006000136
40. Jeong, M. S.; Byeon, C. C.; Cha, O. H.; Jeong, H.; Han, J. H.; Choi, Y. C.; An, K. H.; Oh, K. H.; Kim, K. K.; Lee, Y. H. *NANO* **2008,** *03,* 101–108. doi:10.1142/S1793292008000885
41. Ryuichi, K.; Masami, T.; Michiyoshi, T.; Yahachi, S. *Jpn. J. Appl. Phys.* **1994,** *33,* L1316. doi:10.1143/JJAP.33.L1316
42. Jiang, H.; Gomez-Abal, R. I.; Rinke, P.; Scheffler, M. *Phys. Rev. B* **2010,** *81,* 085119. doi:10.1103/PhysRevB.81.085119
43. Takeuchi, H.; Ha, D.; King, T.-J. *J. Vac. Sci. Technol., A* **2004,** *22,* 1337–1341. doi:10.1116/1.1705593
44. Ciuparu, D.; Ensuque, A.; Shafeev, G.; Bozon-Verduraz, F. *J. Mater. Sci. Lett.* **2000,** *19,* 931–933. doi:10.1023/A:1006799701474
45. Muñoz Ramo, D.; Gavartin, J. L.; Shluger, A. L.; Bersuker, G. *Phys. Rev. B* **2007,** *75,* 205336. doi:10.1103/PhysRevB.75.205336
46. Saito, R.; Fujita, M.; Dresselhaus, G.; Dresselhaus, M. S. *Appl. Phys. Lett.* **1992,** *60,* 2204–2206. doi:10.1063/1.107080
47. Mintmire, J. W.; Dunlap, B. I.; White, C. T. *Phys. Rev. Lett.* **1992,** *68,* 631–634. doi:10.1103/PhysRevLett.68.631
48. Hamada, N.; Sawada, S.-i.; Oshiyama, A. *Phys. Rev. Lett.* **1992,** *68,* 1579–1581. doi:10.1103/PhysRevLett.68.1579
49. Zhang, R.; Fan, L.; Fang, Y.; Yang, S. *J. Mater. Chem.* **2008,** *18,* 4964–4970. doi:10.1039/B808769E
50. Olek, M.; Büsgen, T.; Hilgendorff, M.; Giersig, M. *J. Phys. Chem. B* **2006,** *110,* 12901–12904. doi:10.1021/jp061453e
51. Dutta, M.; Jana, S.; Basak, D. *ChemPhysChem* **2010,** *11,* 1774–1779. doi:10.1002/cphc.200900960
52. Ago, H.; Shaffer, M. S. P.; Ginger, D. S.; Windle, A. H.; Friend, R. H. *Phys. Rev. B* **2000,** *61,* 2286–2290. doi:10.1103/PhysRevB.61.2286
53. Clapp, A. R.; Medintz, I. L.; Fisher, B. R.; Anderson, G. P.; Mattoussi, H. *J. Am. Chem. Soc.* **2005,** *127,* 1242–1250. doi:10.1021/ja045676z
54. Wang, D.; Yang, J.; Li, X.; Geng, D.; Li, R.; Cai, M.; Sham, T.-K.; Sun, X. *Energy Environ. Sci.* **2013,** *6,* 2900–2906. doi:10.1039/C3EE40829A
55. Delgado, J. J.; Chen, X.; Tessonnier, J. P.; Schuster, M. E.; Del Rio, E.; Schlögl, R.; Su, D. S. *Catal. Today* **2010,** *150,* 49–54. doi:10.1016/j.cattod.2009.07.103
56. Müller, J.-O.; Su, D. S.; Wild, U.; Schlögl, R. *Phys. Chem. Chem. Phys.* **2007,** *9,* 4018–4025. doi:10.1039/B704850E
57. Chuang, C.-H.; Wang, Y.-F.; Shao, Y.-C.; Yeh, Y.-C.; Wang, D.-Y.; Chen, C.-W.; Chiou, J. W.; Ray, S. C.; Pong, W. F.; Zhang, L.; Zhu, J. F.; Guo, J. H. *Sci. Rep.* **2014,** *4,* No. 4525. doi:10.1038/srep04525
58. Liang, Y.; Wang, H.; Zhou, J.; Li, Y.; Wang, J.; Regier, T.; Dai, H. *J. Am. Chem. Soc.* **2012,** *134,* 3517–3523. doi:10.1021/ja210924t
59. Grierson, D. S.; Sumant, A. V.; Konicek, A. R.; Friedmann, T. A.; Sullivan, J. P.; Carpick, R. W. *J. Appl. Phys.* **2010,** *107,* 033523. doi:10.1063/1.3284087
60. Zhang, Z.-l.; Brydson, R.; Aslam, Z.; Reddy, S.; Brown, A.; Westwood, A.; Rand, B. *Carbon* **2011,** *49,* 5049–5063. doi:10.1016/j.carbon.2011.07.023
61. Pan, H.; Pruski, M.; Gerstein, B. C.; Li, F.; Lannin, J. S. *Phys. Rev. B* **1991,** *44,* 6741–6745. doi:10.1103/PhysRevB.44.6741
62. El Khakani, M. A.; Le Borgne, V.; Aïssa, B.; Rosei, F.; Scilletta, C.; Speiser, E.; Scarselli, M.; Castrucci, P.; De Crescenzi, M. *Appl. Phys. Lett.* **2009,** *95,* 083114. doi:10.1063/1.3211958
63. Castrucci, P.; Scilletta, C.; Del Gobbo, S.; Scarselli, M.; Camilli, L.; Simeoni, M.; Delley, B.; Continenza, A.; De Crescenzi, M. *Nanotechnology* **2011,** *22,* 115701. doi:10.1088/0957-4484/22/11/115701
64. Ok, J. G.; Tawfick, S. H.; Juggernauth, K. A.; Sun, K.; Zhang, Y.; Hart, A. J. *Adv. Funct. Mater.* **2010,** *20,* 2470–2480. doi:10.1002/adfm.201000249
65. Liu, J.-H.; Saravanan, L. *Mater. Lett.* **2014,** *134,* 30–33. doi:10.1016/j.matlet.2014.07.056
66. Lim, S. Y.; Shen, W.; Gao, Z. *Chem. Soc. Rev.* **2015,** *44,* 362–381. doi:10.1039/C4CS00269E
67. Koo, Y.; Littlejohn, G.; Collins, B.; Yun, Y.; Shanov, V. N.; Schulz, M.; Pai, D.; Sankar, J. *Composites, Part B* **2014,** *57,* 105–111. doi:10.1016/j.compositesb.2013.09.004

BEILSTEIN JOURNAL OF NANOTECHNOLOGY

# Voltammetric determination of polyphenolic content in pomegranate juice using a poly(gallic acid)/multiwalled carbon nanotube modified electrode

Refat Abdel-Hamid* and Emad F. Newair

Full Research Paper

Open Access

Address:
Unit of Electrochemistry Applications (UEA), Chemistry Department, Faculty of Science, Sohag University, Sohag 82524, Egypt

Email:
Refat Abdel-Hamid* - refat.abdelhamid@science.sohag.edu.eg

* Corresponding author

Keywords:
electrochemical sensor; gallic acid; multiwalled carbon nanotubes; pomegranate juice; total phenolic content

*Beilstein J. Nanotechnol.* **2016,** *7,* 1104–1112.
doi:10.3762/bjnano.7.103

Received: 15 January 2016
Accepted: 15 July 2016
Published: 29 July 2016

This article is part of the Thematic Series "Nanostructures for sensors, electronics, energy and environment III".

Guest Editor: N. Motta



## Abstract

A simple and sensitive poly(gallic acid)/multiwalled carbon nanotube modified glassy carbon electrode (PGA/MWCNT/GCE) electrochemical sensor was prepared for direct determination of the total phenolic content (TPC) as gallic acid equivalent. The GCE working electrode was electrochemically modified and characterized using scanning electron microscope (SEM), cyclic voltammetry (CV), chronoamperometry and chronocoulometry. It was found that gallic acid (GA) exhibits a superior electrochemical response on the PGA/MWCNT/GCE sensor in comparison with bare GCE. The results reveal that a PGA/MWCNT/GCE sensor can remarkably enhance the electro-oxidation signal of GA as well as shift the peak potentials towards less positive potential values. The dependence of peak current on accumulation potential, accumulation time and pH were investigated by square-wave voltammetry (SWV) to optimize the experimental conditions for the determination of GA. Using the optimized conditions, the sensor responded linearly to a GA concentration throughout the range of $4.97 \times 10^{-6}$ to $3.38 \times 10^{-5}$ M with a detection limit of $3.22 \times 10^{-6}$ M (S/N = 3). The fabricated sensor shows good selectivity, stability, repeatability and (101%) recovery. The sensor was successfully utilized for the determination of total phenolic content in fresh pomegranate juice without interference of ascorbic acid, fructose, potassium nitrate and barbituric acid. The obtained data were compared with the standard Folin–Ciocalteu spectrophotometric results.

## Introduction

Gallic acid (GA) is a natural polyphenolic compound found in fruits, vegetables and several other plants [1]. The study of the role of GA in providing better therapeutic outcomes against arsenic-induced toxicity showed that GA is effective against arsenic-induced oxidative stress [2]. A facile and ultrasensitive sensor based on gold microclusters electrodeposited on sulfo-

nate-functionalized graphene that was immobilized on the surface of a GCE was fabricated and applied for the simultaneous determination of gallic acid and uric acid [3]. The electrochemical mechanism and optimal test conditions of GA were carefully investigated on a sensor based on chitosan/f$Fe_2O_3$/reduced graphene oxide/GCE. Under optimal conditions, the detection limit was estimated to be $1.5 \times 10^{-7}$ M [4]. An electrochemical sensor coupled with an effective flow-injection amperometric system was developed for determination of GA in a mild neutral conditions. The sensor is based on a poly (melamine) film immobilized on a preanodized screen-printed carbon electrode [5]. A voltammetric determination of GA on a hanging mercury drop electrode was investigated by cathodic adsorptive stripping voltammetry [6]. A sensitive and reliable method was developed using a differential pulse polarographic method for determination of GA in fruit juices with a detection limit of 0.3 μM [7]. Electrochemical sensors based on a carbon paste electrode modified with $SiO_2$ nanoparticles [8] and carbon nanotubes [9,10] were utilized for determination of gallic acid. A sensor based on a carbon paste electrode modified with multiwalled carbon nanotubes was used for voltammetric determination of ellagic acid and gallic acid in an *Myrtus communis*, *Punica granatum* and Itriphal formulation [10]. Glassy carbon electrodes modified with a multiwalled carbon nanotube/*o*-dianisidine derivative [11] and a molecularly imprinted polypyrrole polymer-based film [12] were used for gallic acid analysis with high selectivity. A bimediator amperometric sensor for gallic acid was fabricated by surface modification of a graphite electrode with thionine and nickel hexacyanoferrate [13]. A polyethyleneimine-functionalized graphene oxide modified glassy carbon electrode sensor was developed for sensitive detection of gallic acid [14]. A polyepinephrine modified glassy carbon electrode electrochemical sensor was developed for adsorptive stripping voltammetric determination of gallic acid and successfully applied for the estimation of GA in black tea [15]. The determination of gallic acid and caffeic acid was conducted by using a stable sensor based on a Zn–Al–$NO_3$ layered double hydroxide film/glassy carbon electrode [16].

Recently, pomegranate juice has attracted more scientific attention because of its valuable health effects; especially due to its high content of phenolic compounds [17]. It is a complex drink and a rich source of antioxidants such as phenolic acids, tannins, anthocyanins, procyanidins, and flavonol glycosides [18]. Due to the positive effects of polyphenol antioxidants on human health, the improvement of sensitive and robust methods for their determination gains more importance. Consequently, the measurement of the total polyphenolic content (TPC) is a good representation of the level of antioxidants that exist in a sample [19-21].

The selective and sensitive determination of TPC (GA equivalent, mg GAE $L^{-1}$) is a difficult task, thus simple and fast techniques are still needed for these purposes. Therefore, in continuation of our previous work on the electrochemical study of antioxidants [15,22-27], the objective of present study is to develop a sensitive electrochemical method for the determination of the total phenolic content using poly(gallic acid)/multiwalled carbon nanotube/glassy carbon electrode (PGA/MWCNT/GCE) electrochemical sensor. The polymer may overcome the slow mass transfer on bare GCE or MWCNT/GCE. Thus the modification enhances the redox peak current and could be used with high sensitivity. Recently, the use of nanomaterials for electrode modification has grown exponentially, owing to their advantageous electrochemical properties. Carbon nanotubes are the main representatives of nanomaterials used in the construction of electrochemical sensors with good performance. Multiwalled carbon nanotubes (MWCNTs) were selected due to their advantages such as rapid electron transfer rate and high electrocatalytic activity. The glassy carbon working electrode was electrochemically modified and characterized using scanning electron microscope (SEM), cyclic voltammetry, chronoamperometry and chronocoulometry. To validate the suggested procedure, the determination of total phenolic content in pomegranate juice was performed using square-wave voltammetry. The results collected at optimal conditions were compared with the standard Folin–Ciocalteu spectrophotometric data.

## Results and Discussion

### SEM characterization of PGA/MWCNT composite film

The response of the prepared electrochemical sensor is related to its physical morphology. The surface morphology of the PGA/MWCNT film on a rectangular indium tin oxide (ITO) coated glass slide (resistivity of 8–12 Ω/□) was examined using SEM (Figure 1). The film is deposited on the ITO with the same experimental conditions as for the GCE. As shown, the nanocomposite has a short, tubular topology with a smooth surface. The nanocomposites are uniformly distributed and held together into bundles. The white circular species represent the ends of the CNTs on the surface.

### Electrochemical characterization of PGA/MWCNT/GC modified electrode

#### Cyclic voltammetry

Cyclic voltammograms of 1.0 mM gallic acid in 0.2 M $H_3PO_4$ at three different glassy carbon modified electrodes, PGA/GCE, MWCNT/GCE and PGA/MWCNT/GCE, were recorded at a scan rate of 50 mV/s (Figure 2). Gallic acid shows two irreversible cyclic voltammetric waves on anodic potential sweeping, lacking the corresponding reduction counterparts. An increase in the peak current and a shift of the peak potentials

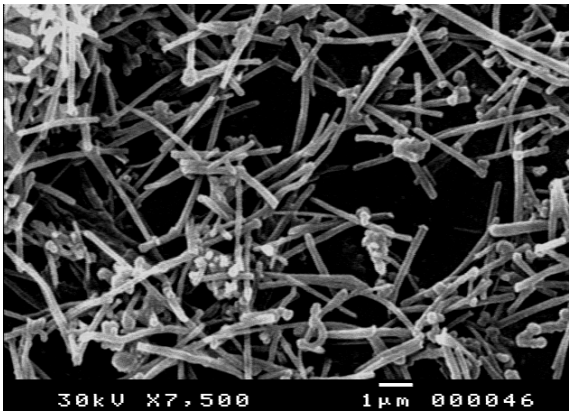


**Figure 1:** SEM morphology of a PGA/MWCNT film nanocomposite at 7,500 magnification.

towards less positive potential values are observed upon the electrochemical modification of the GCE. This reveals that the electrode kinetics is improved. Upon examination of the voltammetric data, it is observed that the first anodic wave is highly sensitive to the modification. GA shows the first CV wave with a peak potential ($E_p^a$) at 0.69 V on the bare GCE. The $E_p^a$ is shifted to 0.61 and 0.53 V on MWCNT/GCE and PGA/MWCNT/GCE, respectively. Furthermore, a significant enhancement in peak current is observed on the two modified electrodes. The enhancement on MWCNT/GCE and PGA/MWCNT/GCE is 1.94 and 2.94 times, respectively, relative to the bare GCE. These observations reveal that the modification of the GCE shows a significant effect on the electrochemical oxidation response of GA. Thus, one can conclude that a PGA/MWCNTS/GCE sensor provides higher activity towards GA oxidation, improves the electrode kinetics, and decreases its over potential of oxidation.

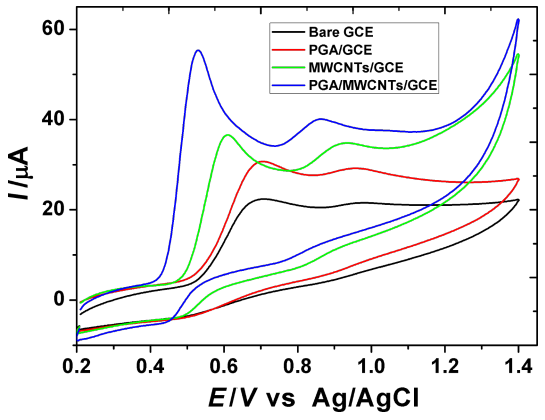


**Figure 2:** Cyclic voltammograms of 1.0 mM GA in 0.2 M $H_3PO_4$ at a scan rate of 50 mV $s^{-1}$ on bare GCE, PGA/GCE, MWCNT/GCE and PGA/MWCNT/GCE.

The cyclic voltammetric behavior of $K_3[Fe(CN)_6]$ on a bare GCE and PGA/MWCNT/GCE modified electrodes was investigated for the determination of true electroactive surface area (data not shown). The area can be estimated for a reversible and diffusion-controlled process according to the Randles–Sevcik [28] equation,

$$i_p = \left(2.69\times10^5\right) n^{3/2} D^{1/2} C_o A \nu^{1/2}, \quad (1)$$

where $i_p$ is the peak current, $n$ is the number of electron transfers in the reaction (which is equal to 1), $D$ is the molecular diffusion coefficient ($cm^2/s$) in solution, $A$ is the active surface area ($cm^2$), $C_o$ is the concentration ($mol/cm^3$) of the probe molecule in the solution, and ν is the scan rate (V/s). The electroactive surface area ($A$) of the bare glassy electrode and its modified composite electrode was determined by cyclic voltammetric response using 1.0 mM solution of $K_3[Fe(CN)_6]$ in 0.2 M potassium chloride solution at a scan rate of 50 mV/s. It was known that the electrochemical reduction of the ferricyanide ion at the GCE is diffusion-controlled. From Equation 1, the electroactive surface area of the subject electrodes was evaluated taking into account a diffusion coefficient for ferricyanide ion of $7.6 \times 10^{-6}$ $cm^2/s$ in 0.2 M KCl [29]. The estimated active surface area values are 0.050 and 0.077 $cm^2$ for bare GCE and PGA/MWCNT/GCE, respectively.

## Chronoamperometry

For comparison, chronoamperometric measurements were employed for estimation of the electroactive surface area. The chronoamperometric behavior of 1.0 mM $K_3[Fe(CN)_6]$ on GCE and PGA/MWCNT/GCE in 0.2 M KCl solution for the first wave at different duration times was performed. For chronoamperometric experiments, the electrode potential was stepped from 0.50 to 0.02 V on GCE and from 0.050 to −0.20 V on PGA/MWCNT/GCE for a fixed duration, τ. The current that passes during τ is measured. The current corresponding to the electrochemical reaction is described by Cottrell's equation [28]:

$$i(t<\tau) = nFAC D^{1/2} \pi^{1/2} t^{-1/2}, \quad (2)$$

where $D$ is the diffusion coefficient ($cm^2/s$), $C$ is the bulk concentration ($mol/dm^3$), τ is the step duration and $n$, $F$, and $A$ have their usual significance. According Cottrell's equation, upon plotting the current response against $t^{-1/2}$, a straight linear line is obtained with a correlation coefficient of 0.999 for all duration times (Figure 3). From the slope, the active surface area was determined. The area of the working electrodes was found to be 0.051 and 0.072 $cm^2$ for bare GCE and PGA/MWCNT/

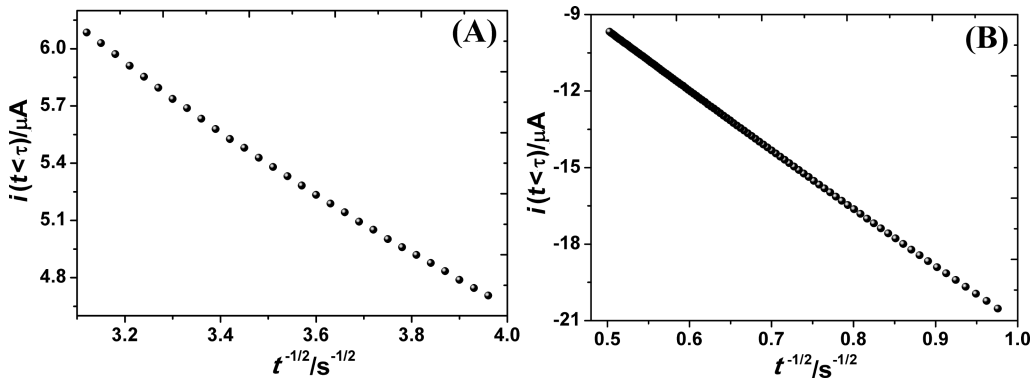


**Figure 3:** Relationship of $i(t < \tau)$ vs ($t^{-1/2}$) chronoamperometry of 1.0 mM $K_3[Fe(CN)_6]$ in 0.2 M KCl on (A) GCE and (B) PGA/MWCNT/GCE.

GCE, respectively. These values are close to the values obtained using the voltammetric method.

The catalytic rate constant ($k_{cat}$) can be evaluated using chronoamperometry. It was determined upon performing chronoamperometry on 0.2 M $H_3PO_4$ solutions in absence and presence of gallic acid. Figure 4 shows the obtained chronoamperograms of GA on the PGA/MWCNT/GCE. The $k_{cat}$ value for the oxidation reaction between GA and the modified GCE was determined using the following equation [30]:

$$\frac{i_{cat}}{i_L} = \pi^{1/2} \left(k_{cat} C t\right)^{1/2}, \quad (3)$$

where $i_{cat}$ and $i_L$ are the currents at constant time in presence and absence of GA, respectively; $k_{cat}$ is the catalytic rate constant (mol $L^{-1}$ $s^{-1}$), $C$ is the bulk concentration of GA (M) and $t$ is the elapsed time (s). The value of $k_{cat}$ was estimated from the slope of the $i_{cat}/i_L$ ratio versus $t^{1/2}$ relationship (inset of Figure 4). At 1.0 mM GA, the determined catalytic rate constant value was found to be $2.75 \times 10^4$ mol $L^{-1}$ $s^{-1}$.

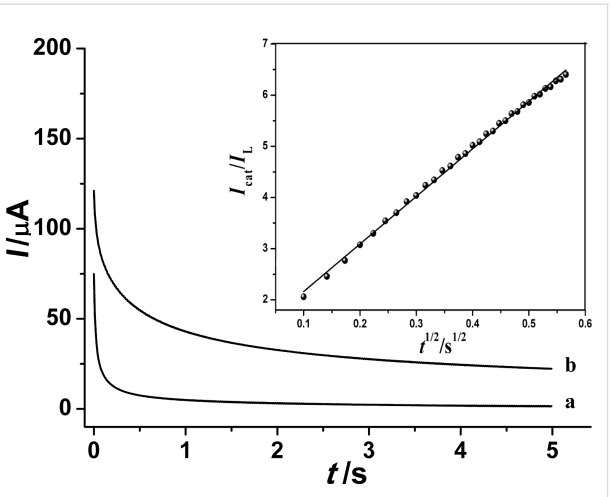


**Figure 4:** Chronoamperograms of PGA/MWCNT/GCE in 0.2 M phosphoric acid in absence (curve a) and presence (curve b) of 1.0 mM GA; the inset shows the relationship of $I_{cat}/I_L$ versus $t^{1/2}$.

## Electrochemical oxidation behavior of gallic acid on PGA/MWCNT/GC modified electrode

### Effect of scan rate

The cyclic voltammetric behavior of 1.0 mM GA was recorded on PGA/MWCNT/GCE in 0.2 M $H_3PO_4$ (pH 2.0) at a scan rate of 50 mV/s. Gallic acid shows two irreversible cyclic voltammetric waves. This behavior was reported earlier by Abdel-Hamid and Newair [27]. The first anodic CV wave was attributed to one-electron transfer oxidation of the −OH group to form an *o*-semiquinone radical cation, which is neutralized on deprotonation. The neutral radical is further oxidized by irreversible loss of the second electron transfer and second proton to the final product giving the second anodic voltammetric wave. The effect of scan rate on cyclic voltammograms of GA was studied on the PGA/MWCNT/GC modified electrode (Figure 5). Upon increasing the scan rate (ν) in the potential scan rate range of 10–100 mV/s, the peak current ($i_p^a$) is proportionally increased with ν. The relationship between the oxidation peak current (log $i_p^a$) and the scan rate (log ν) was constructed (inset of Figure 5). It was found that the log–log plot has a straight linear relationship with a correlation coefficient of 0.972. The linear least-square relationship is represented as

$$\log i_p^a \left(\mu A\right) = 0.972 \log \nu \left(V/s\right) - 3.187. \quad (4)$$

This confirms that the oxidation process is adsorption-controlled process. It concluded that the PGA/MWCNT film facilitates the electron transfer and adsorption of GA onto the electrode surface.

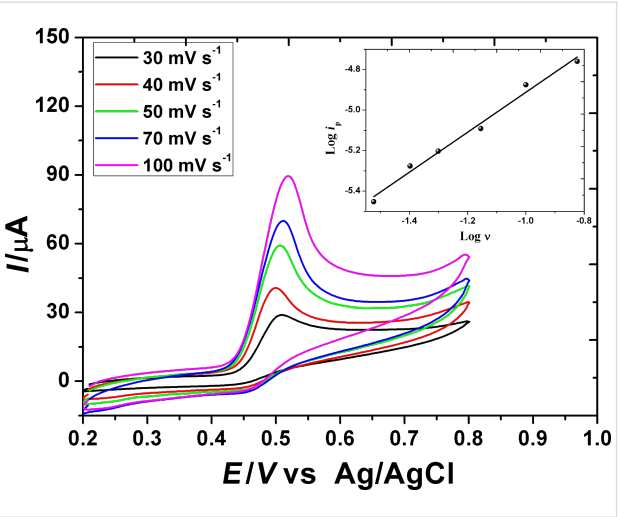


**Figure 5:** Effect of scan rate on the cyclic voltammograms recorded for the first wave of 1.0 mM GA on the PGA/MWCNT/GCE modified electrode in 0.2 M $H_3PO_4$ (pH 2.0). Inset: log $i_p^a$–log υ relationship.

## Accumulation conditions

The square wave adsorptive stripping voltammetric (SWAdSV) method was used for the electrochemical determination of GA using the prepared PGA/MWCNT/GCE sensor. The optimum conditions, accumulation potential, accumulation time and pH were tested using 0.2 M $H_3PO_4$ containing 1.0 mM GA. They were performed by measuring the peak current ($i_p^a$) upon varying each parameter. The effect of accumulation potential on the oxidation peak current of GA at pH 2.0 and an accumulation time of 60 s at different accumulation potentials was carried out. Upon increasing the potential from 0 V, the $i_p^a$ gradually increases and reaches a maximum value at a potential of +0.4 V. Upon further increase of potential, a decrease of the $i_p^a$ was observed. Thus, the optimal accumulation potential of +0.4 V was chosen for the subsequent experiments. The effect of accumulation time on the oxidation peak current at pH 2.0 and accumulation potential of +0.4 V was performed at different times. It was observed that the $i_p^a$ is increased with increasing time from 30 s to a maximum value at 60 s. Upon a further increase of time, a decrease in $i_p^a$ is observed. Therefore, a time of accumulation of 60 s was applied in the subsequent experiments. To optimize the solution pH for the electrocatalytic response of the PGA/MWCNT/GCE towards GA oxidation, at an accumulation potential of +0.4 V and an accumulation time of 60 s, the effect of pH was studied in the pH range of 2.3–5.5. It was observed that the anodic peak potential does shift negatively with increasing pH value. This indicates that a deprotonation reaction took part in the GA oxidation reactions. Upon increasing the pH of the solution from pH 2.3, the oxidation peak current increases to a maximum value at pH 2.6, and then it decreases upon further increase in solution pH. This indicates that the highest oxidation current is obtained at pH 2.6. Thus, it is concluded that the optimal conditions of accumulation potential +0.4 V, accumulation time 60 s and pH 2.6 will be used for GA determination with the PGA/MWCNT/GCE.

## Calibration curve, detection limit, interference, repeatability and stability

It is well known that the square wave adsorptive stripping voltammetric method (SWAdSV) is an effective and rapid electroanalytical method with well-established advantages, including good discrimination against background and low yield detection limits. After optimization of the accumulation conditions, the sensitivity and lower detection limit tests for GA on the PGA/MWCNT/GC electrode in 0.2 M $H_3PO_4$ solution (pH 2.6) were performed. The SW voltammogram profiles of different GA concentrations are shown in Figure 6. A well-defined and sharp oxidation peak is observed on successive additions of standard solution of GA. On plotting the peak current versus GA concentration, the corresponding calibration plot was obtained (inset of Figure 6). It is found that the peak current of GA correlates linearly with the GA concentration in the range of $4.975 \times 10^{-6}$ to $3.381 \times 10^{-5}$ M with a limit of detection (LOD) of $3.22 \times 10^{-6}$ M. The regression relationship is expressed as

$$i_{pa}\,(\mu A) = 0.667C\,(\mu M) + 1.511\times10^{-7}, \quad R^2 = 0.9937. \tag{5}$$

The lower limit of detection was calculated from the calibration data using the following equation:

$$\mathrm{LOD} = \frac{3s}{m}, \tag{6}$$

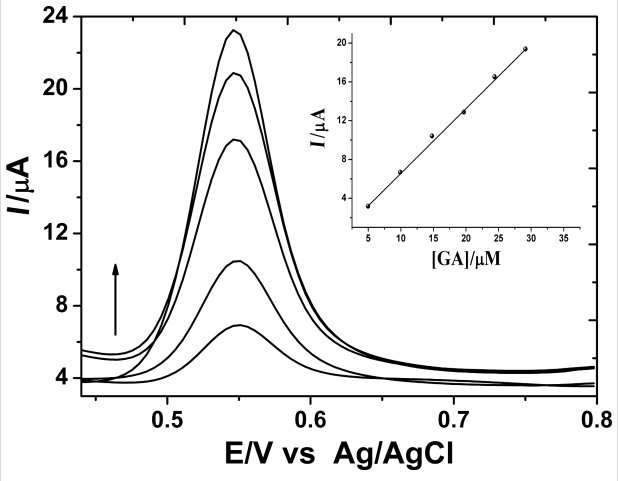


**Figure 6:** SW voltammograms obtained at optimal conditions in 0.2 M $H_3PO_4$ solution containing different GA concentrations. Inset: analytical curve.

where $s$ is the standard deviation of the intercept and $m$ is the slope of the regression line. The analytical performance of the prepared sensor is compared with that of other GA determination methods reported previously as shown in Table 1. The estimated LOD value herein is more or less similar to those previously published using other electroanalytical methodologies. It clear that the present method is fast due to elimination of the extraction and preconcentration steps of the analyte necessary for chromatographic techniques. Furthermore, the present accumulation time is shorter than the other methods with preconcentration time of 15 min, while in the present study the optimal accumulation time was 60 s.

**Table 1:** Comparative results of GA detection on various electrodes.

| electrode | linear range (μM) | LOD (nM) | ref. |
|---|---|---|---|
| AuMCs/SF-GR/GCE[a] | 8.0–500.0 | 10.70 | [3] |
| CS/f$Fe_2O_3$/ERGO/GCE[b] | 10.0–100.0 | 150.00 | [4] |
| SPCE/PME[c] | 0.5–500.0 | 76.00 | [5] |
| DME | 1.0–50.0 | 300.00 | [7] |
| $SiO_2$/CPE[d] | 0.8–100.0 | 250.00 | [8] |
| CNT/CPE | 0.5–15.0 | 300.00 | [9] |

[a]Gold microclusters/sulfonate functionalized grapheme/GCE; [b]Chitosan/fishbone-shaped $Fe_2O_3$/reduced graphene oxide/GCE; [c]Pre-anodized screen-printed carbon electrode/polymelamine; [d]Nano-$SiO_2$/carbon paste electrode.

Selectivity determination is always a consideration in electroanalytical techniques. Therefore, the response of the SWAdSV method for GA on PGA/MWCNT/GCE in 0.2 M $H_3PO_4$ with some possible interfering compounds was studied. It is known that ascorbic acid (AA) is one of the main components present in natural samples. A fixed amount of GA was taken with different amounts of AA. On increasing the concentration of AA to a 1000-fold excess, no influence on the GA response was observed. Moreover, interference from fructose, potassium nitrate and barbituric acid was studied. It was revealed that the response of GA exhibits no change on increasing concentration of these compounds up to a 100-fold excess. This indicates that the PGA/MWCNT/GCE shows higher selectivity for GA. The precision and accuracy of the subject sensor were evaluated by examining the reproducibility and repeatability for many experimental trials. The reproducibility for GA was determined by measuring the relative standard (RSD) value of the oxidation peak current at a fixed concentration of $1.25 \times 10^{-6}$ M GA. The RSD value obtained for the GA response was 2.45%. The repeatability of the modified electrode was evaluated with the same GA concentration. For five successive measurements, the response for the same solution containing $1.45 \times 10^{-6}$ M GA was found to be 2.85%. These results indicate that the method provides a suitable repeatability and reproducibility in the analytical determination of GA. The recovery value of the method was determined to be 101%. Furthermore, the modified electrode exhibits good stability where as much as 95% of the initial peak current was preserved after storage for 3 weeks. This suggests that the efficiency of the PGA/MWCNT/GCE electrode for determination of GA is suitable for practical applications.

### Determination of total phenolic content in pomegranate juice

Figure 7 shows the square-wave voltammogram of a fresh pomegranate juice sample (1:10 dilution), 0.1 mM catechin (CAT) and 0.1 mM GA in 0.2 M $H_3PO_4$ (pH 2.0) on PGA/MWCNT/GCE. The voltammogram shows three anodic peak signals at 0.60, 0.70 and 1.0 V. These signals can be attributed to the oxidation of different polyphenolic compounds, including GA and CAT, as judged from a comparison of their voltammetric response. Thus, it can be concluded that the first wave may dominate the response of GA. Gallic acid is one of the most common references for evaluation of the antioxidant total phenolic content of foodstuff. From the peak current value, the total phenolic content (TPC) can be measured. For confirming the validity of the method, the SWAdSV technique was used for the determination of TPC in fresh pomegranate juice sample. The TPC was determined upon using the standard addition method with a standard solution of GA under the same procedure described earlier with the optimal parameters. The successive increase in concentration of the GA solution was added to the juice sample solution. The typical data obtained are given in Figure 8. The TPC is expressed as mg of gallic acid equivalents (GAE) per liter of juice (mg GAE $L^{-1}$). The TPC value is estimated to be 225.0 mg $L^{-1}$. To confirm the electrochemical method for determination of the TPC in pomegranate juice, the colorimetric method was conducted using the same juice sample. The estimated TPC value is found to be 277.4 mg $L^{-1}$. The observed higher value can be attributed to the fact that all phenols in the real samples can be detected by this method, and furthermore, the Folin–Ciocalteu reagent may react with many nonphenolic substances [31]. This problem can be resolved by using the sensor since the nonphenolic compounds have no interference with the response of the polyphenols. In comparison with Folin–Ciocalteu spectrophotometric procedures, the sensor exhibits better results in terms of sensitivity and selectivity.

## Experimental

### Reagents

Gallic acid, potassium hexacyanoferrate, multiwalled carbon nanotubes (MWCNTs), ethanol, nitric acid, and sulfuric acid were purchased from Sigma-Aldrich (France) and used without any further purification. The stock solution of GA (0.01 M) was prepared in double-distilled water. The stock solutions were

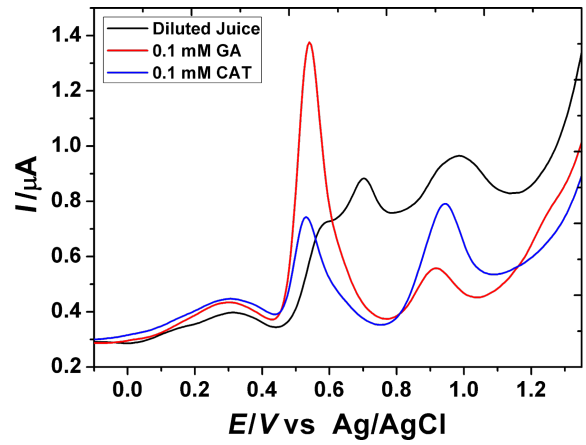


**Figure 7:** SW voltammograms of a pomegranate juice sample (black), 0.1 mM GA (red) and 0.1 mM CAT (blue) in 0.2 M $H_3PO_4$ (pH 2.0) on the PGA/MWCNT/GC modified electrode.

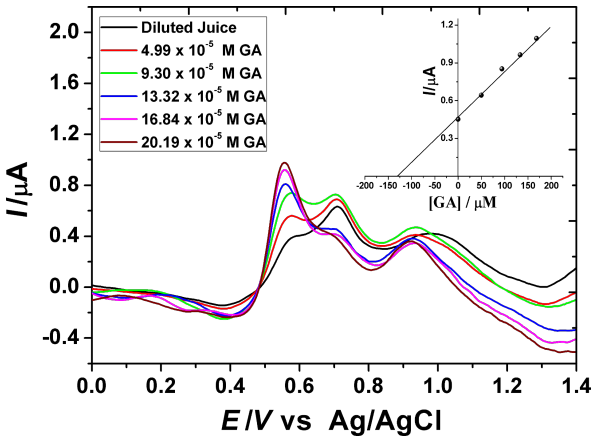


**Figure 8:** SW voltammograms obtained at optimal conditions of a pomegranate juice sample upon addition of different concentrations of GA for determination of TPC. Inset: the analytical results.

protected from light, kept in a refrigerator, and used within the same day of preparation. Pure nitrogen was used for degassing the test solution prior to and throughout the electrochemical measurements. Phosphoric acid solution was used as a supporting electrolyte. Double-distilled water was used for preparation of all solutions. Freshly prepared standard solutions of gallic acid were prepared by dilution of the stock solution with 0.2 M phosphoric acid.

## Instrumentation

Cyclic and square wave voltammetric, chronoamperomeric and chronocoulomeric experiments were performed by using an Autolab PGSTAT128N Potentiostat/Galvanostat (Eco-Chemie, Utrecht, The Netherlands) coupled with NOVA 1.10 software. An electrochemical sensor is comprised of three electrodes: the working (bare or modified glassy carbon electrodes), the reference (Ag/AgCl, aqueous KCl, 3.5 M) and the auxiliary Pt wire electrodes. The surface morphology of a (PGA/MWCNT) composite film was examined using a JOEL scanning electron microscope (JSM T200, Japan) with an electron beam energy of 30 kV. For this purpose, a thin layer of gold (50 Å) was deposited using physical vapor deposition. The pH measurements were performed using a bench top pH meter (HI 2210, HANNA Instruments, Romania) with a combined pH reference electrode. The absorbance of the samples was measured using a V-750ST UV–vis Spectrophotometer (JASCO International Co., LTD., Hachioji, Tokyo, Japan) with Spectra Manager 2 software.

## Preparation of multiwalled carbon nanotube (MWCNT) suspension

Firstly, MWCNTs were treated with a mixture of sulfuric acid and nitric acid (3:1 vol.) for 6 h to remove impurities, reduce bundle sizes and to generate functional groups on their surface. This was then washed several times with double-distilled water until the washing was neutral and then dried at about 70 °C as described by Abdel-Hamid et al. [22]. Secondly, a suspension of MWCNTs was prepared by sonicating a mixture of 30 mg of sodium dodecyl sulfate, 5 mg of treated MWCNTs, 1 mL of *N,N*-dimethylformamide and 1 mL of ethanol for 4 h to form a stable black suspension.

## Sensor construction

The glassy carbon electrode surface was polished with 0.05 μm alumina water slurry using a polishing cloth until the electrode surfaces developed a mirror finish. Then, it was rinsed thoroughly with double-distilled water. The PGA/MWCNT/GC modified electrode was prepared as follows. 20 μL of the MWCNT suspension was drop-casted onto the polished clean glassy carbon electrode to prepare a MWCNT/GC electrode and left for 6 h to dry. The PGA/MWCNT/GCE was fabricated by potentiostatic electropolymerization of gallic acid on the MWCNT/GC electrode by applying an anodic potential of 1.0 V vs Ag/AgCl for 60 s. The prepared electrode was washed several times to remove the electrolyte and the monomer. The electrode was then ready for electrochemical use. The bare and the modified GC electrodes were electrochemically cleaned before the measurements using cyclic voltammetry in a potential range between 0.2 and 1.0 V for 10 cycles at a scan rate of 50 mV/s.

## Preparation of pomegranate juice sample and determination of total phenolic content

The pomegranate juice was obtained by peeling the fruits by hand and the seeds were liquefied using a hand press. The obtained juice was filtered off through a Whatman filter paper

(No. 1). An aliquot of 10.0 mL of pomegranate juice was transferred to a calibrated flask and diluted to a final volume of 100 mL with double-distilled water (1:10 dilution). An aliquot of 100 µL of the dilution was used for the electrochemical standard addition measurements. The total phenolic content in the pomegranate juice sample obtained from the standard addition method was compared with the spectrophotometric Folin–Ciocalteu result [32]. The Folin–Ciocalteu method is based on the reduction of phosphotungstic acid in an alkaline solution, which yielded the phosphotungstic blue. The absorbance of the formed phosphotungstic blue is relative to the number of aromatic phenolic groups and is used for their quantification, using gallic acid as a standard. An aliquot of 20 µL of the raw juice, 1.58 mL of water and 100 µL of Folin–Ciocalteu reagent was mixed. After waiting 8 min, 300 µL of a solution of sodium carbonate (200 g $L^{-1}$) was added. After mixing, the prepared solution was left 2 h at 20 °C and then the absorbance was determined at 765 nm against the blank. The results were expressed using gallic acid as a standard (mg GAE $L^{-1}$).

## Acknowledgements

The authors gratefully acknowledge financial support from the Science and Technology Development Fund (STDF), Egypt, Grant No. (5361). Also, Ali M. Ali and Ahmed El-Kady are thanked for their help in providing the pomegranate fruits.

## References

1. Naczk, M.; Shahidi, F. *J. Pharm. Biomed. Anal.* **2006,** *41,* 1523–1542. doi:10.1016/j.jpba.2006.04.002
2. Pachauri, V.; Flora, S. J. S. *Biochem. Insights* **2015,** *8,* 1–10. doi:10.4137/BCI.S30505
3. Liang, Z.; Zhai, H.; Chen, H.; Wang, Z.; Wang, S.; Zhou, Q.; Huang, X. *Sens. Actuators, B* **2016,** *224,* 915–925. doi:10.1016/j.snb.2015.10.101
4. Gao, F.; Zheng, D.; Tanaka, H.; Zhan, F.; Yuan, X.; Gao, F.; Wang, Q. *Mater. Sci. Eng., C* **2015,** *57,* 279–287. doi:10.1016/j.msec.2015.07.025
5. Su, Y.-L.; Cheng, S.-H. *Anal. Chim. Acta* **2015,** *901,* 41–50. doi:10.1016/j.aca.2015.10.026
6. Abbasi, S.; Daneshfar, A.; Hamdghadareh, S.; Farmany, A. *Int. J. Electrochem. Sci.* **2011,** *6,* 4843–4852.
7. Yilmaza, Ü. T.; Kekillioglu, A.; Mert, R. *J. Anal. Chem.* **2013,** *68,* 1064–1069. doi:10.1134/S1061934813120113
8. Tashkhourian, J.; Nami-Ana, S. F. *Mater. Sci. Eng., C* **2015,** *52,* 103–110. doi:10.1016/j.msec.2015.03.017
9. Souza, L. P.; Calegari, F.; Zarbin, A. J. G.; Marcolino-Júnior, L. H.; Bergamini, M. F. *J. Agric. Food Chem.* **2011,** *59,* 7620–7625. doi:10.1021/jf2005589
10. Goreishi, S. M.; Behpour, M.; Khayatkashani, M.; Motaghedifard, M. H. *Anal. Methods* **2011,** *3,* 636–645. doi:10.1039/c0ay00691b
11. Sundarum, S.; Jagannathan, M.; Abdul Kadir, M. R.; Palanivel, S.; Hadibarata, T.; Yusoff, A. R. M. *RSC Adv.* **2015,** *5,* 45996–46006. doi:10.1039/C5RA06304C
12. Jara-Ulloa, P.; Salgado-Figueroa, P.; Moscoso, R.; Squella, J. A. *J. Electrochem. Soc.* **2013,** *160,* H243–H246. doi:10.1149/2.001306jes
13. Sangeetha, N. S.; Narayanan, S. S. *Anal. Chim. Acta* **2014,** *828,* 34–45. doi:10.1016/j.aca.2014.04.041
14. Luo, J. H.; Li, B. L.; Li, N. B.; Luo, H. Q. *Sens. Actuators, B* **2013,** *186,* 84–89. doi:10.1016/j.snb.2013.05.074
15. Abdel-Hamid, R.; Newair, E. F. *J. Electroanal. Chem.* **2013,** *704,* 32–37. doi:10.1016/j.jelechem.2013.06.006
16. Kahl, M.; Golden, T. D. *Electroanalysis* **2014,** *26,* 1664–1670. doi:10.1002/elan.201400156
17. Shema-Didi, L.; Sela, S.; Ore, L.; Shapiro, G.; Geron, R.; Moshe, G. *Free Radical Biol. Med.* **2012,** *53,* 297–304. doi:10.1016/j.freeradbiomed.2012.05.013
18. Gómez-Caravaca, A. M.; Verardo, V.; Toselli, M.; Segura-Carretero, A.; Fernández Gutiérrez, A.; Caboni, M. F. *J. Agric. Food Chem.* **2013,** *61,* 5328–5337. doi:10.1021/jf400684n
19. Blasco, A. J.; Rogerio, M. C.; González, M. C.; Escarpa, A. *Anal. Chim. Acta* **2005,** *539,* 237–244. doi:10.1016/j.aca.2005.02.056
20. Aguirre, M. J.; Chen, Y. Y.; Isaacs, M.; Matsuhiro, B.; Mendoza, L.; Torres, S. *Food Chem.* **2010,** *121,* 44–48. doi:10.1016/j.foodchem.2009.11.088
21. Kilmartin, P. A.; Zou, H.; Waterhouse, A. L. *J. Agric. Food Chem.* **2001,** *49,* 1957–1965. doi:10.1021/jf001044u
22. Abdel-Hamid, R.; Newair, E. F. *Nanomaterials* **2015,** *5,* 1704–1715. doi:10.3390/nano5041704
23. Abdel-Hamid, R.; Newair, E. F. *J. Indian Chem. Soc.* **2014,** *91,* 607–611.
24. Abdel-Hamid, R.; Newair, E. F. *Arabian J. Chem.* **2016,** *9,* 365–370. doi:10.1016/j.arabjc.2013.02.008
25. Abdel-Hamid, R.; Rabia, M. K.; Newair, E. F. *J. Indian Chem. Soc.* **2013,** *90,* 463–467.
26. Abdel-Hamid, R.; Rabia, M. K.; Newair, E. F. *Arabian J. Chem.* **2016,** *9,* 350–356. doi:10.1016/j.arabjc.2012.06.014
27. Abdel-Hamid, R.; Newair, E. F. *J. Electroanal. Chem.* **2011,** *657,* 107–112. doi:10.1016/j.jelechem.2011.03.030
28. Bard, A. J.; Faulkner, L. R. *Electrochemical Methods: Fundamentals and Applications,* 2nd ed.; Wiley & Sons: New York, NY, U.S.A., 2001.
29. Stevens, N. P. C.; Rooney, M. B.; Bond, A. M.; Feldberg, S. W. *J. Phys. Chem. A* **2001,** *105,* 9085–9093. doi:10.1021/jp0103878
30. Pournaghi-Azar, M. H.; Sabzi, R. *J. Electroanal. Chem.* **2003,** *543,* 115–125. doi:10.1016/S0022-0728(02)01480-8
31. Petković, B. B.; Stanković, D.; Milčić, M.; Sovilj, S. P.; Manojlović, D. *Talanta* **2015,** *132,* 513–519. doi:10.1016/j.talanta.2014.09.025
32. Singleton, V. L.; Rossi, J. A. *Am. J. Enol. Vitic.* **1965,** *16,* 144–158.

BEILSTEIN JOURNAL OF NANOTECHNOLOGY

# Ammonia gas sensors based on $In_2O_3$/PANI hetero-nanofibers operating at room temperature

Qingxin Nie, Zengyuan Pang, Hangyi Lu, Yibing Cai and Qufu Wei*

Full Research Paper

Open Access

Address:
Key Laboratory of Eco-Textiles, Ministry of Education, Jiangnan University, 214122 Wuxi, Jiangsu, China

Email:
Qufu Wei* - qfwei@jiangnan.edu.cn

* Corresponding author

Keywords:
ammonia ($NH_3$); electrospinning; gas sensor; indium(III) oxide ($In_2O_3$); polyaniline (PANI)

*Beilstein J. Nanotechnol.* **2016,** *7,* 1312–1321.
doi:10.3762/bjnano.7.122

Received: 06 April 2016
Accepted: 06 September 2016
Published: 19 September 2016

This article is part of the Thematic Series "Nanostructures for sensors, electronics, energy and environment III".

Guest Editor: N. Motta



## Abstract

Indium nitrate/polyvinyl pyrrolidone ($In(NO_3)_3$/PVP) composite nanofibers were synthesized via electrospinning, and then hollow structure indium oxide ($In_2O_3$) nanofibers were obtained through calcination with PVP as template material. In situ polymerization was used to prepare indium oxide/polyaniline ($In_2O_3$/PANI) composite nanofibers with different mass ratios of $In_2O_3$ to aniline. The structure and morphology of $In(NO_3)_3$/PVP, $In_2O_3$/PANI composite nanofibers and pure PANI were investigated by scanning electron microscopy (SEM), Fourier transform infrared spectroscopy (FTIR), X-ray diffraction (XRD), transmission electron microscopy (TEM) and current–voltage (*I–V*) measurements. The gas sensing properties of these materials towards $NH_3$ vapor (100 to 1000 ppm) were measured at room temperature. The results revealed that the gas sensing abilities of $In_2O_3$/PANI composite nanofibers were better than pure PANI. In addition, the mass ratio of $In_2O_3$ to aniline and the p–n heterostructure between $In_2O_3$ and PANI influences the sensing performance of the $In_2O_3$/PANI composite nanofibers. In this paper, $In_2O_3$/PANI composite nanofibers with a mass ratio of 1:2 exhibited the highest response values, excellent selectivity, good repeatability and reversibility.

## Introduction

With the development of modern industry, environmental pollution in the form of air pollution, water pollution and soil pollution has become ever more serious [1]. With regard to this, considerable attention has been paid to air pollution. Ammonia ($NH_3$), as a highly toxic gas, can be emitted by natural and industrial sources and threaten human health [2-4]. $NH_3$ at concentrations of 50 ppm may irritate the human respiratory system, skin and eyes [4]. Higher concentrations of $NH_3$ will cause blindness, seizures, lung disease and even death [5-7]. So, there is an urgent need to develop a kind of gas sensor with high sensitivity and selectivity to detect $NH_3$ at room temperature.

Metal oxide semiconductors can be applied as sensing materials for monitoring $NH_3$. Ammonia sensors based on $In_2O_3$ [8], $TiO_2$ [9], $SnO_2$ [10], ZnO [11] and $WO_3$ [12] have been reported. Indium oxide ($In_2O_3$) is an n-type semiconductor with a band gap of approximately 3.55–3.75 eV, which has been widely used due to its excellent electrical and optical properties.

$In_2O_3$ also exhibits sensitivity to various vapors and gases, such as $NO_2$ [13], CO [14], $H_2$ [15], acetone [16] and formaldehyde [17]. However, for most metal oxides, there is the drawback of a required high operation temperature, about 300 °C, which will increase the energy consumption [18]. Compared with metal oxides, sensors based on conducting polymers show low power consumption and can be operated at room temperature. In addition, they exhibit a large specific area, small size and low weight, and they are easy to integrate with existing electronics [19,20]. Because of the environmental stability, easy synthesis and reversible doping behavior, polyaniline (PANI), as one of the most commonly used conducting polymers has received considerable attention. However, the sensitivity of PANI remains to be improved [21,22]. To conquer the limitations mentioned above, the combination of metal oxide and conducting polymers have been developed as an effective way to achieve enhanced performance [21,23-27].

In this paper, $In_2O_3$/PANI composite nanofibers were prepared by the combination of electrospinning technique, calcination method and in situ polymerization. This study presents the improved response capabilities of gas sensors based on $In_2O_3$/PANI composite nanofibers, which were synthesized with different ratios between $In_2O_3$ and aniline during the in situ polymerization. All sensors were tested at room temperature in a concentration range of $NH_3$ from 100 to 1000 ppm.

# Experimental

## Materials

Polyvinylpyrrolidone-K90 (PVP-K90, $M_w$ = 1.3 × $10^6$ g/mol) was purchased from Bo Di Industrial Co. Ltd of Tianjin. Indium nitrate hydrate, *N*,*N*-dimethylformamide (DMF), ethyl alcohol, aniline monomer (An), ammonium persulfate (APS), hydrochloric acid (HCl, 37%), ammonium hydroxide ($NH_4OH$) and *m*-cresol were obtained from Sinopharm Chemical Reagent Co., Ltd. (Shanghai, China). All chemicals and reagents were used as received, expect for aniline monomer. Distilled aniline monomer and deionized water were used in this study.

## Preparation of hollow $In_2O_3$ nanofibers

The $In(NO_3)_3$/PVP composite nanofibers were fabricated via single-nozzle electrospinning. $In(NO_3)_3{\cdot}4.5H_2O$ (1.059 g) and PVP (3.529 g) were added into 10 mL ethyl alcohol and 10 mL DMF. The mixture was stirred at 65 °C until all the solutes were fully dissolved. The precursor solution was poured into the syringe for electrospinning. The parameters of the electrospinning were: a needle-to-collector distance of 16 cm, a voltage of 16 kV, and a feed rate of 0.5 mL/h. Then the $In_2O_3$ nanofibers were synthesized by annealing the precursor composite nanofibers at 800 °C for 3 h after heating from room temperature at a rate of 0.5 °C/min.

## Preparation of $In_2O_3$/PANI composite nanofibers

Firstly, 0.1 g $In_2O_3$ nanofibers, which had been ground in an agate mortar, were added into 200 mL 1.2 mol/L HCl solution with ultrasonication treatment. Then a certain amount of aniline in HCl solution was added to the above suspension. After that, 30 mL 1.2 mol/L HCl solution containing APS was slowly dripped into the suspension to initiate the polymerization. The mass ratios of $In_2O_3$ nanofibers to aniline were 1:1, 1:2 and 1:4. The molar ratio of aniline to APS was 1:1. The in situ polymerization of aniline was carried out in an ice bath at 0–5 °C. The reaction lasted for 5 h. The suspension was taken out and left for 30 min, and then washed with deionized water and centrifuged for 5 min. At last, the composite nanofibers were filtered and dried in vacuum at 50 °C for 48 h. The schematic of the preparation of $In_2O_3$/PANI composite nanofibers is illustrated in Figure 1.

## Fabrication of $In_2O_3$/PANI gas sensors

The ground $In_2O_3$/PANI nanofibers and pure PANI were mixed with *m*-cresol to form pastes, in which the weight ratio of $In_2O_3$/PANI or PANI to *m*-cresol was 1:10. Each paste was coated onto interdigital electrodes to construct a sensing film and dried at 55 °C for 2 h in air. Four thin film sensors with different mass ratios of $In_2O_3$ to aniline (0, 1:1, 1:2 and 1:4) were prepared. Correspondingly, the four sensors were denoted as PANI sensor, $In_2O_3$/PANI-1 nanofibers sensor, $In_2O_3$/PANI-2 nanofibers sensor and $In_2O_3$/PANI-3 nanofibers sensor.

## Structural characterization and gas sensing test

The crystal structure of $In_2O_3$ nanofibers was characterized by X-ray diffraction (XRD; D8, Bruker AXS, Germany) in a 2θ region of 3–90° with Cu Kα radiation. The morphologies and structures of the $In_2O_3$ nanofibers, PANI and PANI/$In_2O_3$ composite nanofibers were examined by field emission scanning electron microscopy (FESEM, S-4800 and SU-1510, Hitachi, Tokyo, Japan), transmission electron microscopy (TEM; JEM-2100HR, JEOL), and Fourier transform infrared (FTIR) spectroscopy in the range of 4000–400 $cm^{-1}$ with a 4 $cm^{-1}$ spectral resolution (NEXUS 470 spectrometer, Nicolet, Madison, WI, USA). *I*–*V* measurements were carried out on a CHI 660E electrochemical workstation (CH Instruments, Shanghai, China) with a three-electrode system.

The gas sensing performance of the prepared $In_2O_3$/PANI nanofibers was measured using a custom-built static state gas sensing test system at room temperature (25 ± 1 °C) with a relative humidity of 60 ± 1%. During the gas measurement, the aqueous ammonia was injected into the test chamber using a syringe through a rubber plug. The volume of ammonia injected

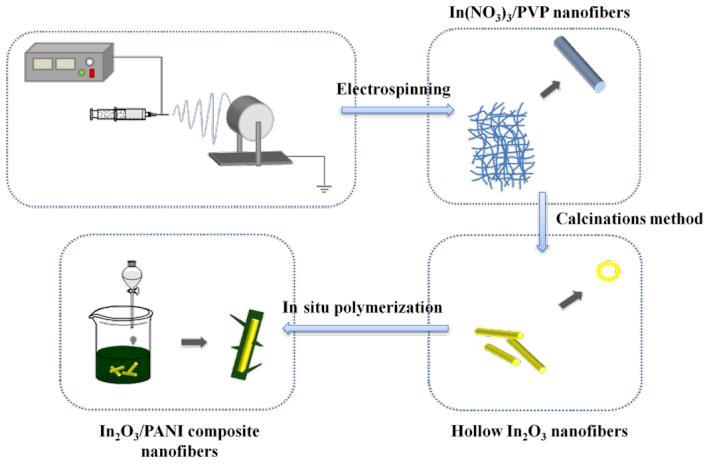


**Figure 1:** Schematic of the preparation of $In_2O_3$/PANI composite nanofibers.

into chamber were 1.3468 μL, 4.0404 μL, 6.734 μL, 10.7744 μL and 13.468 μL resulting in ammonia vapor with concentrations of 100, 300, 500, 800 and 1000 ppm, respectively. The gas response value ($S$) is defined as a ratio of $(R_i - R_0)/R_0$, in which $R_i$ and $R_0$ are the resistance of the sensor in testing gas and air, respectively. Each result was the average value of five tests.

## Results and Discussion

### Materials characterization

The XRD patterns of the nanofibers obtained by annealing $In(NO_3)_3$/PVP composite nanofibers at 800 °C are shown in Figure 2a. It can be seen that the crystal phase of the material was $In_2O_3$, and the diffraction peak of 30.56° was indexed to the (222) crystal plane of the cubic structure of $In_2O_3$. This result confirmed that the final product of calcination was $In_2O_3$.

The chemical structure of the precursor nanofibers, $In_2O_3$ nanofibers and $In_2O_3$/PANI nanofibers were analyzed by FTIR. As shown in Figure 2b, the FTIR spectrum of $In(NO_3)_3$/PVP composite nanofibers exhibits a broad characteristic band around 3382 $cm^{-1}$, which is related to the O–H stretching vibration. It could be the result of absorbing moisture from air. The $–CH_2$ stretching vibration and bending vibration of PVP are attributed to the peaks of around 2951 $cm^{-1}$ and 1423 $cm^{-1}$. The peaks at 1647 $cm^{-1}$ and 1292 $cm^{-1}$ were assigned to the C=O stretching vibration and C≡N antisymmetrical stretching vibration, respectively, in the ring skeleton of PVP. But the characteristic peaks of $In(NO_3)_3$ could not be found in the FTIR spectra. In the spectrum of $In_2O_3$ nanofibers (Figure 2c), the characteristic peaks of PVP have almost vanished. Instead, peaks around 600 $cm^{-1}$, 567 $cm^{-1}$ and 538 $cm^{-1}$ appeared, which are associated with the cubic bixbyite-type structure of $In_2O_3$. The results indicates that PVP was resolved and $In(NO_3)_3$ was converted into $In_2O_3$ during annealing.

Figure 2d presents the FTIR spectra of $In_2O_3$, PANI and $In_2O_3$/PANI nanofibers. The characteristic peaks around 1558 $cm^{-1}$ originating from C=C stretching vibration in the quinoid ring of PANI can be seen. The characteristic bands of 1300 $cm^{-1}$ and 1116 $cm^{-1}$ were attributed to the C–N stretching vibration in the benzenoid ring and the bending vibration plane of C–H bonds in the quinoid ring, respectively. By comparison, the characteristic peaks of $In_2O_3$ also exist in the spectrum of $In_2O_3$/PANI nanofibers. This demonstrated that PANI was coated on the surface of the $In_2O_3$ nanofibers by in situ polymerization. But for $In_2O_3$/PANI-3 nanofibers, the peaks of $In_2O_3$ and PANI showed a significantly decrease which may be caused by the excess of PANI covering.

Figure 3a,b shows SEM images of $In(NO_3)_3$/PVP composite nanofibers and $In_2O_3$ nanofibers, respectively. From Figure 3a, it can be seen that the surface of $In(NO_3)_3$/PVP composite nanofibers was relatively smooth and no beads and droplets appeared. The diameter distribution of $In(NO_3)_3$/PVP nanofibers were mostly in the range of 700–1000 nm. The $In_2O_3$ nanofibers were relatively uniform with diameters of 150–220 nm. These results show that the $In_2O_3$ nanofibers were much rougher and smaller than the precursor nanofibers. In addition, it shows that some nanofibers adhered together in Figure 3b, which is not the case in Figure 3a. It is possible that the solvent was not completely volatilized from the precursor nanofibers membrane. The residual solvent may have re-dissolved the precursor nanofibers and then the dissolved nanofibers were connected along each other during the calcinations.

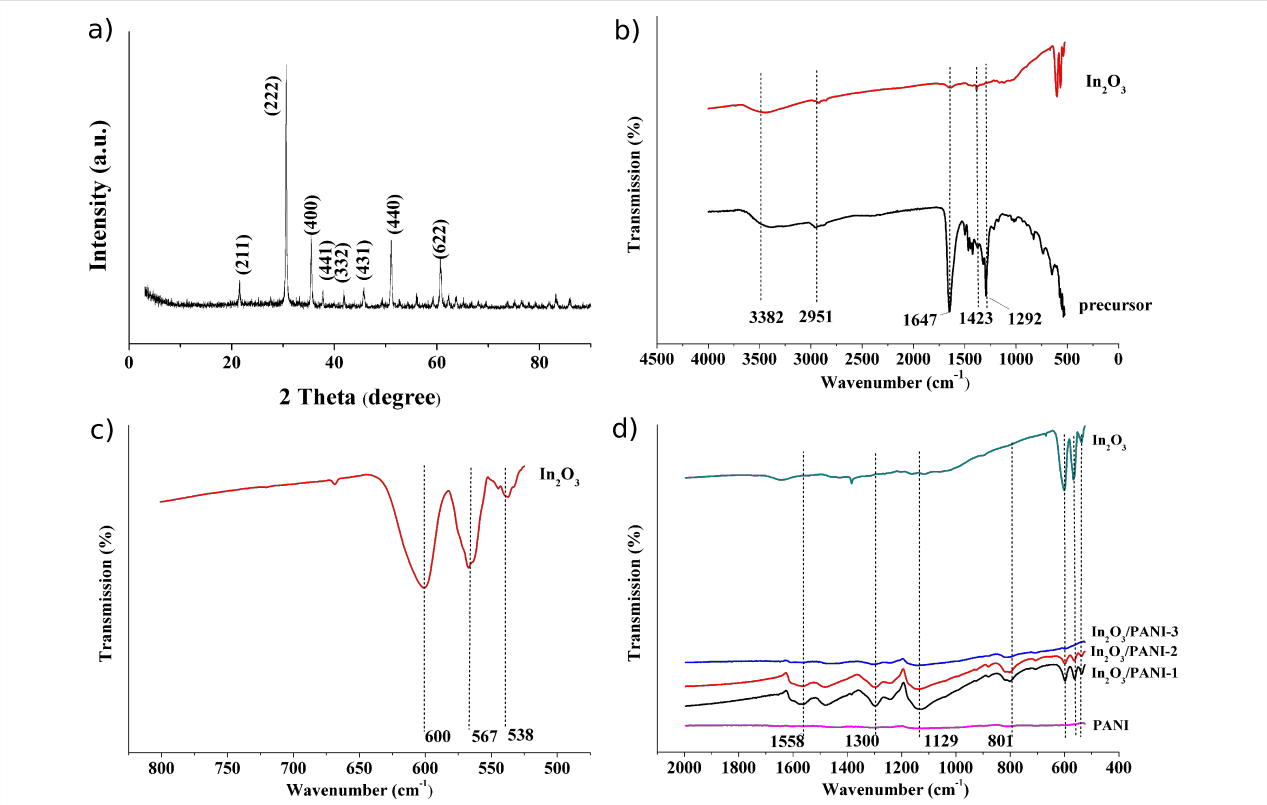


**Figure 2:** a) XRD pattern of $In_2O_3$ nanofibers. FTIR spectra of b) $In(NO_3)_3$/PVP composite nanofibers and $In_2O_3$ nanofibers, c) $In_2O_3$ nanofibers, and d) $In_2O_3$ nanofibers and $In_2O_3$/PANI composite nanofibers.

As the calcination temperature increased, the residual solvent started to volatilize and the $In_2O_3$ nanofibers were gradually formed, but the bonded nanofibers would not segregate during this process, leading to some nanofibers connected along each other.

The cross-sectional image and the TEM image show the detailed structure of $In_2O_3$ nanofibers. In Figure 3c and 3d, it is confirmed that the $In_2O_3$ nanofibers consited of small grains and the hollow structure can be clearly observed. The hollow structure of $In_2O_3$ nanofibers was synthesized by a template-assisted method. PVP as the supporting material of precursor nanofibers was decomposed during the annealing process, and the $In(NO_3)_3$ was transformed into crystalline $In_2O_3$. During calcination, PVP decomposed and gases diffused from the interior to the exterior of the composite nanofibers, leading to crystalline $In_2O_3$ grains constantly moving and tending to be regularly arrayed [16]. As a result, hollow structure of $In_2O_3$ nanofibers was formed during the annealing process.

Current–voltage (*I*–*V*) measurements of PANI, $In_2O_3$/PANI-1, $In_2O_3$/PANI-2 and $In_2O_3$/PANI-3 nanofibers were carried out at room temperature. As shown in Figure 4, the *I*–*V* characteristics of all $In_2O_3$/PANI nanofibers clearly exhibit a nonlinear behavior and it can be observed the rectifying behavior in Figure 4, which might result from the p–n junction between the p-type PANI and n-type $In_2O_3$ [28,29]. It can be observed that the current of $In_2O_3$/PANI showed exponential rise at low voltage and then almost linear rise at high voltages. But for pure PANI, the current showed nearly linear behavior in the forward region, which is attributed to raidply forming polarons and bipolarons in PANI. As some researches mentioned [28-30], the ohmic behavior in this case was related to the formation of an ohmic contact between PANI and $In_2O_3$. Compared with pure PANI, the $In_2O_3$/PANI nanofibers reach a higher current due to the smaller width of the depletion layer between PANI and $In_2O_3$. Moreover, the addition of PANI reduced the width of the depletion layer at the interface and was helpful to form a typical ohmic system [31]. Thus, it can be confirmed that a p–n junction between PANI and $In_2O_3$ had been formed.

## Gas sensing properties

To study the ammonia sensing behavior of the sensors with different ratios of $In_2O_3$ to aniline, the dynamic response of the sensors based on pure PANI and $In_2O_3$/PANI nanofibers towards different $NH_3$ concentrations ranging from 100 to 1000 ppm at room temperature were investigated. As exhibited in Figure 5, it can be seen that the trends of the response and

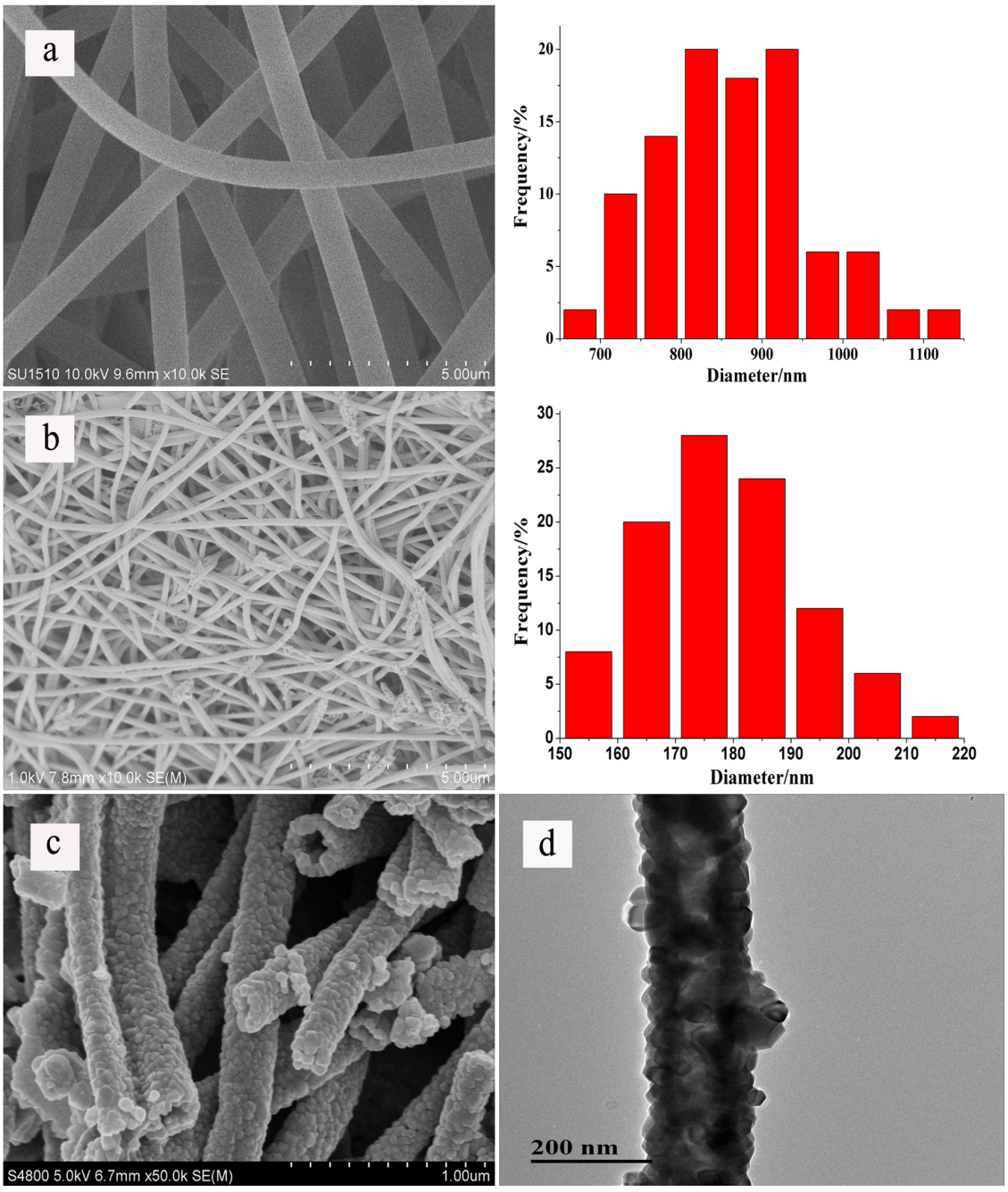


**Figure 3:** SEM images of (a) $In(NO_3)_3$/PVP composite nanofibers (with diameter distributions), (b) $In_2O_3$ nanofibers (with diameter distributions), (c) cross-section of $In_2O_3$ nanofibers. (d) TEM image of $In_2O_3$ nanofibers.

recovery were consistent among the pure PANI and the three $In_2O_3$/PANI nanofibers sensors. The $In_2O_3$/PANI-1 and $In_2O_3$/PANI-2 nanofibers always show a higher response value than pure PANI at the same concentration of $NH_3$.

The response values of pure PANI and these three $In_2O_3$/PANI nanofibers sensors to different concentrations of $NH_3$ are displayed in Figure 6. It can be found that the response values increased with the growth of gas concentration. The responses of pure PANI to 100 ppm, 300 ppm, 500 ppm, 800 ppm, 1000 ppm $NH_3$ were 1.26, 3.11, 5.91, 7.71, 10.09, respectively. The responses of $In_2O_3$/PANI-1 nanofibers sensor were 1.48, 5.32, 14.11, 16.00 and 21.12. For $In_2O_3$/PANI-2 nanofibers sensor, the responses were 1.48, 5.48, 17.67, 36.57 and 53.20, respectively. While for the $In_2O_3$/PANI-3 sensor, the values were only 0.76, 3.32, 4.64, 11.15 and 14.43. It was observed

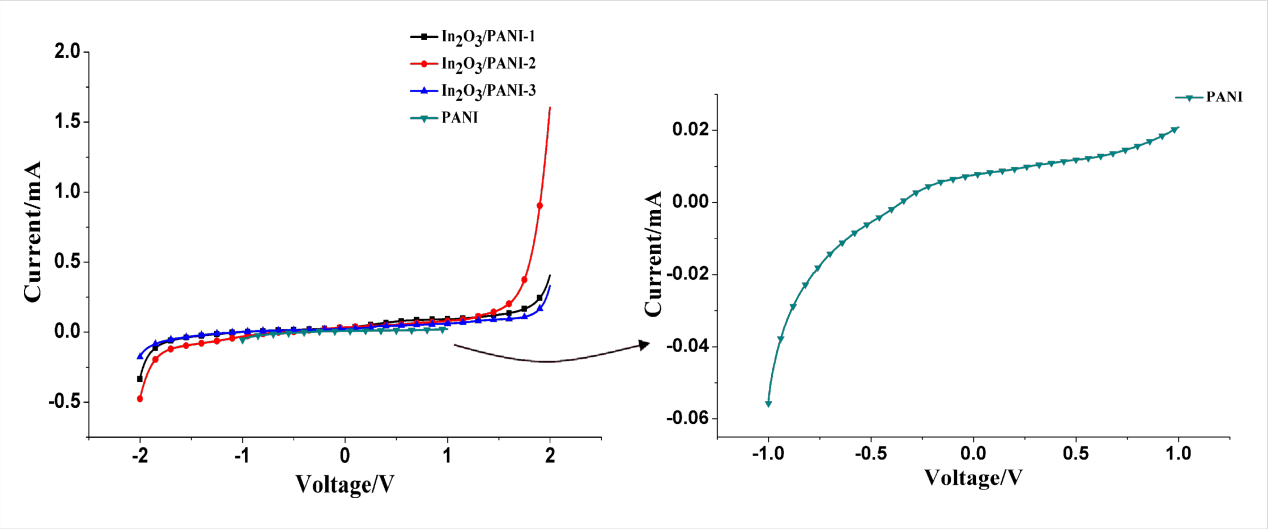


**Figure 4:** Current–Voltage (*I–V*) characteristics of pure PANI and $In_2O_3$/PANI nanofibers.

that at low concentrations of $NH_3$, the responses of these sensors were similar. But with increasing $NH_3$ concentrations, it was very clear that the responses of $In_2O_3$/PANI gas sensors were much higher than pure PANI. The response of $In_2O_3$/PANI-2 exhibited the highest value. The response of $In_2O_3$/PANI-2 to 1000 ppm was about twice as large as that of $In_2O_3$/PANI-1. When the weight ratio of $In_2O_3$ to aniline was raised to 1:4 ($In_2O_3$/PANI-3), the responses to $NH_3$ decreased.

These results revealed that the mass ratio of $In_2O_3$ to aniline had an obvious influence on the $NH_3$ sensing performance of the composite nanofibers. Comparing the sensitivity of three $In_2O_3$/PANI nanofibers sensors, it can be found that the $In_2O_3$/PANI-2 nanofibers sensor delivers the best performance. Therefore, $In_2O_3$/PANI-2 was selected to further investigate the sensing properties.

As mentioned in the Introduction section, 50 ppm $NH_3$ will cause harm to human health. Accordingly, the response of the $In_2O_3$/PANI-2 sensor to 50 ppm, 30 ppm and 10 ppm were investigated. As shown in Figure 7, the response of the $In_2O_3$/PANI-2 sensor to low concentration (10–50 ppm) $NH_3$ was 0.12, 0.48 and 0.94, respectively. Thus it can be seen the $In_2O_3$/PANI-2 sensor had good response performance towards low concentrations of $NH_3$.

The cross-response test was used to evaluate the selectivity of $In_2O_3$/PANI-2 nanofibers sensor. Figure 8 shows the dynamic response of $In_2O_3$/PANI-2 nanofibers sensor to methanol, ethanol, acetone and ammonia at a concentration of 1000 ppm. It is obvious that the $In_2O_3$/PANI-2 nanofibers sensor was almost insensitive to methanol, ethanol and acetone vapors. According to the test results, it can be concluded that $In_2O_3$/PANI-2 nanofibers sensor exhibited unique selectivity to ammonia. A possible mechanism for the selectivity to $NH_3$ is the chemisorption of $NH_3$ on PANI in $In_2O_3$/PANI-2 forming ammonium [32]. Besides, the different gases show different electron affinity values [33], and the varying sensitivity of $In_2O_3$/PANI-2 nanofibers to different gases may be explained by this.

$In_2O_3$/PANI-2 nanofibers sensor was exposed to 1000 ppm ammonia for five times to investigate the repeatability and reversibility. As shown in Figure 9, the recovery of the $In_2O_3$/PANI-2 nanofibers sensor could not fully return to the initial state, and there was a baseline drift of 4% after the first exposure to $NH_3$. This bias was smaller than the results in other reports [34-36]. On the other hand, the response of this sensor slightly decreased with the increasing number of tests. The final response reached 47.42, which was about 89% of the first test. Hence, the $In_2O_3$/PANI-2 nanofibers sensor showed good repeatability and reversibility.

## Gas sensing mechanism

It is well known that the chemical sensors are composed of two parts, an active part and a transduction part, whose function is sensitive to gas analytes and produces a signal that is related to the concentration [19]. In this study, PANI acted as an active element which can react with $NH_3$ resulting in the transformation of PANI from emeraldine salt to emeraldine base by dedoping. The reaction between PANI and $NH_3$ can be described as follows:

$$\mathrm{PANI-H^+ + NH_3 \rightleftharpoons PANI + NH_4^+}$$

The absorption of $NH_3$ caused the deprotonation of the N–$H^+$ site of the emeraldine salt, leading to a significantly increased

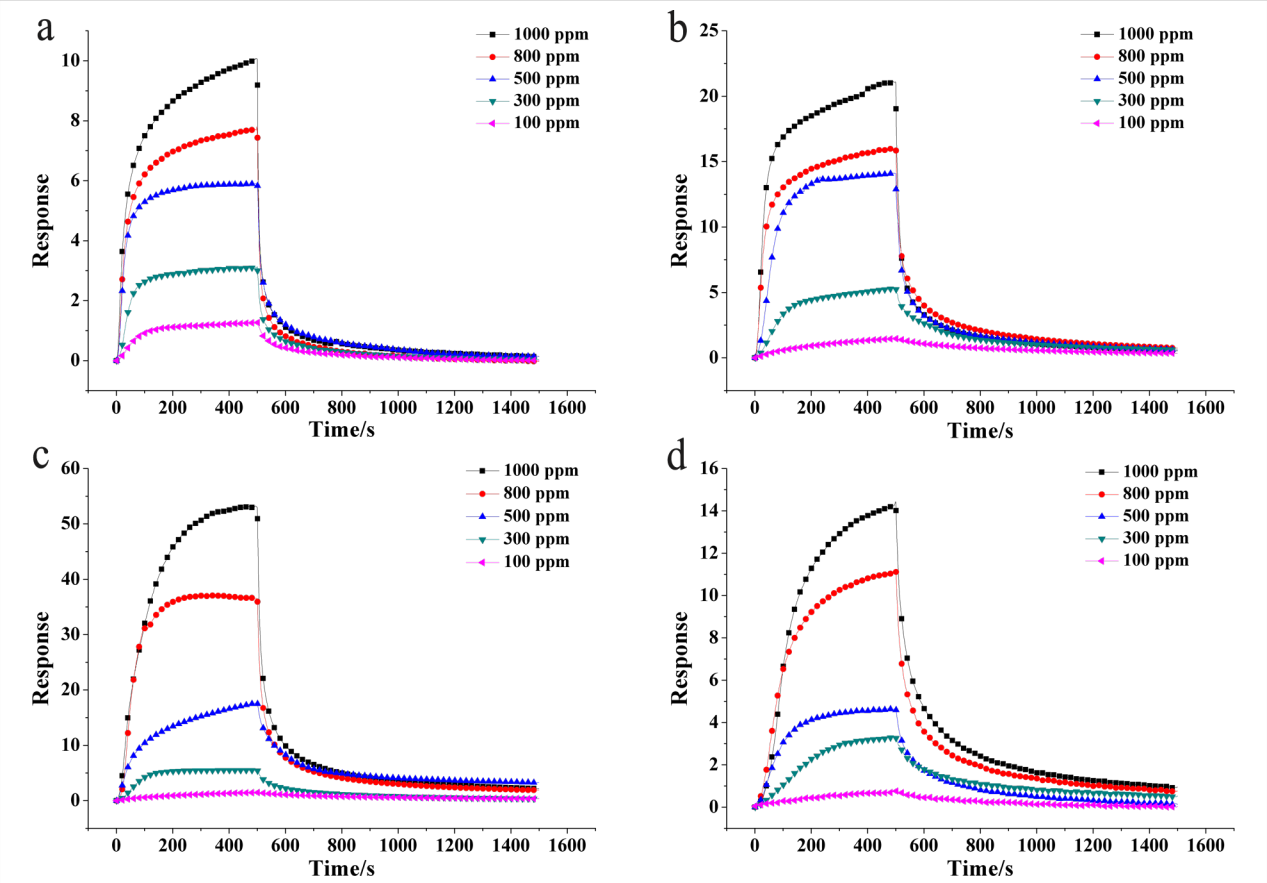


**Figure 5:** Dynamic response of sensors based on (a) pure PANI, (b) $In_2O_3$/PANI nanofibers-1, (c) $In_2O_3$/PANI nanofibers-2 and (d) $In_2O_3$/PANI nanofibers-3 towards 100–1000 ppm $NH_3$ at room temperature.

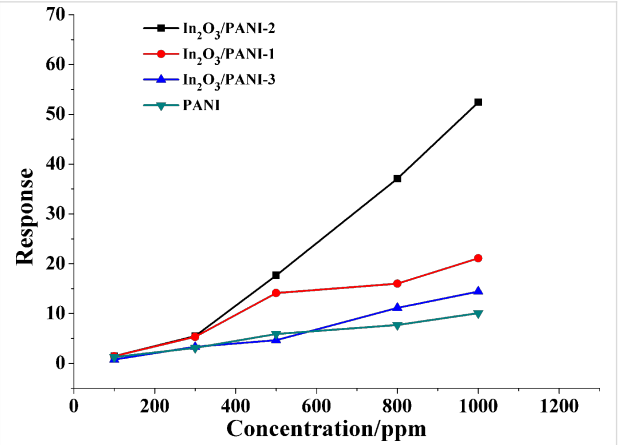


**Figure 6:** The response values of pure PANI and three $In_2O_3$/ PANI nanofibers sensors to different concentration of $NH_3$ at room temperature.

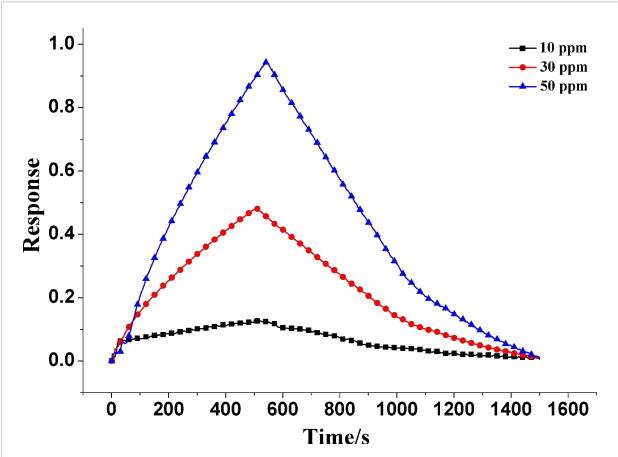


**Figure 7:** Dynamic response of $In_2O_3$/ PANI-2 sensor towards 50 ppm, 30 ppm and 10 ppm $NH_3$ at room temperature.

resistance [37,38]. When this reaction reached equilibrium in $NH_3$ atmosphere, the resistance of the PANI-based sensor maintained a constant value. When the sensor was exposed to air, $NH_3$ is volatilized and the resistance of the PANI composite nanofibers is reduced. Therefore, due to the unique mechanism, PANI (emeraldine salt) based sensors exhibited a great selectivity to $NH_3$.

As the *I*–*V* characteristics show, it is confirmed that p–n heterojunctions had been formed between PANI and $In_2O_3$ nano-

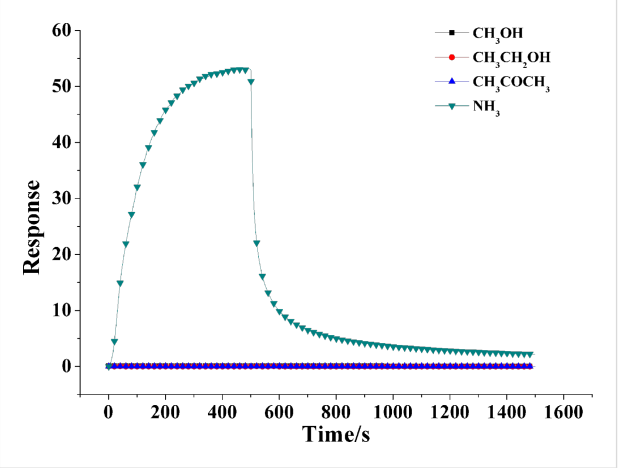


**Figure 8:** Cross-response curves of $In_2O_3$/PANI-2 nanofibers sensor to 1000 ppm methanol, ethanol, acetone and ammonia.

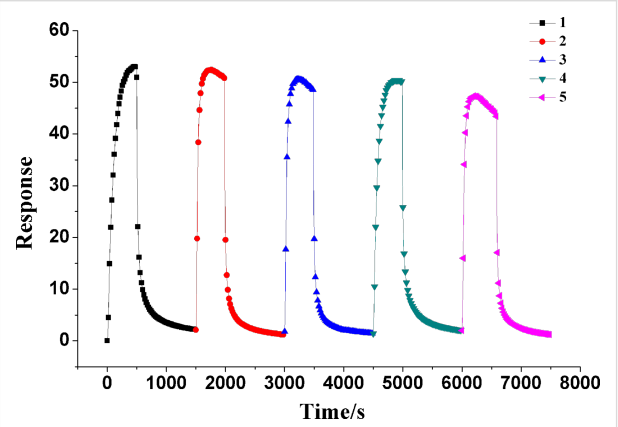


**Figure 9:** Sensing repeatability and reversibility of $In_2O_3$/PANI-2 nanofibers sensor to 1000 ppm $NH_3$ vapor.

fibers, in which PANI is a p-type semiconductor and $In_2O_3$ nanofibers presents as an n-type semiconductor [21,27,34]. The changes of the depletion layer of the p–n heterojuction are shown in Figure 10. The width of the depletion section is related to the doping concentration [39]. With low concentration doping, it needs a sufficiently thick depletion layer to provide impurity atoms to build an internal field. Accordingly, on exposure to $NH_3$, the protons from PANI are transferred to the $NH_3$ molecules, which results in a widening of the depletion layer in the PANI section [40]. Simultaneously, the variation of the PANI region width would have effects on the width of the $In_2O_3$ region and on the p–n junction. The electrons of $In_2O_3$ and holes of PANI move in opposite directions until the new Fermi level ($E_{F\text{-}NH3}$) reaches equilibrium. In this process, the electron transfer between the n-type $In_2O_3$ and p-type PANI is obstructed due to the potential barrier. Thus the depletion layer between PANI and $In_2O_3$ becomes wider and the resistance of the material increases [27,41,42]. According to the

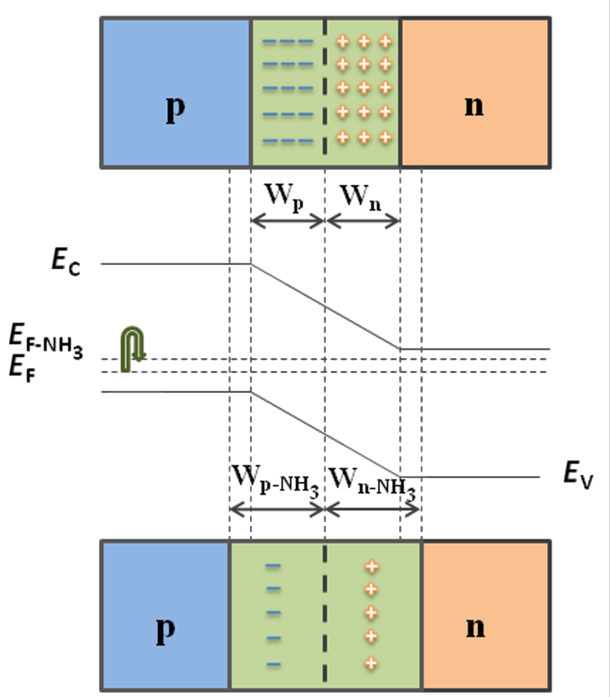


**Figure 10:** Schematic of p–n junction of $In_2O_3$/PANI nanofibers and its potential energy barrier change when exposed to $NH_3$.

response definition ($S = (R_i - R_0)/R_0$), the increase in resistance attributed to the p–n junction increases the sensitivity of composite nanofibers sensors. In addition, the sensitivity of the composite gas sensor materials is also connected to the mass ratio of $In_2O_3$ and aniline.

Because of the smaller amount of polyaniline, which acts as active material in this composite system, the $In_2O_3$/PANI-1 gas sensor showed a lower sensitivity. However, for the $In_2O_3$/PANI-3 gas sensor, the external surface of $In_2O_3$ nanofibers was coated with excess polyaniline, yielding a gas sensing perfomance similar to that of pure PANI. Even the response of $In_2O_3$/PANI-3 to 100 ppm and 500 ppm $NH_3$ was less than that of pure PANI. The p–n junction of $In_2O_3$ and PANI in $In_2O_3$/PANI-3 does not work efficiently. In general, the characteristic of the gas sensitive material response was discrete instead of ideally linear [34,36,43]. For $In_2O_3$/PANI-3 and pure PANI, the characteristic responses were similar. Therefore, it was possible that the response of $In_2O_3$/PANI-3 were less than that of pure PANI, especially towards lower concentrations of $NH_3$. In this study, when the mass ratio of $In_2O_3$ to aniline was 1:2, the gas sensor material exhibited optimum performance in detecting $NH_3$.

## Conclusion

$In_2O_3$/PANI nanofibers with reliable sensing properties towards $NH_3$ were synthesized by electrospinning, calcination and in

situ polymerization. The gas sensors based on $In_2O_3$/PANI nanofibers exhibited a higher sensitivity than pure PANI. The $In_2O_3$/PANI-2 nanofiber sensor exhibited the best sensitivity to $NH_3$ vapor at room temperature, and this sensor was further investigated for its selectivity by interfering with methanol, ethanol and acetone vapors. The results indicated that the $In_2O_3$/PANI-2 nanofiber sensor had excellent selectivity, good repeatability and reversibility. The enhancement of gas sensing performance of $In_2O_3$/PANI nanofiber sensor may be attributed to formation of a p–n junction between $In_2O_3$ and PANI, which existence is confirmed by the *I–V* characteristics.

## References


1. Tang, Y.-L.; Li, Z.-J.; Ma, J.-Y.; Su, H.-Q.; Guo, Y.-J.; Wang, L.; Du, B.; Chen, J.-J.; Zhou, W.; Yu, Q.-K.; Zu, X.-T. *J. Hazard. Mater.* **2014,** *280,* 127–133. doi:10.1016/j.jhazmat.2014.08.001
2. Wu, Z.; Chen, X.; Zhu, S.; Zhou, Z.; Yao, Y.; Quan, W.; Liu, B. *Sens. Actuators, B* **2013,** *178,* 485–493. doi:10.1016/j.snb.2013.01.014
3. Na, K.; Song, C.; Switzer, C.; Cocker, D. R., III. *Environ. Sci. Technol.* **2007,** *41,* 6096–6102. doi:10.1021/es061956y
4. Jabłońska, M.; Palkovits, R. *Appl. Catal., B* **2016,** *181,* 332–351. doi:10.1016/j.apcatb.2015.07.017
5. Swotinsky, R. B.; Chase, K. H. *Am. J. Ind. Med.* **1990,** *17,* 515–521. doi:10.1002/ajim.4700170409
6. Park, S.-J.; Jin, S.-Y. *J. Colloid Interface Sci.* **2005,** *286,* 417–419. doi:10.1016/j.jcis.2005.01.043
7. Yoo, K.-P.; Kwon, K.-H.; Mi, N.-K.; Lee, M. J.; Lee, C. J. *Sens. Actuators, B* **2009,** *143,* 333–340. doi:10.1016/j.snb.2009.09.029
8. Li, C.; Zhang, D.; Lei, B.; Han, S.; Liu, X.; Zhou, C. *J. Phys. Chem. B* **2003,** *107,* 12451–12455. doi:10.1021/jp0361531
9. Biskupski, D.; Herbig, B.; Schottner, G.; Moos, R. *Sens. Actuators, B* **2011,** *153,* 329–334. doi:10.1016/j.snb.2010.10.029
10. Shahabuddin, M.; Sharma, A.; Kumar, J.; Tomar, M.; Umar, A.; Gupta, V. *Sens. Actuators, B* **2014,** *194,* 410–418. doi:10.1016/j.snb.2013.12.097
11. Renganathan, B.; Sastikumar, D.; Gobi, G.; Yogamalar, N. R.; Bose, A. C. *Opt. Laser Technol.* **2011,** *43,* 1398–1404. doi:10.1016/j.optlastec.2011.04.008
12. Nguyen, D. D.; Dang, D. V.; Nguyen, D. C. *Adv. Nat. Sci.: Nanosci. Nanotechnol.* **2015,** *6,* 035006. doi:10.1088/2043-6262/6/3/035006
13. Zhang, D.; Liu, Z.; Li, C.; Tang, T.; Liu, X.; Han, S.; Lei, B.; Zhou, C. *Nano Lett.* **2004,** *4,* 1919–1924. doi:10.1021/nl0489283
14. Miller, D. R.; Akbar, S. A.; Morris, P. A. *Sens. Actuators, B* **2014,** *204,* 250–272. doi:10.1016/j.snb.2014.07.074
15. Zhan, Z.; Jiang, D.; Xu, J. *Mater. Chem. Phys.* **2005,** *90,* 250–254. doi:10.1016/j.matchemphys.2004.01.043
16. Liang, X.; Jin, G.; Liu, F.; Zhang, X.; An, S.; Ma, J.; Lu, G. *Ceram. Int.* **2015,** *41,* 13780–13787. doi:10.1016/j.ceramint.2015.08.060
17. Li, Z.; Fan, Y.; Zhan, J. *Eur. J. Inorg. Chem.* **2010,** *2010,* 3348–3353. doi:10.1002/ejic.201000313
18. Li, H.; Liu, Y.; Luo, L.; Tan, Y.; Zhang, Q.; Li, K. *Mater. Sci. Eng., C* **2016,** *59,* 438–444. doi:10.1016/j.msec.2015.10.036
19. Fratoddi, I.; Venditti, I.; Cametti, C.; Russo, M. V. *Sens. Actuators, B* **2015,** *220,* 534–548. doi:10.1016/j.snb.2015.05.107
20. Lakard, B.; Carquigny, S.; Segut, O.; Patios, T.; Lakard, S. *Metals (Basel, Switz.)* **2015,** *5,* 1371–1386. doi:10.3390/met5031371
21. Gong, J.; Li, Y.; Hu, Z.; Zhou, Z.; Deng, Y. *J. Phys. Chem. C* **2010,** *114,* 9970–9974. doi:10.1021/jp100685r
22. Timmer, B.; Olthuis, W.; van den Berg, A. *Sens. Actuators, B* **2005,** *107,* 666–677. doi:10.1016/j.snb.2004.11.054
23. Pawar, S. G.; Chougule, M. A.; Patil, S. L.; Raut, B. T.; Godse, P. R.; Sen, S.; Patil, V. B. *IEEE Sens. J.* **2011,** *11,* 3417–3423. doi:10.1109/JSEN.2011.2160392
24. Nasirian, S.; Milani, M. H. *Appl. Surf. Sci.* **2015,** *328,* 395–404. doi:10.1016/j.apsusc.2014.12.051
25. Sadek, A. Z.; Wlodarski, W.; Shin, K.; Kaner, R. B.; Kalantar-zadeh, K. *Synth. Met.* **2008,** *158,* 29–32. doi:10.1016/j.synthmet.2007.11.008
26. Betty, C. A.; Choudhury, S.; Arora, S. *Sens. Actuators, B* **2015,** *220,* 288–294. doi:10.1016/j.snb.2015.05.074
27. Pang, Z.; Fu, J.; Luo, L.; Huang, F.; Wei, Q. *Colloids Surf., A* **2014,** *461,* 113–118. doi:10.1016/j.colsurfa.2014.07.038
28. Abaci, S.; Nessark, B.; Riahi, F. *Ionics* **2014,** *20,* 1693–1702. doi:10.1007/s11581-014-1129-9
29. Ameen, S.; Shaheer, A. M.; Ansari, S. G.; Yang, O.-B.; Shin, H.-S. *Superlattices Microstruct.* **2009,** *46,* 872–880. doi:10.1016/j.spmi.2009.09.007
30. Li, Y.; Gong, J.; McCune, M.; He, G.; Deng, Y. *Synth. Met.* **2010,** *160,* 499–503. doi:10.1016/j.synthmet.2009.11.037
31. Pandey, S. S.; Rikitake, K.; Takashima, W.; Kaneto, K. *Curr. Appl. Phys.* **2003,** *3,* 107–113. doi:10.1016/S1567-1739(02)00179-7
32. Tai, H.; Xu, X.; Ye, Z.; Liu, C.; Xie, G.; Jiang, Y. *Chem. Phys. Lett.* **2015,** *621,* 58–64. doi:10.1016/j.cplett.2014.12.052
33. Pawar, S. G.; Chougule, M. A.; Shashwati, S.; Patil, V. B. *J. Appl. Polym. Sci.* **2012,** *125,* 1418–1424. doi:10.1002/app.35468
34. Wang, L.; Huang, H.; Xiao, S.; Cai, D.; Liu, Y.; Liu, B.; Wang, D.; Wang, C.; Li, H.; Wang, Y.; Li, Q.; Wang, T. *ACS Appl. Mater. Interfaces* **2014,** *6,* 14131–14140. doi:10.1021/am503286h
35. Matsuguchi, M.; Asahi, T. *Sens. Actuators, B* **2011,** *160,* 999–1004. doi:10.1016/j.snb.2011.09.017
36. Joulazadeh, M.; Navarchian, A. H. *Synth. Met.* **2015,** *210,* 404–411. doi:10.1016/j.synthmet.2015.10.026
37. Zhang, Y.; Kim, J. J.; Chen, D.; Tuller, L. H.; Rutledge, C. C. *Adv. Funct. Mater.* **2014,** *24,* 4005–4014. doi:10.1002/adfm.201400185
38. Srinives, S.; Sarkar, T.; Mulchandani, A. *Electroanalysis* **2013,** *25,* 1439–1445. doi:10.1002/elan.201300015
39. Mane, A. T.; Navale, S. T.; Patil, V. B. *Org. Electron.* **2015,** *19,* 15–25. doi:10.1016/j.orgel.2015.01.018
40. Bai, S.; Tian, Y.; Cui, M.; Sun, J.; Tian, Y.; Luo, R.; Chen, A.; Li, D. *Sens. Actuators, B* **2016,** *226,* 540–547. doi:10.1016/j.snb.2015.12.007
41. Xu, H.; Ju, D.; Li, W.; Gong, H.; Zhang, J.; Wang, J.; Cao, B. *Sens. Actuators, B* **2016,** *224,* 654–660. doi:10.1016/j.snb.2015.10.076
42. Bai, S.; Ma, Y.; Luo, R.; Chen, A.; Li, D. *RSC Adv.* **2016,** *6,* 2687–2694. doi:10.1039/C5RA20843B
43. Li, Y.; Ban, H.; Yang, M. *Sens. Actuators, B* **2016,** *224,* 449–457. doi:10.1016/j.snb.2015.10.078

BEILSTEIN JOURNAL OF NANOTECHNOLOGY

# An efficient recyclable magnetic material for the selective removal of organic pollutants

Clément Monteil[1], Nathalie Bar[1], Agnès Bee[2] and Didier Villemin[*1]

Full Research Paper

Open Access

Address:
[1]UMR CNRS 6507 LCMT, Normandie Université -ENSICAEN, 6 boulevard du Maréchal Juin, 14050 Caen, France; Tel: +33 2 31 45 28 40 and [2]UMR CNRS 8234 PHENIX, Université Pierre et Marie Curie, 75252 Paris Cedex 05, France

Email:
Didier Villemin[*] - didier.villemin@ensicaen.fr

* Corresponding author

Keywords:
adsorption; magnetic nanoparticles; organic pollutants; phosphonated polyethylenimine

*Beilstein J. Nanotechnol.* **2016,** *7,* 1447–1453.
doi:10.3762/bjnano.7.136

Received: 15 March 2016
Accepted: 21 September 2016
Published: 13 October 2016

This article is part of the Thematic Series "Nanostructures for sensors, electronics, energy and environment III".

Guest Editor: N. Motta



## Abstract

Wastewater cleaning strategies based on the adsorption of materials are being increasingly considered, but the wide variety of organic pollutants at low concentrations still makes their removal a challenge. The hybrid material proposed here consists of a zwitterionic polyethylenimine polymer coating a magnetic core. Polyethylenimine is phosphonated at different percentages by a one-step process and used to coat maghemite nanoparticles. It selectively extracts high amounts of cationic and anionic contaminants over a wide range of pH values, depending on the adjustable number of phosphonate groups introduced on the polymer. After recovering the nanoparticles with a magnet, pollutants are quantitatively released by repeated washing with low amounts of pH-adjusted water. The material can be reused many times without noticeable loss of efficiency and is designed to resist high temperatures, oxidation and harsh conditions.

## Introduction

During the last decades, an increased emphasis was placed on the issue of diffuse contamination of water. Toxic metals and organic pollutants are significant sources of hazard for human health, even at low concentrations [1-3]. Many technologies such as photodegradation, biodegradation, the Fenton process, or extraction by liquid membranes have been developed to eliminate these compounds in wastewater [4-6]. Among them, adsorption-based methods are extensively studied [7,8].

At the same time, the emergence of nanotechnologies has led to a new generation of organic/inorganic nanocomposites with embedded magnetic nanoparticles (NPs) [9-13]. The application of a simple magnetic field is sufficient to collect them, which fosters the development of low-cost recyclable processes. However, while many systems can efficiently remove hazardous metallic ions from waters, the elimination of organic micropollutants is still an issue [11,14]. Most of the materials are exclu-

sively efficient for cationic or anionic molecules, and only few of them have been successfully tested on both [15]. In addition, they often adsorb a limited amount of contaminant, considerably lower than the capacity of activated charcoal.

We report herein a new adsorption process for water remediation, based on partially phosphonated polyethylenimine (PEIP)-coated magnetic nanoparticles (NP-PEIP). The special feature of the PEIP is the presence of numerous ammonium and, more original, phosphonate groups spread on the polymer. Its zwitterionic structure allows the adsorption of any kind of charged contaminant. Unlike many others sorbents, this nanomaterial strongly resists the degradation caused by hydrolysis or oxidation, due to strong covalent Fe–O–P bonds [16]. As a result it can be indifferently used in acidic or basic media, in contrast to other sorbents based on silica shells or coatings with oligosaccharides [17].

# Experimental

## Material and apparatus

Polyethylenimine (25000 Da) was purchased from BASF, phosphorous acid, formaldehyde, hydrochloric acid and sodium hydroxide were obtained from VWR and dyes (methylene blue, MB, and methyl orange, MO) from Sigma-Aldrich. Dialysis tubings were bought from Roth. Absorbance was measured by using a UV–visible Perkin-Elmer Analyst 100 spectrophotometer. The microwave used was a Prolabo Synthewave. A Varian SpectrAA 55 AAS was used to detect potential traces of iron in the supernatants after collecting nanoparticles. Zeta potential measurements were determined by DLS analysis using a Malvern Zetasizer nanoZS model.

## Preparation of the phosphonated polyethylenimine–maghemite material

### Synthesis of nanoparticles

Maghemite ionic ferrofluid ([Fe] = $10^{-2}$ mol/L) was prepared by wet alkaline coprecipitation according to the Massart protocol [18,19]. Iron(III) chloride and iron(II) chloride were co-precipitated at a molar ratio of 1:2, in the presence of ammonium hydroxide solution (28%), at room temperature and under mechanical stirring. Then, a solution of iron(III) nitrate in concentrated nitric acid was added at 80 °C under stirring. After the removal of the supernatant, nanoparticles were washed with acetone and diethylether and then redispersed in a controlled volume of water. The pH value of the ionic ferrofluid was about 2, with $NO_3^-$ as counterion. Nanoparticles are spherical, with an average diameter of 7 nm determined by XRD [17].

### Synthesis of the polyethylenimine phosphonate

Phosphonated polyethylenimine (PEIP) was prepared as previously described [20,21]. An adjustment of the amounts of phosphorous acid and formaldehyde is necessary to obtain phosphonated polyethylenimine with different percentages of phosphonation (P%). We have prepared a large range of phosphonated polyethylenimine with a percentage varying from 5 to 90% [20]. For the calculations, we have considered that a molecule of PEI is constituted of monomers $(CH_2–CH_2–NH)_n$ with an average molecular mass of 43. So, for example, to synthesize PEIP with P% = 20, 3.81 g (0.2 equiv, $4.65·10^{-2}$ mol) of phosphorous acid $H_3PO_3$ were introduced in 10 g of PEI (25000 Da, $4·10^{-4}$ mol of PEI corresponding to $23.2·10^{-2}$ mol of monomer $CH_2CH_2NH$) in 30 mL of water, and the mixture was irradiated (150 W) for 1 min in a microwave oven. 10 mL of concentrated HCl and $9.30·10^{-2}$ mol of a 35% formaldehyde solution were successively added. After 5 min of irradiation, excess of formaldehyde was removed under vacuum and the solution was dialyzed with a nitrocellulose membrane, yielding 85% of PEIP [22].

### Preparation of NP-PEIP*x* powder

An amount of 5 mL of diluted ferrofluid in water ([Fe] = $10^{-4}$ mol·L$^{-1}$) were added dropwise to 10 mL of a PEIP solution (30 mg/mL) adjusted to pH 2 with diluted nitric acid under vigorous stirring. After 15 min, sodium hydroxide was added to destabilize the solution. The supernatant was removed and the precipitate redispersed in 10 mL of 1 mol·L$^{-1}$ nitric acid by sonication. Then acetone was added until NP-PEIP precipitated. These were washed successively with acetone and diethylether and then dried in an oven at 120 °C for 24 h.

### Preparation of stock solutions

MO or MB powders were dissolved in distilled water ($5·10^{-4}$ mol·L$^{-1}$) in order to prepare dye stock solutions.

### Extraction of methyl orange and methylene blue with NP-PEIP

A particles stock solution was prepared by dispersing 5 mg of NP-PEIP powder in 50 mL of distilled water. All the following experiments (pH value, kinetic, maximum of adsorption…) were repeated five times.

### pH Adsorption studies

The experiments were carried out for both NP-PEIP20 and NP-PEIP80. A range of samples was prepared by introducing 10 mL of NP-PEIP stock solution in 10 mL of the dye solution. For all of them, the pH was adjusted between 1 and 14 with either diluted nitric acid or sodium hydroxide solution. After 3 h of stirring, particles were collected with a magnet, and the supernatant was removed. The particles were rinsed twice with 1 mL of distilled water, which was afterwards added to the liquid phase. Supernatant absorbance was monitored by UV–visible spectrophotometry. It is noteworthy that OM exhib-

its acido–basic properties and is used as pH indicator. At pH 14, the OM absorption wavelength does not vary (λ = 465 nm), neither does the molar extinction coefficient ε (Figure S3 in Supporting Information File 1). So, in the case of the MO solution, the supernatants were adjusted to pH 14 by addition of sodium hydroxide before recording the absorption in order to avoid a distortion of the measurements (Figure S4 in Supporting Information File 1). For MB, this problem does not occur and we have established calibration curves according to the pH values (Figure S5 and Figure S6 in Supporting Information File 1).

### Kinetic studies

The experiments were carried out for both NP-PEIP20 and NP-PEIP80. 15 replicate tests were prepared for each dye, using the same protocol as previously, but with a constant pH value (7 for MO, 14 for MB corresponding to the pH value of maximum adsorption). Evolution of absorbance was monitored by spectrophotometry and recorded at different times, changing the sample between measurements.

### Washing step

Acidic and basic wash waters were obtained by adjusting distilled water to pH 2 or 14 with diluted nitric acid (1 mol·L$^{-1}$) and a solution of sodium hydroxide respectively (0.1 mol·L$^{-1}$). 10 mL of NP-PEIP stock solution were mixed with contaminant solutions as described above, at the pH value of maximum adsorption (MO: pH 7, MB: pH 14) for 3 h. After that, the particles were re-dispersed in 20 mL of wash water per milligram of NP-PEIP depending on the pollutant: MO was washed with the acidic solution, MB with the basic one. After 5 min of stirring, the particles were collected with a magnet and the supernatant absorbance of each run was monitored by spectrophotometry.

### Recyclability

Five replicate tests were conducted to guarantee the reproducibility of the results. 20 mg of NP-PEIP (P% = 20) were dispersed in 20 mL of the dye stock solution and vigorously stirred for 4 h. Then, the particles were collected with a magnet and the absorbance of the supernatant was monitored by spectrophotometry. Four washing steps were carried out between each cycle, and the particles were directly reused in the new dye solution batch.

## Results and Discussion

### Magnetic material preparation and conditions of the studies

The novelty of this contribution consists in the use of PEI with phosphonic groups allowing a solid grafting of PEI on the maghemite nanoparticles, by the formation of strong covalent P–O–Fe bonds. The presence of these negative phosphonic groups ensures the stability of NP regardless of the pH value, especially in very basic medium, which is not the case for plain PEI [23].

The phosphonated groups are introduced on PEI through the modification of primary and secondary amines according to the Moedritzer and Irani synthesis [24]. In a previous work we described the synthesis, the coating of maghemite and a characterization of the physicochemical properties of the material [20,22]. As illustrated in Figure 1, PEIP can be customized to contain more or less phosphonated groups, by varying the percentage of amines modified (P%). Between pH 3 and 10, the zeta potential is positive but decreases with the percentage of phosphonation (see Figure S2 in Supporting Information File 1). After the point of zero charge (PZC), the phosphonates induce a negative charge, whereas non-phosphonated PEI-NP display a zeta potential of 0 mV, making PEI-NP unstable at basic pH.

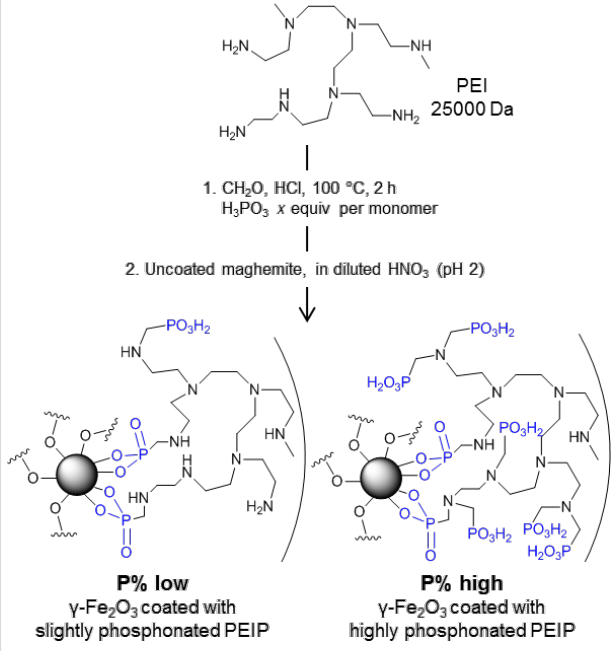


**Figure 1:** Synthesis of NP-PEIP. The number of phosphonates depends on the number of equivalents of phosphorous acid used.

The efficiency of the NP-PEIP in removing pollutants was determined by the adsorption of two organic dyes used as contaminants models: the positively charged (regardless of the pH value) methylene blue (MB) and the negatively charged (from pH 3.4 to basic pH) methyl orange (MO). Such dyes are pollutants themselves. They are widely used for industrial purposes, especially MB in the textile industry [25], they reduce light penetration and photosynthesis in the effluents. Their removal remains a challenge [26].

With the aim of evaluating the interactions of the NP-PEIP material with pollutants in very low quantities, which are considerably harder to remove, the concentration of the dyes was kept below $5 \cdot 10^{-4}$ mol·L$^{-1}$ in all the experiments. This choice of low concentration (which is not a strict limitation) is dictated by the need to be close to the most common pollutions that are often diffuse and characterized by low concentration levels. Moreover, the MO and MB calibration curves have been evaluated (data available in Figures S3–S6 in Supporting Information File 1) and show that their absorptions vary significantly either with the pH or with the concentration. It can be observed that working at low concentrations allows one to avoid the di- or trimerization of MB, which dramatically impacts the wavelength of the maximum absorption.

## Determination of the optimal conditions

First, we studied the pH value at which a maximum of dye is loaded on the particles. Adsorptions in solutions of MO or MB were carried out at different pH values using two types of particles as sorbents: one coated with a slightly phosphonated polymer (P% = 20, NP-PEIP20) and another coated with a highly phosphonated polymer (P% = 80, NP-PEIP80).

Figure 2A shows that the maximum of the anionic dye MO is recovered between pH 4 and 10. The percentage of phosphonation does not significantly affect the pH range of efficiency, only the amount of MO adsorbed: 870 mg/g for NP-PEIP20, whereas 350 mg/g only for NP-PEIP80. On the other hand, the adsorption of the cationic dye MB by NP-PEIP20 is constantly low (≤40 mg/g) below pH 10. We assume that the positive charges on the ammonium groups cause electrostatic repulsions with the cationic dye. In the case of NP-PEIP80, the PEI carried many phosphonate groups and the resulting numerous negative charges decrease the repulsion between ammonium and MB. Consequently, up to 700 mg/g of MB can be extracted by NP-PEIP80. The MB adsorption increases up to 1000 mg/g above pH 10.

The kinetic curves, presented Figure 2B, highlight the fast MO extraction regardless of the P% value. Indeed, 50% of maximum adsorption capacity is reached after only 4 min and 21 min in the two cases. MB is removed more slowly: 37 and 60 min for P% = 80 and P% = 20 respectively, are needed to load half of the pollutants on the NP-PEIP. That confirms the assertion that the adsorption rate is strongly dependent on the amount of phosphonate groups on the polymer. First measurements were monitored only after five minutes: This time was necessary to ensure the collection of all the NP-PEIP with the magnet. It can be explained by the dispersion state of the particles in solution, and the nanometric size. The sensitivity to the magnetic attraction is lower for nanometre-sized beads than for micro- or millimetre-sized beads in which many maghemite nanoparticles are often incorporated in a polymeric network.

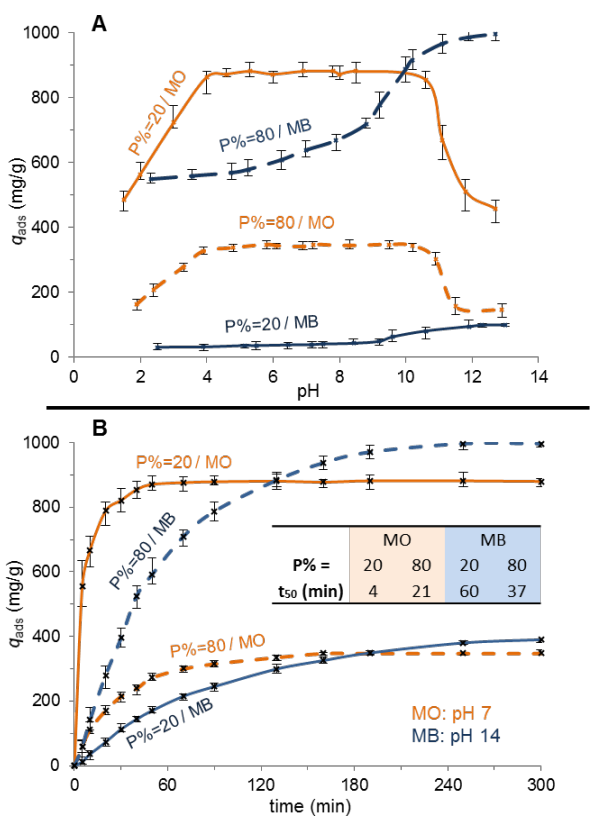


**Figure 2:** A) pH Values at which NP-PEIP20 and NP-PEIP80 adsorb a maximum amount of dye. MO is better adsorbed in the range of pH from 4 to 10. P% does not impact the pH range but the amount of removed dye. For MB, the higher the P% is, the better the extractions are, regardless of the pH value. Maximum amounts are removed at basic pHs. B) Adsorption of MO is faster than that of MB, regardless of the percentage of phosphonate groups.

## Interpretation of the pH-responsive pollutant extraction

To understand these results, a diagram predicting the specific interactions between particles and dyes according to the pH value is showed in Figure 3. Phosphonate functions on the NP-PEIP are in the monodeprotonated $RPO_3H^-$ form above pH 2, and undergo a second deprotonation ($RPO_3^{2-}$) around pH 6.5–7.0. In the presence of both ammonium and phosphonate groups, only ammonium interactions are represented because they are always in the majority, therefore they have strongest influence on the behaviour of the particles.

We can predict that the MO extraction is maximized between pH 3.4 (above its p$K_a$) and pH 10.5, corresponding to the amine deprotonation on the NP-PEIP. In this range of pH, the electrostatic interactions between numerous ammonium and MO sulfonate groups are at the maximum intensity. Concerning the MB,

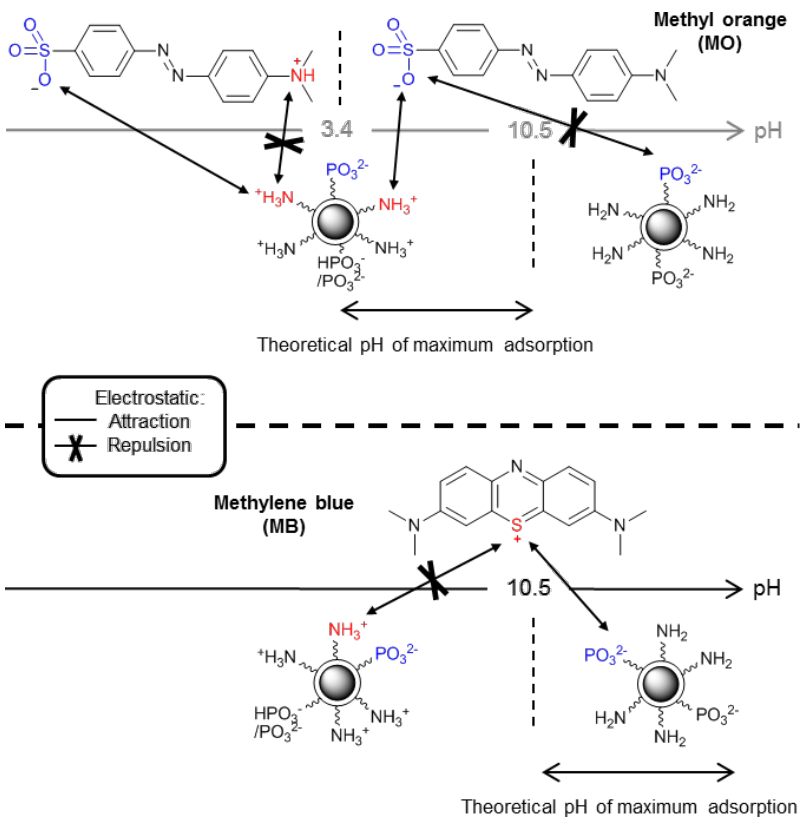


**Figure 3:** Prediction of the best range of pH values for electrostatic attractions between NP-PEIP and MO and MB dyes. Only the major interaction (i.e., ammonium) is represented. For MO, an interaction occurs with sulphates and ammonium groups, until the p$K_a$ ($NH_3^+/NH_2$) is reached. Cationic MB is attracted by the phosphonate groups introduced on PEI at basic pH values.

the sulfur atom is always positively charged. The adsorption therefore increases after the second deprotonation of phosphonate, and is maximized above p$K_a$ of the ammonium/amine deprotonation, where repulsive forces are negligible. All of these results show that, in the case of maghemite coated with phosphonated PEI adsorbing MO and MB, electrostatic interactions are predominant.

## Quantities of pollutant extracted according to the percentage of phosphonation

Performances of remediation for nanoparticles coated with different polymers (P% = 5, 20, 60, 90) are summarized Figure 4. The maximum efficiency is reached at pH 7 for P% = 5, where the system can remove up to 1356 mg·g$^{-1}$ of MO. When P% increases, the amount of adsorbed dyes, $q_{max}$, drop: 882 mg·g$^{-1}$, 510 mg·g$^{-1}$ and up to 314 mg·g$^{-1}$ for NP-PEIP20, NP-PEIP60 and NP-PEIP90, respectively. Referring back to Figure 3, the repulsion between negative charges increases with the number of introduced phosphonate groups. At pH 14, we observe a similar evolution, but all values of $q_{max}$ are much lower because of the absence of electrostatic attraction, whereas all the amino groups are deprotonated.

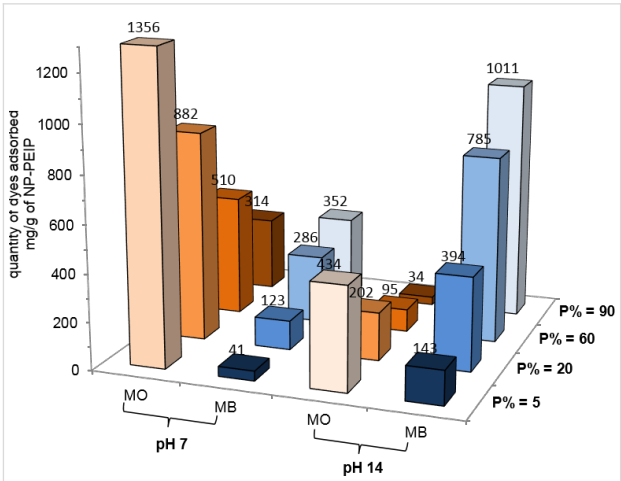


**Figure 4:** Removed amounts of MO and MB dyes by NP-PEIP*x* at pH 7 and 14. P% significantly affects adsorption of MB and MO. At neutral pH, much more MO is eliminated than MB, while the contrary is observed at basic pH.

The phosphonation rate also strongly influences the adsorption of MB. The value of $q_{max}$ is increased to the seven-fold between P% = 5 and P% = 90 at pH 14 with a maximum of

1011 mg·g$^{-1}$. This amount is higher than the commercial activated charcoal (980 mg·g$^{-1}$) and among the largest measured extracted amounts of BM dye [27]. This high $q_{max}$ can be attributed to the composition of NP-PEIP: PEIP represents more than 80% of the particles total weight [20], and under the same conditions maghemite does not adsorb more than 1 mg/mg. In addition, each monomeric unit of the PEIP potentially interacts with charged pollutants through amine or phosphonate groups.

## Washing steps and recyclability of the magnetic particles

The data collected in Figure 4 reveal that the adsorption of MO with NP-PEIP05 is reduced to one third between pH 7 and 14. On the opposite, the MB adsorption falls from 1011 mg·g$^{-1}$ to 352 mg·g$^{-1}$ with NP-PEIP90 when the pH value decreases from 14 to 7. Consequently, the washing process is easy to implement, by successive redispersions of collected particles in basic or acidic water, for anionic MO and cationic MB pollutants, respectively. The washing solutions consist of water adjusted to pH 7 or 14 with nitric acid or sodium hydroxide. Moreover, only 20 mL are enough to wash up to 1 g of magnetic particles. Figure 5A shows that after a full adsorption of MO by NP-PEIP05 (orange bars), more than 68% of dye are released after the first wash and 83% after two successive washes. NP-PEIP90 loaded with MB (blue bars) release 76% and 88% after the first and the second wash, respectively. Consequently, we can reasonably estimate that four washes are enough to obtain a reusable material practically purified.

NP-PEIP05 and NP-PEIP90 were also evaluated in several adsorption/desorption cycles (Figure 5B). A little loss of activity for MO and MB was observed but more than 90% of contaminants were removed after the seventh cycle. The loss in magnetic particles between cycles is negligible compared to the amount of pollutant extracted and in addition, no traces of iron were detected by atomic absorption spectroscopy in the supernatant. The decreasing of effectiveness is already under study.

# Conclusion

The modulation of positive and negative charges of phosphonated polyethylenimine, through the controlled insertion of phosphonate groups on polyethylenimine, can be considered as an advantage for adsorption of organic pollutants. By adjusting the percentage of phosphonation, the pH value and the decontamination time, performances similar to active charcoal are obtained, but with a highly selective adsorption of cationic and anionic contaminants. This recyclable material obtained by an easy and reproducible single-step process is particularly designed for water treatment. Moreover, the PEIP polymer is perfectly adaptable for a future use in other systems such as microbeads or membranes.

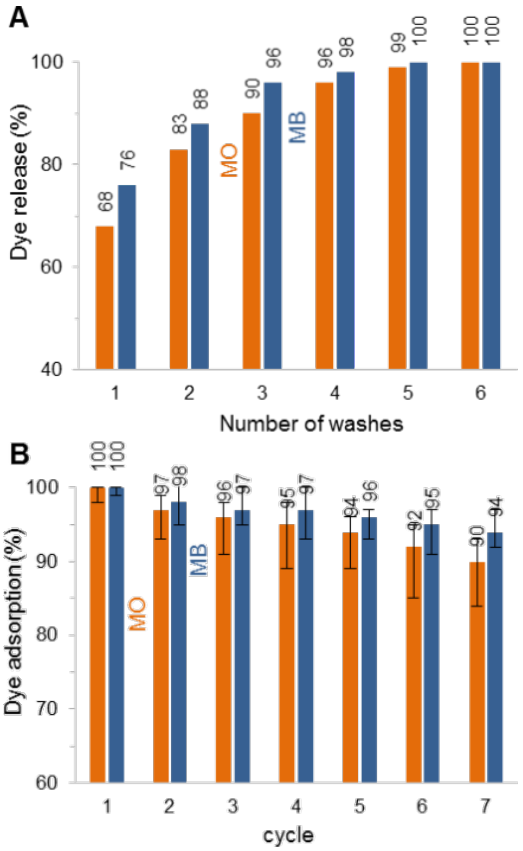


**Figure 5:** A) Cumulative quantities of dyes released after each wash. MO is desorbed from NP-PEIP05 with sodium hydroxide aqueous solution, MB from NP-PEIP90 with diluted nitric acid. B) The efficiency of the dyes extraction remains high after several adsorption/desorption cycles.

# Supporting Information

Supporting information includes a TEM image of the synthetized maghemite nanoparticles, evolution of the zeta potential of maghemite, PEI nanoparticles and PEIP-coated nanoparticles as a function of the pH value, and evolution of the maximum absorption wavelengths and molar extinction coefficients of methyl orange and methylene blue, and corresponding calibration curves.

## Supporting Information File 1

Additional experimental data.
[http://www.beilstein-journals.org/bjnano/content/supplementary/2190-4286-7-136-S1.pdf]

# Acknowledgements

We gratefully acknowledge financial support from the 'Ministère de la Recherche et des Nouvelles Technologies', CNRS (Centre National de la Recherche Scientifique), the

‘Région Basse-Normandie’ and the European Union (FEDER funding). The authors acknowledge the financial support of the french Agence Nationale de la Recherche (ANR), through the program “Investissements d’Avenir”(ANR-10-LABX-09-01), LabEx EMC$^3$.

## References

1. Cotruvo, J. A. *Sci. Total Environ.* **1985,** *47,* 7–26. doi:10.1016/0048-9697(85)90316-X
2. Richardson, S. D.; Ternes, T. A. *Anal. Chem.* **2011,** *83,* 4614–4648. doi:10.1021/ac200915r
3. Schwarzenbach, R. P.; Escher, B. I.; Fenner, K.; Hofstetter, T. B.; Johnson, C. A.; von Gunten, U.; Wehrli, B. *Science* **2006,** *313,* 1072–1077. doi:10.1126/science.1127291
4. Martínez-Huitle, C. A.; Brillas, E. *Appl. Catal., B: Environ.* **2009,** *87,* 105–145. doi:10.1016/j.apcatb.2008.09.017
5. Rivas, B. L.; Pereira, E. D.; Palencia, M.; Sánchez, J. *Prog. Polym. Sci.* **2011,** *36,* 294–322. doi:10.1016/j.progpolymsci.2010.11.001
6. Crini, G. *Bioresour. Technol.* **2006,** *97,* 1061–1085. doi:10.1016/j.biortech.2005.05.001
7. Liu, P.; Zhang, L. *Sep. Purif. Technol.* **2007,** *58,* 32–39. doi:10.1016/j.seppur.2007.07.007
8. Dias, J. M.; Alvim-Ferraz, M. C. M.; Almeida, M. F.; Rivera-Utrilla, J.; Sánchez-Polo, M. *J. Environ. Manage.* **2007,** *85,* 833–846. doi:10.1016/j.jenvman.2007.07.031
9. Khin, M. M.; Nair, A. S.; Babu, V. J.; Murugan, R.; Ramakrishna, S. *Energy Environ. Sci.* **2012,** *5,* 8075–8109. doi:10.1039/c2ee21818f
10. Zhong, L.-S.; Hu, J.-S.; Liang, H.-P.; Cao, A.-M.; Song, W.-G.; Wan, L.-J. *Adv. Mater.* **2006,** *18,* 2426–2431. doi:10.1002/adma.200600504
11. Koehler, F. M.; Rossier, M.; Waelle, M.; Athanassiou, E. K.; Limbach, L. K.; Grass, R. N.; Günther, D.; Stark, W. J. *Chem. Commun.* **2009,** 4862–4864. doi:10.1039/b909447d
12. Obeid, L.; Bée, A.; Talbot, D.; Ben Jaafar, S.; Dupuis, V.; Abramson, S.; Cabuil, V.; Welschbillig, M. *J. Colloid Interface Sci.* **2013,** *410,* 52–58. doi:10.1016/j.jcis.2013.07.057
13. Xu, P.; Zeng, G. M.; Huang, D. L.; Feng, C. L.; Hu, S.; Zhao, M. H.; Lai, C.; Wei, Z.; Huang, C.; Xie, G. X.; Liu, Z. F. *Sci. Total Environ.* **2012,** *424,* 1–10. doi:10.1016/j.scitotenv.2012.02.023
14. Wang, H.; Chen, Q.-W.; Chen, J.; Yu, B.-X.; Hu, X.-Y. *Nanoscale* **2011,** *3,* 4600–4603. doi:10.1039/c1nr11012h
15. Luo, X.; Zhang, L. *J. Hazard. Mater.* **2009,** *171,* 340–347. doi:10.1016/j.jhazmat.2009.06.009
16. Mutin, P. H.; Guerrero, G.; Vioux, A. *J. Mater. Chem.* **2005,** *15,* 3761–3768. doi:10.1039/b505422b
17. Zhao, H.; Xu, J.; Lan, W.; Wang, T.; Luo, G. *Chem. Eng. J.* **2013,** *229,* 82–89. doi:10.1016/j.cej.2013.05.093
18. Massart, R. *IEEE Trans. Magn.* **1981,** *17,* 1247–1248. doi:10.1109/TMAG.1981.1061188
19. Lefebure, S.; Dubois, E.; Cabuil, V.; Neveu, S.; Massart, R. *J. Mater. Res.* **1998,** *13,* 2975–2981. doi:10.1557/JMR.1998.0407
20. Monteil, C.; Bar, N.; Moreau, B.; Retoux, R.; Bee, A.; Talbot, D.; Villemin, D. *Part. Part. Syst. Charact.* **2014,** *31,* 219–227. doi:10.1002/ppsc.201300185
21. Villemin, D.; Moreau, B.; Elbilali, A.; Didi, M.-A.; Kaid, M.; Jaffrès, P.-A. *Phosphorus, Sulfur Silicon Relat. Elem.* **2010,** *185,* 2511–2519. doi:10.1080/10426501003724897
22. Monteil, C.; Bar, N.; Retoux, R.; Henry, J.; Bernay, B.; Villemin, D. *Sens. Actuators, B* **2014,** *192,* 269–274. doi:10.1016/j.snb.2013.09.096
23. Xu, Y.; Qin, Y.; Palchoudhury, S.; Bao, Y. *Langmuir* **2011,** *27,* 8990–8997. doi:10.1021/la201652h
24. Moedritzer, K.; Irani, R. R. *J. Org. Chem.* **1966,** *31,* 1603–1607. doi:10.1021/jo01343a067
25. Bennani Karim, A.; Mounir, B.; Hachkar, M.; Bakasse, M.; Yaacoubi, A. *Rev. Sci. Eau* **2010,** *23,* 375–388. doi:10.7202/045099ar
26. Ali, H. *Water, Air, Soil Pollut.* **2010,** *213,* 251–273. doi:10.1007/s11270-010-0382-4
27. Rafatullah, M.; Sulaiman, O.; Hashim, R.; Ahmad, A. *J. Hazard. Mater.* **2010,** *177,* 70–80. doi:10.1016/j.jhazmat.2009.12.047

## License and Terms

BEILSTEIN JOURNAL OF NANOTECHNOLOGY

# $Sb_2S_3$ grown by ultrasonic spray pyrolysis and its application in a hybrid solar cell

Erki Kärber*[1], Atanas Katerski[1], Ilona Oja Acik[1], Arvo Mere[1], Valdek Mikli[2] and Malle Krunks[1]

Full Research Paper

Open Access

Address:
[1]Laboratory of Thin Film Chemical Technologies, Department of Materials Science, Tallinn University of Technology, Ehitajate tee 5, 19086 Tallinn, Estonia and [2]Chair of Semiconductor Materials Technology, Department of Materials Science, Tallinn University of Technology, Ehitajate tee 5, 19086 Tallinn, Estonia

Email:
Erki Kärber* - erki.karber@ttu.ee

* Corresponding author

Keywords:
absorber; chemical spray pyrolysis (CSP); hybrid solar cell; stibnite ($Sb_2S_3$); ultrasonic atomization

*Beilstein J. Nanotechnol.* **2016,** *7,* 1662–1673.
doi:10.3762/bjnano.7.158

Received: 11 April 2016
Accepted: 17 October 2016
Published: 10 November 2016

This article is part of the Thematic Series "Nanostructures for sensors, electronics, energy and environment III".

Guest Editor: N. Motta



## Abstract

Chemical spray pyrolysis (CSP) is a fast wet-chemical deposition method in which an aerosol is guided by carrier gas onto a hot substrate where the decomposition of the precursor chemicals occurs. The aerosol is produced using an ultrasonic oscillator in a bath of precursor solution and guided by compressed air. The use of the ultrasonic CSP resulted in the growth of homogeneous and well-adhered layers that consist of submicron crystals of single-phase $Sb_2S_3$ with a bandgap of 1.6 eV if an abundance of sulfur source is present in the precursor solution ($SbCl_3/SC(NH_2)_2$ = 1:6) sprayed onto the substrate at 250 °C in air. Solar cells with glass-ITO-$TiO_2$-$Sb_2S_3$-P3HT-Au structure and an active area of 1 $cm^2$ had an open circuit voltage of 630 mV, short circuit current density of 5 mA/$cm^2$, a fill factor of 42% and a conversion efficiency of 1.3%. Conversion efficiencies up to 1.9% were obtained from solar cells with smaller areas.

## Introduction

A solution-based technology coupled with earth abundant materials is an attractive path for affordable next-generation solar cells. The present paper relies on the recently proven concept of $TiO_2/Sb_2S_3$/P3HT solar cells [1-12], in which $Sb_2S_3$ is the light absorber, also called the sensitizer, situated in the electrical junction created by $TiO_2$ and P3HT (polythiophene) as the electron and hole conductor, respectively. For these type of solar cells, fluorine doped tin oxide (FTO) is prevalently used to contact the $TiO_2$ while evaporated Au has been used to contact the P3HT. The use of a polymeric hole conductor coupled with inorganic materials leads to the notation of a hybrid solar cell [13]. Based on dense $TiO_2$ covered by mesoporous $TiO_2$ and then impregnated with a light harvester, the resulting solar cells are commonly referred to as mesoscopic solar cells [14] the first of which, based on $Sb_2S_3$ sensitizer, yielded conversion efficiencies above 3% [15,16].

The central part of the particular system, the $Sb_2S_3$ absorber, has so far been produced mainly by chemical bath deposition (CBD) for which the presence of impurities such as antimony hydroxide is inherent, and it is essential to use post-deposition heat-treatment due to the initially amorphous yield [17]. CBD is also considered as not suitable for large-scale applications unless the conventional low-temperature method is replaced by synthesis at room temperature [18]. The solar cells that rely on the CBD-grown $Sb_2S_3$ and meso-porous $TiO_2$ as the electron conductor have reached a conversion efficiency of 7.5% when post-deposition sulfurization and thermal treatment of $Sb_2S_3$ were used [17]. The introduction of atomic layer deposition (ALD) for growing $Sb_2S_3$ onto a meso-porous $TiO_2$ substrate was successful with respective solar cell efficiencies reaching from 2.6% in the first study in 2013 [19] up to 5.8% in 2014 [5]. The success was attributed to the conformity of the coating by the oxide-free $Sb_2S_3$ layer. Nevertheless, the initial product in ALD is also amorphous and requires an annealing stage to obtain crystalline $Sb_2S_3$.

Another solution-based method, besides CBD, is spin coating, which has been used to obtain $Sb_2S_3$ absorber layers by multiple steps of a coating–annealing procedure [12], or a single-step coating–annealing procedure developed by Choi and Seok in 2015 [20]. The resulting solar cells showed conversion efficiencies of up to 2.3% when based on planar $TiO_2$ [12] and 6.4% [20] when based on mesoporous $TiO_2$. Spin coating is a simple technique and seems attractive for the deposition of oxide-free $Sb_2S_3$ absorber. However, an annealing stage at 300 °C in inert gas atmosphere is involved. Chemical spray pyrolysis (CSP) is a simple and fast method in which a solution of precursor materials is pulverized and the aerosol is then guided by flow of carrier gas onto a hot substrate. The droplets can be produced pneumatically, or, ultrasonically with a piezoelectric generator submerged in the solution bath. The precursors for Sb and S have been $SbCl_3$ and thiourea (tu) [21] or thioacetamide [22], respectively, dissolved in water together with a complexing agent such as tartaric acid to reduce the hydrolysis of the $SbCl_3$ in the spray solution [21,22]. We have observed that the use of tartaric acid as the complexing agent results in unwanted residues in the films grown by pneumatic spray [23]. Alternatively, non-aqueous solvents such as acetic acid or alcohols have been utilized to eliminate problems associated with the hydrolysis of $SbCl_3$ [22,24]. In general, the aqueous solvent tends to result in amorphous $Sb_2S_3$ films whereas films prepared from non-aqueous solvents have been reported as polycrystalline [22,24]. So far, we have shown that for growing $Sb_2S_3$ by pneumatic CSP the use of $SbCl_3$ and thiourea (tu) precursors with an $SbCl_3$/tu molar ratio of 1:3 dissolved in methanol and sprayed on substrate at a temperature of 255 °C leads to films that consist of orthorhombic stibnite and a secondary phase that was identified as $Sb_2O_3$ [23]. To suppress the formation of oxides, an excess of sulfur source in the precursor solution may be required as indicated by similar studies for indium sulfide [25,26], zinc sulfide [27] and tin sulfide [28,29] grown by pneumatic CSP. At the time of the present study, no publications were available on ultrasonically spray-grown $Sb_2S_3$, and on the application of any CSP-grown $Sb_2S_3$ in a solar cell, apart from a photoelectrochemical cell that showed an efficiency of 0.3% [30].

In this work, we report the first results on growing $Sb_2S_3$ by ultrasonic chemical spray pyrolysis (ultrasonic CSP), and on the application of ultrasonic CSP grown $Sb_2S_3$ as an absorber in a hybrid solar cell. The aim of this work is to obtain a single-phase $Sb_2S_3$ absorber by ultrasonic CSP, and to test the $Sb_2S_3$ layer in a planar $TiO_2/Sb_2S_3$/P3HT configuration solar cell. In the present work we will show that by using an excess of thiourea as the sulfur source in the spray solution, such as with a $SbCl_3$/tu molar ratio of 1:6, one can rapidly grow single-phase and crystalline $Sb_2S_3$ by ultrasonic CSP without the post-deposition heat treatment stage, yielding solar cell conversion efficiencies up to 1.9% when coupled with a planar $TiO_2$ layer, also grown by spray in air.

## Results and Discussion

### Influence of the molar ratio of the precursors on phase composition and morphology of the antimony sulfide layers

The films obtained by CSP at 250 °C had differed in appearance and homogeneity depending on the molar ratio of the precursors in the solution. The visually homogeneous and dark layers grown from precursor solutions with Sb/S molar ratios of 1:6 and 1:9 on a glass/ITO/$TiO_2$ substrate show Raman peaks at 145, 393 and 515 $cm^{-1}$, which were attributed to the anatase phase of $TiO_2$ [31], and two prominent peaks at around 282 and 303/310 $cm^{-1}$, which can be attributed to crystalline $Sb_2S_3$ [32-34], see Figure 1, spectrum A and B. Also, the lower intensity peaks at 128 $cm^{-1}$ [32], 155 $cm^{-1}$ [32], 190 $cm^{-1}$ [33] and 238 $cm^{-1}$ [32-34] are expected to belong to crystalline $Sb_2S_3$. Many of these peaks could overlap with those characteristic of various Sb oxides [32,33,35-37]. However, we are guided by the fact that up to 570 °C cubic $Sb_2O_3$ is the most stable form of Sb oxide [38]. We have verified by Raman spectroscopy the peak positions of the cubic $Sb_2O_3$ single layer (Figure 1, spectrum E) produced by heating the Sb precursor ($SbCl_3$) on glass at 450 °C in air. The most intense peak of cubic $Sb_2O_3$ is expected to be present at 255 $cm^{-1}$ [39] and is absent in the as-deposited films produced from 1:6 and 1:9 solutions, suggesting that the oxidation of the Sb precursor is negligible when an abundance of sulfur source is provided in the solution.

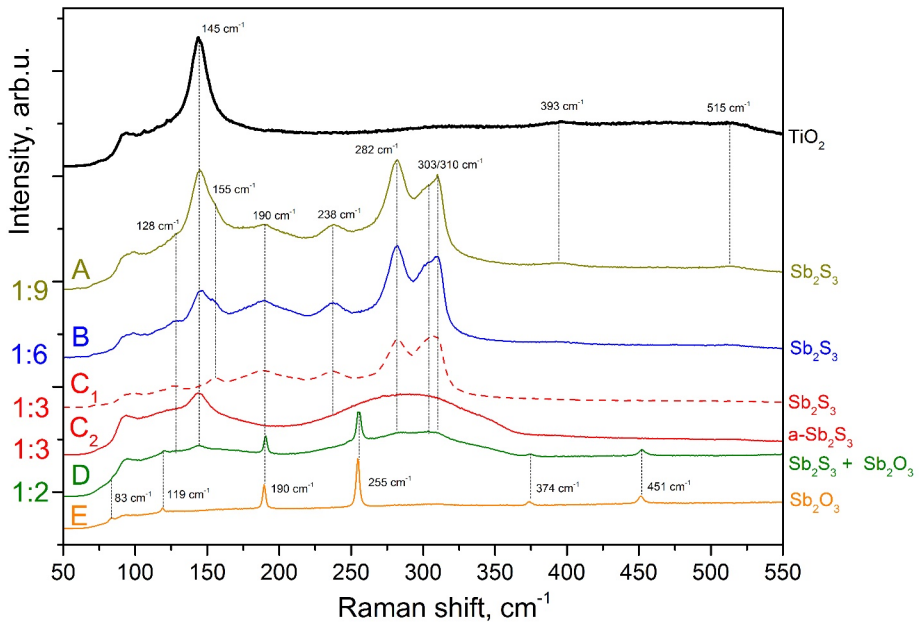


**Figure 1:** Raman spectra A–D of thin layers grown by spraying solutions with Sb/S precursor ratios of 1:9 to 1:2 onto a glass/ITO/$TiO_2$substrate kept at 250 °C. The red dashed line ($C_1$) is for spectrum that is collected from areas less common for sample C, the red solid line ($C_2$) is for spectrum that is prevailing for sample C. The Raman spectra are measured from glass/ITO/$TiO_2$/$Sb_2S_3$ samples after five deposition cycles of $Sb_2S_3$. The spectra remain similar when varying the number of cycles (not shown). As a reference, the Raman spectrum E with peaks attributed to $Sb_2O_3$ belongs to a single layer that was produced by heating the Sb-precursor ($SbCl_3$) on a glass substrate at 450 °C in air, and a Raman spectrum of the $TiO_2$ substrate layer is also given.

On the contrary, the layers grown from 1:3 solutions are heterogeneous. The 1:3 layers show prevailing regions that are visually transparent with an orange hue, and more sparsely located dark regions. Also the surface image by SEM (Supporting Information File 1, Figure S1a) shows varying rough areas with grains and smoother areas with no grains in the layer. The Raman spectra of the layer produced from 1:3 solution is presented in Figure 1 as spectrum $C_1$ (dashed line, characteristic of the dark regions), and as spectrum $C_2$ (solid line, characteristic of the orange colored regions). The broad band centered around 290 $cm^{-1}$ in spectrum $C_2$ is attributed to amorphous antimony sulfide as in other antimony sulfide layers produced by CBD [7,16,40,41] and by ALD [5,19]. The peak at 145 $cm^{-1}$ attributed to $TiO_2$ is also more pronounced in spectrum $C_2$, presumably due to the higher transparency of the amorphous layer to the green laser beam when compared to regions with higher crystallinity (spectrum $C_1$). Secondly, the 145 $cm^{-1}$ peak appears to be more intense as we increase the precursor ratio from 1:3 to 1:6 (spectrum $C_1$ vs B), or increasing from 1:6 to 1:9 (spectrum B vs A). As the increase in thiourea content in the spray solution leads to layers composed of particles with gaps in between that leave the $TiO_2$ substrate partly exposed (SEM images for 1:6 samples to be discussed below are presented in Figure 2), it seems reasonable to assume that the coverage of $TiO_2$ by $Sb_2S_3$ dictates the emerging of the Raman signal at 145 $cm^{-1}$, which was attributed to the $TiO_2$ substrate.

To further scrutinize the phase composition of the layers, and to verify the effect of the precursor ratio, we have presented Raman spectra of layers grown from 1:2 solution. When evaluated by Raman spectroscopy, the 1:2 layer was very heterogeneous. To illustrate this we have chosen one spectrum that clearly shows the signal from antimony oxide (Figure 1, spectrum D). The presence of oxide is indicated by the sharp peaks at 83 $cm^{-1}$ [36,37], 119 $cm^{-1}$ [35,37], 190 $cm^{-1}$ [32,33,35,37,39,42,43], 255 $cm^{-1}$ [32,33,35,37,39], 374 $cm^{-1}$ [32,33,35,39] and 452 $cm^{-1}$ [32,33,35,37,39] that correspond to cubic $Sb_2O_3$. According to the SEM study, sparsely distributed pyramidal crystals were present in the layer (Supporting Information File 1, Figure S1b) that according to EDX were composed of antimony and oxygen only. Such $Sb_2O_3$ crystals have also been reported to be present after annealing the CBD-grown antimony sulfide films at 300 °C [44]. Indeed, the lowering of the content of the sulfur source in the spray solution is expected to favor the formation of oxide phases when growing metal sulfide layers by spray pyrolysis [25-29]. Additionally, we note that the amorphous regions in the layer produced from 1:3 solutions (Figure 1, spectrum $C_2$) after annealing at 320 °C for 30 min in $N_2$ atmosphere showed the presence of crystalline $Sb_2O_3$ in addition to crystalline $Sb_2S_3$ when evaluated by micro-Raman spectroscopy (not shown), indicating the presence of a non-crystalline oxygen-containing phase prior to annealing in $N_2$. EDX results support this propo-

sition as the S/Sb atomic ratio of 1.3 indicates a deficiency of sulfur (when compared to the expected S/Sb ratio of 1.5 in the $Sb_2S_3$ target compound) in the layers as-grown with a precursor ratio of 1:3. Thus, the use of Sb/S precursor ratios higher than 1:3 in the spray solution clearly has an advantage when aspiring an oxide-free $Sb_2S_3$ absorber layer.

In summary, based on Raman spectroscopy, oxide-free layers of crystalline $Sb_2S_3$ can be grown by spray pyrolysis onto the $TiO_2$ substrate at 250 °C in air by using precursor ratio of 1:6 or 1:9 in the solution, yielding the use of 1:6 ratio as sufficient. Following this result we will regard 1:6 ratio as an optimum to produce $Sb_2S_3$ absorber layers for the $TiO_2$/absorber/P3HT solar cells.

## Evolution of the morphology and optical properties of $Sb_2S_3$ layers with a varying number of deposition cycles

According to the SEM study, the layers grown from 1:6 solutions consist of flake-like particles, and coalesced flakes, with gaps in between that leave the $TiO_2$ substrate partly exposed (Figure 2). The flakes are composed of S and Sb with a ratio of 1.53 measured by EDX that within measurement uncertainty corresponds to stoichiometric $Sb_2S_3$.

The number density of $Sb_2S_3$ flakes on the $TiO_2$ substrate increases with the number of growth cycles, suggesting that some of the nucleation sites are preferential. The nucleation of secondary $Sb_2S_3$ crystals is evident when using a higher SEM magnification (Supporting Information File 1, Figure S2). In addition, the flakes grow laterally and in height, the approximate sizes of the flakes are presented in the caption of Figure 2. The resulting increase of the overall coverage density is in correspondence with the decrease of the optical transmittance (Supporting Information File 1, Figure S3).

For the calculation of the absorption coefficient α, we used 100 nm as a rough estimation of the optically effective thickness of the $Sb_2S_3$ layer based on the SEM image of $Sb_2S_3$ grown using three cycles (Figure 3).

The resulting values of the absorption coefficient α of the $Sb_2S_3$ layers are presented in Figure 4. The α values remain above $5 \times 10^4$ $cm^{-1}$ right from the absorption edge at 1.6 eV, throughout the visible region 1.8–3.1 eV, and in the near-UV region (Figure 4A). The high values of α are in accordance with those in literature in which we find α values of (7–9) × $10^4$ $cm^{-1}$ in the range of 2.0–3.5 eV for crystalline $Sb_2S_3$ with an $E_g$ of 1.7 eV prepared by RF sputtering [45]. The absorption coeffi-

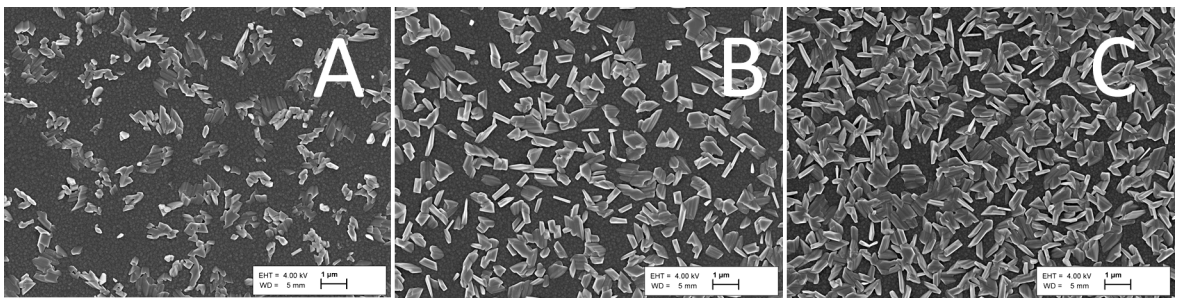


**Figure 2:** SEM images of $Sb_2S_3$ crystalline flakes grown by spraying solutions with a precursor ratio of 1:6 onto a $TiO_2$ substrate kept at 250 °C using 3, 7 and 11 deposition cycles, depicted in images A, B and C, respectively. The linear dimensions of the flakes, or coalesced flakes, are in the range of 200–800 nm, 500–1200 nm and 800–1500 nm in panels A, B and C, respectively.

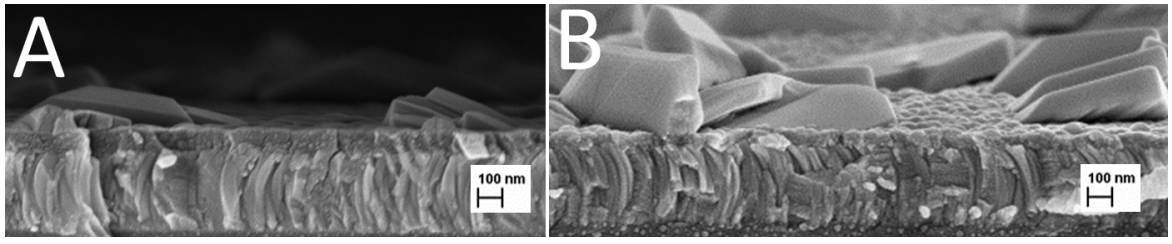


**Figure 3:** Cross-sectional SEM image of the glass/ITO/$TiO_2$/$Sb_2S_3$ structure, the topmost $Sb_2S_3$ layer consists of nanoparticles grown by ultrasonic CSP using three spray cycles (A) or nine spray cycles (B).

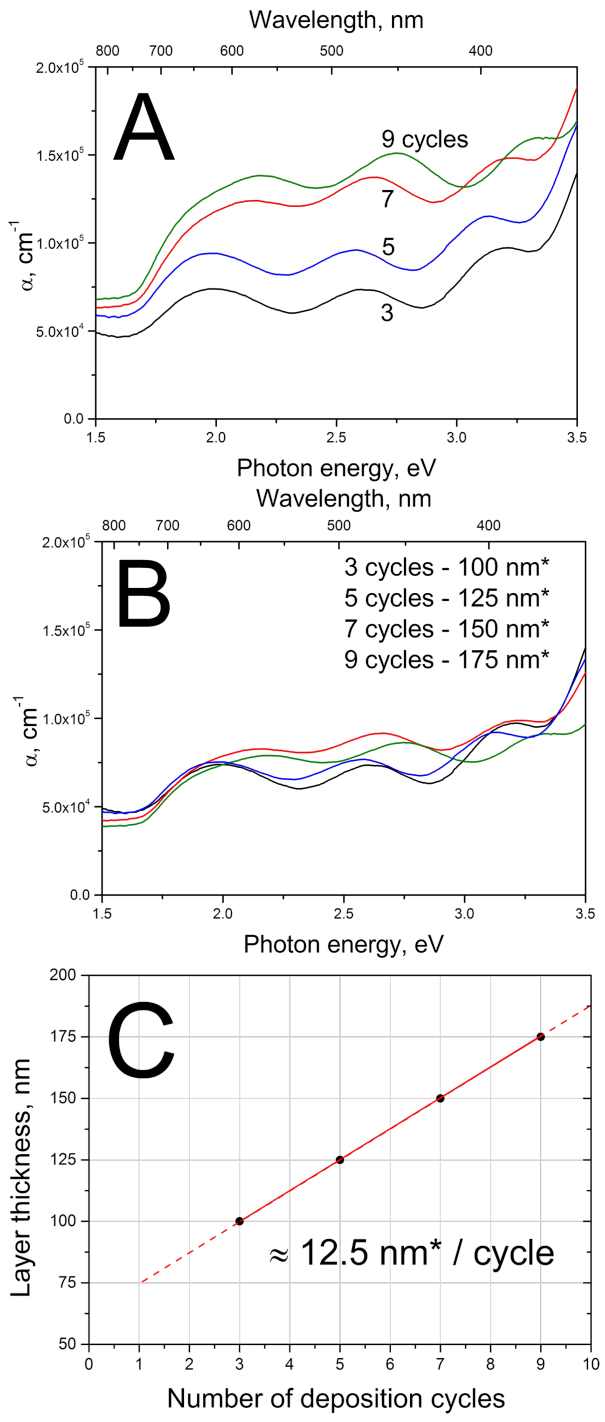


**Figure 4:** A: Absorption coefficient α of $Sb_2S_3$ layers of nanoparticles grown by ultrasonic CSP with 3–9 deposition cycles, calculated based on the optical transmittance of the glass/ITO/$TiO_2$/$Sb_2S_3$ stack, assuming a $Sb_2S_3$ layer thickness of 100 nm; B: α, after applying a correction for the effective thickness by fitting, the units with the asterisk (nm*) stand for the fitted optical thickness; C: growth rate of the $Sb_2S_3$ layer based on the fitted effective layer thicknesses. The interference in each spectrum is due to the transparent thin film ITO/$TiO_2$ substrate; the bandgap of $TiO_2$ is around 3.3 eV.

cients of the layers grown with more than three cycles are likely to be overestimated (Figure 4A) due to the similar thickness of 100 nm assumed for all layers of $Sb_2S_3$ nanoparticles. Thus, a correction for the effective layer thicknesses was made by fitting with the criterion of overlapping values of α for all samples (Figure 4B). For example, the estimation of 175 nm for the effective optical thickness of the nine cycles of $Sb_2S_3$ sample seems to be apt, since the height of the flakes in the nine cycles of $Sb_2S_3$ sample remains at 200–300 nm (Figure 3B).

However, we are herein not so much interested in the absolute values of the thicknesses of the layers, considering that the obtained optical thicknesses are not expected to exactly coincide with the height of the nanoparticulate layers seen from SEM images. Also, in addition to the effective layer height, the effective optical thickness will be influenced by the increase of the coverage as was seen in Figure 2. Instead, the growth rate of the spray-grown $Sb_2S_3$ is more informative, and can be plotted (Figure 4C) based on the fitted effective optical thicknesses.

Considering that a cycle lasted for 3 min, the deposition rate of 12.5 nm per cycle accounts to 0.07 nm·$s^{-1}$ for the ultrasonic spray method, in which we use raw chemicals for the deposition of crystalline $Sb_2S_3$ at around 250 °C in air. A higher but close to comparable growth rate of 0.14 nm·$s^{-1}$ is reported for growing $Sb_2S_3$ by RF sputtering from a preformed high-purity $Sb_2S_3$ target, in vacuum environment, and with a post-deposition annealing at 400 °C under sulfur vapor to obtain crystalline, dense, smooth and stoichiometric $Sb_2S_3$ films [45]. For ALD, the growth rate of $Sb_2S_3$ film has been reported to be 0.002 nm·$s^{-1}$ (0.056 nm·$cycle^{-1}$, 33.5 s·$cycle^{-1}$) prior to annealing in $H_2S$ atmosphere [5]. Similarly, the conventional CBD requires hours of processing time prior to the annealing procedure [46,47], yielding growth speeds around 0.003 nm·$s^{-1}$ for $Sb_2S_3$ films [47].

The bandgap ($E_g$) of $Sb_2S_3$ was 1.6 eV irrespective of the number of deposition cycles used when grown using spray of 1:6 solutions onto a glass/ITO/$TiO_2$ stack (Figure 5). The bandgap of the $Sb_2S_3$ was calculated using the spectra of the absorption coefficient of the glass/ITO/$TiO_2$/$Sb_2S_3$ layer stacks (Figure 4B). The bandgaps obtained are in accordance with an $E_g$ of 1.55–1.72 eV reported for $Sb_2S_3$ films deposited by spray pyrolysis [48]. Theoretical calculations predict an even lower direct optical transition of 1.40 eV [49]. An absorber bandgap of 1.65 eV is found in solar cells with $Sb_2S_3$ prepared by ALD [5,19] or in solar cells with $Sb_2S_3$ prepared by CBD, as estimated from the photocurrent edge at around 750 nm in the published EQE plots [2,4,6-9,11,12,15-17,40,41,50-53]. Any $E_g$ larger than 1.7 eV up to 2.6 eV have been attributed to nanocrystalline $Sb_2S_3$ [1,44,54], or to amorphous $Sb_2S_3$

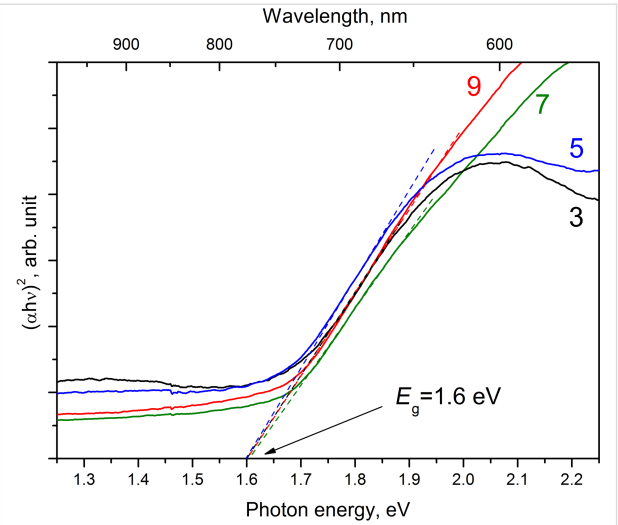


**Figure 5:** Tauc plot of the optical transmittance spectra of the glass/ITO/$TiO_2$/$Sb_2S_3$ layer stack, using α from Figure 4B. The linear part of the absorption edge when extended to the *x*-axis at $y = 0$ is used to determine the bandgap of $Sb_2S_3$. $Sb_2S_3$ was grown for three, five, seven and nine deposition cycles by exposing a glass/ITO/$TiO_2$ substrate kept at 250 °C to a spray solution containing $SbCl_3$ and $SC(NH_2)_2$ at a molar ratio of 1:6.

[6,44,45,53], while it is also known that contamination, most notably with oxygen, can significantly increase the bandgap value of metal sulfide films [23,55,56]. Values of 1.52–1.55 eV are reported for layers of nanotubes, -rods, or -flakes that consist of single phase $Sb_2S_3$ [57-59]. A study on the correlation between the Sb/S ratio in the films and the corresponding values of $E_g$ suggest that values around 1.6 eV are expected for crystalline and stoichiometric $Sb_2S_3$ (S/Sb = 1.5) films [60]. Thus, based on the low optical bandgap of 1.6 eV, along with the S/Sb ratio of 1.53 obtained by EDX, we can deduce that layers of single-phase stoichiometric $Sb_2S_3$ crystals can be prepared by using the CSP technique.

To sum up, based on the single-phase $Sb_2S_3$ composition of the layers as determined by Raman spectroscopy, and supported by the optical study, namely a bandgap of 1.6 eV, as well as an absorption coefficient of ca. $10^5$ $cm^{-1}$ in a wide region of optical photon energies, and the high growth rate of 0.07 $nm \cdot s^{-1}$ as evaluated by using optical transmittance spectroscopy, we can conclude that $Sb_2S_3$ grown by ultrasonic CSP can be considered as a candidate for the use as an absorber material in a solar cell based on an inorganic sensitizer. We emphasize that the end product of a single-stage growth at 250 °C in air was crystalline and oxide-free $Sb_2S_3$. No additional annealing was needed. This alone can be considered an advantage when comparing the potential of spray to other solution based methods, such as CBD or spin coating, for growing $Sb_2S_3$.

## Properties of the $TiO_2$/$Sb_2S_3$ nanoparticle/P3HT solar cell

The highest efficiencies of each cell were observed after being exposed to AM1.5 illumination for up to 45 min, varying from sample to sample. The general trends in the evolution of the current–voltage curve and series resistance, due to light soaking, are presented in the Supporting Information File 1 (Figure S4). The study of the cause behind this light-soaking effect is not within the scope of the present work. Proposed explanations for this behavior include the filling of electron traps in $TiO_2$ near the $TiO_2$/P3HT interface [61], adsorbed oxygen released during light soaking from $TiO_2$ and photocatalytic effects due to the presence of $TiO_2$ [40,52,61].

An SEM image of the cross-section of the glass/ITO/$TiO_2$/$Sb_2S_3$ structure, of the glass/ITO/$TiO_2$/$Sb_2S_3$/P3HT/Au structure, and a sketch of the latter, is presented in Figure 6.

## Current–voltage (*I*–*V*) parameters

The principal characteristics of record solar cells with a spray-grown $Sb_2S_3$ absorber prepared using Sb/S of 1:6 in the precursor solution and seven spray cycles are presented in the first two rows of Table 1. The $V_{OC}$ of about 618 mV is comparable to that obtained in a similar planar device that uses $Sb_2S_3$ prepared by spin coating [12] and lower than that obtained in a cell that uses mesoporous $TiO_2$ and P3HT [3]. The current density

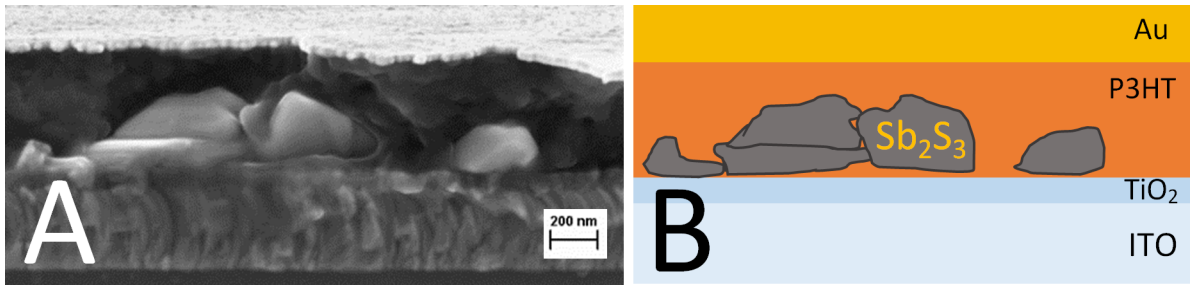


**Figure 6:** A: Cross-sectional SEM image of the glass/ITO/$TiO_2$/$Sb_2S_3$/P3HT/Au solar cell, the 5-cycle $Sb_2S_3$ layer consists of nanoparticles grown by ultrasonic CSP, and B: a corresponding sketch of the solar cell.

**Table 1:** A review of the main parameters ($V_{OC}$, $J_{SC}$, FF, eff.) of solid state solar cells that use $Sb_2S_3$ absorber on top of a planar, fibrous, or mesoporous (mp) $TiO_2$ layer. The technologies for growing $Sb_2S_3$ are denoted as "spray" for chemical spray pyrolysis, CBD for chemical bath deposition, ALD for atomic layer deposition, and "spin-c." for spin coating.

| $TiO_2$ morphology | $Sb_2S_3$ technology | hole conductor(s) | $V_{OC}$, mV | $J_{SC}$, mA/cm$^2$ | FF, % | eff., % | area, cm$^2$ | year | ref. |
|---|---|---|---|---|---|---|---|---|---|
| planar | spray | P3HT | 618 | 6 | 51 | 1.9 | 0.017 | 2016 | this study |
| planar | spray | P3HT | 635 | 5 | 42 | 1.3 | 1 | 2016 | this study |
| planar | spin-c. | P3HT | 616 | 8.1 | 46 | 2.3 | 0.16 | 2015 | [12] |
| mp | spin-c. | PCPDTBT | 596 | 16 | 67 | 6.4 | 0.12 | 2015 | [20] |
| mp | CBD | PCPDTBT–PCBM and PEDOT:PSS | 548 | 14 | 68 | 5.1 | n.a.[a] | 2015 | [18] |
| mp | spin-c. | P3HT | 680 | 9.5 | 52 | 3.4 | n.a.[a] | 2014 | [3] |
| planar | ALD | P3HT and PEDOT:PSS | 666 | 15 | 58 | 5.8 | 0.16 | 2014 | [5] |
| mp | CBD | PCPDTBT | 711 | 16 | 65 | 7.5 | 0.16 | 2014 | [17] |
| mp | CBD | P3HT and PEDOT:PSS | 550 | 13 | 62 | 4.4 | 0.12 | 2014 | [4] |
| planar | CBD | CuSCN | 455 | 12 | 59 | 3.3 | 0.1 | 2013 | [50] |
| planar | CBD | P3HT | 630 | 6.1 | 35 | 1.4 | 0.09 | 2013 | [10] |
| mp | CBD | polyaniline nanobelts | 1100 | 6.9 | 50 | 3.8 | 0.12 | 2013 | [66] |
| nanofiber | CBD | P3HT and PEDOT:PSS | 603 | 9.9 | 39 | 2.3 | 0.04 | 2013 | [11] |
| nanowire | CBD | P3HT and PEDOT:PSS | 500 | 17 | 53 | 4.5 | 0.31 | 2012 | [7] |
| mp | CBD | PCPDTBT-PCBM | 595 | 16 | 66 | 6.3 | 0.16 | 2012 | [9] |
| mp | CBD | P3HT:Au | 626 | 13 | 61 | 4.9 | 0.16 | 2012 | [2] |
| mp | CBD | CuSCN | 584 | 13 | 53 | 4.1 | 0.25 | 2012 | [53] |
| mp | CBD | PCPDTBT | 616 | 15 | 66 | 6.2 | 0.1 | 2011 | [51] |
| mp | CBD | spiro-MeOTAD | 610 | 11 | 48 | 3.1 | 0.49 | 2010 | [16] |
| mp | CBD | CuSCN | 560 | 12 | 58 | 3.7 | 0.54 | 2010 | [52] |
| mp | CBD | CuSCN | 490 | 14 | 49 | 3.4 | 0.15 | 2009 | [15] |

[a]Not available, has not been disclosed in the paper.

of 6 mA·cm$^{-2}$ is on the low side when compared to values above 10 mA·cm$^{-2}$ obtained in devices that rely on the mesoporous $TiO_2$ as the electron conductor, or when compared to a planar cell based on ALD-grown $Sb_2S_3$ [5]. The latter corroborates the benefit of a conformal coating and controlled thickness that is characteristic for ALD. As we have previously shown, the use of ZnO nanorods as the structured substrate and an electron conductor for a spray-grown absorber will provide a gain of the current density up to 2.5 times when compared to a planar device [62,63]. Also, the gap filling by a polymeric hole conductor could be expected to be easier in case vertical nanorods are used instead of porous $TiO_2$ [13,64,65], current densities as high as 17 mA·cm$^{-2}$ has been obtained using vertical nanowires of $TiO_2$ [7]. The search for higher fill factors correlates with the search for the best hole-conductor [51], the highest fill factors have been obtained by using PCPDTBT as the hole conductor (Table 1).

It is known that a higher active area of the solar cells tend to result in lower FF and lower conversion efficiency, attributed to resistance losses [15]. Nevertheless, larger areas are preferred in the long term. In the second row of Table 1, we have presented cell parameters from 1 cm$^2$ area, reflecting the results on the largest area declared so far for $TiO_2$/$Sb_2S_3$/P3HT-type solar cells. Indeed, a loss is present when compared to results from the 0.017 cm$^2$ area solar cell, the FF decreases from 51% to 42%, and the conversion efficiency decreases from 1.9% to 1.3% brought about by an increase in the series resistance from 2.7 Ω cm$^2$ to 30 Ω cm$^2$.

The results reflect that we have reached a decent entry for the studies of $Sb_2S_3$-based solar cells and further development looks very promising, e.g. when varying the hole conductor, or, changing the morphology of the layer responsible for the collection of electrons from planar to nanostructured. In either configuration, flat or structured, the $Sb_2S_3$ is expected to be a continuous absorber layer. Such a further development, a conformal $Sb_2S_3$ layer deposited by ultrasonic spray on top of a nanostructured electron conducting substrate, is presently in progress.

## External quantum efficiency

The external quantum efficiency (EQE) of the glass/ITO/$TiO_2$/$Sb_2S_3$/P3HT/Au solar cell is presented in Figure 7. The gain of EQE is almost linear when increasing the number of cycles from three to nine, which could be expected considering a homogeneous decrease of the transmittance of the glass/ITO/$TiO_2$/$Sb_2S_3$ stack (Supporting Information File 1, Figure S3). The photocurrent edge at around 1.6 eV (775 nm) corresponds well to the absorption edge of the ITO/$TiO_2$/$Sb_2S_3$ stack (Figure 5).

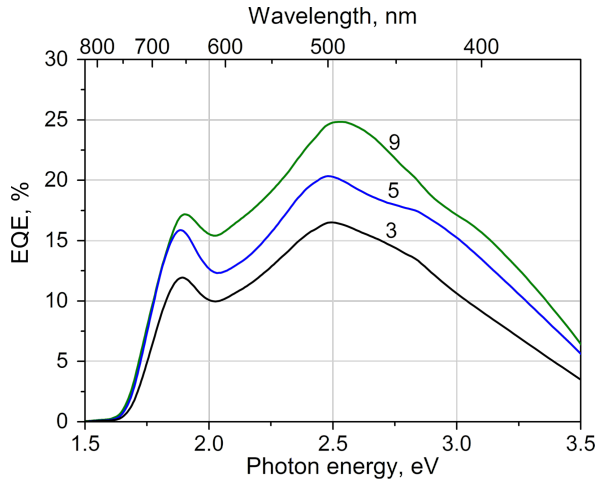


**Figure 7:** External quantum efficiency of glass/ITO/$TiO_2$/$Sb_2S_3$/P3HT/Au solar cells. $Sb_2S_3$ layer was grown by spray pyrolysis of a precursor solution with an Sb/S molar ratio of 1:6 using three, five and nine deposition cycles.

The absorption by P3HT has an onset at 1.9 eV (650 nm) [3,8], and it can be seen that there is a depression of EQE in the absorbing region of P3HT (Figure 7). This was also the observation in the case of a cell based on mesoporous $TiO_2$ but with otherwise similar stack order, the decline was not observed in the case of other hole conductors used such as PCPDTBT [51]. The conclusion is that the photogenerated carriers of different type in the $Sb_2S_3$ absorber should ideally be separated into their respective conductor layers. However, the additional generation of electron–hole pairs in P3HT adversely affects the carrier separation. This filter effect due to absorption in P3HT was overcome by the formation of PCBM electron channels that bridge the hole conductor directly to $TiO_2$ [9,18]. Thus, even for a planar cell, we can expect higher current densities than the 6 mA·cm$^{-2}$ obtained (Table 1) when alternative hole conductors will be exploited.

The short-circuit current $J_{SC}$ and the accompanied increase of the conversion efficiency of the glass/ITO/$TiO_2$/$Sb_2S_3$/P3HT/Au solar cells had their maximum at seven deposition cycles of $Sb_2S_3$, and the results are presented in Table 1. When adding growth cycles, the initial rise in the conversion efficiency is due to the rise in $J_{SC}$ owing to the added volume of $Sb_2S_3$ absorber layer, followed by a decline after seven cycles of $Sb_2S_3$ deposition owing to the drop of FF of the cell (not shown). Such behavior reflects the inevitable need to optimize absorber thickness. The observed decline in the solar cell performance after the optimum absorber thickness is reached has been attributed to losses due to increased recombination in thicker absorber layers [8,10-12]. The optimum thickness herein was reached at seven cycles of $Sb_2S_3$ grown by CSP, which corresponds to a fitted $Sb_2S_3$ thickness of 150 nm (Figure 4B). For comparison, for a planar cell with CBD grown $Sb_2S_3$ the optimum $Sb_2S_3$ thickness was found to be 250 nm [10].

By integrating the EQE spectra of a cell over the A.M1.5 solar spectrum, one can evaluate the current density that a particular cell can ideally produce under standard irradiance. Such an integration product should ideally be comparable to the $J_{SC}$ obtained from the *I*–*V* measurements. For the EQE presented in Figure 7, the integration products for the samples with three, five and nine deposition cycles are 4.1, 5.5 and 6.4 mA/cm$^2$, respectively. This sequence compares fairly well to that obtained from the *I*–*V* measurements: 2.7, 4.4 and 5.7 mA/cm$^2$, respectively. The variance is not alarming at this point of studies and can, in the first approach, be attributed to differences in the measurement conditions. Namely, the EQE measurements were performed under low-intensity monochromatic light to avoid any effects owing to the exposure to white light, as opposed to the *I*–*V* measurements performed under the A.M1.5 conditions. The photoconductivity of the hole conductor, as discussed above, might also contribute to the variance between the integrated EQE and the $J_{SC}$. Table 1 also presents the $J_{SC}$ of 6 mA·cm$^{-2}$ for a cell that had seven cycles of $Sb_2S_3$ deposited, well in line with the $J_{SC}$ values for small area samples with five and nine cycles of $Sb_2S_3$ deposited. Ultimately, the true focus of the present study was to obtain a single phase absorber material by spray technique, and the preliminary test of the performance of the material in a solar cell. Optimization of the current density and spectral response is our next goal.

To sum up, at the moment the major reasons behind the low current densities are likely the lack of a continuous $Sb_2S_3$ layer, and/or a non-optimal choice of the hole conductor, as also emphasized in the previous section. To further boost the current density, one is likely to benefit from the use of a stuctured electron-conducting substrate such as a layer of ZnO nanorods.

## Conclusion

We focused on the optimization of the properties of $Sb_2S_3$ grown by chemical spray pyrolysis (CSP) of an ultrasonically

nebulized precursor solution, and on the application of ultrasonic CSP grown $Sb_2S_3$ as an absorber in a hybrid solar cell.

The use of ultrasonic CSP resulted in the growth of layers that consist of sub-micrometer single-phase crystalline $Sb_2S_3$ particulates that cover the $TiO_2$ substrate homogeneously in case an abundance of the sulfur source (Sb/S molar ratio 1:6 or above) is used in the precursor solution. Secondly, a relatively low content of sulfur source (such as 1:2 or 1:3) in the precursor solution resulted in a heterogeneous composition of the layer – a mixture of phases as well as a visually inhomogeneous coverage – and is thus undesired. Conversely, the abundance of sulfur in the precursor solution, such as 1:6 or 1:9, suppresses the formation of oxide during the growth of the $Sb_2S_3$ film at a substrate temperature of 250 °C in the CSP process in air.

We reported the first results on the use of spray-grown $Sb_2S_3$ in planar $TiO_2/Sb_2S_3$/P3HT solar cells. Low-cost hybrid solar cells with crystalline $Sb_2S_3$ nanoparticulate absorber fabricated by chemical spray pyrolysis in air exhibit a conversion efficiency of 1.3% from an active area of 1 $cm^2$. Further development is in progress, the outlook will be to grow the $Sb_2S_3$ layer onto a structured substrate such as a ZnO nanorod layer.

# Experimental

## Technology of layers and solar cells

We used a commercial 300 nm indium tin oxide (ITO) coated 1.1 mm glass with a sheet resistance of 10 $\Omega \cdot sq.^{-1}$ from Zentrum für Sonnenenergie- und Wasserstoff-Forschung Baden-Württemberg (ZSW).

The $TiO_2$ layer was deposited by ultrasonic CSP onto the ITO using a spray solution of titanium(IV) isopropoxide precursor (0.1 $mol \cdot L^{-1}$) and acetylacetonate (both solutions from Merck Schudart OHG) at a molar ratio of 1:4 dissolved in ethanol [67,68], using a substrate temperature of 340 °C, followed by annealing at 450 °C for 30 min in air to assure the formation of the anatase phase. The thickness of the $TiO_2$ layer remained between 80 and 100 nm as estimated from scanning electron microscopy (SEM) images.

For growing $Sb_2S_3$, the precursor solution was prepared inside a glove box with controlled humidity (less than 14 ppm). The solution contained $SbCl_3$ (with $Sb^{3+}$ concentration of 15 mmol/L) and $SC(NH_2)_2$ precursors at a molar ratio of 1:$x$ ($x$ = 2, 3, 6, 9) in methanol as the solvent. $SbCl_3$ was purchased from Sigma-Aldrich (≥99.0%, p.a.) and $SC(NH_2)_2$ from Merck (≥99.0%, p.a.). The precursor solution was ultrasonically nebulized at 1.5 MHz and the resulting aerosol was guided onto the $TiO_2$ substrate by using compressed air as the carrier gas at a flow rate of 5 $L \cdot min^{-1}$.

The deposition temperature 250 °C was chosen by relying on the fact that the $SbCl_3$ and thiourea (tu) form the $Sb(tu)_2Cl_3$ complex compound in methanol and undergo thermal decomposition slightly above 200 °C according to a TG-DTA study [69]. This is characteristic for different metal chloride–thiourea complexes such as $In(tu)_3Cl_3$ [25,70], $Sn(tu)_2Cl_2$ [28] and CuCl–tu complexes with different stoichiometry [71]. To generalize, not only chlorides but also the $SbI_3$ complex with tu, $Sb(tu)_3I_3$, decompose at around 200 °C [72]. Also, our preparatory study on the use of $SbCl_3$ and tu for growing $Sb_2S_3$ films by spray pyrolysis [23] indicated the use of 250 °C as a suitable growth temperature according to thermal analysis of the $Sb(tu)_2Cl_3$ with tartaric acid as the complexing agent. Besides the requirement stemming from the use of the precursor, temperatures of above 225 °C are required for the crystallization of $Sb_2S_3$ [44].

Samples were prepared with the number of $Sb_2S_3$ growth cycles ranging from three up to 18. One deposition cycle accounts for a condition when the spray nozzle has passed twice over the substrate with an area of about 20 $cm^2$ in 3 min, using 12 mL of solution. Thus, the solution consumption rate was around 0.2 $mL \cdot min^{-1} \cdot cm^{-2}$.

To apply the P3HT as the hole conductor, the glass/ITO/$TiO_2$/$Sb_2S_3$ stack was immersed into a room temperature solution of 2 wt % regioregular poly(3-hexylthiophene-2,5-diyl), by Sigma-Aldrich, in chlorobenzene, followed by drying of the sample at 50 °C for 10 min in air and further drying of the sample in vacuum ($4 \cdot 10^{-6}$ Torr) at 170 °C for 5 min. The thickness of P3HT layer remained below 400 nm, as estimated from SEM images.

The Au layer was deposited onto the P3HT by thermal evaporation of metallic Au for 10 min under a pressure of $2 \cdot 10^{-6}$ Torr through a metal mask with a number of holes that had an area of 1.7 $mm^2$ each. Alternatively, larger contacts of 1 $cm^2$ were physically isolated by scribing the solar cell. The thickness of the Au layer was around 50 nm.

For light soaking of the glass/ITO/$TiO_2$/$Sb_2S_3$/P3HT/Au solar cell from the glass side we used a 300 W quartz–tungsten–halogen (QTH) lamp at a distance that resulted in 100 $mW \cdot cm^{-2}$ irradiance on the solar cell. The light soaking was carried out under open-circuit conditions for a minimum of 20 min, in a stream of ambient air provided by a cooling fan, until maximum conversion efficiency was reached.

## Characterization of layers and solar cells

For structural characterization, Raman spectra were measured in a backscattering configuration at room temperature using a confocal micro-Raman spectrometer HORIBA Jobin Yvon

Model HR 800. The excitation radiation wavelength was 532 nm, the power density was sufficiently low without excessive heating the sample area of ca 100 μm$^2$, during 100 s of data acquisition there were no signs of thermal alteration of the sample.

The analysis of the elemental composition of the films was performed by energy dispersive X-ray (EDX) analysis using Bruker spectrometer with ESPRIT 1.8 system at the Zeiss HR FESEM Ultra 55 scanning electron microscope (SEM) operating at an accelerating voltage of 10 kV. The same SEM system was used for visualization of the morphology of the layers and of the cross-section of the solar cells at an electron beam accelerating voltage of 4 kV.

Current–voltage scans of the solar cells were used to obtain the principal characteristics of the solar cells: voltage under open circuit conditions ($V_{OC}$), current density under short-circuit conditions ($J_{SC}$), the fill factor (FF) and the conversion efficiency (η) under AM1.5 standard conditions. The standard conditions were simulated by using the illumination of a 300 W quartz–tungsten–halogen (QTH) lamp at a distance that was adjusted by using a calibrated silicon solar cell as the detector. The active area of the solar cells is defined by the back contact area of 1.7 mm$^2$ or 1 cm$^2$.

The total transmittance spectra of the layers and solar cells were measured in the wavelength range of 300–1500 nm on a Jasco V-670 spectrophotometer equipped with an integrating sphere. The absorption coefficient was calculated as $\alpha = d^{-1} \cdot \ln(T^{-1})$, where $d$ is the layer thickness and $T$ is the total transmittance, i.e. the sum of diffuse and specular transmittance. A Tauc plot was used to determine the bandgap of $Sb_2S_3$ layers assuming a direct optical transition.

The external quantum efficiency (EQE) of the solar cells was measured in the range of 350–1000 nm on a Newport Oriel kit that contains a 300 W Xe lamp, high-resolution monochromator (Cornerstone 260), digital dual-channel lock-in detector (Merlin), and a calibrated silicon reference detector. The Xe lamp is a light source that simulates the conventional AM1.5 spectrum for testing solar cells. The dispersed light from the Xe lamp (incident on the solar cell as monochromatic light) was optically chopped at 30 Hz. The EQE is defined as the number of collected charge carriers per incident photon. The EQE is a unitless characteristic (EQE < 1) given by $EQE(\lambda) = (hc/q\lambda) \times J_{SC}(\lambda)/P(\lambda)$, where $J_{SC}(\lambda)$ (A·m$^{-2}$) is the spectrally resolved short-circuit current of the solar cell, $P(\lambda)$ (W·m$^{-2}$) is the calibrated light intensity incident on the solar cell as function of wavelength λ, and $hc/q\lambda$ is the energy (eV) of the incident photon. The samples were covered with a black cloth during the EQE measurements to avoid any photoactive effects in the component layers due to the ambient white light, only the low-intensity monochromatic light was incident on the cell. To validate the EQE result, the integrated product the EQE(λ) and solar irradiance $I_{AM1.5}(\lambda)$ was calculated by using the online tool Open Photovoltaics Analysis Platform, and compared with the $J_{SC}$ obtained from the current–voltage scan.

## Supporting Information

Additional SEM images, optical transmittance spectra, and current–voltage curves.

### Supporting Information File 1

Additional experimental data.
[http://www.beilstein-journals.org/bjnano/content/supplementary/2190-4286-7-158-S1.pdf]

## Acknowledgements

The work is financially supported by Estonian Ministry of Education and Research (IUT19-4), Estonian Science Foundation (ETF9081), and by the European Regional Development Fund through the project TK141 “Advanced materials and high-technology devices for energy recuperation systems“.

## References

1. Lee, D. U.; Woo Pak, S.; Gook Cho, S.; Kyu Kim, E.; Seok, S. I. *Appl. Phys. Lett.* **2013,** *103,* 023901. doi:10.1063/1.4813272
2. Lim, C.-S.; Im, S. H.; Kim, H.-j.; Chang, J. A.; Lee, Y. H.; Seok, S. I. *Phys. Chem. Chem. Phys.* **2012,** *14,* 3622. doi:10.1039/C2CP23650H
3. Lindblad, R.; Cappel, U. B.; O'Mahony, F. T. F.; Siegbahn, H.; Johansson, E. M. J.; Haque, S. A.; Rensmo, H. *Phys. Chem. Chem. Phys.* **2014,** *16,* 17099. doi:10.1039/C4CP01581A
4. Kim, J. K.; Veerappan, G.; Heo, N.; Wang, D. H.; Park, J. H. *J. Phys. Chem. C* **2014,** *118,* 22672–22677. doi:10.1021/jp507652r
5. Kim, D.-H.; Lee, S.-J.; Park, M. S.; Kang, J.-K.; Heo, J. H.; Im, S. H.; Sung, S.-J. *Nanoscale* **2014,** *6,* 14549–14554. doi:10.1039/C4NR04148H
6. Nikolakopoulou, A.; Raptis, D.; Dracopoulos, V.; Sygellou, L.; Andrikopoulos, K. S.; Lianos, P. *J. Power Sources* **2015,** *278,* 404–410. doi:10.1016/j.jpowsour.2014.12.067
7. Cardoso, J. C.; Grimes, C. A.; Feng, X.; Zhang, X.; Komarneni, S.; Zanoni, M. V. B.; Bao, N. *Chem. Commun.* **2012,** *48,* 2818. doi:10.1039/c2cc17573h
8. Chang, J. A.; Rhee, J. H.; Im, S. H.; Lee, Y. H.; Kim, H.-j.; Seok, S. I.; Nazeeruddin, Md. K.; Gratzel, M. *Nano Lett.* **2010,** *10,* 2609–2612. doi:10.1021/nl101322h
9. Chang, J. A.; Im, S. H.; Lee, Y. H.; Kim, H.-j.; Lim, C.-S.; Heo, J. H.; Seok, S. I. *Nano Lett.* **2012,** *12,* 1863–1867. doi:10.1021/nl204224v
10. Reeja-Jayan, B.; Manthiram, A. *RSC Adv.* **2013,** *3,* 5412. doi:10.1039/c3ra23055d

11. Zhong, J.; Zhang, X.; Zheng, Y.; Zheng, M.; Wen, M.; Wu, S.; Gao, J.; Gao, X.; Liu, J.-M.; Zhao, H. *ACS Appl. Mater. Interfaces* **2013,** *5,* 8345–8350. doi:10.1021/am401273r
12. You, M. S.; Lim, C.-S.; Kwon, D. H.; Heo, J. H.; Im, S. H.; Chae, K. J. *Org. Electron.* **2015,** *21,* 155–159. doi:10.1016/j.orgel.2015.02.015
13. Wright, M.; Uddin, A. *Sol. Energy Mater. Sol. Cells* **2012,** *107,* 87–111. doi:10.1016/j.solmat.2012.07.006
14. Grätzel, C.; Zakeeruddin, S. M. *Mater. Today* **2013,** *16,* 11–18. doi:10.1016/j.mattod.2013.01.020
15. Itzhaik, Y.; Niitsoo, O.; Page, M.; Hodes, G. *J. Phys. Chem. C* **2009,** *113,* 4254–4256. doi:10.1021/jp900302b
16. Moon, S.-J.; Itzhaik, Y.; Yum, J.-H.; Zakeeruddin, S. M.; Hodes, G.; Grätzel, M. *J. Phys. Chem. Lett.* **2010,** *1,* 1524–1527. doi:10.1021/jz100308q
17. Choi, Y. C.; Lee, D. U.; Noh, J. H.; Kim, E. K.; Seok, S. I. *Adv. Funct. Mater.* **2014,** *24,* 3587–3592. doi:10.1002/adfm.201304238
18. Gödel, K. C.; Choi, Y. C.; Roose, B.; Sadhanala, A.; Snaith, H. J.; Seok, S. I.; Steiner, U.; Pathak, S. K. *Chem. Commun.* **2015,** *51,* 8640–8643. doi:10.1039/C5CC01966D
19. Wedemeyer, H.; Michels, J.; Chmielowski, R.; Bourdais, S.; Muto, T.; Sugiura, M.; Dennler, G.; Bachmann, J. *Energy Environ. Sci.* **2013,** *6,* 67–71. doi:10.1039/C2EE23205G
20. Choi, Y. C.; Seok, S. I. *Adv. Funct. Mater.* **2015,** *25,* 2892–2898. doi:10.1002/adfm.201500296
21. Gadakh, S. R.; Bhosale, C. H. *Mater. Chem. Phys.* **2003,** *78,* 367–371. doi:10.1016/S0254-0584(02)00101-3
22. Rajpure, K. Y.; Bhosale, C. H. *Mater. Chem. Phys.* **2002,** *73,* 6–12. doi:10.1016/S0254-0584(01)00350-9
23. Kriisa, M.; Krunks, M.; Oja Acik, I.; Kärber, E.; Mikli, V. *Mater. Sci. Semicond. Process.* **2015,** *40,* 867–872. doi:10.1016/j.mssp.2015.07.049
24. Rajpure, K. Y.; Bhosale, C. H. *J. Phys. Chem. Solids* **2000,** *61,* 561–568. doi:10.1016/S0022-3697(99)00240-1
25. Otto, K.; Oja Acik, I.; Tõnsuaadu, K.; Mere, A.; Krunks, M. *J. Therm. Anal. Calorim.* **2011,** *105,* 615–623. doi:10.1007/s10973-011-1507-8
26. Otto, K.; Katerski, A.; Mere, A.; Volobujeva, O.; Krunks, M. *Thin Solid Films* **2011,** *519,* 3055–3060. doi:10.1016/j.tsf.2010.12.027
27. Dedova, T.; Krunks, M.; Gromyko, I.; Mikli, V.; Sildos, I.; Utt, K.; Unt, T. *Phys. Status Solidi A* **2014,** *211,* 514–521. doi:10.1002/pssa.201300215
28. Polivtseva, S.; Oja Acik, I.; Krunks, M.; Tõnsuaadu, K.; Mere, A. *J. Therm. Anal. Calorim.* **2015,** *121,* 177–185. doi:10.1007/s10973-015-4580-6
29. Polivtseva, S.; Oja Acik, I.; Katerski, A.; Mere, A.; Mikli, V.; Krunks, M. *Energy Procedia* **2014,** *60,* 156–165. doi:10.1016/j.egypro.2014.12.358
30. Rajpure, K. Y.; Bhosale, C. H. *Mater. Chem. Phys.* **2000,** *63,* 263–269. doi:10.1016/S0254-0584(99)00233-3
31. Shen, J.; Wang, H.; Zhou, Y.; Ye, N.; Li, G.; Wang, L. *RSC Adv.* **2012,** *2,* 9173. doi:10.1039/c2ra20962d
32. Avila, L. F.; Pradel, A.; Ribeiro, S. J. L.; Messaddeq, Y.; Nalin, M. *Physica B* **2015,** *458,* 67–72. doi:10.1016/j.physb.2014.11.011
33. Makreski, P.; Petruševski, G.; Ugarković, S.; Jovanovski, G. *Vib. Spectrosc.* **2013,** *68,* 177–182. doi:10.1016/j.vibspec.2013.07.007
34. Kadıoğlu, Y. K.; Üstündağ, Z.; Deniz, K.; Yenikaya, C.; Erdoğan, Y. *Instrum. Sci. Technol.* **2009,** *37,* 683–696. doi:10.1080/10739140903252956
35. Zeng, D. W.; Xie, C. S.; Zhu, B. L.; Song, W. L. *Mater. Lett.* **2004,** *58,* 312–315. doi:10.1016/S0167-577X(03)00476-2
36. Cody, C. A.; DiCarlo, L.; Darlington, R. K. *Inorg. Chem.* **1979,** *18,* 1572–1576. doi:10.1021/ic50196a036
37. Panasenko, A. E.; Zemnukhova, L. A.; Ignat'eva, L. N.; Kaidalova, T. A.; Kuznetsov, S. I.; Polyakova, N. V.; Marchenko, Yu. V. *Inorg. Mater.* **2009,** *45,* 402–408. doi:10.1134/S002016850904013X
38. Gilliam, S. J.; Jensen, J. O.; Banerjee, A.; Zeroka, D.; Kirkby, S. J.; Merrow, C. N. *Spectrochim. Acta, Part A* **2004,** *60,* 425–434. doi:10.1016/S1386-1425(03)00245-2
39. Ma, X.; Zhang, Z.; Li, X.; Du, Y.; Xu, F.; Qian, Y. *J. Solid State Chem.* **2004,** *177,* 3824–3829. doi:10.1016/j.jssc.2004.07.005
40. Ito, S.; Tanaka, S.; Manabe, K.; Nishino, H. *J. Phys. Chem. C* **2014,** *118,* 16995–17000. doi:10.1021/jp500449z
41. Ito, S.; Tsujimoto, K.; Nguyen, D.-C.; Manabe, K.; Nishino, H. *Int. J. Hydrogen Energy* **2013,** *38,* 16749–16754. doi:10.1016/j.ijhydene.2013.02.069
42. Ge, S.; Wang, Q.; Shao, Q.; Zhao, Y.; Yang, X.; Wang, X. *Appl. Surf. Sci.* **2011,** *257,* 3657–3665. doi:10.1016/j.apsusc.2010.11.101
43. Kim, H. W.; Kim, H. S.; Na, H. G.; Yang, J. C.; Kebede, M. A.; Lee, C. *Ceram. Int.* **2011,** *37,* 593–598. doi:10.1016/j.ceramint.2010.09.050
44. Krishnan, B.; Arato, A.; Cardenas, E.; Das Roy, T. K.; Castillo, G. A. *Appl. Surf. Sci.* **2008,** *254,* 3200–3206. doi:10.1016/j.apsusc.2007.10.098
45. Versavel, M. Y.; Haber, J. A. *Thin Solid Films* **2007,** *515,* 7171–7176. doi:10.1016/j.tsf.2007.03.043
46. Mane, R. S.; Lokhande, C. D. *Mater. Chem. Phys.* **2003,** *78,* 385–392. doi:10.1016/S0254-0584(02)00155-4
47. Savadogo, O.; Mandal, K. C. *Sol. Energy Mater. Sol. Cells* **1992,** *26,* 117–136. doi:10.1016/0927-0248(92)90131-8
48. Boughalmi, R.; Boukhachem, A.; Kahlaoui, M.; Maghraoui, H.; Amlouk, M. *Mater. Sci. Semicond. Process.* **2014,** *26,* 593–602. doi:10.1016/j.mssp.2014.05.059
49. Carey, J. J.; Allen, J. P.; Scanlon, D. O.; Watson, G. W. *J. Solid State Chem.* **2014,** *213,* 116–125. doi:10.1016/j.jssc.2014.02.014
50. Christians, J. A.; Kamat, P. V. *ACS Nano* **2013,** *7,* 7967–7974. doi:10.1021/nn403058f
51. Im, S. H.; Lim, C.-S.; Chang, J. A.; Lee, Y. H.; Maiti, N.; Kim, H.-J.; Nazeeruddin, Md. K.; Grätzel, M.; Seok, S. I. *Nano Lett.* **2011,** *11,* 4789–4793. doi:10.1021/nl2026184
52. Nezu, S.; Larramona, G.; Choné, C.; Jacob, A.; Delatouche, B.; Péré, D.; Moisan, C. *J. Phys. Chem. C* **2010,** *114,* 6854–6859. doi:10.1021/jp100401e
53. Tsujimoto, K.; Nguyen, D.-C.; Ito, S.; Nishino, H.; Matsuyoshi, H.; Konno, A.; Asoka Kumara, G. R.; Tennakone, K. *J. Phys. Chem. C* **2012,** *116,* 13465. doi:10.1021/jp208937j
54. Mane, R. S.; Lokhande, C. D. *Mater. Chem. Phys.* **2003,** *82,* 347–354. doi:10.1016/S0254-0584(03)00271-2
55. Barreau, N.; Marsillac, S.; Albertini, D.; Bernede, J. C. *Thin Solid Films* **2002,** *403–404,* 331–334. doi:10.1016/S0040-6090(01)01512-7
56. Barreau, N. *Sol. Energy* **2009,** *83,* 363–371. doi:10.1016/j.solener.2008.08.008
57. Chen, G.-Y.; Zhang, W.-X.; Xu, A.-W. *Mater. Chem. Phys.* **2010,** *123,* 236–240. doi:10.1016/j.matchemphys.2010.04.002
58. Kavinchan, J.; Thongtem, T.; Thongtem, S. *Mater. Lett.* **2010,** *64,* 2388–2391. doi:10.1016/j.matlet.2010.07.075
59. Zhu, Q.-A.; Gong, M.; Zhang, C.; Yong, G.-b.; Xiang, S. *J. Cryst. Growth* **2009,** *311,* 3651–3655. doi:10.1016/j.jcrysgro.2009.04.024

60. Mahanty, S.; Merino, J. M.; León, M. *J. Vac. Sci. Technol., A* **1997,** *15,* 3060. doi:10.1116/1.580847
61. Kuwabara, T.; Yano, K.; Yamaguchi, T.; Taima, T.; Takahashi, K.; Son, D.; Marumoto, K. *J. Phys. Chem. C* **2015,** *119,* 5274–5280. doi:10.1021/jp509879v
62. Kärber, E.; Abass, A.; Khelifi, S.; Burgelman, M.; Katerski, A.; Krunks, M. *Sol. Energy* **2013,** *91,* 48–58. doi:10.1016/j.solener.2013.01.020
63. Krunks, M.; Kärber, E.; Katerski, A.; Otto, K.; Oja Acik, I.; Dedova, T.; Mere, A. *Sol. Energy Mater. Sol. Cells* **2010,** *94,* 1191–1195. doi:10.1016/j.solmat.2010.02.036
64. Yang, L.; Cappel, U. B.; Unger, E. L.; Karlsson, M.; Karlsson, K. M.; Gabrielsson, E.; Sun, L.; Boschloo, G.; Hagfeldt, A.; Johansson, E. M. J. *Phys. Chem. Chem. Phys.* **2012,** *14,* 779–789. doi:10.1039/C1CP23031J
65. Hsu, C.-Y.; Chen, Y.-C.; Lin, R. Y.-Y.; Ho, K.-C.; Lin, J. T. *Phys. Chem. Chem. Phys.* **2012,** *14,* 14099–14109. doi:10.1039/c2cp41326d
66. Lan, Z.; Zhang, X.; Wu, J.; Lin, J.; Huang, M.; Zhao, H. *Electrochim. Acta* **2013,** *108,* 337–342. doi:10.1016/j.electacta.2013.06.121
67. Oja, I.; Mere, A.; Krunks, M.; Nisumaa, R.; Solterbeck, C.-H.; Es-Souni, M. *Thin Solid Films* **2006,** *515,* 674–677. doi:10.1016/j.tsf.2005.12.243
68. Oja Acik, I.; Junolainen, A.; Mikli, V.; Danilson, M.; Krunks, M. *Appl. Surf. Sci.* **2009,** *256,* 1391–1394. doi:10.1016/j.apsusc.2009.08.101
69. Ozturk, I. I.; Kourkoumelis, N.; Hadjikakou, S. K.; Manos, M. J.; Tasiopoulos, A. J.; Butler, I. S.; Balzarini, J.; Hadjiliadis, N. *J. Coord. Chem.* **2011,** *64,* 3859–3871. doi:10.1080/00958972.2011.633603
70. Otto, K.; Bombicz, P.; Madarász, J.; Oja Acik, I.; Krunks, M.; Pokol, G. *J. Therm. Anal. Calorim.* **2011,** *105,* 83–91. doi:10.1007/s10973-011-1524-7
71. Madarász, J.; Krunks, M.; Niinistö, L.; Pokol, G. *J. Therm. Anal. Calorim.* **2015,** *120,* 189–199. doi:10.1007/s10973-015-4481-8
72. Zhong, G. Q.; Luan, S. R.; Wang, P.; Guo, Y. C.; Chen, Y. R.; Jia, Y. Q. *J. Therm. Anal. Calorim.* **2006,** *86,* 775–781. doi:10.1007/s10973-005-6959-2

## License and Terms

BEILSTEIN JOURNAL OF NANOTECHNOLOGY

# Tandem polymer solar cells: simulation and optimization through a multiscale scheme

Fanan Wei[1], Ligang Yao[1], Fei Lan[2], Guangyong Li[*2] and Lianqing Liu[*3,4]

Full Research Paper

Open Access

Address:
[1]School of Mechanical Engineering and Automation, Fuzhou University, Fuzhou, 350116, China, [2]Department of Electrical and Computer Engineering, University of Pittsburgh, Pittsburgh, PA, USA, [3]State Key Laboratory of Robotics, Shenyang Institute of Automation, CAS, Shenyang, China, and [4]University of Chinese Academy of Sciences, Beijing, China

Email:
Guangyong Li[*] - gul6@pitt.edu; Lianqing Liu[*] - lqliu@sia.cn

* Corresponding author

Keywords:
genetic algorithm; Monte Carlo simulation; simplex searching; tandem polymer solar cells

*Beilstein J. Nanotechnol.* **2017,** *8,* 123–133.
doi:10.3762/bjnano.8.13

Received: 12 April 2016
Accepted: 15 December 2016
Published: 12 January 2017

This article is part of the Thematic Series "Nanostructures for sensors, electronics, energy and environment III".

Guest Editor: N. Motta



## Abstract

In this paper, polymer solar cells with a tandem structure were investigated and optimized using a multiscale simulation scheme. In the proposed multiscale simulation, multiple aspects – optical calculation, mesoscale simulation, device scale simulation and optimal power conversion efficiency searching modules – were studied together to give an optimal result. Through the simulation work, dependencies of device performance on the tandem structures were clarified by tuning the thickness, donor/acceptor weight ratio as well as the donor–acceptor distribution in both active layers of the two sub-cells. Finally, employing searching algorithms, we optimized the power conversion efficiency of the tandem polymer solar cells and located the optimal device structure parameters. With the proposed multiscale simulation strategy, poly(3-hexylthiophene)/phenyl-C61-butyric acid methyl ester and (poly[2,6-(4,4-bis-(2-ethylhexyl)-4*H*-cyclopenta[2,1-*b*;3,4-*b*]dithiophene)-alt-4,7-(2,1,3-benzothiadiazole)])/phenyl-C61-butyric acid methyl ester based tandem solar cells were simulated and optimized as an example. Two configurations with different sub-cell sequences in the tandem photovoltaic device were tested and compared. The comparison of the simulation results between the two configurations demonstrated that the balance between the two sub-cells is of critical importance for tandem organic photovoltaics to achieve high performance. Consistency between the optimization results and the reported experimental results proved the effectiveness of the proposed simulation scheme.

## Introduction

Polymer solar cells, also known as organic solar cells, have been attracting a wealth of attention due to their great potential as an alternative to the presently extensively used inorganic solar cells. However, the wide application of polymer solar cells is still highly restricted by their poor device performance (especially, the low power conversion efficiency (PCE)) when com-

pared with their inorganic counterparts. Therefore, great efforts have been devoted to improving the performance of polymer photovoltaics. To fulfil this goal, various methods, including annealing [1], active materials modification [2] and device structures tuning [3,4], were employed and explored. According to the reports by different research groups, exciting achievements have been witnessed in the past decade [5], among which tandem structures [6-8], created by stacking two single organic solar cells together, have been demonstrated to be one of the most effective solutions.

Due to the unavoidable mismatch between the absorption spectrum of active materials and that of the sunlight, a large portion of the sunlight energy will be lost in organic photovoltaics when a single active material is employed. Thus, as illustrated in Figure 1, the concept of a tandem structure provides a promising solution to this issue by expanding the absorption spectrum using two types of active materials with different band gaps. More and more works [9-11] verify that tandem or triple polymer solar cells can greatly enhance the PCE as compared to single cell devices. However, thus far, structures of tandem polymer solar cells have not been intensively studied given the complexity, and there is still a large margin for the improvement of such devices.

To date, a significant amount of trial-and-error experimental work [7,12] has been conducted to refine tandem device structures, however, experimental work is tedious and far from efficient. Considering the strong optical and electrical coupling between the two sub-cells in tandem photovoltaics, to optimize device performance, it is essential to tune the thickness of both active layers. Furthermore, existing evidence suggests that the distribution of donor/acceptor (D/A) in the active layer is critical in determining the final device performance [1,6]. What also must be considered is that the weight ratio between donor and acceptor is another important factor impacting the PCE of tandem polymer solar cells [12]. Taking all these factors into consideration, the optimization of a tandem structure using trail-and-error experiments can be not only of high cost, but sometimes futile.

Contrary to trail-and-error experiments, simulation is a much more cost-effective tool to tackle this problem. Considering the heavy coupling between the two sub-cells, the simulation and optimization of tandem solar cells are still of great challenge. Even so, some pioneering works on this issue have already been reported [13-19]. Optical coupling between the two sub-cells was investigated and the possible maximum current density through the tandem device was evaluated [16-19]. It was found that the current density cannot be further improved until the photon absorption in the two sub-cells is balanced [16-18]. Some work has been devoted to evaluate the balance of carrier mobility in the two sub-cells [17,18] and even the device performance was estimated according to *J*–*V* curve characteristics constructed through simulations. However, we found that most of the simulation work was focused on tuning the thickness of active layers [20], while efforts were rarely devoted to the optimization of the internal material distribution and D/A weight ratio in the active layers of tandem organic solar cells. The latter, as demonstrated in this work, is critical for optimizing the performance of tandem polymer cells.

In this paper, by taking all the impacting factors into consideration, we mimic the photocurrent generation process and subsequently optimize the device structures in tandem polymer solar cells with poly(3-hexylthiophene)/phenyl-C61-butyric acid methyl ester (P3HT/PCBM) and (poly[2,6-(4,4-bis-(2-ethylhexyl)-4*H*-cyclopenta[2,1-*b*;3,4-*b*]dithiophene)-alt-4,7-(2,1,3-benzothiadiazole)])/PCBM (PCPDTBT/PCBM). The *J*–*V* curves of the device were acquired through a multiscale simulation scheme. Then performance indices were evaluated and related to the thickness, inner morphologies and the weight ratio

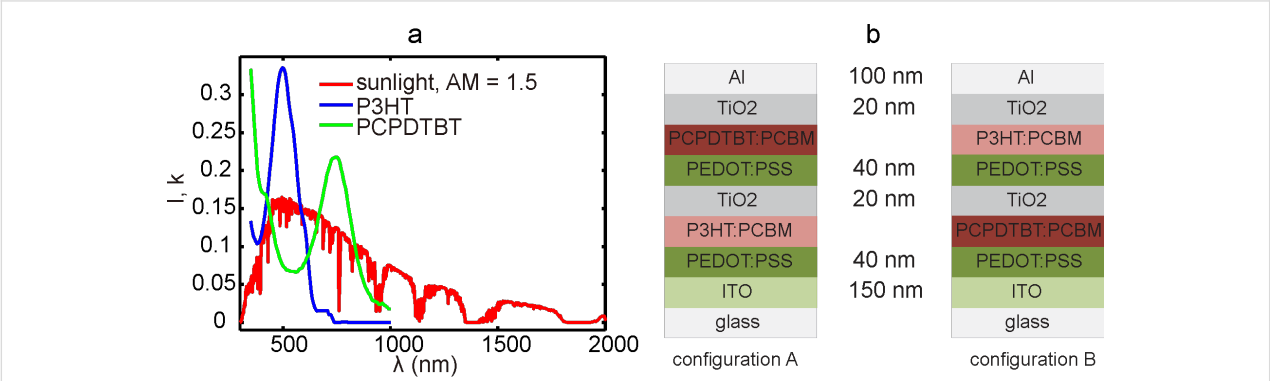


**Figure 1:** (a) Spectrum of sunlight and different active materials used in tandem organic solar cells. (b) The two configurations (configuration A: left; configuration B: right) of tandem polymer solar cells investigated in this paper.

of the active layers. Finally, using a simplex searching algorithm and genetic algorithm (GA), a global optimal PCE value was found and the corresponding device parameters were obtained. In order to prove the viability of our proposed simulation approach, two different configurations of the tandem devices, as shown in Figure 1b, were both tested and compared with each other.

## Multiscale Simulation of Tandem Polymer Solar Cells

To simulate the photocurrent generation process and subsequently evaluate the performance indices for tandem photovoltaics, we designed and realized a simulation scheme and denoted it as multiscale simulation. As illustrated in Figure 2, the schematic of the proposed multiscale simulation was divided into four parts: optical calculation module, mesoscale simulation module, device scale simulation module, and finally, optimal PCE searching module.

### Optical decoupling in optical calculation module

In tandem polymer solar cells, the two stacked sub-cells are optically highly coupled. Thus, an optical decoupling process is required before any evaluation of device performance.

In the optical calculation part developed here, the complex refractive index of the blend with varied D/A weight ratios (2:1, 3:2, 1:1, 2:3 and 1:2) in the P3HT/PCBM layer was calculated using bulk effective medium method [21]. The optical parameters for pure P3HT and PCBM were provided by McGehee et al. [22]. In the reported experiments [8,23,24], the D/A weight ratio of PCPDTBT/PCBM in polymer solar cells has been varied between 2:1 and 1:4. Due to the lack of optical index for pure PCPDTBT, the weight ratio of PCPDTBT/PCBM was fixed to be a reasonable value of 1:2 in the following simulation work. For all other materials besides the active materials, the complex refractive indices were acquired from [25]. Then, with the optical indices of all the materials in the system known, optical transfer matrix theory [26] was adopted to evaluate the photon absorption efficiency in active layers of the two sub-cells. By conducting the calculation under varied active layer thicknesses (from 1 nm to 400 nm with an interval of 1 nm) and weight ratios, the dependencies of the photon absorption efficiency on the device structures were clarified. Meanwhile, the thickness of the other layers in the device was fixed to the values shown in Figure 1b. Herein, the influence of the inner distribution of the blended materials were ignored because, to our best knowledge, there is no strong evidence to support the contribution of internal morphology to the photon absorption in active layers.

### Bridging macroscale and microscale through mesoscale simulation

As discussed above, the distribution of material at the microscale also affects device performance. To quantize this affect, we need to bridge the gap between microscale and macroscale in the simulation system. In our previous work [27], a mesoscale simulation, i.e., a Monte Carlo (MC) simulation, has been

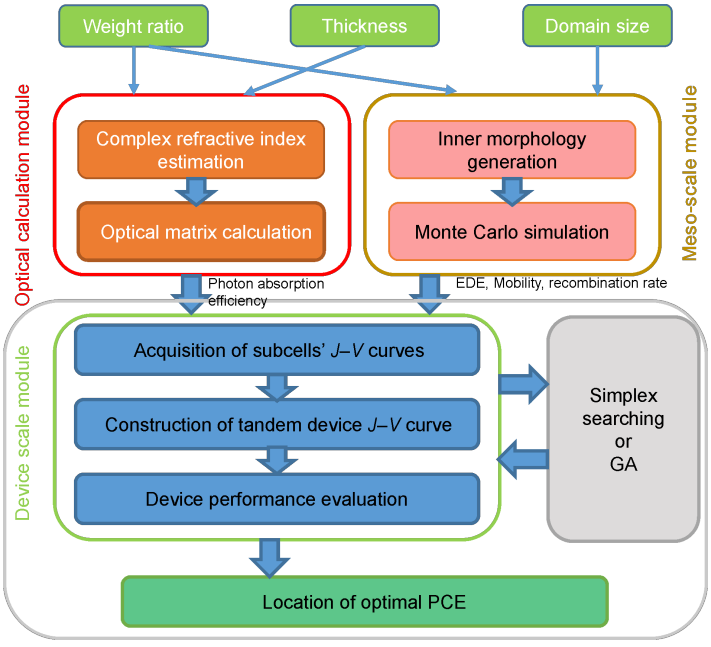


**Figure 2:** Schematic of the proposed simulation strategy for investigation and optimization of organic solar cells.

developed to meet this requirement. At the mesoscale, with the weight ratio and average domain size as input parameters, MC simulations were carried out to compute the effective charge carrier mobility and recombination rate. Firstly, the internal morphology in active layers was generated through a simulated annealing method [27]. In the simulated annealing method, the Ising model is adopted to generate the morphology with desired donor–acceptor distribution. Details of the morphology generation process is available in Supporting Information File 1. The simulated morphology agrees well with that acquired from actual experiments (Supporting Information File 1, Figure S1). Then, the distribution of donor and acceptor materials in the blend was quantized using the average domain size ($a$) defined in [27]. A series of morphologies with domain size ranging from 6 nm to 20 nm were prepared. The interval of domain size between adjacent morphologies was 2 nm. The lattice size in the generated morphologies was set to be 3 nm; and the size of the generated morphologies was 180 × 180 × 90 nm. The thickness of the active layers was fixed to be 90 nm in this work for simplification. Using the generated morphologies, generation, transport, recombination and extraction of charge carriers were mimicked and recorded in the MC simulation. The MC simulation was realized through the first reaction method (FRM) (the flow chart of FRM is presented in Supporting Information File 1, Figure S2). The details of FRM are illustrated in Supporting Information File 1. Based on the simulation of exciton transportation, dissociation and extinction processes, exciton dissociation efficiency (EDE, defined in Equation 1) was obtained, which is crucial for the calculation of charge carrier generation rate in the active layers. Electron and hole mobility was related to the average domain size and the electric field in the active layers. Since charge carrier recombination is the main cause of energy loss in organic solar cells, both the bimolecular and monomolecular recombination rate were evaluated (defined as in Equation 2 and Equation 3) and related to the domain size and electric field. A monomolecular recombination event was defined as the recombination between one free carrier and one carrier stuck in traps or dead ends in the active layer, while other recombination events were classified as bimolecular. Then, we varied the D/A weight ratios in the P3HT/PCBM active layer and repeated the mesoscale simulations. For more details of the MC simulation adopted here, please refer to [27]. Some of the parameters used in the MC simulation are presented in Table 1 (see below).

$$EDE = \frac{n_{\text{ex\_diss}}}{n_{\text{exciton}}} \tag{1}$$

where, $n_{\text{ex\_diss}}$ and $n_{\text{exciton}}$ are the number of dissociated excitons and the total number of generated excitons in the simulation, respectively. The recombination rates are

$$\gamma_{\text{bi}} = \frac{n_{\text{bi}}}{Vtnp} \tag{2}$$

$$\gamma_{\text{mo}} = \frac{n_{\text{mo}}}{Vt\max(n, p)} \tag{3}$$

where, $n_{\text{bi}}$ and $n_{\text{mo}}$ are the numbers of recombined electron–hole pairs through bimolecular and monomolecular recombination routes, respectively. $V$ denotes the total volume of the studied domain and $t$ is the elapsed time. $n$ and $p$ are the concentration of electrons and holes in the system.

## Device performance evaluation through device scale simulation

At the device scale, simulation can give a full picture of the system by considering boundary conditions. Thus, it is reliable to calculate the device performance for tandem solar cells at the device scale.

The photon absorption efficiency, EDE, carrier mobility and recombination rate were inputs into the device scale simulation module [25] and $J$–$V$ curves of each single sub-cell were acquired through solving drift–diffusion equations. Device scale simulation was performed for both sub-cells separately. The critical parameters used in the device scale simulation are listed in Table 1. Then, the $J$–$V$ curve of the tandem device was

**Table 1:** The parameters used in the multiscale simulation.

| Symbol | Value | Unit | Notes |
|---|---|---|---|
| $T$ | 298 | K | temperature |
| $\mu^0_{\text{e\_PCBM}}$ | 0.02 [28] | $cm^2/(Vs)$ | local electron mobility in PCBM |
| $\mu^0_{\text{h\_P3HT}}$ | 0.003 [29] | $cm^2/(Vs)$ | local hole mobility in P3HT |
| $\mu^0_{\text{h\_PCPDTBT}}$ | 0.1 [24] | $cm^2/(Vs)$ | local hole mobility in PCPDTBT |
| $E_{\text{g\_P3HT}}$ | 1.05 [25] | eV | effective band gap of P3HT/PCBM |
| $E_{\text{g\_PCPDTBT}}$ | 1.0 [16] | eV | effective band gap of PCPDTBT/PCBM |

constructed by matching the current density of the two sub-cells. Since the two sub-cells are in series, the current density through each of the sub-cells should be the same. The search for the identical current density point was realized by increasing the applied voltage on one sub-cell and decreasing the voltage on the other one by the same amount, while keeping the total applied voltage constant. Applying the same rule, the whole *J–V* curve was acquired by going through all the voltage points.

### Tandem polymer solar cell optimization through searching algorithms

To the best of our knowledge, the optimization of tandem polymer solar cells were most simply conducted by traversing the whole space in the work reported in [16-20]. Taking the high complexity into account, the computational load would be too high if accurate optimization results are required for tandem polymer solar cells.

For the purpose of relieving computational load and optimizing tandem device structures with all the structure parameters considered, we employed two searching algorithms: simplex searching [30] and GA [31]. In simplex searching, five points were randomly generated in the studied domain, where each point contained all the four investigated variables: thickness ($d$) and domain size ($a$) of the two active layers ($d_{P3HT/PCBM}$, $d_{PCPDTBT/PCBM}$, $a_{P3HT/PCBM}$, $a_{PCPDTBT/PCBM}$). Then, during the searching process, the points were updated according to the schematic and flow chart (Figure S3 and S4, in Supporting Information File 1). On the other hand, for GA searching, six samples (six points) with four traits (the four variables) were prepared. During each iteration, the best two samples were selected as the parent ones. The child samples were generated using the two parent samples through inheritance, crossover and mutation operations, as illustrated in Supporting Information File 1, Figure S5. Through both algorithms, the searching process was conducted for different D/A weight ratios. The detailed illustration of the two optimization methods are presented in Supporting Information File 1.

## Results and Discussion

Through the bulk effective medium approach, the complex refractive index for the P3HT/PCBM blend with different weight ratios was calculated and presented in Figure 3a. As shown in Figure 3b, refractive index for PCPDTBT/PCBM blend was acquired from [25] . From the optical calculation module, the photon absorption efficiency (Figure 3c,d) of the two active layers were computed under varied thickness values for the two layers. Then, as presented in Figure 3e,f, the possible maximum short circuit current density ($J_{sc}$) through the device was estimated by assuming that all the absorbed light energy will contribute to the final electric energy with no loss. From Figure 3, it is obvious that configuration A has a much better balance between the two sub-cells than configuration B. Therefore, the possible current density was estimated to be much higher for the configuration with P3HT/PCBM sub-cell at the front of the incident light. For all the estimated maximum current density maps corresponding to the case of different P3HT/PCBM weight ratios under different configurations, please refer to Supporting Information File 1, Figure S6.

In the mesoscale simulation, knowledge of morphology is required before MC simulations can be performed. For each weight ratio value, three series of morphologies were generated. A series of morphologies for 1:1 P3HT/PCBM are shown in Figure 4a. The connectivity ratio (as defined in [21]) for one series of morphologies of 1:1 P3HT/PCBM is related to the domain size and displayed in Figure 4b. Through the MC simulation, we evaluated EDE, carrier mobility, recombination rate, and also clarified their dependence on domain size and electric field; corresponding plots of these data are shown in Figure 5 and Figure 6. At each data point, the simulations were repeated three times representing the three different morphologies at each domain size and at each weight ratio value. As shown in Figure 5 and Figure 6, EDE decreases with domain size, but keeps almost constant with electric field. Since excitons can only dissociate into electrons and holes at the interface between donor and acceptor, EDE is expected to decrease with domain size because the D/A interface area reduces as domain size increases. On the other hand, excitons are neutral and immune to the external and internal electric field; this explains our observation of independence of EDE on electric field. As indicated from Figure 4b, the connectivity ratio increases with the domain size. Then, as domain size increases, it will be easier for charge carriers to transport through the blend, and more difficult for carriers to recombine with each other. The corresponding results, shown in Figure 5a.2–5 and Figure 6a.2–4, correlate well with the assumptions as discussed above. As observed from Figure 5b.2–5 and Figure 6b.2–4, both the evaluated mobility and recombination rate tend to decrease with the electric field. An appropriate explanation is that many of the carriers can be captured in dead ends or traps because of the complex inner structures in the blend. In such a case, the high electric field will reduce the possibility for the trapped carriers to jump out from the traps, which leads to a lower effective carrier mobility. However, since electrons and holes will be dragged towards the opposite side by the electric field, a higher electric field will guarantee the separation of electrons and holes and subsequently leads to lower recombination rate, both bimolecular and monomolecular.

The device performance indices were calculated from the tandem device's *J–V* curve, constructed from the *J–V* curves of

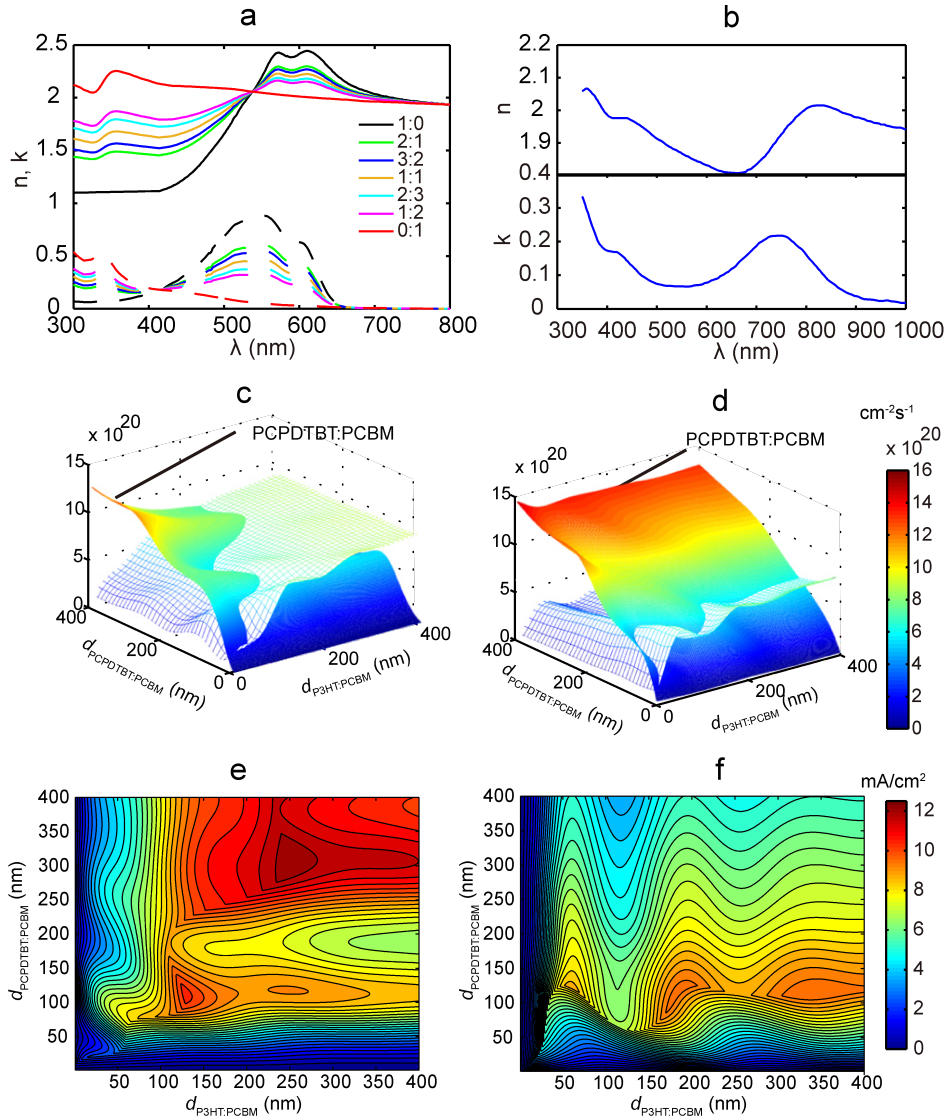


**Figure 3:** Optical parameters and simulation results from the optical calculation module. The complex refractive index of the P3HT/PCBM blend (a) with different D/A weight ratio (the solid lines are for *n*, and the dashed lines are for *k*) and PCPDTBT/PCBM (b) with weight ratio of 1:2. (c) and (d) (sharing the same color code scale) present the photon absorption efficiency calculated for configuration A and B, respectively. The weight ratios of P3HT/PCBM and PCPDTBT/PCBM active layers are 1:1 and 1:2. The maximum photocurrent estimated according to the photon absorption efficiency for the two device configurations is displayed in (e) and (f) (e and f share the same color code scale).

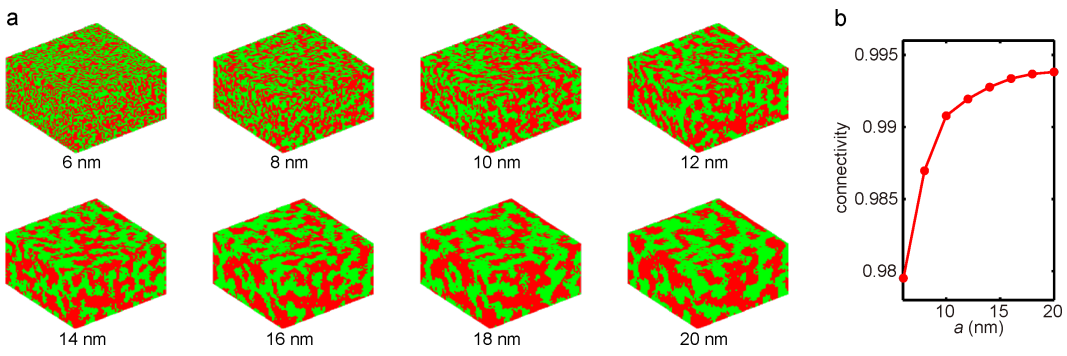


**Figure 4:** (a) Morphologies generated for 1:1 P3HT (green)/PCBM (red) and (b) the dependence of the connectivity ratio on the domain size for the morphologies in (a).

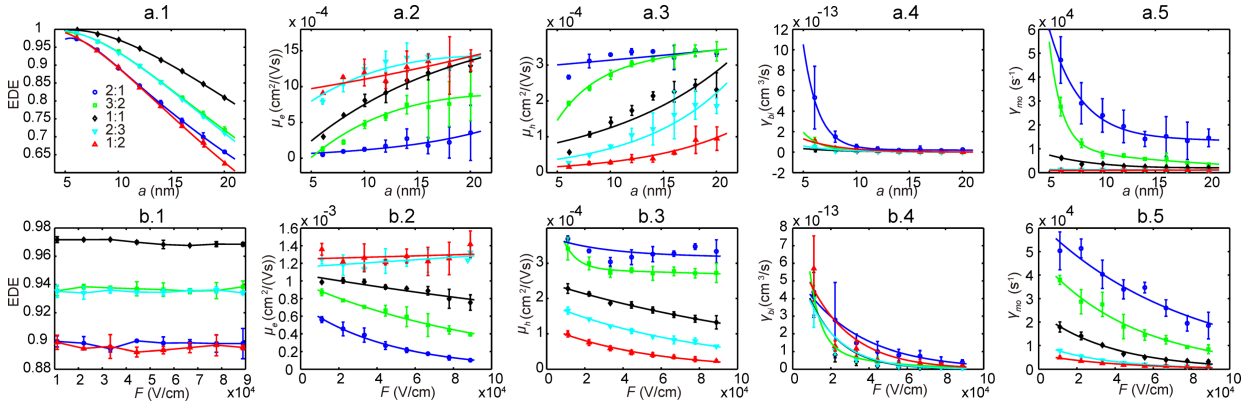


**Figure 5:** MC simulation results for P3HT/PCBM active layer with different D/A weight ratios. (a.1–5) presents the EDE, electron and hole mobility, bimolecular and monomolecular recombination rate with respect to domain size. (b.1–5) presents the results with respect to electric field.

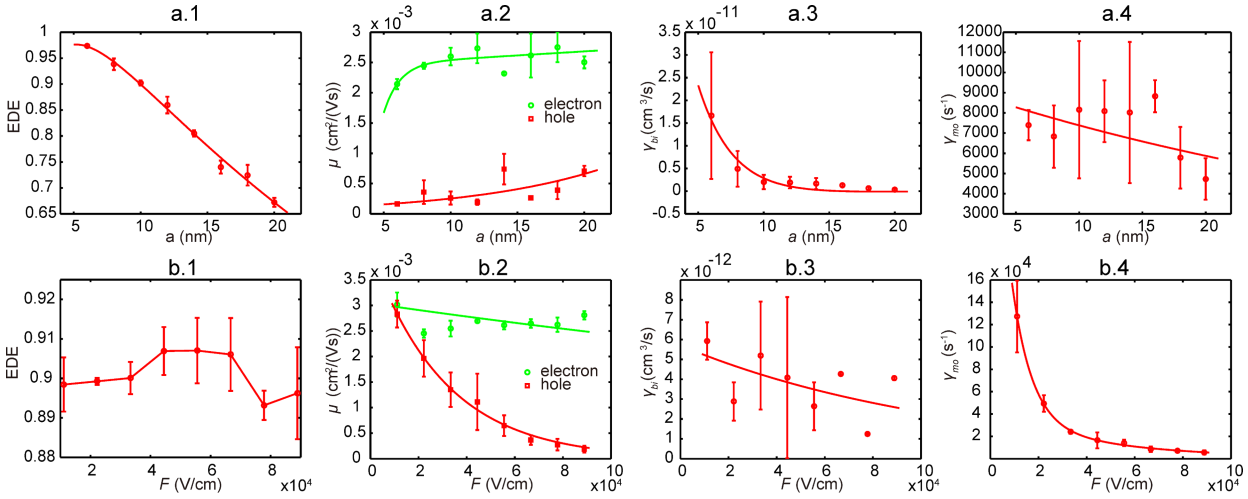


**Figure 6:** MC simulation results for PCPDTBT/PCBM (1:2) active layer. (a.1–4) presents the EDE, carrier mobility, bimolecular and monomolecular recombination rate with respect to domain size. (b.1–4) presents the results with respect to electric field.

the two sub-cells (illustrated in Figure 7). With the domain size fixed at 10 nm for both active layers, we acquired the device performance indices with respect to active layer thickness changing from 50 nm to 400 nm with an interval of 10 nm. As demonstrated in Figure 8, $J_{sc}$, open circuit voltage ($V_{oc}$), fill factor (FF) and PCE are obtained for both the two configurations investigated. Considering the independence of photon absorption efficiency on the active layer thickness, the agreement between the $J_{sc}$ map (as shown in Figure 8a.1 and 8b.1) and the map of possible maximum current shown in Figure 3e,f, suggests that the $J_{sc}$ of tandem polymer solar cells is largely determined by the photon absorption efficiency. Smaller thickness means higher electric field in the device; higher electric field leads to lower recombination rate, which results in higher $V_{oc}$ and FF. These discussions are in conjunction with the results presented in Figure 8a.2,3 and 8b.2,3. For different

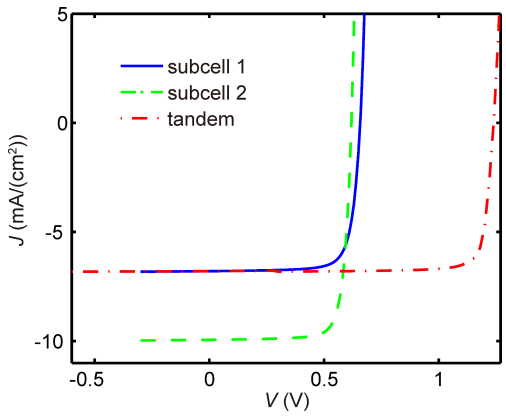


**Figure 7:** One example of a *J*–*V* curve for a tandem structure constructed from *J*–*V* curves of sub-cells. Sub-cell 1 is based on P3HT/PCBM, while sub-cell 2 is based on PCPDTBT/PCBM.

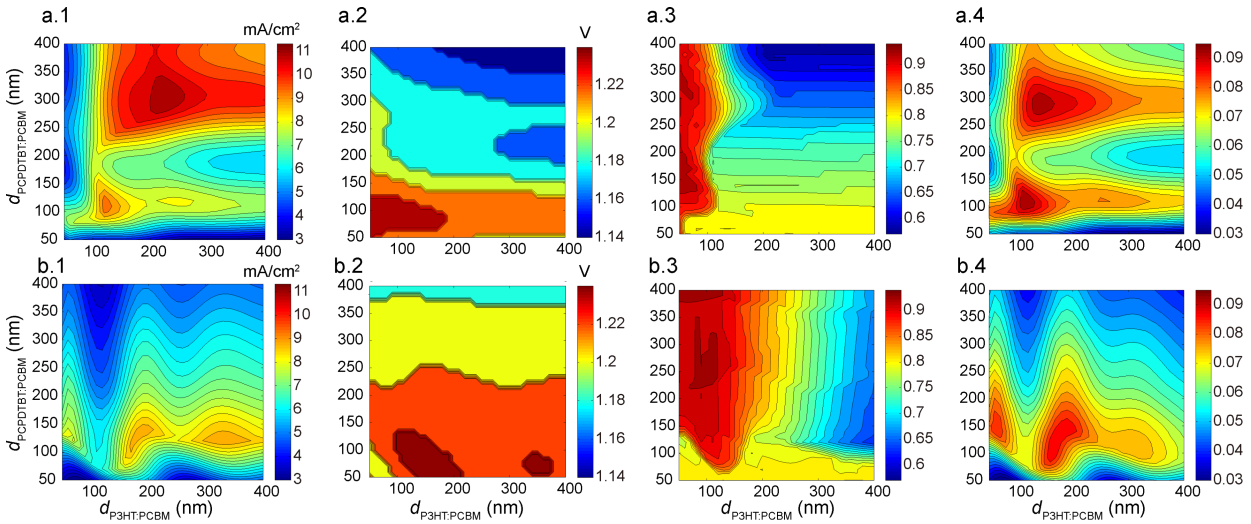


**Figure 8:** Device performance calculated through the multiscale simulation for configuration A (a) and B (b). a.1 and b.1 show $J_{sc}$ with respect to thickness. a.2 and b.2 present $V_{oc}$. FF is given in a.3 and b.3. PCE is presented in a.4 and b.4. Here, the weight ratios for P3HT/PCBM and PCPDTBT/PCBM are 1:1 and 1:2, respectively.

weight ratios, the PCE values are all estimated and their dependence on the active layer thickness and domain size are presented in Supporting Information File 1, Figure S7 and Figure S8, respectively.

Next, the searching algorithms were employed to locate the optimal PCE value with respect to thickness, domain size and weight ratio of the two active layers. In order to check the effectiveness of the searching algorithms, tests were performed with domain size and weight ratio values fixed. The starting points, as indicated in Figure 9a using red circles, were generated randomly. As the number of searching iterations increases, both simplex searching method and GA reach the same optimal PCE value with the location (P3HT/PCBM layer thickness of 141 nm, PCPDTBT/PCBM layer thickness of 106 nm). Both algorithms find the PCE peak value of 0.919, which proves the effectiveness of the searching methods in tackling this issue. Additionally, while traversing the whole space to calculate all the PCE values takes over 24 hours, the optimization algorithms acquired the optimal PCE value within 10 minutes. On the other hand, GA is expected to jump out of local optimal PCE because of the mutation operation in the child sample generation process, while the simplex method tends to be easily trapped at the local peak.

Finally, the optimization of a tandem structure with all active layer parameters ($d_{P3HT/PCBM}$, $d_{PCPDTBT/PCBM}$, $a_{P3HT/PCBM}$, $a_{PCPDTBT/PCBM}$, and $\eta_{P3HT/PCBM}$ (D/A ratio in P3HT/PCBM active layer)) taken into consideration was conducted using the two searching algorithms as discussed above. By repeating the searching behaviour at least ten times for each P3HT/PCBM weight ratio value using both of the algorithms, we get the

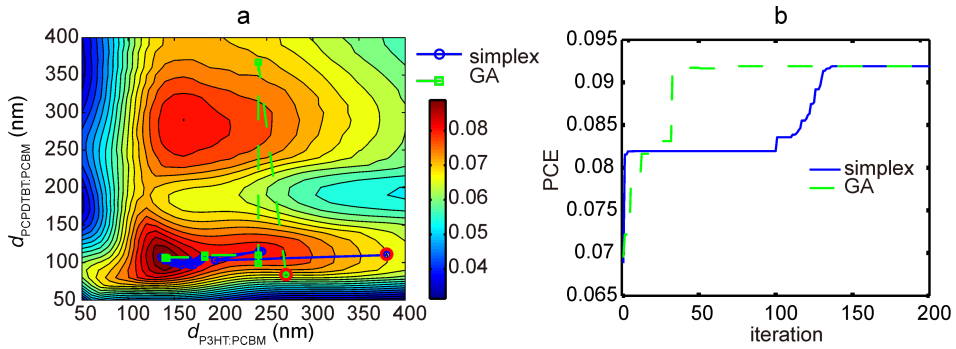


**Figure 9:** (a) Presents the evolution of optimized active layer thicknesses during the search of the optimal PCE value. Both the simplex searching algorithm and GA are tested. The random start points are indicated by the red circles. The corresponding PCE value evolutions are displayed in (b). Here, the weight ratios are 1:2 for both P3HT/PCBM and PCPDTBT/PCBM.

initially optimized PCE values. Then, to check whether the PCE values were globally optimized, the corresponding locations for the initial optimal PCE values were delivered into both algorithms as one of the starting points. The acquired PCE values were recognized as the global peak until no further increase was observed when both of the algorithms were performed. The final optimization results are listed in Table 2. As indicated by Table 2 and Figure 10, the configuration with P3HT/PCBM as the front sub-cell facing the incident light achieves relatively better performance than the configuration with PCPDTBT/PCBM at the front. As a lower band gap, active material, PCPDTBT has considerably stronger optical absorption than P3HT. Thus, if the sub-cell with PCPDTBT is put first, a large portion of light energy will be harvested by the PCPDTBT based sub-cell. Therefore, a significant unbalance, as indicated from Figure 3d,f, between the two sub-cells will be evidenced, which ruins the device performance in configuration B. Then, the tandem structure of configuration B will attempt to counteract the unbalance by increasing the thickness of the P3HT/PCBM layer and simultaneously reducing the PCPDTBT/PCBM layer thickness. Therefore, in configuration B, $d_{P3HT/PCBM}$ is much higher than $d_{PCPDTBT/PCBM}$ in the optimized structure. As shown in Table 2, the PCE champion is configuration A with 1:1 P3HT/PCBM; and the optimal PCE is almost 10%. For almost all configurations and weight ratios, the optimized device is located with active layer thickness between 100 nm and 200 nm and an average domain size between 6 nm and 11 nm. A thick active layer can ensure high current density, but meanwhile leads to serious recombination and low FF. On the other hand, lower domain size will lead to higher EDE, but also lower carrier mobility and higher recombination rate. Therefore, thickness and domain size should be tuned to proper values in optimized device. As revealed from the results, the tandem device benefits from much more than it suffers from low domain size and the optimal active layer thickness values are in line with those of most reported PCE works [7,8,13,15].

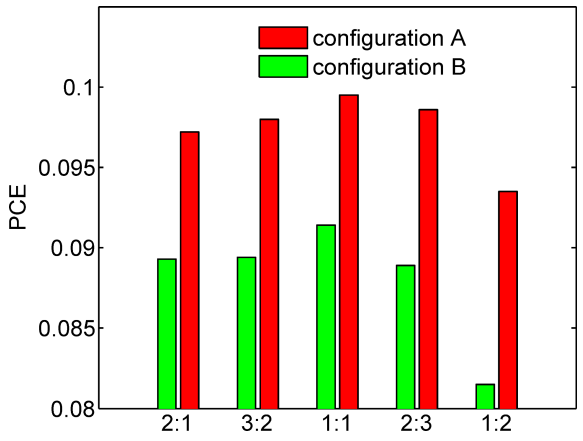


**Figure 10:** Optimal PCE values for different configurations and different D/A weight ratios in the P3HT/PCBM blend.

Due to the lack of data for the refractive index of pure PCPDTBT polymer, we have fixed the D/A weight ratio in the PCPDTBT/PCBM layer to be 1:2. However, as demonstrated in Supporting Information File 1, Figure S7 and S8, the D/A weight ratio of the active layer impacts the PCE value significantly. Therefore, the performance of the tandem device investigated is to be further optimized with the D/A weight ratio of PCPDTBT/PCBM layer varied.

## Conclusion

In summary, we have proposed a multiscale simulation and have demonstrated its capability in the simulation and optimization of tandem organic solar cells. Both optical and electric coupling between the two stacked sub-cells were overcome through our optical calculation module and the device scale simulation module, respectively. The performance criteria of the tandem solar cells based on P3HT, PCPDTBT and PCBM were evaluated through the simulation work and related to the thickness, domain size and D/A weight ratios in the active layers. Finally,

**Table 2:** Optimized device parameters of both the two configurations in a tandem structure studied herein.

| Devices | | $d_{P3HT/PCBM}$ (nm) | $d_{PCPDTBT/PCBM}$ (nm) | $a_{P3HT/PCBM}$ (nm) | $a_{PCPDTBT/PCBM}$ (nm) | PCE |
|---|---|---|---|---|---|---|
| A | 2:1 | 120 | 110 | 7 | 7 | 0.0972 |
| | 3:2 | 120 | 110 | 7 | 6 | 0.0980 |
| | **1:1** | **120** | **108** | **8** | **7** | **0.0995** |
| | 2:3 | 130 | 108 | 9 | 6 | 0.0986 |
| | 1:2 | 150 | 106 | 10 | 7 | 0.0935 |
| B | 2:1 | 64 | 144 | 6 | 8 | 0.0893 |
| | 3:2 | 171 | 94 | 10 | 7 | 0.0894 |
| | **1:1** | **170** | **107** | **10** | **7** | **0.0914** |
| | 2:3 | 172 | 91 | 10 | 6 | 0.0889 |
| | 1:2 | 175 | 78 | 11 | 7 | 0.0815 |

we found the optimal device structure parameters through both simplex algorithm and GA. The optimized tandem device parameters were in agreement with those reported in fabricated devices. This work not only provides promising guidance for tandem polymer solar cell fabrication, but also sheds light on the fundamental principles of tandem photovoltaic devices. Additionally, this approach can be easily applied to optimizing tandem solar cells based on other materials as long as the refractive index and local carrier mobility of the new materials are available.

## Supporting Information

Comparison between experimental morphology and simulated morphology, the flow chart of FRM, the illustration of simplex searching algorithm and GA. Additional simulation results, including the projected current density and PCE with respect to active layer thickness and active layer domain size.

### Supporting Information File 1

Additional simulation results and information used for calculations.
[http://www.beilstein-journals.org/bjnano/content/supplementary/2190-4286-8-13-S1.pdf]

### Supporting Information File 2

MATLAB code for the morphology generation process.
[http://www.beilstein-journals.org/bjnano/content/supplementary/2190-4286-8-13-S2.zip]

## Acknowledgements

The authors gratefully acknowledge the financial support from Youth Foundation of Fuzhou University (Grant No. 0020-510262). The authors would like to thank Minlin Jiang (from the Department of Electrical and Computer Engineering, University of Pittsburgh) and Dong Wang (from Shenyang Institute of Automation, Chinese Academy of Sciences) for helpful discussions.

## References

1. Li, G.; Shrotriya, V.; Huang, J. S.; Yao, Y.; Moriarty, T.; Emery, K.; Yang, Y. *Nat. Mater.* **2005,** *4,* 864–868. doi:10.1038/nmat1500
2. Scharber, M. C.; Mühlbacher, D.; Koppe, M.; Denk, P.; Waldauf, C.; Heeger, A. J.; Brabec, C. L. *Adv. Mater.* **2006,** *18,* 789–794. doi:10.1002/adma.200501717
3. He, Z. C.; Zhong, C. M.; Su, S. J.; Xu, M.; Wu, H. B.; Cao, Y. *Nat. Photonics* **2012,** *6,* 591–595. doi:10.1038/nphoton.2012.190
4. Park, H. J.; Kang, M.-G.; Ahn, S. H.; Guo, L. J. *Adv. Mater.* **2010,** *22,* E247–E253. doi:10.1002/adma.201000250
5. National Renewable Energy Laboratory. Reported timeline of solar cell energy conversion efficiencies. https://upload.wikimedia.org/wikipedia/commons/3/39/PVeff%28rev160812%29.jpg (accessed Jan 5, 2017).
6. You, J. B.; Dou, L. T.; Yoshimura, K.; Kato, T.; Ohya, K.; Moriarty, T.; Emery, K.; Chen, C.-C.; Gao, J.; Li, G.; Yang, Y. *Nat. Commun.* **2013,** *4,* No. 1446. doi:10.1038/ncomms2411
7. Kouijzer, S.; Esiner, S.; Frijters, C. H.; Turbiez, M.; Wienk, M. M.; Janssen, R. A. J. *Adv. Energy Mater.* **2012,** *2,* 945–949. doi:10.1002/aenm.201100773
8. Kim, J. Y.; Lee, K.; Coates, N. E.; Moses, D.; Nguyen, T.-Q.; Dante, M.; Heeger, A. J. *Science* **2007,** *317,* 222–225. doi:10.1126/science.1141711
9. McMeekin, D. P.; Sadoughi, G.; Rehman, W.; Eperon, G. E.; Saliba, M.; Horantner, M. T.; Haghighirad, A.; Sakai, N.; Korte, L.; Rech, B.; Johnston, M. B.; Herz, L. M.; Snaith, H. J. *Science* **2016,** *351,* 151–155. doi:10.1126/science.aad5845
10. Lu, S.; Guan, X.; Li, X.; Sha, W. E. I.; Xie, F.; Liu, H.; Wang, J.; Huang, F.; Choy, W. C. H. *Adv. Energy Mater.* **2015,** *5,* No. 1500631. doi:10.1002/aenm.201500631
11. Li, K.; Li, Z.; Feng, K.; Xu, X.; Wang, L.; Peng, Q. *J. Am. Chem. Soc.* **2013,** *135,* 13549–13557. doi:10.1021/ja406220a
12. Dou, L.; You, J.; Yang, J.; Chen, C.-C.; He, Y.; Murase, S.; Moriarty, T.; Emery, K.; Li, G.; Yang, Y. *Nat. Photonics* **2012,** *6,* 180–185. doi:10.1038/nphoton.2011.356
13. Li, W.; Furlan, A.; Hendriks, K. H.; Wienk, M. M.; Janssen, R. A. J. *J. Am. Chem. Soc.* **2013,** *135,* 5529–5532. doi:10.1021/ja401434x
14. Zhou, Y.; Fuentes-Hernandez, C.; Shim, J. W.; Khan, T. M.; Kippelen, B. *Energy Environ. Sci.* **2012,** *5,* 9827–9832. doi:10.1039/c2ee23294d
15. Gevaerts, V. S.; Furlan, A.; Wienk, M. M.; Turbiez, M.; Janssen, R. A. J. *Adv. Mater.* **2012,** *24,* 2130–2134. doi:10.1002/adma.201104939
16. Namkoong, G.; Boland, P.; Lee, K.; Dean, J. *J. Appl. Phys.* **2010,** *107,* 124515. doi:10.1063/1.3448271
17. Boland, P.; Lee, K.; Dean, J.; Namkoong, G. *Sol. Energy Mater. Sol. Cells* **2010,** *94,* 2170–2175. doi:10.1016/j.solmat.2010.07.007
18. Dennler, G.; Forberich, K.; Ameri, T.; Waldauf, C.; Denk, P.; Brabec, C. J.; Hingerl, K.; Heeger, A. J. *J. Appl. Phys.* **2007,** *102,* 123109. doi:10.1063/1.2825651
19. Persson, N.-K.; Inganäs, O. *Sol. Energy Mater. Sol. Cells* **2006,** *90,* 3491–3507. doi:10.1016/j.solmat.2006.05.009
20. Zuo, L. J.; Chang, C.-Y.; Chueh, C.-C.; Zhang, S.; Li, H.; Jen, A. K.-Y.; Chen, H. *Energy Environ. Sci.* **2015,** *8,* 1712–1718. doi:10.1039/C5EE00633C
21. Bottenfield, C. G.; Wei, F.; Park, H. J.; Guo, L. J.; Li, G. *Energy Technol.* **2015,** *3,* 414–422. doi:10.1002/ente.201402152
22. Burkhard, G. F.; Hoke, E. T.; McGehee, M. D. *Adv. Mater.* **2010,** *22,* 3293–3297. doi:10.1002/adma.201000883
23. Gu, Y.; Wang, C.; Russell, T. P. *Adv. Energy Mater.* **2012,** *2,* 683–690. doi:10.1002/aenm.201100726
24. Morana, M.; Wegscheider, M.; Bonanni, A.; Kopidakis, N.; Shaheen, S.; Scharber, M.; Zhu, Z.; Waller, D.; Gaudiana, R.; Brabec, C. *Adv. Funct. Mater.* **2008,** *18,* 1757–1766. doi:10.1002/adfm.200701428
25. Liu, L. Performance optimization of organic solar cells by simulation and characterization. Ph.D. Thesis, University of Pittsburgh, Pittsburgh, PA, U.S.A., 2011.

26. Hoppe, H.; Arnold, N.; Sariciftci, N. S.; Meissner, D. *Sol. Energy Mater. Sol. Cells* **2003,** *80,* 105–113. doi:10.1016/S0927-0248(03)00137-5
27. Wei, F.; Liu, L.; Liu, L.; Li, G. *IEEE J. Photovoltaics* **2013,** *3,* 300–309. doi:10.1109/JPHOTOV.2012.2216507
28. Nakamura, J.-i.; Murata, K.; Takahashi, K. *Appl. Phys. Lett.* **2005,** *87,* 132105. doi:10.1063/1.2058210
29. Pandey, S. S.; Takashima, W.; Nagamatsu, S.; Endo, T.; Rikukawa, M.; Kaneto, K. *Jpn. J. Appl. Phys., Part 2* **2000,** *39,* L94–L97. doi:10.1143/jjap.39.l94
30. Nelder, J. A.; Mead, R. *Comput. J.* **1965,** *7,* 308–313. doi:10.1093/comjnl/7.4.308
31. Barricelli, N. A. *Methodos* **1957,** *9,* 143–182.

## License and Terms

BEILSTEIN JOURNAL OF NANOTECHNOLOGY

# Comparison of four functionalization methods of gold nanoparticles for enhancing the enzyme-linked immunosorbent assay (ELISA)

Paula Ciaurriz[1], Fátima Fernández[1], Edurne Tellechea[1], Jose F. Moran[2] and Aaron C. Asensio[*1]

Full Research Paper

Open Access

Address:
[1]Cemitec (Multidisciplinary Center of Technologies for Industry), Polígono Mocholí, Plaza Cein 3, Noain 31110, Spain and [2]IdAB-CSIC-UPNA-GN (Institute of Agro-Biotechnology), Public University of Navarre, Campus Arrosadía s/n, Pamplona 31006, Spain

Email:
Aaron C. Asensio[*] - acabrera@cemitec.com

* Corresponding author

Keywords:
allergen; ELISA enhancement; functionalization; gliadin; gold nanoparticle

*Beilstein J. Nanotechnol.* **2017,** *8,* 244–253.
doi:10.3762/bjnano.8.27

Received: 13 May 2016
Accepted: 02 January 2017
Published: 25 January 2017

This article is part of the Thematic Series "Nanostructures for sensors, electronics, energy and environment III".

Guest Editor: N. Motta



## Abstract

The enzyme-linked immunosorbent assay (ELISA) technique is based on the specific recognition ability of the molecular structure of an antigen (epitope) by an antibody and is likely the most important diagnostic technique used today in bioscience. With this methodology, it is possible to diagnose illness, allergies, alimentary fraud, and even to detect small molecules such as toxins, pesticides, heavy metals, etc. For this reason, any procedures that improve the detection limit, sensitivity or reduce the analysis time could have an important impact in several fields. In this respect, many methods have been developed for improving the technique, ranging from fluorescence substrates to methods for increasing the number of enzyme molecules involved in the detection such as the biotin–streptavidin method. In this context, nanotechnology has offered a significant number of proposed solutions, mainly based on the functionalization of nanoparticles from gold to carbon which could be used as antibody carriers as well as reporter enzymes like peroxidase. However, few works have focused on the study of best practices for nanoparticle functionalization for ELISA enhancement. In this work, we use 20 nm gold nanoparticles (AuNPs) as a vehicle for secondary antibodies and peroxidase (HRP). The design of experiments technique (DOE) and four different methods for biomolecule loading were compared using a rabbit IgG/goat anti-rabbit IgG ELISA model (adsorption, directional, covalent and a combination thereof). As a result, AuNP probes prepared by direct adsorption were the most effective method. AuNPs probes were then used to detect gliadin, one of the main components of wheat gluten, the protein composite that causes celiac disease. With this optimized approach, our data showed a sensitivity increase of at least five times and a lower detection limit with respect to a standard ELISA of at least three times. Additionally, the assay time was remarkably decreased.

## Introduction

Enzyme-linked immunosorbent assay (ELISA) is a technique based on the ability of antibodies to bind specifically to an antigen and has been used for more than 55 years [1]. Nowadays, it is the most commonly used technique for routine monitoring and analysis [2,3]. Initially, the antigen–antibody interaction was monitored by means of radioactive species, but soon these methods were replaced by easier to read and safer enzymatic systems, where is peroxidase (HRP) the most commonly used reporter enzyme due its stability and performance [2-4]. The success of ELISA relies on its detection limit, specificity, reproducibility and the possibility of high throughput screening, although the assay normally takes several hours to develop the response [3].

Despite all the advantages, the sensitivity of ELISA for certain systems is limited [5], pointing to the need for novel strategies that could improve the ELISA limit of detection (LOD). Some strategies have been explored to enhance sensitivity, such as redox complexes, electroactive molecules and metal ions [6]. Along these lines, several nanotechnology-based strategies have been proposed involving nanoparticle-based solutions [5,7-12]. Nanoparticles can serve as excellent carriers for specific recognition molecules such as antibodies or probes as well reporter molecules. Due to their high surface/volume ratio, they present more binding sites for capture elements and for reporting tags leading to amplification of the analytical signal in a single recognition reaction [6,8]. Luo and co-workers showed better sensitivities and shortened times for the detection of C-reactive proteins by using a quantum-dot-labeled immunoassay [13]. Accordingly, an improvement in sensitivity of 5,000 times for the detection of the ataxia telangiectasia mutated protein by functionalized multiwalled carbon nanotubes was observed by Zhang et al. [7].

However, the most significant improvements in signal have been rendered by gold nanoparticles (AuNPs), presenting promising unique chemical and physical properties, as well as biological compatibility [5,14,15]. AuNPs possess the advantages of easy synthesis and narrow size distribution together with an easy and efficient surface modification compatible with linkers or biomolecules [16].

A critical step for obtaining gold complexes is the conjugation of biomolecules to AuNPs. Increasingly, the process of loading biomolecules to the nanoparticle surface it is considered more important, as its properties or biochemical activity can be changed. It was shown that several parameters such as surface chemistry, pH, stabilizing agents as well as addition procedure strongly affect final coverage and efficiency of biomolecules [17,18]. Moreover, the AuNP–biomolecule binding can be completed by different procedures. Biomolecules can be simply adsorbed on the nanoparticle surface by means of electrostatic or hydrophobic interactions, leading to a high number of proteins per particle and random orientation of biomolecules [8,12]. Other studies reported more stable covalent immobilization, where a better control of particle coverage is achieved and even the binding orientation can be controlled [19-21]. Each of the described procedures present advantages and disadvantages such as leakage of non-covalently attached biomolecules or loss of biomolecule activity due to aggressive protocols [22,23]. Thus, an optimal conjugation strategy will depend on the final application. To the best of our knowledge, there are no specific studies on the effect of conjugation strategy on the potential of gold complexes to improve ELISA sensitivity. Hence, the main objective of this work is to compare, under similar conditions, different functionalization strategies in order to know which one is the best approach for this kind of application.

In this work, a simple model for detection of rabbit IgG by AuNPs conjugated to goat anti-rabbit IgG (Ab) and HRP (AuNPs-Ab-HRP) was assayed to elucidate the best conditions for biomolecule binding and ELISA enhancement. We explored the effect of four different described procedures for binding antibodies and HRP to AuNP surfaces in order to enhance ELISA sensitivity. Afterwards, the strategy which demonstrated better sensitivity was used for detection of gliadin from wheat gluten, one of the main proteins of wheat gluten [24]. Gluten refers to a group of proteins contained in wheat, barley and rye and is thought to be the cause of celiac disease (CD). CD is an autoimmune enteropathy that causes mucosal damage in the small intestine, leading to malabsorption upon intake of gluten containing food [25]. Consequently, it is essential to use a highly sensitive and specific technique for gluten analysis in food. Nowadays, the method internationally accepted by the Codex Alimenatarious Comission is the sandwich ELISA assay [24]. Therefore, any strategy that could improve the detection limit generates considerable interest.

## Results and Discussion

### Conjugation of anti-rabbit IgG and HRP to AuNPs by direct adsorption and directional conjugation

The aim of this work is to compare different AuNP functionalization methods in order to know which one is the best for enhancing the ELISA signal (Figure 1). As a first approach, two different strategies for conjugation of proteins to nanoparticles were evaluated: adsorption of biomolecules on nanoparticles by electrostatic/hydrophobic interactions or directional binding by means of a linker (Figure 1a,b).

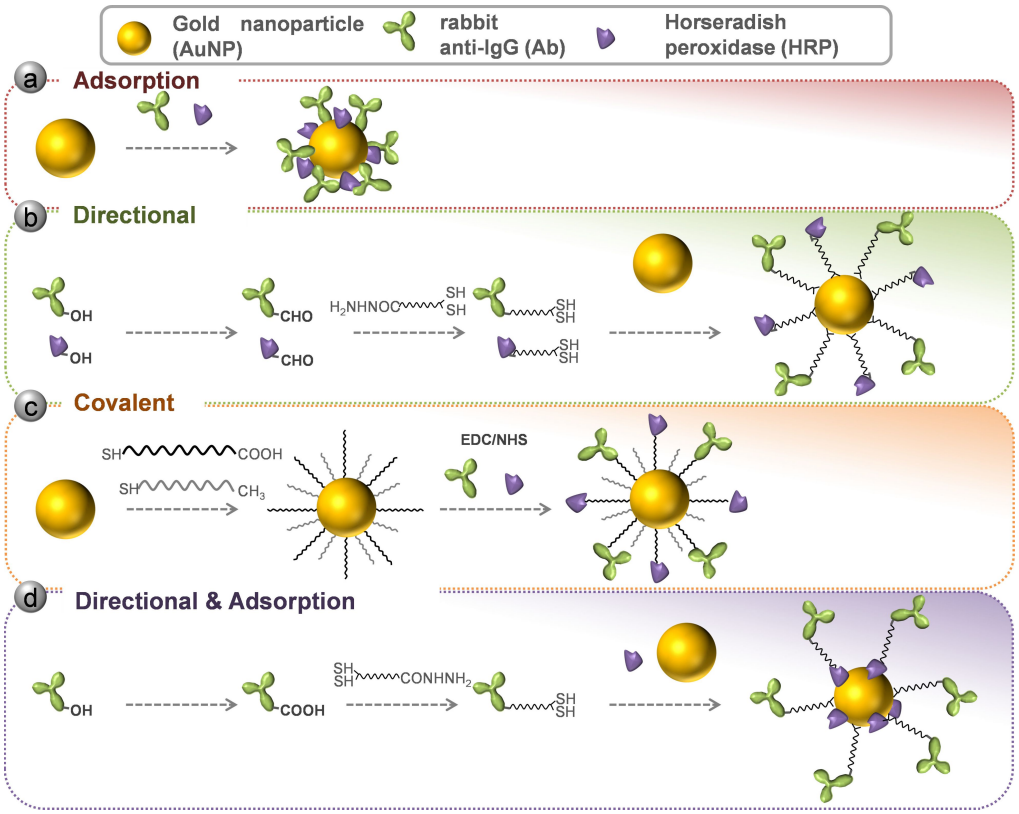


**Figure 1:** Schematic representation of the four different functionalization methods explored in this work. (a) Direct adsorption. (b) Directional conjugation with control of antibody and HRP orientation. (c) Covalent conjugation through antibody and HRP amine groups. (d) Combination of directional and adsorption strategy for antibody and HRP.

For the first one (adsorption), a protocol was set up regarding previous work on the matter [8,26]. In the case of the directional strategy, a previously described protocol was followed [20]. A hetero-bifunctional linker, hydrazide-polyethylene glycol-dithiol, was used to control the orientation of the molecules on the surface of the nanoparticle. Hydrazide is able to react with aldehyde groups that can be generated by oxidizing the carbohydrates of glycosylated proteins, such as antibodies [20]. For this purpose, antibody and HRP carbohydrates were oxidized with periodate in order to attach the mentioned linker at the Fc region of the antibody. Modified HRP and antibodies were mixed with the AuNPs, triggering a covalent binding.

## HRP/Ab ratio optimization for direct adsorption and directional conjugation

In order to elucidate the best conditions for nanoparticle and biomolecule assembly, the HRP/Ab molar ratio is known to be one of the most influential parameters in AuNP complexes as well as the probe concentration [6,8,12]. Furthermore, to cover all the possible combinations of parameters, while keeping the number of calculations to a minimum, a design of experiments technique (DOE) [27] was applied. Through DOE, the influence of the HRP/Ab ratio and AuNP concentration on ELISA performance can be easily studied. The DOE experiment was performed using different ratios between HRP and goat anti-rabbit IgG (1:5, 1:40 and 1:75 HRP/Ab) to elucidate the best conditions for the two functionalization strategies evaluated, that is, direct adsorption of biomolecules and directional assembly. These conjugates were evaluated with a fixed concentration of rabbit IgG (1 µg/mL) coated in a microplate well. Moreover, the influence of AuNP probes at different dilutions was also considered. For each HRP/Ab ratio, three different concentrations of AuNP probes (0.05, 0.4 and 0.75 AU) were assayed. The results were evaluated in terms of percent with respect to maximal signal at 450 nm. As a result, optimized ratios of 1:57 and 1:44 were obtained for the adsorption and directional methods, respectively (Figure 2).

These ratios are close to similar works performed with carbon nanotubes and covalent conjugation of HRP and anti-IgG, where an optimal ratio of 1:50 HRP/Ab was also found [7]. However, they differ from the work of Zhou and coworkers, which was developed using 20 nm AuNPs and a direct adsorption strategy, where they found 1:6 as the optimal ratio for

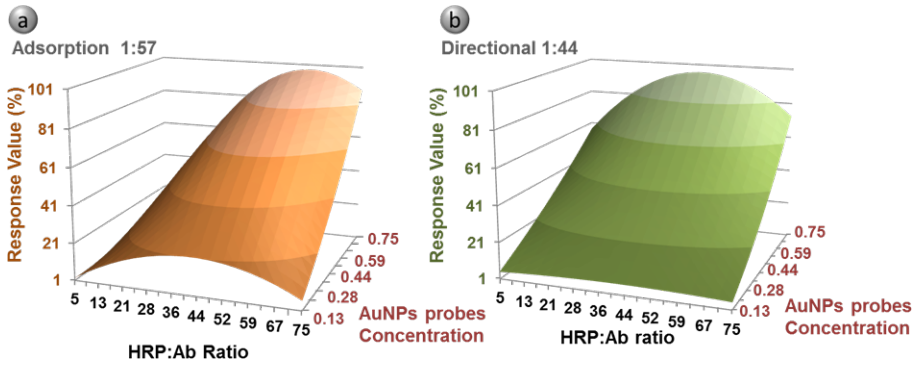


**Figure 2:** DOE experimental results for adsorption (a) and directional (b) methods. Estimation of the effect on response of HRP/Ab ratio and AuNP probe concentration. The layout displays the response value as percent of the maximal HRP signal at 450 nm. Coefficient of determination of DOE results $R^2$ = 0.9485 (a) and $R^2$ = 0.9768 (b).

HRP/Ab [8]. A similar ratio (1:3) was selected by Wu et al. when modifying 15 nm AuNPs for the detection for *Samonella typhimurium* [5]. These differences could be due to longer incubation times in the mentioned references, around 3 and 24 hours respectively, compared to 1 hour applied in our protocols. In addition, the ratios HRP/Ab assessed by these authors are lower than the ones considered in our work. Besides the dissimilar procedures employed, it is described that different variations in ionic strength, pH, protein order addition, as well as the inherent protein properties may modify the amount of biomolecules bound to the nanoparticle surface [17,21,28]. In this study, where two different biomolecules meet at the AuNP surface, the surface chemistry, different affinities towards gold and the microenvironment may have a great influence on the antibody nature and affinity for the antigen. This underlines the need of a simultaneous comparison between different strategies in order to obtain the most suitable protocol for this particular application.

On the other hand, as mentioned, the concentration of gold complexes must be taken into account for enhancing the ELISA signal. Therefore, in DOE experiments the influence of increasing the AuNP concentration (0.05, 0.4 and 0.75 AU) was also assessed. As seen in Figure 2, the increase of AuNPs results in a better performance up to the concentration assayed. Thus, as a first approach, a concentration of 0.5 a.u. AuNPs was applied in the ELISA characterization. Nevertheless, the influence of complex dilution was further assayed with the selected functionalization strategy.

## Adsorption and directional strategies: comparison by ELISA

Conjugates were assayed by ELISA using rabbit IgG as the target. In all cases, AuNP probes were compared to a regular anti-rabbit IgG HRP conjugated antibody (Ab-HRP) to compare the sensitivity reached with the different methodologies (Figure 3a,b). Accordingly, the results were evaluated in terms of signal/noise (S/N) which represents the absorbance at 450 nm of samples in the presence and absence of IgG, respectively. The S/N ratio of samples conjugated by adsorption showed a higher response than directional conjugates or Ab-HRP. This was an unforeseen result, as better efficiency was expected due the directional conjugation, where more antigen-binding sites on the fragment antigen-binding (Fab) portion of the antibody are directed outward from the gold surface and therefore available for antigen binding [19-21]. Periodate is widely used for HRP conjugation to biomolecules [2,29,30]. For this reason, we considered it appropriate to follow the protocol of Kumar et al. [20] for directional functionalization of AuNP with Ab and HRP. However, this kind of protocol may cause partial enzyme denaturation, as periodate is a powerful oxidant and could decrease HRP activity to a great degree [2].

## New biofunctionalization strategies with covalent and directional/adsorption: comparison by ELISA

As described above, we decided to evaluate two other new approaches (Figure 1c,d). One approach is covalent conjugation, where antibodies and HRP are covalently bound to the surface by the means of a PEG linker through its free amine groups using the EDC/NHS carbodiimide method [30]. The second is a merge of the previously assayed procedures, combining the directional binding of the antibody with the adsorption of the HRP to the AuNP surface (directional and adsorption procedure). For the covalent strategy we set up the conjugation procedure according to previous works [19] and the DOE results. In the case of the directional/adsorption procedure, the protocol for directional Ab loading and concentration of HRP from adsorption method were applied.

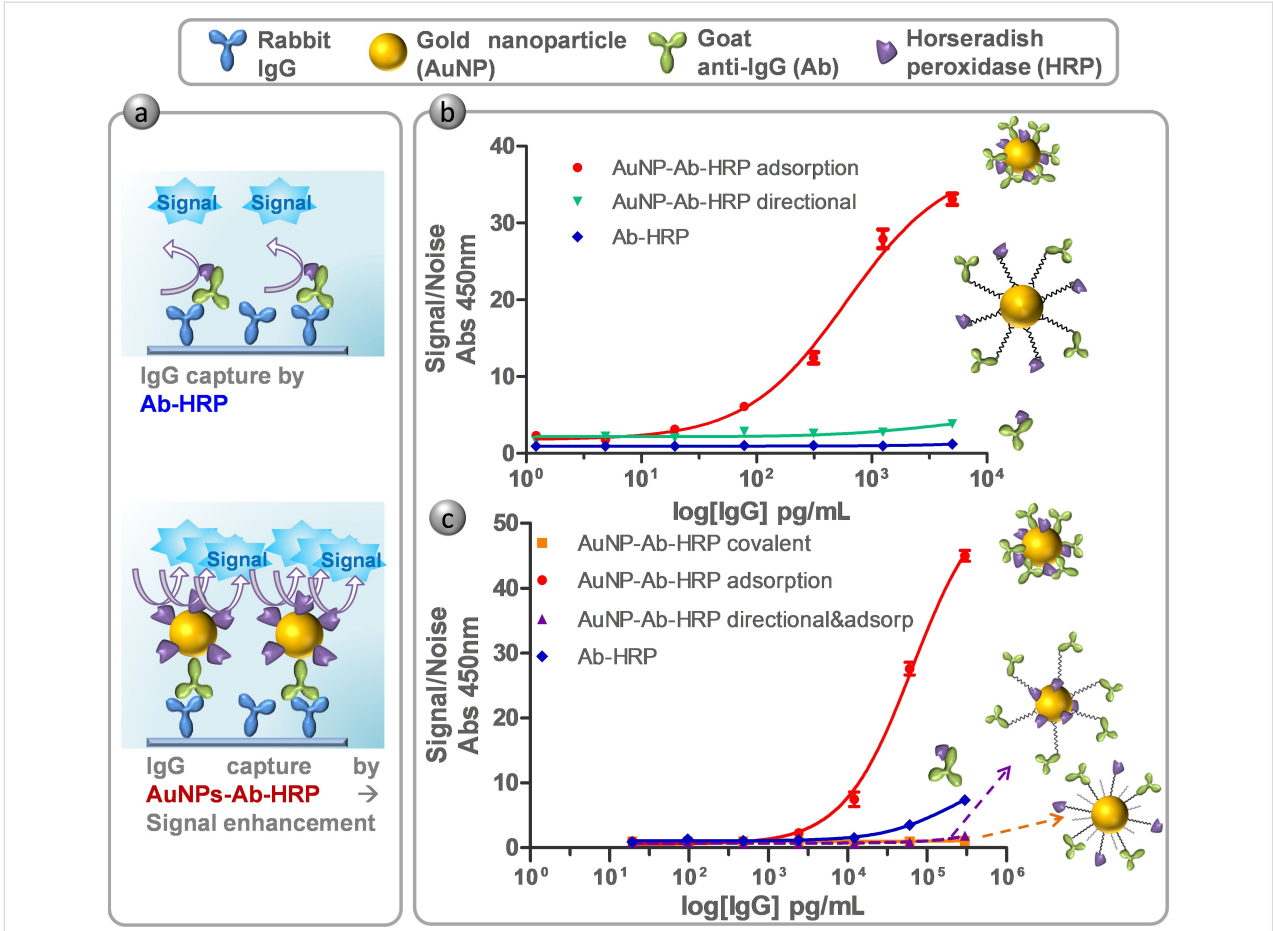


**Figure 3:** (a) Schematic representation of model ELISA and the basis of enhancement by means of AuNP probes. (b) Result of ELISA comparing AuNP probes prepared by adsorption (red curve), directional conjugation (green) and labelled secondary antibody (Ab-HRP, blue). (c) Result of ELISA comparing AuNP probes prepared by adsorption (red), covalent (orange), directional and adsorption (purple) and Ab-HRP (blue). Results are represented as the S/N ratio which represents the absorbance at 450 nm of samples in the presence and absence of IgG, respectively.

Consequently, ELISA was assessed for comparing the new proposed strategies as well as the direct adsorption that already yielded good results (Figure 3c). Once more, adsorption conjugation resulted in better S/N response than the Ab. Surprisingly, new conjugation strategies (covalent and directional/adsorption) resulted in worse S/N values than direct adsorption and even more than Ab-HRP, although it is described that covalent and site specific immobilization leads to more stable and better defined composition conjugates [19,20,31]. In an attempt to better understand these data, it was found that the HRP molecule (Uniprot accession number P80679) presented a lower number of free amine groups (few lysine amino acid residues) compared to the antibody molecule. The lower availability of free amino groups could hamper the attachment of peroxidase in the covalent strategy (Figure 1c), although more experiments should be performed to confirm this. Consequently, this would lead to lower peroxidase coverage and thus lower ELISA enhancement. The combination of the directional and adsorption strategy would be presented as best alternative according to this hypothesis, however, ELISA experiments showed a low S/N ratio compared to other methodologies. The combined strategy implies a two-step functionalization, where the antibody is first directionally bound to the surface, and secondly, HRP is added for a direct adsorption loading. The sequential procedure inevitably signifies less free binding sites on the nanoparticle surface after the first step. It was previously described how the arrangements of biomolecules can affect complex coverage and behavior [17]. Moreover, Marie-Eve Aubin-Tam and coworkers showed how ligand charges around the particle can strongly influence protein structure, and therefore, activity [32]. Both factors would indicate lower peroxidase coverage/activity in this functionalization strategy.

In contrast, direct adsorption often leads to protein multilayers, as biomolecules have numerous residues which can non-specifically adsorb on AuNP surfaces [33]. Gagner et al. described how high protein loading resulted in lower loss of protein activity and secondary structure [34]. They assumed that subsequent

adsorption of protein in multilayers allowed the conjugate to recover activity and remain stable. Taking into account the published results and considering our data, we postulated that the total number of proteins bound to AuNPs could probably be higher by the direct adsorption method than for the others strategies, resulting in lower protein denaturation and a higher S/N ratio.

## Optimization of AuNP concentration in ELISA

Once the best functionalization strategy (adsorption) was defined, the influence of the concentration of the complex was probed in an ELISA model. As described above (Figure 2), the higher AuNP concentration, the higher the signal. Accordingly, this hypothesis was checked with four different concentrations of AuNP conjugates: 0.25, 0.5, 0.75 and 1.00 a.u. (Figure 4).

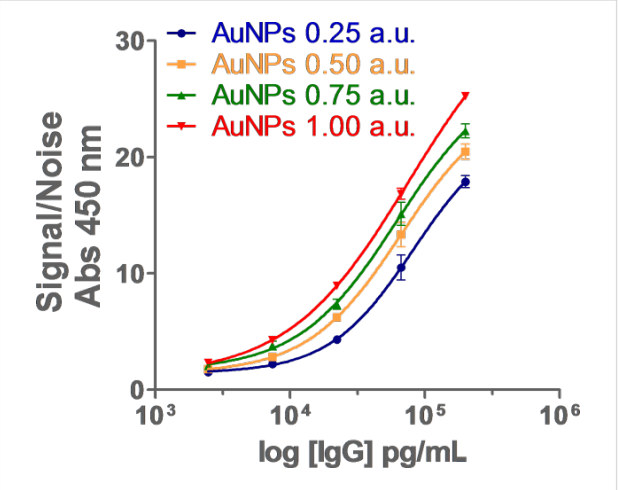


**Figure 4:** Optimization of AuNP probe concentration to be used in ELISA. Assayed concentrations: 0.25, 0.5, 0.75 and 1.00 Au. Results are normalized as S/N ratio which represents the absorbance at 450 nm of samples in the presence and absence of IgG, respectively.

In fact, it was confirmed that the higher concentration of AuNPs, the higher the S/N. However, it was expected that doubling the concentrations of the conjugates (i.e., from 0.5 a.u. to 1 AU) would result in an increase of S/N. This effect was not observed, where the concentrations of 0.75 a.u. and 1 a.u. produced only an increase of 9% and 23% S/N in ratio at 200 ppb of IgG. Additionally, the concentration of 1 a.u. induced a higher unspecific signal. The best balance between high sensitivity and reduced utilization of AuNP probes, as well as low unspecific signal, was found at a concentration of 0.5 a.u. Moreover, this result is consistent with the literature, as published by Ambrosia and co-workers in studying the effect of AuNP complexes in enhanced ELISA for the detection of breast cancer biomarkers [12]. In this work, the authors assessed three different concentrations of AuNP probes (ranging approximately from 1.4 to 0.014 AU) discarding the highest and lowest concentrations due to unspecific signal and low signal enhancement, respectively.

## Enhanced gliadin ELISA

Once defined as the best strategy for ELISA enhancement of IgG/anti-IgG for conjugation of AuNPs to Ab, the adsorption method was tested for the detection of a real analyte, namely, gliadin. Gliadin (which can be also subdivided into α-gliadin, γ-gliadin and ω-gliadin) is a prolamin protein present in wheat gluten and one of the presumed causes of celiac disease [24]. The official detection method by Codex Alimenatarius Commission is a sandwich ELISA assay. For this reason, it was selected as a proof-of-concept for improving the detection limit based on AuNPs conjugates and application to commercial rabbit polyclonal antibody (anti-gliadin).

An indirect ELISA was selected for the analysis (reference), where gliadin was coated on the ELISA plate at different concentrations (0–1 μg/mL dilutions 1:5) (Figure 5). After blocking, the primary antibody for gliadin was added at the supplier's recommended dilution (1:5,000). Subsequently, the secondary antibody (Ab-HRP or AuNPs probes) was added at optimal dilution (i.e., 1:10,000 for commercial antibody and 0.5 a.u. for AuNPs conjugates) and recorded signals were compared. As seen in Figure 5, enhanced ELISA provides a higher signal, therefore improving the sensitivity, and also the detection limit.

The enhanced procedure resulted in more than seven times higher S/N values at $1 \times 10^6$ pg/mL than regular ELISA. The LOD, estimated as the blank signal plus three times the blank standard deviation, reveals a theoretical LOD near 180 pg/mL for this enhanced ELISA, whereas conventional ELISA presents a theoretical LOD close to 500 pg/mL. The improvement of three times the LOD is similar to other works using the same functionalization strategy (adsorption) and 20 nm AuNPs [8,12]. Moreover, it should be pointed out that only a 5 min incubation with 3,3',5,5'-tetramethylbenzidine (TMB) is needed to reach a measurable and even saturated signal (depending on target concentration), while classical ELISA often requires at least 30 min to develop the color. Therefore, this enhanced strategy could help not only for improving the sensitivity and detection limit of ELISA performance, but also for decreasing the ELISA assay time as other authors have proposed [35]. This extended assay time is recognized as one of the major handicaps nowadays of the ELISA assay [3]. In addition, this improved methodology has the potential for improving the detection of other target antigens by indirect ELISA, as AuNPs are functionalized with a universal goat secondary antibody. Another possibility is to use this method in direct ELISA by conjugating primary antibodies and HRP on AuNPs. Many of

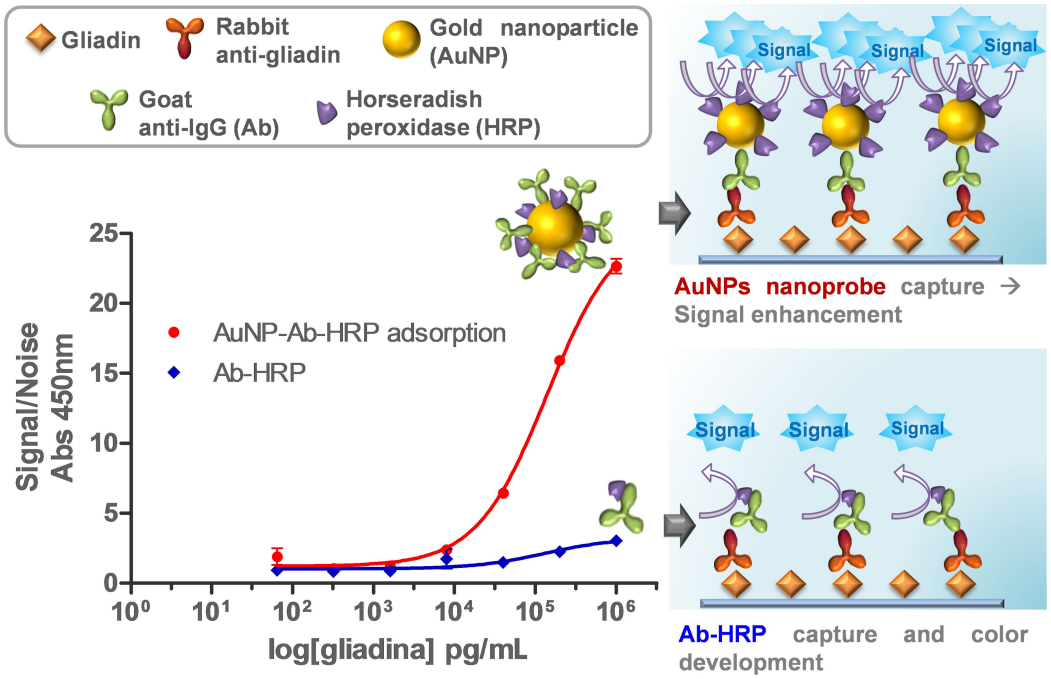


**Figure 5:** Schematic representation of gliadin detection by indirect ELISA and the basis of enhancement by means of AuNP probes. (Inset) Result of gliadin ELISA comparing AuNP probes prepared by adsorption (red curve) and Ab-HRP (blue). Results are represented as S/N ratio which represents the absorbance at 450 nm of samples in the presence and absence of IgG respectively. Coefficient of determination $R^2$ = 0.9968 for AuNP probes and $R^2$ = 0.7971 for Ab-HRP. Note that assayed concentrations are around the theoretical LOD of Ab-HRP.

the allergen determinations by ELISA use this strategy, but more research on this is necessary to confirm this.

## Conclusion

In summary, our main objective at the start of the work was to elucidate whether a covalent loading or directional binding of biomolecules on AuNPs could lead to better results than simple direct adsorption for an enhanced ELISA application. For this purpose, four different functionalization methods of AuNPs with HRP and goat anti-rabbit IgG were used in order to enhance the ELISA sensitivity with respect to regular ELISA. The synthesized AuNPs probes were assessed in model rabbit IgG and anti-rabbit IgG ELISA by comparing the colorimetric S/N ratio. The direct adsorption method prevails as the better option with respect to the other methodologies due its performance, presenting in addition an easier preparation (no chemical steps are needed). This method was applied for improving gliadin detection by indirect ELISA. The application of AuNP probes reduced the theoretical LOD to 180 pg/mL, which is three times lower than regular ELISA, and led to an increase of at least seven times in sensitivity at level of $1 \times 10^6$ pg/mL. This strategy could help to shorten ELISA assay times, making it less time consuming as well as increasing sensitivity and the LOD of the experiment. In addition, this methodology could be extended to other ELISA systems where a secondary labelled antibody is needed. Moreover, it could be a suitable methodology for combining primary antibodies with HRP, avoiding tedious chemical labelling procedures.

## Experimental

### 20 nm gold nanoparticle synthesis

All glassware was cleaned with aqua regia ($HNO_3$/HCl, 3:1), rinsed with deionized water and let dry before use. 20 µL of 30% $HAuCl_4 \cdot 3H_2O$ was added to 95 mL of deionized water in a 100 mL flask and heated to boiling under vigorous stirring. 5 mL of 1% aqueous sodium citrate was added to the solution, changing color from yellow to dark red. The nanoparticles were maintained at boiling for 15 min after the complete color change and then removed from heat. Stirring was maintained until the flask reached room temperature. AuNPs and conjugates were characterized by dynamic light scattering (DLS) using a zeta potential analysis system (Zetasizer Nano Z, Malvern Instrumentd, Worcestershire, UK), field emission scanning electron microscope (Carl Zeiss) and UV–vis spectrophotometer (Supporting Information File 1, Figure S1).

### Gold nanoparticle functionalization

Four different strategies were assayed in this work and are schematized in Figure 1. For the direct adsorption functionalization, 133 µL of 15 mM borate buffer pH 8.7 were added to

1 mL of AuNPs synthetized as described above to adjust the pH. The appropriated amount of goat anti-rabbit IgG and horseradish peroxidase were added and allowed to react under agitation in a carrousel for 30 min. Afterwards, sucrose was incorporated to a final concentration of 5% and incubated for 30 min. Finally, 160 µL of 3% bovine serum albumin (BSA) were added and shaken for 10 min. Thereafter the sample was centrifuged (7,500*g* 30 min) to remove unbound protein and AuNPs were re-suspended in 1 mL of 2 mM borate buffer pH 8.7 containing 5% sucrose, 2% glycerol, 0.5% BSA, and 0.01% Tween. The washing step was repeated once and the AuNP probe was re-suspended in 100 µL of the mentioned borate buffer. The complex concentration was measured by absorption at 520 nm and kept at 4 °C until use.

For the directional functionalization, the protocol of Kumar and co-workers was followed with slight modifications [20]. Anti-rabbit goat IgG (Ab) and HRP were oxidized with periodate and incubated with the linker hydrazine dithiol. Briefly, 100 µL of Ab 1 mg/mL was incubated with 30 µL of 100 mM phosphate pH 7.4 and 10 µL of periodate 100 mM protected from light for 30 min. In the case of peroxidase, 200 µL of HRP 3 mg/mL were incubated with 20 µL of periodate 100 mM protected from light for 20 min. After these incubation times, 500 µL of PBS were added respectively to quench the reaction. Thereafter, 1.97 µL of 23.5 mM linker hydrazine dithiol were added and mixed for 2 h at room temperature protected from light. The proteins were buffer exchanged against phosphate buffer 10 mM pH 7.4 using a Hi-Trap desalting column using an Äkta Prime apparatus (GE-Healthcare, Upsala, Sweden). The Ab-linker and HRP-linker concentrations were measured by absorption at 280 nm and 403 nm, respectively, as well as by Bradford assay (data not shown). Afterwards, the appropriated amount of Ab-linker and HRP-linker were mixed with 1 mL of AuNPs and incubated for 20 min. Thereafter, 100 µg of m-PEG thiol were added and mixed again for 20 min. Subsequently, 100 µL of 1 mg/mL of BSA were incubated for 10 min more. Samples were centrifuged (5,000*g* 30 min) and re-suspended in 1 mL phosphate buffer 10 mM pH 7.4 containing 0.5% BSA and 0.01% Tween 20. This step was repeated twice but after the last wash, the complex was re-suspended in 400 µL. The complex concentration was measured by absorption at 520 nm and kept at 4 °C until use.

In case of the directional/adsorption functionalization, the protocol of both methods was followed with some modifications. Briefly, to 1 mL of synthesized AuNPs, 133 µL of 15 mM borate buffer pH 8.7 were added to adjust the pH. Then, the appropriate amount of Ab-linker was added to reach a final concentration of 2.25 ppm and the solution was mixed for 20 min at room temperature. After antibody incubation, the sample was mixed with nonmodified HRP to a final concentration of 144 ppm and shook for 20 min. Thereafter, sucrose (5%), BSA (0.5%), and Tween 10 (0.01%) were added to assure complex stability. The mixture was allowed to react for 10 min and purified by centrifugation at 7,500*g* for 30 min. The AuNP probe was re-suspended in 1 mL of borate buffer pH 8.7 containing 5% sucrose, 2% glycerol, and 0.01% Tween. The washing step was repeated once and the complex was re-suspended in 100 µL of mentioned buffer. The complex concentration was measured by absorption at 520 nm and kept at 4 °C until use.

Covalent functionalization was achieved using hetero-bifunctional linkers of polyethyleneglycol (PEG). In this case, AuNPs were incubated overnight with methyl-PEG-thiol (mPEG thiol, $n = 6$) and PEG-thiol acid ($n = 7$) in order to create a mixed monolayer of linker on the nanoparticle. 1 mL containing 0.075 M of mPEG thiol and 0.025 M of PEG-thiol acid was added to 100 mL of synthetized AuNPs and maintained overnight under stirring. Subsequently, the AuNPs were washed by centrifugation at 18,000*g* for 30 min and the obtained pellet was re-suspended in a smaller volume of water to arrive at a concentration factor of approximately ×30. The conjugation to antibody and peroxidase was achieved by applying the carbodiimide method to carboxylic groups of PEG-thiol acid [30]. Accordingly, 750 µL of AuNPs-PEG where added to 750 µL of a mixture of EDC/NHS 40/20 mM and incubated for 30 min at room temperature. Thereafter, AuNPs were centrifuged at 18,000*g* for 30 min and re-suspended in 1,500 µL of a solution containing 25 ppm Ab and 440 ppm HRP in borate buffer pH 8.7 and incubated for 4 h at room temperature. Finally, AuNP-Ab-HRP complexes were washed twice at 18,000*g* for 30 min and re-suspended in 300 µL Tris-HCl 20 mM pH 8.8 20% glycerol and 1% BSA. The complex concentration was measured by absorption at 520 nm and kept at 4 °C until use.

In all cases, the incubation of the proteins with AuNPs was made at room temperature stirring the mixture in a carrousel.

## Design of experiments

To build the design of experiments (DOE) matrix, some conjugations of AuNPs with antibody and HRP and simple ELISA assays were developed. For this, samples were functionalized at different ratios of HRP/Ab (1:5, 1:40, 1:75) according to the adsorption and directional procedure described above. 96-Multiwell plates were coated with a fixed concentration of rabbit IgG (1 µg/mL) 1 h at 37 °C in 10 mM carbonate buffer pH 9.6. Afterwards, these plates were washed one time with phosphate buffer saline (PBST, 0.5% Tween 20), blocked with 1% BSA in PBST and incubated with the different samples of AuNP probes for 30 min. For each HRP/Ab ratio, three different concentrations of AuNP probes (measured as the absor-

bance at 520 nm) were assayed, 0.05, 0.25 and 0.50 absorbance units (AU). Subsequently, the plates were washed three times with PBST and 100 µL of HRP substrate were added (TMB 0.1 mg/mL, 0.006% $H_2O_2$ in 40 mM pH 5.5 citrate buffer). After 15 min at room temperature, the reaction was stopped by adding 50 µL of 4 N $H_2SO_4$ and the absorbance was measured at 450 nm in a Synergy Mx microplate reader from Biotek.

The results were used to build a surface-of-response graphic and to determine the best HRP/Ab ratio and probe concentration in order to optimize the ELISA using DOE pro XL 2010 software from Microsoft.

### ELISA rabbit IgG probed by goat anti-IgG-HRP and AuNP conjugates

The ELISA plate was coated using different rabbit IgG concentrations (ranging 0–1 µg/mL) in carbonate buffer 10 mM pH 9.6 for 4 h at RT or overnight at 4 °C. Then the plates were washed three times with PBST and blocked using BSA 1% in PBST at 37 °C for 30 min. The plates were washed three times with PBST and incubated with 100 µL of goat anti-rabbit IgG-HRP conjugated (Ab-HRP, dilution 1:10,000) or AuNP probes (AuNP-Ab-HRP) at the appropriate concentration at 37 °C for 30 min in buffer NaPi 10 mM pH 7.4, 0.5% BSA and 0.05% Tween 20. The plates were washed four times with PBST and incubated 5 min with HRP substrate. The reaction was stopped by adding 50 µL of $H_2SO_4$ 4 N and the absorbance was measured at 450 nm in a microplate reader. For each step a volume of 100 µL was used, except for the washing step where 300 µL were used. A curve log(agonist)–response was adjusted to obtained data $y = \min + (\max - \min)/(1 + 10^{\log(EC50 - X)})$.

### ELISA gliadin probed by goat anti-IgG and AuNP conjugates

The ELISA plate was coated using different gliadin concentrations ranging from 0–1 µg/mL dilutions 1:5 in carbonate buffer 10 mM pH 9.6 4 h at RT. Then, the plates were washed three times with PBST and blocked with BSA 1% in PBST at 37 °C for 30 min. The plates were washed three times with PBST and incubated with rabbit anti-gliadin antibody diluted 1:5,000 times in PBST for 30 min at room temperature. The plate was washed three times with PBST and incubated with the appropriated amount of anti-IgG-HRP (from now Ab-HRP, dilution 1:10,000) or Au probes at 37 °C for 30 min in the buffer NaPi 10 mM pH 7.4, 0.5% BSA and 0.05% Tween 20. The plates were then washed four times with PBST and incubated for 5 min with HRP substrate. The reaction was stopped by adding 50 µL $H_2SO_4$ 4 N and read at 450 nm. For each step, a volume of 100 µL was used, except for the washing step where 300 µL were used. A curve log(agonist)–response is adjusted to obtained data $y = \min + (\max - \min)/(1 + 10^{\log(EC50 - X)})$.

## Materials

The BSA fraction VI for blocking was purchased from Merck. ELISA Maxisorb plates were acquired from Nunc. The linker PEG6-hydrazide aromatic dialkanedithiol was used for derivation of antibody and HRP in the directional conjugation and was obtained from NanoScience Instruments. The linkers mPEG-thiol ($n = 6$) and PEG-thiol acid ($n = 7$) for the covalent functionalization were acquired from Polypure. Rabbit IgG, polyclonal goat anti-rabbit IgG, goat anti-rabbit IgG HRP conjugated, HRP type VI, gliadin from wheat gluten, rabbit anti-gliadin and all other chemicals used were purchased from Sigma-Aldrich.

## Supporting Information

### Supporting Information File 1

Additional figure.
[http://www.beilstein-journals.org/bjnano/content/supplementary/2190-4286-8-27-S1.pdf]

## Acknowledgements

The authors would like to thank the Government of Navarra, Department of Innovation, Business and Employment for financial support within the project SABioD.

## References

1. Yalow, R. S.; Berson, S. A. *J. Clin. Invest.* **1960,** *39,* 1157–1175. doi:10.1172/JCI104130
2. Porstmann, T.; Kiessig, S. T. *J. Immunol. Methods* **1992,** *150,* 5–21. doi:10.1016/0022-1759(92)90061-W
3. Rebe Raz, S.; Haasnoot, W. *TrAC, Trends Anal. Chem.* **2011,** *30,* 1526–1537. doi:10.1016/j.trac.2011.04.016
4. Deshpande, S. S. *Enzyme Immunoassays;* Springer: Berlin, Germany, 1996. doi:10.1007/978-1-4613-1169-0
5. Wu, W.; Li, J.; Pan, D.; Li, J.; Song, S.; Rong, M.; Li, Z.; Gao, J.; Lu, J. *ACS Appl. Mater. Interfaces* **2014,** *6,* 16974–16981. doi:10.1021/am5045828
6. Cao, X.; Ye, Y.; Liu, S. *Anal. Biochem.* **2011,** *417,* 1–16. doi:10.1016/j.ab.2011.05.027
7. Zhang, Q.; Zhao, B.; Yan, J.; Song, S.; Min, R.; Fan, C. *Anal. Chem.* **2011,** *83,* 9191–9196. doi:10.1021/ac2023684
8. Zhou, Y.; Tian, X.-L.; Li, Y.-S.; Pan, F.-G.; Zhang, Y.-Y.; Zhang, J.-H.; Yang, L.; Wang, X.-R.; Ren, H.-L.; Lu, S.-Y.; Li, Z.-H.; Chen, Q.-J.; Liu, Z.-S.; Liu, J.-Q. *Biosens. Bioelectron.* **2011,** *26,* 3700–3704. doi:10.1016/j.bios.2011.02.008
9. Oaew, S.; Charlermroj, R.; Pattarakankul, T.; Karoonuthaisiri, N. *Biosens. Bioelectron.* **2012,** *34,* 238–243. doi:10.1016/j.bios.2012.02.011
10. Shen, Z.; Hou, N.; Jin, M.; Qiu, Z.; Wang, J.; Zhang, B.; Wang, X.; Wang, J.; Zhou, D.; Li, J. *Gut Pathog.* **2014,** *6,* 14. doi:10.1186/1757-4749-6-14
11. Jiang, T.; Song, Y.; Wei, T.; Li, H.; Du, D.; Zhu, M.-J.; Lin, Y. *Biosens. Bioelectron.* **2016,** *77,* 687–694. doi:10.1016/j.bios.2015.10.017

12. Ambrosi, A.; Airò, F.; Merkoçi, A. *Anal. Chem.* **2010,** *82,* 1151–1156. doi:10.1021/ac902492c
13. Luo, Y.; Zhang, B.; Chen, M.; Jiang, T.; Zhou, D.; Huang, J.; Fu, W. *J. Transl. Med.* **2012,** *10,* 24. doi:10.1186/1479-5876-10-24
14. Song, S.; Qin, Y.; He, Y.; Huang, Q.; Fan, C.; Chen, H.-Y. *Chem. Soc. Rev.* **2010,** *39,* 4234–4243. doi:10.1039/c000682n
15. Jans, H.; Huo, Q. *Chem. Soc. Rev.* **2012,** *41,* 2849–2866. doi:10.1039/C1CS15280G
16. Daniel, M.-C.; Astruc, D. *Chem. Rev.* **2004,** *104,* 293–346. doi:10.1021/cr030698+
17. Ciaurriz, P.; Bravo, E.; Hamad-Schifferli, K. *J. Colloid Interface Sci.* **2014,** *414,* 73–81. doi:10.1016/j.jcis.2013.09.039
18. Tellechea, E.; Wilson, K. J.; Bravo, E.; Hamad-Schifferli, K. *Langmuir* **2012,** *28,* 5190–5200. doi:10.1021/la2050866
19. Fernández, F.; Sánchez-Baeza, F.; Marco, M.-P. *Biosens. Bioelectron.* **2012,** *34,* 151–158. doi:10.1016/j.bios.2012.01.036
20. Kumar, S.; Aaron, J.; Sokolov, K. *Nat. Protoc.* **2008,** *3,* 314–320. doi:10.1038/nprot.2008.1
21. Puertas, S.; Batalla, P.; Moros, M.; Polo, E.; del Pino, P.; Guisán, J. M.; Grazú, V.; de la Fuente, J. M. *ACS Nano* **2011,** *5,* 4521–4528. doi:10.1021/nn200019s
22. Aubin-Tam, M.-E.; Hamad-Schifferli, K. *Biomed. Mater. Bristol Engl.* **2008,** *3,* 034001. doi:10.1088/1748-6041/3/3/034001
23. Cifuentes-Rius, A.; de Puig, H.; Kah, J. C. Y.; Borros, S.; Hamad-Schifferli, K. *ACS Nano* **2013,** *7,* 10066–10074. doi:10.1021/nn404166q
24. Mena, M. C.; Lombardía, M.; Hernando, A.; Méndez, E.; Albar, J. P. *Talanta* **2012,** *91,* 33–40. doi:10.1016/j.talanta.2011.12.073
25. Tjon, J. M.-L.; van Bergen, J.; Koning, F. *Immunogenetics* **2010,** *62,* 641–651. doi:10.1007/s00251-010-0465-9
26. Geoghegan, W. D.; Ackerman, G. A. *J. Histochem. Cytochem.* **1977,** *25,* 1187–1200. doi:10.1177/25.11.21217
27. Patrick, J.; Whitcomb, M. J. A. *DOE Simplified: Practical tools for effective experimentation,* 3rd ed.; CRC Press: Hoboken, NJ, U.S.A., 2015.
28. Geoghegan, W. D. *J. Histochem. Cytochem.* **1988,** *36,* 401–407. doi:10.1177/36.4.3346540
29. Nygren, H.; Hansson, H. A. *J. Histochem. Cytochem.* **1981,** *29,* 266–270. doi:10.1177/29.2.6265544
30. Hermanson, G. T. *Bioconjugate Techniques,* 3rd ed.; Academic Press: Boston, MA, U.S.A., 2013; pp 259–273. doi:10.1016/B978-0-12-382239-0.00004-2
31. Rao, S. V.; Anderson, K. W.; Bachas, L. G. *Microchim. Acta* **1998,** *128,* 127–143. doi:10.1007/BF01243043
32. Aubin-Tam, M.-E.; Hamad-Schifferli, K. *Langmuir* **2005,** *21,* 12080–12084. doi:10.1021/la052102e
33. Aubin-Tam, M. E.; Hamad-Schifferli, K. In *Symposium O – Nanoparticles and Nanostructures in Sensors and Catalysis,* MRS Online Proceedings Library Archive: Cambridge, MA, U.S.A., 2005.
34. Gagner, J. E.; Lopez, M. D.; Dordick, J. S.; Siegel, R. W. *Biomaterials* **2011,** *32,* 7241–7252. doi:10.1016/j.biomaterials.2011.05.091
35. Zhan, L.; Wu, W. B.; Yang, X. X.; Huang, C. Z. *New J. Chem.* **2014,** *38,* 2935. doi:10.1039/c4nj00253a

## License and Terms